UNIVERSITY OF SOUTHAMPTON

PERFORMANCE PREDICTION OF HIGH LIFT RUDDERS OPERATING UNDER STEADY AND PERIODIC FLOW CONDITIONS

James Charles Date

Doctor of Philosophy

FACULTY OF ENGINEERING AND APPLIED SCIENCE
SCHOOL OF ENGINEERING SCIENCES, FLUID-STRUCTURE INTERACTION RESEARCH GROUP

July 2001

UNIVERSITY OF SOUTHAMPTON

ABSTRACT

FACULTY OF ENGINEERING AND APPLIED SCIENCE
SCHOOL OF ENGINEERING SCIENCES, FLUID-STRUCTURE INTERACTION RESEARCH GROUP

Doctor of Philosophy

PERFORMANCE PREDICTION OF HIGH LIFT RUDDERS OPERATING UNDER STEADY AND PERIODIC FLOW CONDITIONS

James Charles Date

A detailed investigation has been conducted into the use of Reynolds-Averaged Navier-Stokes (RANS) methods, for predicting the performance of conventional and high lift rudder sections, operating under free stream and periodic propeller flow conditions. The standard and RNG $k-\varepsilon$ turbulence models with wall functions are applied. A methodical step wise approach to solving the propeller-rudder flow problem is shown to be necessary, in order to ensure the highest degree of accuracy and credibility in the results. By conducting detailed verification and validation studies at every stage of the research, the critical parameters required for accurate rudder performance prediction, in terms of skin frictional drag, pressure drag and lift force are identified. Steady state and time-accurate computations of the free stream flow over a NACA 0012 section fitted with a Gurney flap are conducted. Good agreement is found between the computed and experimental results, validating the RANS method for predicting flows about high lift rudder sections with blunt trailing edge features. The RANS method is shown to be capable of predicting the performance response of both conventional and high lift rudder sections, when subjected to periodic transverse gusts, similar to the flow produced in the race of a propeller. The research presents the first published RANS computations for high lift Schilling rudder sections, operating under free stream and periodic flow conditions. The high quality grids created around the rudder sections investigated, consisted of between 40000 and 85000 grid nodes.

Contents

In loving memory of my Grandparents

Mr & Mrs A. Savelio

and

Mr & Mrs A.C. Date

ACKNOWLEDGEMENTS

I would like to take this opportunity to thank a number of people whose encouragement, support and friendship have been vital in helping me through, what can be described in fluid dynamic terms, as three "turbulent" years.

Special thanks goes to Dr. Stephen Turnock for his supervision, enthusiasm and guidance, especially at the difficult times.

I would also like to thank Dr. Anthony Molland, for his continual interest in my research, and for providing me with ideas and encouragement.

I cannot begin to express my gratitude to my close friends in both Bristol (AKA "The Bristol Massive") and Southampton. Your support and friendship during my Ph.D. has meant a great deal. No longer will there be any comedy value in the rhetorical question, "Haven't you finished yet"?

Thanks to Hamworthy KSE Group Limited, Fleets Corner, Poole, Dorset BH17 0JT, for fully funding my Ph.D. studentship in the School of Engineering Sciences, Ship Science.

Finally, I would like to thank my parents, Robert and Mary, who have supported me throughout my academic endeavours. Without your encouragement, understanding and patience, none of this could have been possible.

NOMENCLATURE

A	Three-dimensional axial force	(kg m/s^2)
A_R	Rudder area	(m^2)
B	Constant in log-law layer equation	
C	Courant number	
C_{BM}	Bending moment coefficient	
C_D	Three-dimensional drag coefficient	
C_{DI}	Induced drag coefficient	
C_{D0}	Three-dimensional zero-lift drag coefficient	
C_F	Three-dimensional frictional drag coefficient	
C_L	Three-dimensional lift coefficient	
C_M	Three-dimensional torque moment coefficient	
C_N	Three-dimensional normal force coefficient	
C_p	Pressure coefficient	
C_{PV}	Three-dimensional viscous pressure drag coefficient	
C_R	Three-dimensional resultant force coefficient	
D	Propeller diameter	(m)
D	Three-dimensional drag force	(kg m/s^2)
D_F	Three-dimensional frictional drag force	(kg m/s^2)
D_I	Induced drag force	(kg m/s^2)
D_{PV}	Three-dimensional viscous pressure drag force	(kg m/s^2)
E	Log-layer constant	
F_n	Froude Number	
I	Grid point index	
J	Grid point index	
J	Advance ratio	
K	Grid point index	
K_T	Thrust coefficient	

L	Three-dimensional lift force	(kg m/s^2)
L	Characteristic length	(m)
N	Number of propeller blades	
N_{it}	Number of outer iterations	
P	Propeller pitch	(m)
P	Mean pressure obtained from time-averaging process	(kg/m s^2)
P_k	Production of kinetic energy	(m^2/s^2)
R	Total resultant force	(kg m/s^2)
R_n	Reynolds number	
S_t	Strouhal number	
T	Period	(s)
T_i	Turbulence intensity	
U_i	Mean velocity component in the Cartesian direction i	(m/s)
U_∞	Free stream velocity	(m/s)
V	Ship speed	(m/s)
a	Two-dimensional axial force	(kg m/s^2)
b	Rudder span	(m)
c	Rudder chord	(m)
c	Wave speed	(m/s)
c_d	Two-dimensional drag coefficient	
$\overline{c_d}$	Two-dimensional mean drag coefficient	
c_d^*	Two-dimensional normalised drag coefficient	
$\overline{c_d^*}$	Two-dimensional mean normalised drag coefficient	
c_{d0}	Two-dimensional zero-lift drag coefficient	
c_{d0}^*	Two-dimensional normalised zero-lift drag coefficient	
c_f	Two-dimensional frictional drag coefficient	
c_l	Two-dimensional lift coefficient	
$c_{l,max}$	Two-dimensional maximum lift coefficient	
c_m	Two-dimensional torque moment coefficient	

c_n	Two-dimensional normal force coefficient	
c_{pv}	Two-dimensional viscous pressure drag coefficient	
c_r	Two-dimensional resultant force coefficient	
cp_c	Centre of pressure chord-wise from L.E.	(m)
cp_s	Centre of pressure span-wise from root	(m)
$c_{\varepsilon 1}$	Constant in standard and RNG $k-\varepsilon$ turbulence models	
$c^*_{\varepsilon 1}$	Constant in RNG $k-\varepsilon$ turbulence model	
$c_{\varepsilon 2}$	Constant in standard and RNG $k-\varepsilon$ turbulence models	
c_μ	Constant in standard $k-\varepsilon$ turbulence model	
d	Location of the stock from L.E.	(m)
d	Two-dimensional drag force	(kg m/s^2)
d	Base dimension	(m)
d_f	Two-dimensional frictional drag force	(kg m/s^2)
d_{pv}	Two-dimensional viscous pressure drag force	(kg m/s^2)
f	Frequency	(Hz)
f_i	Body force term in the Cartesian direction i	(kg m/s^2)
g	Acceleration due to gravity	(m/s^2)
h	Gurney flap height	(m)
k	Turbulent kinetic energy	(kg m^2/s^2)
k	Induced drag factor	
k	Reduced frequency	
l	Two-dimensional lift force	(kg m/s^2)
l	Turbulent length scale	(m)
n	Revolutions per second	(1/s)
n_ζ	Number of grid cells in the wake of a section	
n_η	Number of grid cells radiating from a section	
n_ξ	Number of grid cells around a section	
n_ψ	Number of grid cells across the T.E. of a Schilling section	
p	Pressure	(kg/m s^2)

p'	Pressure fluctuation	(kg/m s^2)
p_∞	Pressure in undisturbed far field	(kg/m s^2)
r	Distance of outer boundaries from section	(m)
t	Maximum rudder thickness	(m)
t	Time	(s)
u	Velocity component in the x-direction	(m/s)
u_i	Velocity component in the Cartesian direction i	(m/s)
u_i'	Velocity fluctuation component in the Cartesian direction i	(m/s)
u_p	First node velocity away from the wall	(m/s)
u^+	Non-dimensional first node velocity from wall	
$\overline{u_i'u_j'}$	Reynolds stresses	(m^2/s^2)
v	Velocity component in the y-direction	(m/s)
v_0	Transverse gust velocity amplitude in the y-direction	(m/s)
x_i	Cartesian coordinates, $i = 1, 2, 3$	(m)
x_p	Propeller longitudinal location	(m)
x_v	Vertex node location in the x-direction	(m)
y_p	Propeller lateral location	(m)
y_p	First node location away from the wall	(m)
y^+	Non-dimensional first node distance from wall	
z_p	Propeller vertical location	(m)
Λ	Aspect ratio	
α	Angle of incidence	(deg)
α_ε	Constant in RNG $k-\varepsilon$ turbulence model	
α_E	Effective angle of incidence	(deg)
α_k	Constant in RNG $k-\varepsilon$ turbulence model	
α_{stall}	Stall angle of incidence	(deg)
β	Drift angle	(deg)
β	Variable used in the RNG $k-\varepsilon$ model	
δ_{ij}	Kronecker delta	

ε	Dissipation rate of turbulent kinetic energy	(m^2/s^3)
η	Variable in RNG $k-\varepsilon$ turbulence model	
η_0	Variable in RNG $k-\varepsilon$ turbulence model	
κ	Von Kármán constant	
μ	Dynamic viscosity	(kg/m s)
ν	Kinematic viscosity	(m^2/s)
ν_t	Kinematic eddy viscosity	(m^2/s)
ξ	Propeller coverage ratio	
ρ	Fluid density	(kg/m^3)
σ_ε	Constant in standard $k-\varepsilon$ model	
σ_k	Constant in standard $k-\varepsilon$ model	
τ_w	Local skin friction	(kg/m s^2)
ω	Circular passage frequency	(rad/s)

GLOSSARY

ASME	American Society of Mechanical Engineers
CFD	Computational Fluid Dynamics
CFL	Courant-Friedrichs-Lewy
DNS	Direct Navier-Stokes
DNV	Det Norske Veritas
FORTRAN	Formula Translation
GUI	Graphical User Interface
HSVA	Hamburgische Schiffbau-Versuchsanstalt GmbH
IDEAS	Trademark of Structural Dynamics Research Corporation
IfS	Institut für Schiffbau
IMO	International Maritime Organisation
ITTC	International Towing Tank Conference
LDA	Laser Doppler Anemometry
L.E.	Leading Edge
LES	Large Eddy Simulations
MSC	Maritime Safety Committee
NACA	National Advisory Committee for Aeronautics
PATRAN	Trademark of MacNeal-Schwendler Corporation
PISO	Pressure Implicit with Splitting Operators
QUICK	Quadratic Upstream Interpolation for Convective Kinetics
RANS	Reynolds-Averaged-Navier-Stokes
RNG	Renormalization Group
R.P.M	Revolutions Per Minute
SIMPLE	Semi-Implicit Method for Pressure-Linked Equations
T.E.	Trailing Edge
URF	Under Relaxation Factor
VLCC	Very Large Crude Oil Carrier

Chapter 1

Introduction

1.1 Motivation

A wide variety of vehicles operate in the marine environment, from small unmanned deep sea craft, to very large crude oil carriers (VLCCs). The vast majority of these craft are directionally controlled with the aid of some form of movable control surface, or rudder. The manoeuvrability of a vessel is highly dependent on the design and location of its rudder, and the nature of the flow field in which the rudder operates. Often the rudder will be located directly aft of the propulsor, in order to make good use of the added velocity in the race, and so provide an increased turning force. However, being located in this asymmetric, accelerating and swirling flow field, signifIcantly alters the rudder performance characteristics from those encountered when operating in a free stream [1]. The propulsor has the effect of altering the local flow velocity and incidence passing over the rudder, thus altering its performance.

Accurate estimation of both steady and unsteady performance characteristics, i.e. the forces and moments, of rudders is necessary for a number of reasons:

- Safety Requirements

  The manoeuvrability of a ship is a fundamental component of its safety, and as such is subject to certain standards and regulations. The regulations dictating the minimum manoeuvring criteria of vessels are enforced by the International Maritime Organisation (IMO) [2]. In order to quantify a ship's manoeuvrability, and hence assess its compliance with the requirements of the IMO at the design stage, the forces and moments acting on the rudder need to be accurately estimated.

- Structural Design

  For many vessels, the rudder is the sole means of directional control. It is, therefore, of paramount importance that rudders are designed to withstand the forces anticipated in operation. In order to determine the rudder scantling, stock, bearing and steering gear particulars, the forces and moments acting on the rudder must be known. Class rules such as those derived by Lloyds Register [3], Det Norske Veritas (DNV) [4] and others provide naval architects with rudder structural design criteria, based on a combination of theory and full scale data. However, when these rules are applied to some more extreme types of rudder, the forces may not be adequately predicted, leading to the specification of inappropriate design particulars. There is, therefore, a need for accurate force estimation in order to quantify any possible errors, and to facilitate better structural design, and the development of class rules which reflect the true performance of different rudder devices.

- Efficiency

  Increasing pressures on ship owners and operators for their ships to be efficient and fast, means that the reduction of ship drag is of major importance. Although the rudder drag on a ship, such as a VLCC, accounts for a small proportion of the total ship drag, any possible reductions are of importance, in order to improve the overall efficiency of the vessel. Even small improvements

($< 1\%$) can have a major impact on propulsive power and hence operating costs [5]. A rudder can, depending upon its type, design and location, increase the propulsive efficiency of a vessel, by recovering some of the energy lost in the race. An efficient rudder will, therefore, have low drag and be optimised to give the highest level of overall propulsive efficiency.

- Optimisation of Design

  Often, at the design stage of a vessel, the naval architect is presented with difficult decisions as to the type and design of the rudder which should be fitted. The choice of rudder is usually dictated by the owner and master mariner's preference, through experience. However, certain types of rudder are often overlooked, as knowledge of their actual performance may be limited. A single tool, which could be used to predict the performance of different sections on the same benchmark, would therefore be useful, potentially opening up new design options.

The need for research into theoretical rudder performance prediction was expressed by the International Towing Tank Committee (ITTC) in 1987 [6] and repeated more recently in 1999 [7].

Advances in computing technology over the last two decades have resulted in the development of a number of theoretical approaches, which can be used to predict rudder performance. These methods fall under the general heading of Computational Fluid Dynamics (CFD). The most widely used of these theoretical approaches, at the current time, involves solution of the Reynolds-Averaged Navier-Stokes (RANS) equations. Using this approach, it is theoretically possible for the viscous performance of practically any shaped rudder section to be predicted. This capability makes the RANS approach an attractive method for obtaining the important manoeuvring, structural and efficiency design information required by naval architects.

Although the RANS solution approach has been used for a number of years, its full

capabilities have yet to be exploited for rudder design. However, this current state of the art technology has the ability, if correctly applied, to provide answers to many of the key issues surrounding the complex hull, propeller and rudder interaction problem.

1.2 Aims and Objectives

At the current time, it is not possible to use RANS methods to predict the full unsteady interaction of the hull, propeller and rudder, to the level required or demanded by designers [8, 9]. The aim of this research has been to address a number of the problems associated with using the RANS method to predict accurately the performance of conventional and high lift rudders, operating within the periodic wake produced behind a ship's propeller. In order to obtain a better understanding of problems associated with RANS flow modelling, the complex propeller-rudder flow problem was broken down into a number of smaller investigations. Each investigation was focused at addressing one or a number of critical aspects associated with the RANS modelling of steady and periodic flows around two-dimensional rudder sections. The primary objectives of the work were as follows:

- To investigate the various methods which can be used to predict steady and unsteady rudder performance, and to highlight the problems associated with both experimental and computational performance prediction methods.
- To conduct two-dimensional performance predictions of conventional and high lift rudder sections operating under free stream conditions, and to identify the critical parameters which need to be considered in order to obtain credible solutions.
- To assess the two-dimensional performance of conventional and high lift rudder sections, subjected to periodic flow conditions similar to those produced in a

propeller race, thereby making an assessment of the effect that flow unsteadiness has on rudder performance.

- To investigate the issue of model to full size rudder scaling.

Particular attention was focused on capturing, and understanding the complex two-dimensional flow phenomena around various rudders, with the aim of improving design. Through the use of detailed validation studies, it was hoped that greater confidence in the use of RANS methods in the marine context, could be achieved. The knowledge gained from the work presented, will provide important information as to the considerations needed to obtain credible solutions to the whole hull, propeller and rudder interaction problem, using the RANS method, when adequate computing resources become available.

1.3 Rudder Design Criteria

Rudder design is a compromise between a number of opposing requirements, which have varying priorities according to the vessel in question. The traits usually striven for in a good rudder design are: minimal drag, maximum turning ability, high directional stability and high controllability. Other important considerations are low weight, ease of construction, a large degree of structural integrity and high reliability. An effective rudder design, therefore, requires a careful compromise between manoeuvrability, hydrodynamics and structural performance.

1.3.1 Manoeuvring

As previously stated, a vessel must satisfy a number of manoeuvring criteria. As of July 1994 the IMO introduced interim manoeuvring standards applying to ships of all rudder and propulsion configurations over 100 m in length, and to all Gas

and Chemical carriers regardless of size. IMO Resolution A.751(18) [10] recommends the manoeuvring performance standards, MSC/Circ.644 [2] provides guidance for the application of those standards, whilst MSC/Circ.389 [11] addresses the problem of defining manoeuvring characteristics, and their estimation during design. The IMO guidelines state, that all ships should have manoeuvring qualities which permit them to keep course, to turn, to check turns, to operate at acceptably slow speeds and to stop, all in a satisfactory manner. However, ship owners/operators often introduce more stringent requirements depending upon the operational role of their vessel. The manoeuvring characteristics which must be considered in order to fulfil these requirements are listed below:

- Initial turning ability
- Sustained turning ability
- Yaw checking ability
- Stopping ability
- Course-keeping ability

Of the above five manoeuvring characteristics the initial turning, yaw checking and course-keeping abilities are the most important. These manoeuvring characteristics are quantified through a number of tests carried out in the initial ship sea trials, as recommended in the Manoeuvring Trial code of the ITTC [12] and the IMO circular MSC/Circ.389 [11]. The standard manoeuvring tests carried out during ship trials usually involve a number of the following:

- Turning circle test
- Spiral manoeuvre
- Pull-out manoeuvre

- Zigzag manoeuvre
- Stopping trial
- Hard rudder test
- Man-overboard manoeuvre

The IMO requires that these manoeuvres be carried out at the ship service speed in deep water (water depth $>$ 2.5 ship draft), little wind (less than Beaufort 4) and calm water, to ensure comparability with other ships. Many ship owner/operators extend the IMO tests to slow speeds in order to assess the ability of the vessel to manoeuvre safely, both at reduced speeds and in a restricted environment.

The rudder, other control surfaces and control devices are responsible for fulfilling the afore mentioned manoeuvring criteria. Although a number of control devices are often used to assist in the control of a vessel, the rudder is by far the most prominent. The effectiveness of a rudder as a directional control device is related to the magnitude of the force produced normal to the centre line of the vessel.

1.3.2 Hydrodynamics

The hydrodynamics of a rudder obviously dictate the attainable forces, which have vital implications upon manoeuvrability, as already mentioned. However, in terms of hydrodynamics, the second most important consideration is powering. From a ship powering point of view, it is desirable to minimise all the possible components of drag, in particular any drag from appendages, such as rudders. An efficient rudder design endeavours to maximise the lift/drag ratio within the typical operational incidence range. For a rudder operating in a propeller race, local flow incidence angles of between 10 and 15 degrees are not uncommon, in the zero incidence position [5]. Hence, reducing rudder drag between these angles of incidence, can improve the

efficiency of the vessel. It must also be noted, that prudent location of some types of rudder, can actually recover some of the rotational energy which would otherwise have been lost in the race, due to the damping or stator effect the rudder has on the rotating race [13, 14].

1.3.3 Structures

The structural engineering of a rudder not only has very clear implications upon reliability engineering, but also implicit influences upon its hydrodynamic capabilities. Often, a compromise needs to be made between the hydrodynamic and structural requirements of the rudder. One common decision naval architects are faced with, is the selection of a rudder section which has sufficient thickness, in order to accommodate the stock with the correct diameter, so as to satisfy the structural requirements. It should also be noted that distortion of the rudder, due to imposed loadings can often alter the hydrodynamic performance [15].

1.4 Rudder Performance

The rudder of a ship can be considered as part of a servo system, providing the transverse force and hence the turning moment needed for a vessel to change its attitude. The manoeuvring characteristics of a ship and thereby the effectiveness of its rudder, are directly related to the lift and drag forces acting on it. The action of these rudder forces through to the ship itself, results in the development of a torque and bending moment at the rudder stock. A concise outline of the forces and moments which act on a rudder will be given in the following section, since they will be referred to extensively throughout the Thesis. The theory behind the generation of the forces about lifting sections can be found in most general fluid dynamic texts and as such, will not be detailed here. White [16] provides a good general introduction to the

theory of lifting flows.

1.4.1 Rudder Forces

Figure 1 shows the forces acting on a three-dimensional rudder, i.e. rudder of finite aspect ratio, at an angle of incidence α, in a free stream of U_∞, unaffected by the wake of a ship or propeller race. The two principal forces acting on the rudder are lift (also known as side force) L, and drag D. The lift force acts perpendicular to the free stream, whilst the drag force acts in a direction parallel to the free stream. These forces are seen to act from a single point, known as the centre of pressure. The total resultant force R acting on the rudder, is obtained when the lift and drag forces are added vectorially. Resolution of the lift and drag forces into the ship axis system, gives rise to normal N and axial A force components. The rudder force components are usually expressed in terms of non-dimensional parameters. The standard ITTC non-dimensional [17] rudder force parameters are shown below in Equation 1 to Equation 4.

$$C_L = \frac{L}{\frac{1}{2}\rho A_R U_\infty^2} \tag{1}$$

$$C_D = \frac{D}{\frac{1}{2}\rho A_R U_\infty^2} \tag{2}$$

$$C_R = \sqrt{{C_L}^2 + {C_D}^2} \tag{3}$$

$$C_N = C_L \cos(\alpha) + C_D \sin(\alpha) \tag{4}$$

where, U_∞ is the free stream speed, ρ is the density of the fluid, A_R is the rudder plan form area (bc) and α is the rudder incidence angle.

The non-dimensional forces acting on a two-dimensional rudder, i.e. rudder of infinite aspect ratio, are usually represented by lower case coefficient parameters as shown

below in Equation 5 to Equation 8, where l and d denote the two-dimensional lift and drag forces per unit span acting on a rudder section of chord c.

$$c_l = \frac{l}{\frac{1}{2}\rho c U_\infty^2} \tag{5}$$

$$c_d = \frac{d}{\frac{1}{2}\rho c U_\infty^2} \tag{6}$$

$$c_r = \sqrt{{c_l}^2 + {c_d}^2} \tag{7}$$

$$c_n = c_l \cos(\alpha) + c_d \sin(\alpha) \tag{8}$$

1.4.2 Rudder Drag

The drag coefficient of a rudder can be regarded as being a measure of its efficiency, the smaller the drag for a given lift, the more effective the rudder. The drag force acting on a three-dimensional rudder consists of three components, frictional drag, viscous pressure drag and induced drag. For a rudder operating in the vicinity of the free-surface, there may also be a wave-making component of drag, however, this force is usually small and in this work will be neglected.

The frictional drag acting on a rudder, results from the viscous shearing stresses within the fluid boundary layer close to the rudder surface. The non-dimensional forms of this frictional drag force, for both three and two-dimensional rudders are given by Equation 9 and Equation 10.

$$C_F = \frac{D_F}{\frac{1}{2}\rho A_R U_\infty^2} \tag{9}$$

$$c_f = \frac{d_f}{\frac{1}{2}\rho c U_\infty^2} \tag{10}$$

The viscous pressure drag, as the name suggests, results from the viscous nature of the fluid, although less directly than the frictional drag. This drag force occurs, due to distortion of the fluid flow around the rudder, as a result of the developing boundary layer and if present, regions of separation. Fundamentally, this occurs because the pressure forces at the front and rear of the rudder section, are not being balanced due to energy losses within the boundary layer. The non-dimensional forms of this pressure drag force for both three and two-dimensional rudders, are given by Equation 11 and Equation 12.

$$C_{PV} = \frac{D_{PV}}{\frac{1}{2}\rho A_R U_\infty^2} \tag{11}$$

$$c_{pv} = \frac{d_{pv}}{\frac{1}{2}\rho c U_\infty^2} \tag{12}$$

When a three-dimensional rudder operates at an angle of incidence, another drag force, known as induced drag, is experienced by the rudder. This drag force is produced as a consequence of the difference in pressure between the two sides of the rudder, which promotes the formation of vortices at the rudder tips. These vortices manifest themselves as a down-wash across the rudder, thus modifying the free stream inflow incidence angle. This effective rotation induces a component of normal force acting in the free stream direction, giving rise to an added drag component. The non-dimensional form of this induced drag force is given by Equation 13.

$$C_{DI} = \frac{D_I}{\frac{1}{2}\rho A_R U_\infty^2} \tag{13}$$

Classical three-dimensional lifting surface theory [16] approximates the total drag on a three-dimensional lifting surface of high aspect ratio, using the classical formula given in Equation 14.

$$C_D = C_{D0} + \frac{k}{\pi \Lambda} C_L^2 \tag{14}$$

where, C_{D0} is the three-dimensional zero-lift drag coefficient, Λ is the rudder aspect ratio and k is the induced drag factor, the value of which depends on plan-form shape,

i.e. taper ratio, with a minimum value of $\frac{1}{\pi\Lambda}$. Ignoring any end effects, C_{D0} can be assumed equal to the two-dimensional zero-lift drag coefficient, c_{d0}. In reality both C_{D0} and c_{d0} vary with incidence angle, depending on the relative contributions of c_{pv} and c_f as shown in Equation 15.

$$c_{d0} = c_{pv}(\alpha) + c_f(\alpha) \tag{15}$$

However, for lifting surfaces operating at low incidence angles, the relative contributions from c_{pv} and c_f are often considered constant.

1.4.3 Rudder Moments

The normal force component mentioned previously, is responsible for the generation of the torque moment about the stock. The product of the normal force times the distance of the chord-wise centre of pressure from the rudder stock, yields the torque moment; as shown in Figure 1. The non-dimensional form of this torque moment for a three-dimensional rudder is defined in Equation 16.

$$C_M = \frac{C_N \times (d - cp_c)}{c} \tag{16}$$

where, cp_c is the dimensional chord-wise location of the centre of pressure, and d is the stock location, both measured from the leading edge.

The total resultant force component mentioned previously, is responsible for the generation of the bending moment on the rudder stock about the root section. The product of the normal force times the distance of the span-wise centre of pressure from the rudder root, yields the bending moment; as shown in Figure 1. The non-dimensional form of this bending moment is defined in Equation 17.

$$C_{BM} = \frac{C_R \times cp_b}{b} \tag{17}$$

where, cp_b is the dimensional span-wise location of the centre of pressure, measured from the rudder root, and b is the rudder span.

1.4.4 Hull, Propeller and Rudder Flow

For a rudder in its operational condition, there exists a complex flow regime. The action of the hull through the water creates a non-uniform turbulent wake-field, which reaches the propeller and is then accelerated before passing over the rudder. In addition, the drift angle of the vessel relative to its direction of motion, can result in a skewed inflow into the propeller disk. The presence of a free surface and possible shallow water effects will also distort the inflow into the propeller disk. The performance of a rudder operating in this regime is significantly different from the performance experienced in a free stream. As such, the whole hull, propeller and rudder interaction problem is complex, consisting as it does, of steady, periodic and unsteady flows. Often, the influence of the hull on the flow is neglected, making it easier for the underlying physics of the flow for an isolated rudder and propeller to be investigated. The research presented in this Thesis will also neglect any flow effects resulting from the presence of an upstream hull.

1.4.5 Governing Rudder Performance Parameters

It was shown in the previous section that there a number of forces and moments acting on rudder operating at an angle of incidence. In order to address the hull, propeller and rudder interaction problem, it is necessary to identify the various independent parameters which affect these performance characteristics. The magnitude of these forces and moments are dependent on a number of parameters, relating to the fluid flow, geometry and location of rudder.

A number of researchers have carried out systematic experiments to quantify the effects of these parameters on rudder performance, with some of the most significant investigations being those conducted by Stierman [13, 14], English and Bain [18], Mathis and Gregory [19], Kerwin and Lewis [20], Turnock [21], Molland and Turnock [22] and Smithwick [23].

Molland and Turnock [22] have shown that the performance characteristic variables of C_L and C_D can be expressed as a function of non-dimensional variables, where the section shape, twist distribution etc. of the rudder and propeller are assumed fixed, see Equation 18.

$$C_L, C_D = f[J, R_n, \beta], [\alpha, \Lambda, t/c, d/c], [P/D], [x_p/D, y_p/D, z_p/D, \xi] \tag{18}$$

From Equation 18, it can be seen that for a particular propeller-rudder combination that the parameters reduce those given in Equation 19.

$$C_L, C_D = f[J, R_n, \beta], [\alpha], [P/D] \tag{19}$$

If follows that, for a given ship, relationships for manoeuvring should consider the above parameters. From these, the two fundamental controlling parameters are the propeller advance ratio J and the rudder incidence angle α. Reynolds number R_n and drift angle β will have less affect. Momentum theory, indicates that propeller induced velocities vary as a function of propeller thrust loading K_T/J^2 which is independent of P/D. This parameter is commonly used in propeller-rudder interaction studies. The geometrical group of parameters determines the magnitude of the influence of J and α on the performance of the propeller and rudder.

1.5 High Lift Rudders

The conventional rudder (plate or faired section) is an effective and simple manoeuvring device which has been used for several millenia. However, conventional rudders are most effective toward the high end of a ship's speed range, and/or when the propeller race speeds are high, since the generated lift force varies proportionally to the square of the speed. Consequently, conventional rudders often fail to provide the necessary turning force, needed for safe slow speed manoeuvring, in ports and restricted waterways.

This has lead to the development of what are classified as high lift rudders, whereby, the lift producing capabilities of a conventional rudder arrangement, positioned aft of a propeller are improved by the use of improved rudder profiles, and/or mechanical attachments. A number of different high lift systems have been designed, although only a small number have been utilised for practical reasons. A comprehensive review of various high lift rudder devices is provided by Cooke [24] and in the Pilotage and Ship Handling Handbook [25]. The most common high lift rudders are the flapped and modified profile types. Examples of these can be seen in Figure 2.

Flapped rudders are one of the oldest forms of high lift rudder, dating back to the late 1800s. Their design has remained virtually unchanged to the present day. These rudders usually consist of a conventional type rudder, fitted with a trailing edge flap. The flap angle is either controlled independently, or as function of the rudder incidence. Since a flap is used to provide the high lift characteristic, flapped rudders can be designed with sections similar to those of conventional rudder profiles. This allows the flapped rudder to exhibit a similar zero-incidence drag as conventional rudders, whilst being able to a achieve a significantly higher lift force, for a given incidence angle. The major draw back of flapped rudders, is the damage vulnerability of the flap and the poor vectoring of thrust at large angles of incidence.

Modified profile rudders produce better lift characteristics, through the use of high lift section profiles. The IfS [26], HSVA [27] and Schilling [28, 29] profiles are among the most frequently used high lift profiles. These sections all have greater maximum thickness to chord ratios, and more rounded leading edges than conventional rudders, promoting good flow properties over a wide range of rudder incidences. Both the IfS and HSVA sections have profiles which taper smoothly down to a trailing edge of relatively small thickness. However, the Schilling form is rather different, being equipped with a blunt "fish-tail" trailing edge. This trailing edge feature promotes flow acceleration and lift recovery over rear of the section, whilst significantly delaying the onset of stall [25]. The fish-tail trailing edge also improves the course-keeping ability of a vessel, with the only penalty being a small augment in drag [29]. The

main advantage of the Schilling over other high lift systems, like the flapped rudder, is that it is capable of operating at high angles of incidence, and vectoring between $50 - 70\%$ of the propellers ahead thrust, at angle of 90 degrees or greater to the ship centre line, with little or no forward movement [30]. Schilling rudders also have an advantage over flapped rudders, that their one piece construction is less vulnerable to damage.

The need for research in the field of high lift rudder performance was expressed by Hamworthy KSE, a leading manufacturer of high lift rudders. Wishing to improve the design and development of their Schilling type high lift rudders, Hamworthy KSE have been responsible for funding the research described in this Thesis. Through this research, Hamworthy KSE hoped to further their knowledge of the complex flows which exist around Schilling rudders.

1.6 Conclusions to Chapter

The motivation, together with the primary aims and objectives of the research detailed in this Thesis have been outlined.

An overview of the fundamental rudder performance characteristics, and the parameters which influence them have been presented. The implications of placing a rudder in the flow region directly aft of a hull-propeller arrangement have also been discussed.

It has been shown that an effective rudder design, demands a careful compromise between a number of opposing requirements. These requirements generally fall into one of three categories, manoeuvring, hydrodynamics and structures.

The advantages of fitting high lift rudders, together with a brief discussion of the various high lift rudders in common use was also given.

Chapter 2

Rudder Performance Prediction

2.1 Overview of Chapter

This chapter describes the various experimental, and theoretical methods which can be used to predict the performance of a rudder, operating under both free stream and propeller flow conditions. The merits and limitations of these approaches are discussed. Particular attention is focused on the use of theoretical methods, and the verification and validation procedures which need to be followed, if the solutions are to be regarded with any level of confidence. A research strategy aimed at addressing the important issues/implications surrounding the use of the RANS approach, in the modelling of high performance rudders, operating under steady and periodic flow conditions is outlined.

2.2 Experimental Methods

Before the advent of the computer and numerical modelling techniques, the principal way of predicting rudder performance, with reasonable accuracy, was through the use

of empirical techniques, such as model testing, or the extrapolation/interpolation of full scale ship rudder data. Today, even though advanced computational modelling methods exist, experimental testing is still the most widely used rudder performance prediction method. The most common experimental testing procedures are:

- Self-propelled free running model tests
- Open-water or wind tunnel tests
- Cavitation tunnel tests

These methods have become standardised during the last 50 years [7], and therefore have achieved a reasonable level of credibility. However, these methods have always had a number of significant drawbacks.

2.2.1 Limitations of Experimental Methods

The main difficulty with experimental modelling techniques is scale effect. Scale effect may be defined as the difference of the full-scale rudder performance, from that predicted through the scaling of the model test results. This can be attributed to the fact that experimental tests result in the laws of dynamic similitude being violated. The laws of dynamic similitude that apply to the lifting rudder problem are those governing cavitation, aeration, friction and wave-making [31, 32]. The extent to which these laws are violated in the testing procedure, dictates the amount by which the scaling process will be in error.

For free running model tests, all three of the laws of similitude must be satisfied. This means that Froude's law (which governs the dynamics of wave-making), Reynolds law (which governs the dynamics of the frictional drag and boundary layer growth) and

cavitation index effect, must be satisfied. The Froude number for a particular free-surface ship flow is characterised by Equation 20.

$$F_n = \frac{V}{\sqrt{gL}} \tag{20}$$

where V is the ship speed, g is acceleration due to gravity and L is the ship length.

The Reynolds number for a particular ship flow is characterised by Equation 21.

$$R_n = \frac{VL}{\nu} \tag{21}$$

where V is the ship speed, L is the ship length and ν is the kinematic viscosity.

Compliance of Froude number similitude leads to desirable conditions, where the ship model is small and the speed is low. However, this often results in the model Reynolds number being significantly lower than that of the full size ship. In particular, the Reynolds number may be such that the flow over the rudder is laminar, rather than fully turbulent, as in the case of the full scale vessel. Appendix A provides a simple calculation to highlight this problem. This is unfortunate, since Reynolds number effects can exert a very strong influence on the rudder performance, particularly with regard to the angle of attack at which stall occurs, and the maximum lift coefficient which is produced by the rudder. If the flow over the model's rudder is laminar, then premature stall can occur, giving conservative estimates of the maximum lift coefficient and rudder stall angle [5, 31, 32].

Open-water/Wind tunnel tests have the advantage that Froude's law does not need to be satisfied, hence allowing the tests to be carried out at higher Reynolds numbers, better satisfying Reynolds law [31]. It is still, however, often difficult to obtain a satisfactory correlation between the model and full scale test results. Problems such as wind tunnel blockage effects and transition stimulation can all contribute to errors in the correlation procedure.

With regard to cavitation, it is believed that there may be a scale effect due to the dissimilar cavitation indices, between model and full scale [31, 32]. However, since

cavitation usually occurs at lower speeds, when open-water and cavitation tunnel model tests are run in compliance with Froude's law, this effect will be minimal. In comparison with Reynolds effects, cavitation effects are believed to be less severe.

As yet, no satisfactory criterion has been established which can account for the effects of aeration in model ship correlation [31, 32]. With the atmospheric pressure being the same for both model and ship, this usually leads to aeration occurring sooner in the model. Fortunately, when aeration does occur, it is visible, and hence can generally be avoided, by incorporating a barrier between the free-surface and the top of the rudder.

So far, only the scale effects, resulting from the free stream operation of the rudder have been considered. The complex interaction between the hull, propeller and rudder introduces even more scale effect problems, which cannot be easily accounted for in model-ship scaling calculations [33]. One notable scale effect is that the ratio of the propeller velocity to free stream velocity in the model is often larger than that for the ship [5, 32]. This results in the model having an increased drag coefficient, which requires the propeller to operate at a greater slip ratio than the ship. This might result in the manoeuvring characteristics, being incorrectly predicted in the case of the ship. However, this scale effect is thought to be offset by the compensatory effect of the hull boundary layer wake, which is thicker in the case of the model, and leads to a reduction in the propeller disc inflow velocity.

As has been highlighted, experimental approaches to ship rudder performance prediction, based on experimental techniques are dogged with scaling problems, as a consequence, theoretical approaches to rudder modelling have been developed in an attempt to circumvent some of these problems.

2.3 CFD Rudder Modelling Methods

The past two decades have seen a steady increase in the use of CFD for solving engineering problems, as a direct result of advances in computer technology. As the capabilities of computer hardware have advanced, so has the complexity of numerical methods used for solving fluid flow problems. Constraints on computing resources meant that only simplified numerical methods could be implemented in the early years. These methods required numerous assumptions to be made about the fluid flow, which in turn introduced modelling errors. However, with the level of computing power available today, it is possible to implement more complex CFD methods, involving fewer assumptions, which are better able to model the physical world.

The most common area for the application of CFD, has been the aerospace industry. As a result, a great deal of research has been focused on the development of numerical methods, which can predict the flow over fuselages, wings and rudders. A number of these methods are equally well suited to modelling ship rudder flows. The four most prominent CFD methods are listed below:

- Lifting line methods
- Panel or boundary element methods
- Reynolds-Averaged Navier-Stokes (RANS) methods
- Large Eddy Simulations (LES) and Direct Navier-Stokes (DNS) methods

However, of the four methods listed above, only the first three are commonly applied to wing and rudder flows. There are numerous ways of incorporating the effect of an upstream propeller, within the first three numerical methods, using various levels of approximation. All four methods vary in complexity, and have certain advantages and disadvantages. A brief discussion of these four numerical approaches will be given,

in the context of finding the best method or combination of methods, for estimating ship rudder performance.

2.3.1 Lifting Line Methods

This is a basic method which can be used to solve lifting surface flows. The theory behind this approach is attributed to the work of Glauert [34]. Here, the lifting surface and wake are modelled as a series of horseshoe vortices, known as a lifting line. A detailed explanation of this method is given in the text by Katz and Plotkin [35].

This method, has the advantage that it provides good estimates of span-wise loading, and induced drag, whilst remaining simple to implement and computationally inexpensive. However, due to the model's simplicity, it has many drawbacks. The theory is limited to lifting surfaces of relatively high aspect ratio, and assumes that the wake is aligned in the local flow direction. It also assumes that the lifting surface is of zero thickness, and therefore neglects any flow effects resulting from section camber and thickness. As it is based on potential flow theory, this method neglects viscous flow effects, hence, is unable to directly model frictional drag, flow separation and stall. An example of the application of this method to a ship rudder operating in a free stream, in its most detailed form, is presented by Molland [36, 37].

An upstream propeller can be incorporated within the lifting line model using a form of strip theory approach. The upstream propeller effect, can be accounted for by modifying the inflow velocity and incidence across the rudder span, using blade element momentum theory. Although this approach neglects the span-wise cross flow along the rudder, satisfactory predictions of rudder performance have been obtained, as demonstrated by Molland [38].

2.3.2 Panel or Boundary Element Methods

In the early 60s, as a consequence of increased computing power, a new numerical approach to the lifting surface problem, known as the panel method or boundary element method began to emerge. This method promised to overcome many of the problems of the early lifting line approaches. This technique allows the treatment of more complex geometries, and actually models the lifting surface itself, allowing the effects of thickness and camber to be calculated. The basic principal of the panel method is based on the superposition of source/sinks, vortices and/or doublet elements over the lifting surface, such that the boundary conditions on the body, across the wake and in the far field are satisfied. Extensive research has been carried out in this field. A detailed overview of this method is provided by the pioneer of panel methods, Hess [39], and in the text by Katz and Plotkin [35].

The advantage of this method, is that it can be used to model actual geometries without simplification of the geometry. Although panel methods are significantly more complex than lifting line methods, the computational effort required is still significantly less than that needed for field methods, like RANS. Wright and Turnock [15] found a panel code used to solve a three-dimensional rudder flow required only one percent of the computational effort needed by a RANS code to solve the same flow problem. The reason for this, is that panel method computations are carried out on the body, wake and far field boundaries, and not on whole fluid domain, as done by the RANS method. Panel methods also allow greater scope in the numerical procedure, allowing various levels of detail to be modelled. Even complex flow features such as wake roll up, and unsteadiness can be incorporated. However, being based on potential flow theory, like the lifting line method, frictional drag, separation and stall effects are not directly accounted for.

Subsequent developments in the field, now mean that viscous effects can be approximated through the use of boundary layer methods, coupled within the panel code.

However, panel methods are generally unsuitable for modelling lifting flows, over sections which have blunt trailing edge features, or regions of large separation and vortex shedding, since the method requires the steady Kutta condition [35] to be satisfied at the trailing edge. Applying a virtual trailing edge condition, whereby, the trailing edge is extended, and faired to the shape of the separation streamlines aft of the blunt trailing edge has been used to circumvent this problem, as shown by Jeffrey [40] and Couser [41]. However, this is a crude approximation and the results are indicative of this.

It is also possible to incorporate unsteady propeller effects within the panel method. Turnock [21], Tamsshima et al [42], Söding [43, 44] and Li and Dyne [45] have all successfully used boundary element methods to model ship rudders operating under both free stream and propeller flow conditions. A detailed review of these, and other panel code investigations is given by Turnock [21]. It has been shown that the panel method gives good overall performance prediction when compared to experimental results.

2.3.3 RANS Methods

The previous discussions identified the limitations of using potential theory in rudder flow calculations. Although boundary layer approximations can be used to simulate the effect of viscosity on the flow, these methods still introduce another level of approximation. Another solution approach, which has developed rapidly over the past three decades, involves solving the RANS equations. A detailed description of this method is given in Chapter 3. The RANS approach does, however, place significantly more demand on computer resources than potential methods, since the whole fluid domain is discretised. The computing requirement for accurate full three-dimensional RANS computations is currently well beyond the capabilities of all but the largest research establishments. However, detailed two-dimensional computations are within the capabilities of more modest computing facilities.

The RANS approach has been around for a number of years, and has been successfully applied to a number of marine problems. One of the most common applications of the RANS method is in the prediction of ship resistance. A number of the most recent RANS investigations into ship flows are presented in the Gothenburg 2000 [46] and Numerical Towing Tank Symposium [47] proceedings. Surprisingly, limited research has been conducted on marine rudder flows using the RANS approach, with the researchers Chau [48], El Moctar and Muzaferija [49], Simonsen [8], Wright and Turnock [15, 50] having the only published works known to the Author.

Propeller effects can be incorporated within the RANS method using one of two approaches. The simplest way is to model the propeller as an actuator disk. This method involves applying body forces, i.e. the source terms in the momentum equations, to the cells located within the propeller disk, such that the flow is accelerated in the same way as a propeller with an infinite number of blades, with the required thrust and torque. This actuator disk approach was first proposed by Schetz and Favin [51] and has been widely implemented over the years. However, this method only accounts for the axial and tangential forces, and neglects any radial force components which would be present in the real flow. For simplicity, the effect of the propeller is usually represented as circumferentially averaged body forces, input into the steady RANS momentum equations, hence, neglecting any unsteady effects. It is perfectly feasible for unsteady body forces to be included in unsteady RANS momentum equations. However, due to the high computing overheads associated with time-accurate simulations, these computations are uncommon. Recent investigations using the circumferentially averaged body forces, and time varying body force approaches have been carried out by Stern et al [52, 53], Wright and Turnock [15, 50], Tzabiras [54] and Simonsen [8]. Various degrees of success have been obtained using this body force method, with qualitative results comparing more favourably than the quantitative results. However, in Kodama's [55] review of hull, propeller and rudder interactions, he states that agreement with experimental data is not yet satisfactory, using this method.

The second, and more complex, way of incorporating propellers within the RANS model, is to compute the actual unsteady flow over the real rotating propeller geometry. This method is extremely complicated, requiring the generation of complex non-matching grids around the hull, propeller and rudder geometries, with fixed and rotating frames of reference. In addition, this approach needs to take into account the different time scales in the flow, as the propeller flow requires a much smaller time step than the ship flow. It goes without saying, that this approach requires extremely large computing resources. The most advanced calculations of this kind have been carried out by McDonald and Whitefield [56] and Abdel-Maksoud et al [9]. Although promising results have been obtained, increased computing power is needed before the full potential of this method can be exploited.

2.3.4 DNS and LES Methods

Direct Numerical Simulation (DNS) and Large Eddy Simulation (LES) computations of marine flows are as yet uncommon. DNS involves the direct solution of the unsteady Navier-Stokes equations, and are thought to be capable of resolving even the smallest eddies and time scales of turbulence within a flow. Although the DNS method does not require any additional closure equations (as in the case of the RANS method), very fine grids and extremely small time steps need to be used, in order to obtain accurate solutions. This method is currently confined to simple flow problems at relatively low Reynolds numbers. DNS computations of the fully turbulent high Reynolds number flows associated with ship flows await major advances in computational hardware. A detailed discussion of DNS solvers and the future of CFD are presented in the texts by Anderson [57] and Wilcox [58]. Although DNS solvers are presently limited to solving low Reynolds flows, they are playing a role in further RANS code turbulence model development.

Like DNS codes, the use of LES solvers is rare and mainly the preserve of the CFD researcher. LES is a method that can be used to predict accurately the large scale

turbulent structures within a flow, requiring a sub-grid scale model to represent the smaller scale eddies. Although only the large scale eddies are resolved individually, this still requires the use of extremely fine grids, making solutions expensive and demanding on present computer resources. Recently this method has been successfully utilised in solving numerous high Reynolds number problems, like the turbulent flow over a NACA 0012 aerofoil, carried out by Creismeas [59]. It is widely believed that LES codes will become the new standard in calculating turbulent flows, with ever increasing computing power, long before DNS solvers. A discussion of LES method is presented by Wilcox [58].

2.4 Verification and Validation in CFD

Continued advances in computing power and the ever reducing costs of computing hardware, means that CFD methods are no longer confined to the research environment. These advances have lead to the development of many CFD packages aimed at the commercial market. As a result, CFD is now widely utilised throughout the engineering community. The widespread use of such packages has raised the important question of quality assurance, and has resulted in various attempts to develop quality standards. These quality standards are aimed at improving confidence within the industry. Unlike experimental techniques, which have a large body of knowledge and methods which can be used to estimate the experimental error and uncertainty (which are widely accepted), numerical techniques of error and uncertainty evaluation are less mature.

Recognising the need for verification and validation in the marine CFD sector, the International Towing Tank Conference (ITTC) in conjunction with the American Society of Mechanical Engineers (ASME) has been at the forefront in establishing guidelines and standards. The proposed standards address all aspects of the CFD process. A detailed resume of these guidelines can be found in the proceedings of

ITTC [33] and the ASME Editorial Policy Statement on the Control of Numerical Accuracy [60]. These guidelines require researchers to investigate the numerical uncertainty of their CFD computations. The major emphasis of these standards has been to ensure that a known level of accuracy is achieved by flow solvers. As yet there is no standard method for evaluating numerical uncertainty, accepted by the CFD community, hence, it is a subject of much debate, together with the exact definitions of verification and validation. However, the simple definition of verification and validation given by Blottner [61], provides a broad definition which encompasses many of the accepted interpretations: "Verification is solving the equations right, and validation is solving the right equations". Stern et al [62] discuss many of the verification and validation issues surrounding CFD.

CFD investigations which require a high level of confidence in the results must include both verification and validation stages. Depending on the CFD approach used, different verification and validation methods must be employed. The subsequent discussions will be focused on the specific requirements of the RANS method.

2.4.1 Verification

The verification stage of any RANS investigation must assess the uncertainty of the method, by investigating the dependence of the numerical model on its boundary locations, discretisation approach and iterative solution method.

As will be described in Chapter 3, the selection of the correct boundary conditions which describe the physical domain being modelled, is critical in obtaining valid RANS solutions. Assuming that correct boundary conditions have been prescribed, the dependence of the flow solution on the location of these boundaries must be investigated. Usually this is done by moving the boundaries until an important integrated global parameter such as lift, drag or field parameter like velocity or pressure, at some location within the flow, becomes insensitive to the boundary movement. It must be

noted that this approach usually only applies to unbounded fluid flow problems.

Investigation of the error and uncertainty resulting from the use of finite difference approximations of the governing RANS equations, is probably the most important component of any RANS study. Discretisation of a fluid domain, which theoretically has an infinite number of continuum values, inevitably results in errors. The problem of discretisation uncertainty or error is usually addressed through spatial and temporal (unsteady flows only) discretisation studies.

A spatial discretisation or grid independence study involves obtaining solutions on successively refined grids. The purpose of this exercise is to determine the sensitivity of the flow solution to the size of mesh used to discretise the fluid domain. Depending on the number of meshes computed, estimates of discretisation error and order of accuracy can be made. A number of systematic approaches to the quantification of uncertainty and order of accuracy have been proposed. Stern et al [62] advocate error estimates based on a form of Richardson extrapolation [63] using three model grids systematically refined in the three co-ordinate directions, whilst Eca and Hoekstra [64] argue that this method is unreliable, favouring the use of more than three grids. Ideally asymptotic convergence of an important integrated global parameter such as lift, drag or field parameter like velocity or pressure at some important location in the flow, should occur as the computational mesh is refined. However, in practice, asymptotic convergence is sometimes hard to achieve because of numerical problems associated with the solver being used. The process of finding a grid independent solution can be a complex one, especially when three-dimensional grids are considered, as the grid properties in each dimension are often interrelated with regard to the flow-field variables. Many researchers follow the approach of Stern et al [62] to discretisation error estimation, successively refining their grids in all the dimensions by the same refinement factor and subsequently estimating the error. The author believes that this approach is flawed and results in meshes which are over-refined in some areas and under-refined in others. The authors experience has shown that highly

refined grids often produce solutions which violate the asymptotic convergence criteria on which Stern et al's [62] uncertainty estimation is based. The author favours a more detailed independence study approach, whereby, grid refinement is carried out in each of the three dimensions in turn. This approach allows grid nodes to be concentrated in specific areas and has an advantage over Stern et al's [62] approach, in that there is less overkill or wastage of nodes located in regions with relatively low flow gradients. The disadvantage of this method is that it requires the creation of many different grids.

It must be noted that the degree of grid independence for a particular CFD model, should be related to the degree of accuracy needed in the final solution. The difference between a fully grid independent solution and an error of 1% in the solution, can often result in a 10-fold increase in the number of cells. Accepting a possible 1% error can, therefore, save time and money, when extreme accuracy is not necessary.

Time-accurate flow computations should include a temporal time step independence study, whereby, the temporal time accuracy of the flow solution is assessed. In the same way as the grid independence study, the time step size used should be varied, and its effect on the solution investigated.

Many CFD solution techniques like the RANS approach, obtain solutions to the discretised governing equations using iterative or time-marching equation solvers. A steady state converged solution is said to have been achieved, when all the flow field variables across the domain stop changing, from iteration to iteration. Many solvers quantify the global error in the computed field values from iteration to iteration, by calculating the residual imbalance of the momentum and continuity equations. The residual error associated with the continuity equation, is usually referred to as the mass source residual, which is described in detail in Chapter 3. The mass source residual is commonly used as the stopping criteria in RANS computations. Hence, every RANS investigation should assess the effect this mass source residual stopping criteria, has on the accuracy of the results. Chapter 3 discusses in detail the

importance of setting the correct mass source residual stopping criteria.

2.4.2 Validation

The final stage of any RANS investigation is the validation of the numerical solution. This requires some form of benchmark solution, to which the numerical solution can be compared. Model test data, full scale data and some analytical solutions are commonly used as benchmarks, for assessing the validity of RANS flow solutions. Validation is not a simple procedure and has as much to do with the accuracy of the benchmark solution, as the accuracy of the RANS solution itself. Good agreement between experimental and numerical results does not necessarily mean that the numerical model is correct. Close agreement might result from the cancellation of errors or large uncertainties in the experimental data. Like verification, validation has also received a considerable amount of attention, and is the subject of much discussion. Stern et al [62] provides a detailed discussion on the subject of CFD code validation. Ultimately, good validation of CFD results requires high quality experimental data, whose level of uncertainty is quantified. Published results of this calibre are often hard to find.

Although general validation of a commercial code is the responsibility of the vendor, the final user must appreciate the need for careful verification and validation studies in order to assess the validity of the code in solving his/her problem. Detailed verification and validation studies, as recommended by the ITTC and ASME, will be applied to all the solutions presented in this Thesis.

2.5 Research Strategy

The previous discussion of CFD methods highlighted a number of approaches, which could be used to estimate rudder performance. These methods ranged from the most

basic lifting line approach, to the more complex RANS method. Based on the findings of the literature review used to compile the CFD rudder modelling methods section, it was decided that a research programme aimed at assessing the capabilities of the RANS method, for rudder performance prediction would be conducted. The RANS method was chosen in preference to the other methods described, because it is considered to be the current state of the art for modelling practical marine flow problems, and would remain so for the next decade at least. Although a number of recent investigations have used the RANS method to predict the full unsteady hull, propeller and rudder flow regime, the accuracy of these results is far from satisfactory. A number of problems are responsible for this lack of accuracy; grid generation problems, grid resolution problems, transient time step considerations, turbulence model limitations, insufficient computing power and lack of detailed verification and validation.

Rather than tackle the full three-dimensional hull, propeller and rudder interaction problem, with inadequate computing resources, it was decided that the research would be better focused on addressing a number of the problems outlined above, using a less demanding, but representative two-dimensional rudder-propeller model. The ultimate aim of this research programme, was the accurate modelling of flows around high lift sections with blunt trailing edges, such as the Schilling. RANS computations of steady and time-accurate flows about Schilling sections have yet to be conducted, as they present a number of difficult challenges, as identified by Söding [43].

As was explained earlier, detailed verification and validation studies must be conducted in order to gain confidence in CFD. It was decided that the whole unsteady propeller-rudder problem would be broken down into four validation stages. This would allow a detailed performance assessment of the RANS method to be made, before utilising it to solve a number of flows around different types of high lift rudder. A schematic of the research programme is shown in Figure 3. The aim of each validation stage was to assess in isolation, a number of the important criteria and considerations needed for accurate modelling of high performance rudders, using the

RANS method. It was hoped that by starting with a simple flow model and progressively increasing its complexity, a better understanding of the requirements of the whole unsteady propeller-rudder RANS model would be obtained. Dealing with simple flow problems, gradually increasing the complexity of the model, and quantifying the accuracy at each stage, is the only way of assuring the engineering community of the validity of the results obtained.

An un-complicated initial investigation using the RANS approach was sought. The steady flow over a two-dimensional flat plate was chosen for this purpose. Despite its simplicity, this investigation allowed many of the important aspects of the RANS method to be explored without the added complications of grid generation. The primary aims of this investigation were as follows:

- Determine the critical grid and solver parameters needed for accurate skin friction prediction.
- Assess the performance of different turbulence models in flows with zero pressure gradient.
- Validate the predicted skin friction against published experimental data over a range of Reynolds numbers.

The second verification and validation investigation was focused on solving the steady flow over a two-dimensional NACA 0012 aerofoil. The primary aims of this investigation were as follows:

- Determine the critical grid and solver parameters needed for accurate conventional rudder performance prediction.
- Assess the performance of different turbulence models in solving flows with pressure gradients and regions of separation.

- Validate the predicted rudder performance against published experimental data.

The third verification and validation investigation was focused on solving the under-converged steady state and time-accurate flow over a NACA 0012 aerofoil fitted with a Gurney flap. The primary aims of this investigation were as follows:

- Determine the critical grid and solver parameters needed to capture periodic vortex shedding behind bluff bodies, and to provide accurate predictions of performance.
- Investigate the implications of using either under-converged steady state or time-accurate solution approaches, for solving flows known to exhibit vortex shedding.
- Validate the predicted flow field and section performance, against published experimental data.

After completing the verification and validation studies, to confirm the validity of the RANS method in solving free stream flows over both conventional and high lift type sections, an investigation into the performance of different conventional and high lift rudder sections was conducted. A conventional NACA 0020 and a generic high lift Schilling type rudder section were chosen for this study. The aims of this investigation were as follows:

- Investigate the effect of Reynolds Number and flow type, on free stream rudder performance and its implication in model-ship scaling.
- Investigate the free stream performance effect of fish-tail trailing edges, like those fitted to Schilling rudders.
- Obtain a better understanding of the flow physics associated with Schilling rudder flows.

The final verification and validation investigation was focused on modelling both conventional and high lift rudders, operating under simplified two-dimensional periodic inflow conditions, similar to those produced in a propeller race. The objectives of this investigation were two-fold. Firstly, to establish a plausible flow model which could be used to simulate two-dimensional periodic flow conditions experienced by a rudder operating downstream of a propeller. The second objective, was to obtain a better understanding of the effect periodic flows have on rudder performance. The primary aims of this investigation were as follows:

- To devise a method which allows two-dimensional periodic flow conditions experienced by a rudder operating downstream of a propeller to be simulated.
- In the absence of detailed experimental validation data, to assess the validity of the method, against classical linear theory at low amplitudes and reduced frequencies.
- Assess the effect of periodic flow disturbances of high amplitude, at various reduced frequencies on conventional and high lift rudder sections.

2.6 Organisation of Thesis

The work presented in this Thesis can be divided into six main threads, following a common theme of verification and validation. These are: explanation of the RANS solution approach and required grid generation procedure (Chapters 3 and 4); validation of the RANS solution approach in the prediction of flat plate skin friction (Chapter 5); validation of the RANS method in the prediction of NACA 0012 section performance (Chapter 6); validation of the RANS solution approach in the prediction of the performance of a NACA 0012 section fitted with a Gurney flap (Chapter 7); investigation of high lift section performance (Chapter 8); validation of the RANS method in the prediction of periodic flows about high lift rudder sections (Chapter

9). The first and last sections of each Chapter summarise, respectively, the context and significant findings of that Chapter. Thus, by reading these Sections only, it is possible to understand the development of the Thesis, and the important findings of the research presented. Chapter 10 summarises the major findings of the entire Thesis, as well as presenting some recommendations for future research. A number of Appendices are also included which discuss in more detail: model-ship rudder scaling (Appendix A); geometric progression distribution formulae (Appendix B); hyperbolic distribution formulae (Appendix C) and linear unsteady aerofoil theory (Appendix D). All tables and figures are placed at the end of the Thesis.

Chapter 3

Governing Equations and RANS Solver Detail

3.1 Overview of Chapter

The commercial RANS flow solver CFX-4.3 was used to facilitate the rudder performance predictions presented in this Thesis. The following Chapter presents the fundamental fluid flow governing equations, along with a brief description of the numerical approach used by CFX-4.3 and similar RANS codes, in formulating a solution to these equations. Particular attention is focused on the specification of the initial and/or boundary conditions and the selection of the appropriate solver parameters, needed to obtain solutions to external flow problems, such as rudder flows. It is hoped that many of the techniques and procedures introduced in this Chapter will prove valuable to any engineer faced with using a RANS code for the first time.

3.2 Governing Equations

3.2.1 Complete Navier-Stokes Equations

The governing equations which describe the motion of viscous, incompressible fluids are the complete Navier-Stokes equations, named after the fluid dynamicists Navier and Stokes who derived the constituent momentum equations at the beginning of nineteenth century. They consist of a coupled system of five nonlinear partial differential equations, made up of equations of continuity, momentum and energy. These equations are derived by accounting for the changes of mass, momentum and energy within a infinitesimally small fluid element, resulting from fluid flow across its boundaries and/or due to any sources within the fluid element itself. For incompressible flows, the density is assumed to be constant, and the Navier-Stokes equations reduce to a set of four coupled partial differential equations; the continuity equation and three momentum equations. From here on, only the incompressible Navier-Stokes equations will be referred to. The conservation form of the governing equations will be presented. All equations will be expressed in compact Cartesian tensor form; where x_i or (x, y, z) are the Cartesian co-ordinates and u_i or (u_x, v_y, w_z) are the Cartesian velocity components.

Equation 22 is the continuity equation, accounting for the conservation of mass within a fluid.

$$\frac{\partial u_i}{\partial x_i} = 0 \tag{22}$$

Equation 23 is the momentum equation, classically known as the Navier-Stokes equation and accounts for the conservation of momentum within a fluid.

$$\frac{\partial(\rho u_i)}{\partial t} + \frac{\partial(\rho u_i u_j)}{\partial x_j} = -\frac{\partial p}{\partial x_i} + \frac{\partial}{\partial x_j}\left(\nu\left[\frac{\partial u_i}{\partial x_j} + \frac{\partial u_j}{\partial x_i}\right]\right) + f_i \tag{23}$$

The first term on the left hand side of Equation 23 is due to the temporal change in momentum and the second term accounts for convection. The first term on the right

hand side of Equation 23 gives the momentum change due to the pressure gradient and the second term accounts for the diffusion due to viscosity. The third term on the right hand side of Equation 23 accounts for any body forces which may exist in the fluid, like those resulting from the inclusion of a propeller, or more usually gravity.

The development of the finite volume method used by CFX-4.3 and other flow solvers, results from the integration of the conservative form of the complete Navier-Stokes equations over a three-dimensional control volume, as explained by Versteeg and Malalasekera [65]. The resulting equations express the exact conservation of the relevant flow properties within the control volume. This direct relationship between the physical conservation principle, and the governing equations form one of the main attractions of the finite volume method.

Currently no general closed-form solutions have been obtained to the complete Navier-Stokes equations, except for a few special cases. Hence, a numerical method involving some form of discretisation of the partial differential equations is used in order to solve them. Further information on the development of these finite difference approximations can again be found in texts by Anderson [57] and Versteeg and Malalasekera [65].

3.2.2 Reynolds-Averaged Navier-Stokes Equations

Although the complete Navier-Stokes equations govern both laminar and turbulent flows, they are not suitable for the direct computation of turbulent flows. To do so would require computers in the order of 10^6 times faster than today's fastest supercomputer, computing on extremely fine grids and over a large number of time steps, in order to capture the turbulent motion at the smallest time and length scales, as stated by Speziale [66].

For engineers dealing with practical problems, in which they are mainly concerned with quantitative properties such as average forces, a computational procedure known

as Reynolds-averaging can be applied to turbulent flows, giving useful results without the need to model the effects of every eddy within the flow. This method was first proposed by Reynolds [67]. In the Reynolds-averaged approach to turbulence, the flow variables are resolved into time mean and fluctuating components, as shown by Equation 24 and Equation 25.

$$u_i = U_i + u_i' \tag{24}$$

$$p = P + p' \tag{25}$$

On substitution into the complete Navier-Stokes equations, and following time-averaging, the unsteady Reynolds-Averaged Navier-Stokes (RANS) equations are obtained. The time-averaged form of the continuity equation is given by Equation 26. The time-averaged Navier-Stokes momentum equation is given by Equation 27, where $\overline{u_i'u_j'}$ denotes the time-average of $u_i'u_j'$ and is known as the specific Reynolds stress tensor. This stress tensor consists of six unknown independent stresses, acting in the normal and shear directions.

$$\frac{\partial U_i}{\partial x_i} = 0 \tag{26}$$

$$\frac{\partial(\rho U_i)}{\partial t} + \frac{\partial(\rho U_i U_j)}{\partial x_j} = -\frac{\partial P}{\partial x_i} + \frac{\partial}{\partial x_j}\left(\nu\left[\frac{\partial U_i}{\partial x_j} + \frac{\partial U_j}{\partial x_i}\right]\right) - \frac{\partial\left(\rho\overline{u_i'u_j'}\right)}{\partial x_j} + f_i \tag{27}$$

3.2.3 Turbulence and Turbulence Modelling

As was shown in the previous section, Reynolds-averaging of the complete Navier-Stokes equations gives rise to six additional unknown independent stresses. A computational procedure known as turbulence modelling, is used to predict these stress terms. This provides closure to the time-averaged complete Navier-Stokes equations, based on the turbulence effects of the mean flow. The complex phenomena of turbulence precludes the use of simple formulae in the calculation of these unknown

stress terms. Consequently, no single turbulence model exists which can be applied universally to any turbulent flow problem. For a turbulence model to be useful in an engineering sense, it must have wide applicability, a known level of accuracy in its application to different flow problems and remain un-complicated and easy to implement. A number of turbulence models have been developed over the years, all varying in their complexity and suitability to certain flow situations. Turbulence models can be roughly divided into four main categories; Algebraic (zero-equation), one-equation, two-equation and stress-transport models. A complete discussion of turbulence and turbulence modelling is beyond the scope of this Chapter. However, a brief description of the theory behind the most widely used turbulence models, the two-equation or standard $k-\varepsilon$ turbulence model and its Renormalization Group (RNG) variant will be given. These two turbulence models will be used exclusively throughout the research. More detailed discussions of turbulence and turbulence modelling can be found in Versteeg and Malalasekera [65] and Wilcox [58].

3.2.3.1 Standard $k-\varepsilon$ Turbulence Model

The $k-\varepsilon$ turbulence model is probably the most widely used turbulence model to date, and was chosen for this reason as the turbulence model in this research. The $k-\varepsilon$ turbulence model computes the Reynolds stresses based on the Boussinesq [68] eddy hypothesis for Newtonian fluids, whereby the Reynolds stresses are related to the mean rate of deformation, turbulent kinetic energy and turbulent viscosity within a fluid, as expressed in Equation 28.

$$\overline{\rho u_i' u_j'} = -\nu_t \left(\frac{\partial U_i}{\partial x_j} + \frac{\partial U_j}{\partial x_i} \right) + \frac{2}{3} \rho \delta_{ij} k \tag{28}$$

where ν_t is known as the eddy viscosity and depends on the local turbulence in the flow and δ_{ij} is Kronecker delta ($\delta_{ij} = 1$ if $i = j$ and $\delta_{ij} = 0$ if $i \neq j$) which makes the formula applicable to the normal Reynolds stresses. Equation 28 is commonly known as the isotropic eddy viscosity model, since it predicts the normal turbulent stresses as being the same in all directions, even though it is known that these stresses are not

generally isotropic. The eddy viscosity, v_t, is determined from the turbulent kinetic energy, $k = \frac{1}{2}\overline{u_i' u_i'}$, and the rate of turbulent dissipation, $\varepsilon = \nu \overline{\frac{\partial u_i'}{\partial x_k} \frac{\partial u_i'}{\partial x_k}}$, using Equation 29. Physically, turbulent kinetic energy, k, is the kinetic energy per unit mass of the turbulent fluctuations within a flow. The rate of turbulent dissipation, ε, is the rate at which turbulent kinetic energy is converted into thermal internal energy within a fluid. Equation 29 is derived from dimensional analysis of the velocity and length scales which characterise the turbulent exchange of momentum.

$$\nu_t = \rho c_\mu \frac{k^2}{\varepsilon} \tag{29}$$

where c_μ is an empirical coefficient generally set to 0.09. k and ε are determined from the two transport equations (hence, the name two-equation turbulence model), Equation 30 and Equation 31.

$$\frac{\partial(\rho k)}{\partial t} + \frac{\partial(\rho k U_j)}{\partial x_j} = \frac{\partial}{\partial x_j}\left[\left(\nu + \frac{\nu_t}{\sigma_k}\right)\frac{\partial k}{\partial x_j}\right] + P_k - \rho\varepsilon \tag{30}$$

$$\frac{\partial(\rho \varepsilon)}{\partial t} + \frac{\partial(\rho \varepsilon U_j)}{\partial x_j} = \frac{\partial}{\partial x_j}\left[\left(\nu + \frac{\nu_t}{\sigma_\varepsilon}\right)\frac{\partial \varepsilon}{\partial x_j}\right] + c_{\varepsilon 1} P_k \frac{\varepsilon}{k} - c_{\varepsilon 2}\rho\frac{\varepsilon^2}{k} \tag{31}$$

where $\sigma_k, \sigma_\varepsilon, c_{\varepsilon 1}$ and $c_{\varepsilon 2}$ are empirical constants obtained from experiments on a wide range of turbulent flows. The standard constants and the ones used in this research are given in Table 1. P_k in Equation 30 and Equation 31 is the generation rate of turbulent kinetic energy and is given by Equation 32.

$$P_k = -\overline{u_i' u_j'}\frac{\partial U_i}{\partial x_j} \tag{32}$$

The standard $k - \varepsilon$ turbulence model described, has been widely used, validated and shown to perform well in a variety of applications. However, like all turbulence models it has a number of deficiencies. Useful references which discuss the weaknesses of the standard $k - \varepsilon$ turbulence model and the implications these weaknesses have on different flow solutions, are given by Versteeg and Malalasekera [65], Wilcox [58], Leschziner [69], Guilmineau et al [70] and Rhie and Chow [71]. In the context of the research presented later in the Thesis, i.e. flows over lifting sections, a number of the weaknesses associated with the standard $k - \varepsilon$ turbulence model are outlined below:

- The standard $k-\varepsilon$ has been found to over-predict the turbulent kinetic energy in regions of impingement and re-attachment, leading to the poor prediction of boundary layer development around leading edges and bluff bodies.
- The standard $k-\varepsilon$ turbulence model has been found to give poor prediction of flow separation from surfaces under the action of adverse pressure gradients. Often, the real flow is found to be much closer to separation or more separated than the computed flow.
- Flow recovery following separation re-attachment is often poorly predicted as a result of the implementation of wall functions within the standard $k-\varepsilon$ turbulence model.
- The standard $k-\varepsilon$ turbulence model is often poor at predicting highly swirling flows, where the turbulent flow field is anisotropic, such as in regions of re-circulation and vortex shedding.
- Laminar and transitional flows cannot be calculated with the standard $k-\varepsilon$ turbulence model.

In spite of its seeming large number of deficiencies, the standard $k-\varepsilon$ turbulence model still remains the major work-horse of industrial turbulent flow computations, in preference to models which incorporate improved physical modelling of turbulence. The reason for this is probably because the standard $k-\varepsilon$ turbulence model is relatively simple, stable and has deficiencies which have been quantified.

3.2.3.2 RNG $k-\varepsilon$ Turbulence Model

Recent advances in turbulence modelling have lead to the development of a variation on the standard $k-\varepsilon$ turbulence model, the RNG $k-\varepsilon$ turbulence model, in an attempt to overcome some of the deficiencies of the standard model [65]. New statistical mechanics approaches have lead to the development of new mathematical formalisms.

In conjunction with a limited number of assumptions regarding the statistics of small scale turbulence these new formalisms, provide a basis for the extension of the basic eddy viscosity models. This model involves representing the small scale turbulence, by means of a random forcing function within the complete Navier-Stokes equations. The RNG procedure developed by Yakhot et al [72] systematically removes the small scales of motion from the governing equations by expressing their effects in terms of larger scale motions and a modified viscosity. The subsequent modified transport equations for k and ε are given by Equation 33 and Equation 34 and additional coefficient equations Equation 35 and Equation 36. The only adjustable coefficient is β, which is calculated from near-wall turbulence data. All other coefficients are either fixed, or explicitly computed as part of the RNG solution process. The constants used by the RNG model are given in Table 2.

$$\frac{\partial(\rho k)}{\partial t} + \frac{\partial(\rho k U_j)}{\partial x_j} = \frac{\partial}{\partial x_j}\left[\alpha_k \left(\nu + \nu_t\right) \frac{\partial k}{\partial x_j}\right] + P_k - \rho\varepsilon \tag{33}$$

$$\frac{\partial(\rho \varepsilon)}{\partial t} + \frac{\partial(\rho \varepsilon U_j)}{\partial x_j} = \frac{\partial}{\partial x_j}\left[\alpha_\varepsilon \left(\nu + \nu_t\right) \frac{\partial \varepsilon}{\partial x_j}\right] + c^*_{\varepsilon 1} P_k \frac{\varepsilon}{k} - c_{\varepsilon 2}\rho\frac{\varepsilon^2}{k} \tag{34}$$

$$c^*_{\varepsilon 1} = c_{\varepsilon 1} - \frac{\eta\left(1 - \eta/\eta_0\right)}{1 + \beta\eta^3} \tag{35}$$

$$\eta = P_k^{1/2}\frac{k}{\varepsilon} \tag{36}$$

The RNG turbulence model is generally regarded as being better than the standard $k - \varepsilon$ turbulence model [72], overcoming some of its deficiencies. However, it still suffers from the inability of predicting anisotropy of turbulence. This turbulence model still needs to be widely validated in order to obtain the same credibility as the standard $k - \varepsilon$ turbulence model.

3.3 Boundary Conditions

In order to obtain correct solutions from the governing equations, it is necessary to define the initial and/or boundary conditions for the dependent field variables P, k and ε, that describe the problem to be solved. The correct selection of these boundary condition variables, is fundamental to obtaining accurate flow solutions. The use of unrealistic and badly posed boundary conditions can lead to spurious and incorrect flow solutions, or more usually rapid solver divergence. The two most frequently used linear boundary conditions are, the Dirichlet and Neumann conditions [57]. The Dirichlet condition is the specification of the value of the dependent variable on the boundary of the computational domain. The Neumann condition is the specification of the normal component of the gradient of a dependent variable on the boundary. The various boundary conditions used in this research, and how their values are determined, will be outlined.

3.3.1 Inlet

The inlet boundary condition is a form of Dirichlet boundary condition. On an inlet boundary, the dependent variables of U_i, k and ε are prescribed explicitly. The pressure is not set for incompressible flows, since it is extrapolated from downstream in the fluid domain. The variables of U_i are set according to the inflow velocity of the problem. The turbulence quantities k and ε, however, are often difficult to specify. If the computations are to be compared with experimental data, the inlet turbulence quantities of k and ε should be set according to measured values found from the experiments. These measurements are seldom available to researchers, making it hard for comparisons to be made on the same benchmark. When this is the case, investigations into the sensitivity of the flow solution to the selection of k and ε parameters must be carried out.

If measurements of turbulence intensity do exist and the turbulent length scale of the

problem is known, then crude estimates of k and ε can be made. The turbulence level or turbulence intensity within a flow is defined by Equation 37, which reduces to Equation 38 if all the Reynolds stresses are assumed equal.

$$T_i = \frac{\sqrt{\frac{1}{3}\left(\overline{u'^2} + \overline{v'^2} + \overline{w'^2}\right)}}{U_\infty} \tag{37}$$

$$T_i = \frac{\sqrt{\overline{\overline{u'^2}}}}{U_\infty} \tag{38}$$

Substituting Equation 38 into the equation for kinetic energy, Equation 39, an expression for k based on the turbulence intensity can be obtained, Equation 40.

$$k = \frac{1}{2}\left(\overline{u'^2} + \overline{v'^2} + \overline{w'^2}\right) \tag{39}$$

$$k = \frac{3}{2}T_i^2 U_\infty^2 \tag{40}$$

The specification of the rate of dissipation of kinetic energy ε is more difficult. Estimates of ε can be made if measurements of the turbulent length scale l of the problem exist using Equation 41, [58, 65].

$$\varepsilon = c_\mu^{3/4}\frac{k^{3/2}}{l} \tag{41}$$

If the flow is known to be free of residual turbulence, (which is extremely unusual especially in the case of wind tunnel experiments) k and ε can be set to zero, the free stream undisturbed condition. In practice, both k and ε are set to small values, say 1.0×10^{-4}, to avoid solver convergence problems where k and ε can turn negative. If the upstream inlet boundary is placed far enough upstream, the choice of k and ε is less critical as they tend to dissipate to low values.

3.3.2 Wall

The wall boundary condition requires that the velocity on the wall satisfies the no-slip condition. Also, on the wall k is zero and ε is non-zero. The $k-\varepsilon$ turbulence models

can only be applied to regions which are fully turbulent and cannot be applied in regions where viscous effects are dominant, such as those found in the laminar sub-layer. The wall function approach proposed by Launder and Spalding [73] can be used to overcome this problem.

From experimental work it is known that near-wall flows have a characteristic multi-layered structure within the boundary layer as shown in Figure 4. This consists of a laminar sub-layer (viscous force dominated) close to the wall, followed by a buffer layer (viscous and turbulent forces of similar magnitude) and then an outer turbulent core (turbulent stress force dominated). Direct methods of resolving the turbulent eddies within this boundary layer, require extremely fine grids down to the wall, through the laminar sub-layer, which is computationally intensive and very costly. However, most RANS codes use turbulence models that employ wall functions, based on the universal law of the wall [74]. The use of wall functions avoids the need for fine grids in the laminar sub-layer, by making use of empirical fits within this region. The turbulence models used in this research all make use of this wall function approach. When dealing with near-wall flows, positions and velocities within the boundary layer are usually considered in non-dimensional form, y^+ and u^+

y^+ is a local Reynolds number, with length scale in the direction perpendicular to the wall and velocity based on the wall shear stress, as represented by Equation 42.

$$y^+ = \frac{\Delta y_p}{\nu}\sqrt{\frac{\tau_w}{\rho}} \tag{42}$$

u^+ is a non-dimensional form of velocity at a distance away from a wall as represented by Equation 43.

$$u^+ = \frac{u_p}{\sqrt{\tau_w/\rho}} \tag{43}$$

Non-dimensional analysis and experimental work has shown that the specific flow structures within the boundary layer lie within strict bounds of y^+, and these are used in the formulation of wall functions [65]. Positions within the boundary layer in which $y^+ \leqslant 11.63$ are regarded as being laminar in structure and positions where

$y^+ \geqslant 11.63$ are considered as being turbulent. It has been shown that within these two regions, two different functional relationships exist between y^+ and u^+. These are shown in Equation 44 and Equation 45, for the laminar linear sub-layer and for the turbulent log-law regions respectively [65].

$$u^+ = y^+ \tag{44}$$

$$u^+ = \frac{1}{\kappa} \ln E y^+ = \frac{1}{\kappa} \ln y^+ + B \tag{45}$$

The constants in Equation 45 are determined from experiment. For hydraulically smooth walls the Von Kármán constant, $\kappa = 0.4$, and the log-layer constant, $E = 9.793$ (or $B = 5.5$). Roughness can be simulated by increasing the value of E. The buffer layer crossover value of 11.63, is found by finding the intersection of the linear laminar sub-layer profile; Equation 44 and the log-law turbulent profile; Equation 45.

The use of wall function turbulence models places specific requirements on the grids used in solving turbulent flow problems. When considering turbulent near-wall flows, the most critical grid parameter is the near-wall grid spacing. It is of paramount importance, that near-wall grid spacing is selected in accordance with the requirements of the wall function. In wall function turbulent calculations, a y^+ of 11.63 usually sets the lower limit for the distance of the first cell, to the wall boundary, with the optimum near-wall position lying somewhere between $y^+ = 30$ and 500, [65]. It must also be remembered that whilst the first cell spacing is critical in accurate near-wall flow modelling, enough cells should be placed within the boundary layer, to resolve the flow gradients. The use of wall functions, therefore, poses a special grid independence problem for near-wall flows.

3.3.3 Mass Flow Outlet

The mass flow boundary condition is a form of Neumann boundary condition. Here the gradient of the dependent field variables U_i, k and ε normal to the boundary are

initially set to zero and, later, U_i is modified to have a constant gradient, in order to maintain global mass continuity. The pressure is extrapolated from upstream [75]. This boundary condition relies on the assumption that the flow is fully developed when it reaches the outlet. Therefore, all outlet boundaries should be placed far enough downstream, to ensure that the fluid flow is fully developed, i.e. zero flow variable gradients in the flow direction. Positioning an outlet too close to an area with a flow disturbance, may result in solution errors, since the assumed outlet condition of zero flow gradient does not hold. With regard to bluff body flows, it has been shown that there will be an area of reversed flow downstream. This reversed flow, will violate the outlet boundary condition of outward flow, if the outlet is placed too close to the body. It is necessary in the case of incompressible flows for global mass continuity to be maintained in order for the pressure correction equation to be well posed. This means that the total flow out of the domain must equal the total flow into the domain at all stages of the solution procedure. This is achieved by setting the normal derivatives of U_i to zero at the end of the velocity update, followed by working out the discrepancy in mass conservation. A constant multiple of unit outward normal is then added to the U_i at each outlet control volume in order to ensure global mass conservation. Thus the zero gradient condition of U_i is modified. The normal velocity gradient is in fact equal to a constant multiple of the unit outward normal [75].

3.3.4 Pressure Outlet

The pressure outlet boundary condition is a mixed boundary condition in which the Dirichlet boundary condition is applied to the P field variable and the Neumann boundary condition is applied to U_i, k, and ε. As for the mass flow outlet boundary condition, the assumption of zero normal gradient for U_i is assumed, i.e. the fully developed approximation. However, unlike the mass flow boundary condition, U_i is not later modified to achieve global mass conservation. This is instead taken care of by the velocity-pressure correction procedure [75].

3.3.5 Symmetry Plane

The symmetry plane boundary condition is also a mix of the Dirichlet boundary condition and Neumann boundary condition. Here the normal velocity components to the symmetry plane, and the normal gradients of k and ε together with the parallel velocity components, are set to zero. The shear stresses on the symmetry plane are, therefore, also set to zero.

3.3.6 Positioning of Boundaries

It is important that all boundaries are positioned to ensure that they have no demonstrable effect on the flow solution. In any CFD study, where high accuracy results are required, a sensitivity study should be carried out, to demonstrate that the interior flow solution is unaffected by the location of the boundaries. It must also be remembered that it is not good practice to place boundaries at excessive distances from the body. This wastes valuable computational resources, which could be put to better use in resolving areas with high flow gradients.

3.4 CFX-4.3 Flow Solver

The RANS flow solver used in this research was CFX-4.3, a structured multi-block, fully implicit finite volume flow code produced by AEA Technologies [75]. Solutions are obtained on multi-block grids produced by MESHBUILD, CFX-4.3's own grid generation module or other grid generation programs. A variation upon the Rhie-Chow [71] solution algorithm is implemented within CFX-4.3. The non-linear complete Navier-Stokes equations are solved to yield the velocity components by means of a two step iterative process. An inner iteration is used to solve for the spatial coupling for each variable, and an outer iteration is used to solve for the coupling between

variables. Each variable is taken in sequence regarding all the other variables as fixed and a linearised difference equation for the variable is formed for every control volume in the flow domain. The equations are then handed over to a linear equation solver, which then returns the updated values of that variable. The non-linearity of the original equations is simulated by reformatting the coefficients of the discrete equations, using the most recently calculated values of the variables, before each outer iteration. The calculation of pressure throughout the domain is slightly different, since it does not obey a transport equation. Instead, simplified versions of the discrete momentum equations are used to derive a functional relationship between a correction to the pressure, and corrections to the velocity components in each control volume. Substitution of this expression into the continuity equation, leads to an equation linking the pressure correction with the continuity error in the control volume. This set of equations is then solved in the same way as the transport equations, using a linear equation solver. The solution is used to update the pressure and to correct the velocity field though the functional relationship, in order to enforce mass conservation. One of two pressure coupling algorithms for incompressible flows can be implemented within CFX-4.3. Either the Semi-Implicit Method for Pressure-Linked Equations (SIMPLE) [76] or Pressure Implicit with Splitting of Operators (PISO) [77] pressure correction algorithms can be used. A number of linear equation solver options exist within CFX-4.3. The default solvers use Block Stone's method [75] for all equations, apart from the turbulence quantities where line relaxation is used. These default solvers were used in the research presented. A study of the performance of the various available equation solvers within CFX-4.3 is given by Wakefield [78]. A complete description of the CFX-4.3 flow solver can be found in the CFX-4.3 user manual [75].

3.5 Obtaining a Solution

The governing equations, along with the boundary conditions required to solve them, have been presented. The process of obtaining a solution using a solver such as CFX-4.3, is a complex procedure, which cannot be carried out by just executing a list of tasks one after the other. Often, the solver must be run, the results checked and then re-run with slight adjustments to the model, in order to improve the solution. The production of a good simulation usually results from a continual process of trial and error. The use of a commercial flow solver means that much of the numerical solution process is hidden from the user. Some parameters important in the solution process often need to be prescribed by the user, in order to obtain satisfactory solution progression and final results. This section will introduce these solver parameters and detail their effects on the solution process.

3.5.1 Differencing Schemes

The accuracy of a flow solution is dependent on the choice of differencing scheme employed in approximating the Navier-Stokes equations. The type of differencing scheme, dictates the way in which the partial derivatives in the governing Navier-Stokes equations, are replaced with algebraic difference quotients, based on the flow field variables at the faces of the control volumes. A variety of differencing schemes exist, all with varying orders of accuracy. Essentially, the use of a greater number of surrounding control volume faces, in formulating the difference quotients, usually constitutes a higher order accurate differencing scheme. The choice of differencing scheme used for a particular flow solution, depends on the flow type and the degree of accuracy expected from the flow solution. High order accurate differencing schemes, have the advantage over the lower order schemes, that they generally need fewer total grid points to obtain comparable overall accuracy, but this is often at the expense of increased computer time. Lower order schemes are often more robust than higher

order schemes, and can cause fewer convergence problems, especially when used on grids of poor quality.

The three most common differencing schemes used in finite volume flow codes are; upwind (first order), Quadratic Upstream Interpolation for Convective Kinetics or QUICK (third order) and hybrid (second order) [65]. The upwind differencing scheme forms, the difference quotients based on the value of the upstream control volume face, whereas, QUICK uses a three point upstream weighted quadratic interpolation. The hybrid interpolation combines an upwind interpolation with a central differencing scheme, which uses one upstream and one downstream face for interpolation.

Similar differencing scheme approaches, are applied to transient problems in order to calculate the time dependent partial derivatives in the Navier-Stokes equations, in terms of algebraic difference quotients based on the variables at different time levels. Backward [65] and Quadratic differencing, are two of the most common time marching differencing schemes used by finite volume codes like CFX-4.3.

3.5.2 Iterative Solution Process

As has already been mentioned, the solution process used is iterative. This means that an initial solution, normally a "guessed" solution, is required at the start of the solution process. The numerical equations are then used to produce a more accurate approximation to the numerically correct solution, which is one in which all the variables of each control volume satisfy the governing equations. During this iterative process, the updated solution field variables at the end of the iteration can be very different from those at the start of the iteration. Ideally, as the solution proceeds towards convergence these differences should decrease. In order to quantify if the solution process is converging, an error measure known as the residual is used. This error term is formulated from the numerical equations being solved. At the end of each iteration the latest solution is used to generate all the terms in the various

partial differential equations. For example, if all the terms in the momentum equation are placed on the left hand side of the equation, and the individual components are calculated, then the terms should sum to give zero. As the solution is only an approximation to the required values of the variable, the sum will not be zero. It is this sum that is the residual error. As the solution process progresses from iteration to iteration, the residual errors from each equation should reduce. If this is the case, the solution is said to be converging. If the residuals become ever larger, then the process is said to be diverging. CFX-4.3 and similar solvers output the residuals for both the momentum, continuity, and turbulence transport equations in an output file, enabling quick assessment of the progress of the solution.

3.5.2.1 Convergence Stopping Criteria

Most solvers use the residual error from the continuity equation, commonly known as the mass source residual, as the stopping criteria for defining a solution as converged. The mass source residual, is the sum of the absolute values (the L_1 norm [79]) of the net mass fluxes into or out of every control volume in the flow, and thus has the dimensions of kg/s. For the continuity equation to be satisfied and hence the solution converged, this must equal zero. In practice a small residual tolerance is set by the user, dependent on the accuracy expected from the solution. The specification of this tolerance is problem specific, and can only be determined after running a problem for a number of iterations whilst studying the convergence history of an important property, like an integrated global parameter such as lift, drag, or a field parameter like velocity or pressure, at some location within the flow. From this data, the minimum mass source tolerance needed to obtain a converged solution, in terms of the flow property of interest can be found. The selection of the correct mass source tolerance for a problem, can mean the difference between obtaining a solution in 100s of iterations rather than in 1000s of iterations with no noticeable increase in

accuracy in results. The default mass source residual stopping criteria within CFX-4.3 is 1.0×10^{-6}, however, this criteria may in some computations be too onerous, as will be shown later. A study into the effect of the mass source tolerance stopping criteria is presented in Chapter 6.

3.5.2.2 Iterations on Inner Equations

Up until now, it has been assumed that the solution process has been converging from iteration to iteration. This is rarely the case and residual errors become larger from iteration to iteration instead. In the previous section it was mentioned that iterative solution algorithms are used to provide solutions to the sets of simultaneous equations. Usually solvers like CFX-4.3 provide controls which allow the user to control the way in which this process is carried out. One control is the number of inner iterations used to solve the simultaneous equations. Increasing this can often help the convergence of difficult problems. Poor convergence of the inner pressure correction iteration, in particular, can lead to loss of mass conservation and solver divergence. Therefore, increasing the number of iterations on pressure can sometimes help. It must be noted, that increasing the number of inner iterations can greatly increase the solution time, so the smallest number of inner iterations as possible should always be sought. Unless otherwise stated only one iteration on the inner equations will be used in this research.

3.5.2.3 Under-Relaxation

Another parameter which can be used to control the inner iteration solution process, specifically in steady state problems, is "Under-Relaxation". Under-relaxation has several interlinked purposes in the inner solution process. Firstly, and principally, the amount by which a variable would change, if the equations were solved as they stand is reduced. Difficulties caused by instability due to, amongst other factors, the non-linearity of the equations, are overcome in this way. Under-relaxation is

implemented by scaling the coefficient of the variable in the control volume by an under-relaxation factor (URF) in the range $0 < URF < 1.0$. The smaller the factor, the more under-relaxation is employed.

A secondary purpose of under-relaxation which is a consequence of modifying the equations in the way described earlier, is that the linear equation solver is presented with an easier problem to solve. A small URF yields a more diagonally dominant matrix, whilst causing more work for the solver. For the above reasons, an under-relaxed problem, although more stable, may take more time to reach the required minimum mass source residual. This is because the amount by which a variable would change is reduced and hence the time to reach a converged value is increased. If the computational mesh is complex and the control volumes are not near cuboid in shape, the relaxation factors applied to the equations might need to be reduced, in order to obtain convergence. The standard URF values used throughout this research are given in Table 3.

3.5.3 Transient Flows and Time Stepping

So far only the solution parameters specific to the control of steady state solution processes have been discussed. Another means of controlling the overall solution process is to use a time dependent solution scheme. This approach can be used for transient flows, or steady state flows with convergence difficulties. Such schemes reproduce the physical changes that a flow would undergo if it were changing with time. For steady state problems, this can be used as a means of smoothing out the way in which the solution changes from one iteration to another, as an alternative to under-relaxation. With time dependent schemes, the main controlling factor is the value of the time step. This is set to give the smallest number of time steps as possible, whilst maintaining a smoothly converging solution, in which all the complex physics within the flow are resolved. For steady state problems, only the converged solution, after what is effectively an infinite period of time, is required and so the

time step can be large. For transient problems where time variation is of importance, the time step has to be small enough to model accurately the temporal changes in the flow variables.

For transient problems, it is difficult to determine the value of the time step necessary to obtain a converging solution, as the stability criteria of the complete Navier-Stokes equations cannot be found analytically. The choice of time step depends on the time scales of the important flow features which need to be resolved in the flow. Using too large a time step can often result in resolution of non-physical flow behaviour. Although from a numerical stability point of view, the time step used by implicit solvers does not have to satisfy the Courant-Friedrichs-Lewy (CFL) condition, given in Equation 46, it is often advisable for relatively small time steps close to the CFL limit to be initially used.

$$C = c\frac{\Delta t}{\Delta x} \leqslant 1 \tag{46}$$

where C is the Courant Number, c is the speed of propagation of some important flow feature, Δt is the time step and Δx is the grid spacing in the direction of propagation.

Using this (CFL) criteria, an estimate of the time step needed in transient problems can be made. Based on this condition, a time step of the order of magnitude of the residence time of a fluid particle passing through a control volume is often used. The residence time, is the time it would take a fluid particle to move through a cell from one face to the opposite face. For example, if a fluid particle moves in the x-direction with a velocity u, the residence time and hence the time step necessary to capture this movement would be given by Equation 47.

$$\Delta t = \frac{\Delta x}{u} \tag{47}$$

This calculation is typically carried out on a control volume, which is known to be located at a point with the greatest flow instability, such as the vortex street in bluff body flows. Care must, however, be taken to ensure that the time step used, is not

so small that the Reynolds-averaging assumptions are violated, i.e. averaging time $\ll \Delta t$.

For steady state problems with convergence problems, the time step is often set close to the Courant limit and slowly increased by means of adaptive time stepping, whereby, the time step is increased by a fixed factor at each new time step. This approach can also be applied to transient flows when seeking an optimum time step, hence, rapid convergence.

3.5.4 User FORTRAN

Although CFX-4.3 and similar solvers allow the definition of the initial and/or boundary conditions, and solver parameters through a command file, there is often a need to specify more complex information such as unsteady boundary conditions. CFX-4.3 allows the user to generate FORTRAN subroutines, defining such additional information, which can then be compiled and linked with the main solver libraries to provide a modified solver program.

3.5.5 Data Output

CFX-4.3 like other flow solvers allows the output of a wide range of data throughout and at the end of the solution process. The output data is written to two files. A dump (*.dmp*) file containing flow field variables at every grid node, together with the geometry information, and an output (*.fo*) file containing information such as integrated wall forces and pressures at various times throughout the solution process. A dump file can be output any number of times throughout the solution process, whilst, the output data file is only generated at the end of the solution. When, and what type of data, is included in the output file, is defined in the command file. Depending on the problem and/or if the solution is transient, these files can

be extremely large, typically 400MB for some of the long transient runs presented. The dump files produced can be processed using some form of visualisation package. The large output files, however, need to be post-processed in order to extract the important information. A post-processing program was developed by the Author specifically to do this.

3.5.6 Data Visualisation

Although the basic visualisation tool CFX-VIEW is provided within the CFX-4.3 suite of software, the flow field data contained within the dump (*.dmp*) files were visualised using "Fieldview" [80], a commercial visualisation tool specifically developed for viewing finite volume flow solver data.

3.6 Solution Troubleshooting

As previously mentioned, obtaining a valid, converged solution is often a continual process of trial and error. Even though much of the solver detail is hidden from the user, many parameters still exist for the user to define, all of which can influence the solution process, as has been shown. Knowing which parameters to change, in order to obtain a converged solution which is correct in the physical sense, is an art in itself, one which is not readily discussed in CFD texts. This section will discuss the reasons for solver divergence and present possible remedies to these problems.

3.6.1 Solver Divergence

The most likely cause of solver divergence or convergence to the wrong solution is often due to incorrect problem specification. The specification of conflicting or non-physical properties, user subroutines and/or boundary conditions, can all lead to

convergence problems. Careful checking of these is necessary before other possible causes are sought.

If the problem has been specified correctly, is physically reasonable and has a well defined stable mathematical solution, yet still fails to converge satisfactorily, then numerical difficulties may be suspected. Many of these problems can be rectified by the selection of more conservative solution parameters. Likely causes and possible solutions to poor solver convergence are given below:

- Incorrect initial and/or boundary conditions

  The single most common cause of a solution failing to converge, is prescription of incorrect initial and/or boundary conditions. This can usually be remedied by carefully examining the command file. If the errors in the boundary conditions are not easily identifiable, and some form of output field data has been produced, it is useful to visualise the data as this often indicates the source of error in the initial model. If the initial conditions are suspected as being the cause of initial solver divergence, it can often prove advantageous to run a laminar, or potential flow case of the problem, and restart the more complex problem using the field values generated from the solution.

- Poor mesh quality

  With multi-block finite volume flow codes, the definition of a poor mesh, is one who's control volumes differ in shape greatly from a cuboid. Non-orthogonal grids can cause convergence problems, due to inaccurate calculation of fluxes through the control volume faces. Smoothing the grid and making it more orthogonal by altering the block shape and/or structure, can often help overcome this. Non-orthogonal grids are often unavoidable, especially around complex geometries. Rapid changes in cell size/aspect ratio can also cause solver divergence and must generally be avoided, especially in areas where rapid changes in flow variables are expected. Most convergence problems that do manifest

themselves can usually be counteracted with suitable under-relaxation of the transport equations, in particular the turbulent transport equations. A process known as deferred correction, which under-relaxes the turbulent transport equations early on in the solution and slowly increases them as the solution progresses, is often used and is explained in the CFX-4.3 user manual [75].

- False diffusion

  False diffusion, or numerical diffusion, is the side-effect that results from the truncation errors associated with discretisation. Depending on the differencing scheme used, its effect is prominent in flows where the flow is not aligned with the grid lines. It results in the distributions of the transported properties becoming smeared. Most prominent false diffusion occurs when upwind schemes are used. The degree of false diffusion also increases with Reynolds number. False diffusion can be minimised by using higher order differencing schemes, such as hybrid or QUICK. A comprehensive study into the effect of false diffusion on flow solutions, for various differencing schemes, is discussed by Versteeg and Malalasekera [65].

- Incorrect time step size

  As previously mentioned, in transient calculations it is necessary for the time step to be set such that the temporal changes in the flow variables are adequately captured. If this is not the case, then the solver will have difficulty in converging each time step iteration. As such, this should be the first indicator of solver divergence in transient problems, and be reduced accordingly.

- Turbulence model problems

  The use of a turbulence model can bring its own convergence problems. Two problems which have been identified in this research are; slow or non-convergence, due to incorrect first cell size on wall boundaries and divergence due to negative calculated values of k and ε from the turbulence transport equations.

The first problem arises, when the first grid cell size near to a wall boundary is specified such that it violates the lower criteria of $y^+ \geqslant 11.63$ on which the wall function approach, employed within the standard and RNG $k - \varepsilon$ turbulence models, is fundamentally based. It has been shown, that too small a cell size can result in excessive computational effort being employed, in order to obtain a converged solution, since the transport equations are being applied right down through the viscous sub-layer. Ensuring that the first cell size satisfies at least the minimum criteria of $y^+ \geqslant 11.63$, usually resolves this problem.

The second problem of negative calculated values of k and ε often arise when higher order upwind and QUICK differencing schemes are applied to the turbulence equations, or when the shear layer is not adequately resolved by the grid. It is recommended, even when using high order differencing schemes on the velocity terms, that lower order schemes such as upwind or hybrid should be used for the k and ε terms, thus ensuring positive results. Although the upwind and hybrid schemes are of lower order, the overall accuracy of the flow solution is usually unaffected, since k and ε are dominated by production and dissipation [75].

3.6.2 Non-Physical Flow Results

Once a converged solution has been obtained, all that is known is that the solution satisfies the numerical equations for that mesh, to some order of accuracy. It is further required that the converged solution bears some relationship to the physical flow expected from the problem. This should be confirmed by comparing the numerically calculated flow structures with those expected from experiments. If there are significant differences between the numerical and physical flows, then the computational model might need to be modified. Differences might be caused by one or more of the following:

- Unsuitable boundary conditions

  The prescription of unsuitable boundary conditions, or boundary conditions which are incorrectly located, can over or under constrain the flow being modelled, resulting in non-physical flow results. Careful selection and placing of boundary conditions can overcome this problem. The outlet boundary condition location can often cause such problems, as previously discussed.

- Insufficient mesh density

  Insufficient mesh density in regions where large gradients in the flow variables are occurring, can cause non-physical results. This is overcome by ensuring that the grid density is increased in such areas. Particular attention should be paid to placing extra grid nodes within boundary layers and areas in which vortical flows are known to exist.

- Incorrect time step size

  Using too large a time step in transient simulations, can result in the resolution of incorrect flow physics. If this is suspected to be the case, the time step should be reduced towards the CFL limit, as previously discussed.

- Inadequate physical modelling

  The use of turbulence models which form simplistic approximations to the actual physical flow, can lead to incorrect physical results. The flow type and turbulence model being used, will dictate the level of error in the physical results. This can only be overcome by testing different turbulence models on the problem and analysing the results.

3.7 Computation Hardware

The CFX-4.3 computations presented in this Thesis were run using Southampton University's Irixcompute and Irixresearch services. The specifications of these services

are given in Table 4. When specific computational performance data is presented, the computing resource used will be detailed.

3.8 Conclusion to Chapter

The complete Navier-Stokes equations, which describe the motion of viscous incompressible fluid flows, have been presented. As explained, direct solution of these equations for common turbulent engineering flows is beyond the capacity of even the largest supercomputers available today. However, by considering the mean turbulent flow, and applying a process known as Reynolds time-averaging, a new set of equations which are more readily solved, can be obtained. These equations, known as the RANS equations, require the use of a suitable turbulence model for closure.

For engineering applications, where mean flow properties or mean forces, are of primary importance, the RANS method can provide sufficiently accurate information. However, the accuracy of results obtained using the RANS approach, are dependent on the selection of an appropriate turbulence model. A discussion of two of the most commonly used turbulence models, the standard and RNG $k-\varepsilon$ turbulence models, has been given.

The correct solution of the RANS equations is dependent on the selection of the appropriate initial and/or boundary conditions. A description of the most commonly implemented boundary conditions was given. An overview of the CFX-4.3 RANS flow solver used in the subsequent research was also presented, together with an explanation of the important solver parameters which need to be correctly set, in order to obtain converged RANS solutions.

Obtaining physically correct and converged solutions using the RANS approach is an art in itself, involving the careful selection of many different boundary conditions and solver parameters. A troubleshooting section was included within the Chapter,

discussing reasons for solver divergence and non-physical flow results, together with possible remedies which can be used to rectify any such problems.

Chapter 4

Grid Generation

4.1 Overview of Chapter

The rudiments of the finite volume RANS solution approach, were presented in Chapter 3. However, the success and accuracy of this method in obtaining a solution, is primarily dependent on the type and quality of the computational grid used to discretise the flow domain. This Chapter introduces the multi-block grid generation approach favoured by many flow solvers, including CFX-4.3. The methodology behind multi-block grid generation is introduced, along with a brief description of the software used in this research to create such grids. Also presented are the multi-block topologies used to generate the grids about the various rudder sections investigated later in the Thesis.

4.2 Multi-Block Grid Generation

The finite volume solution method described in Chapter 3, requires the modelled flow domain to be discretised into a number of finite three-dimensional control volumes. The multi-block grid generation method, generates these control volumes from an unstructured arrangement of structured block grids, which conform together to represent the flow geometry being modelled. These blocks must be topologically cuboidal, although they can, and often are, distorted to the shape of the problem being investigated. Figure 5 shows a typical single block C-Grid topology/grid constructed around an aerofoil. Each block is made up of a hierachial structure of object elements; block vertex nodes, edges and faces. The block vertex nodes define the block vertex co-ordinates, and hence the start and end locations of the edges, which make up the block. The block edges are shaped so that they conform with the geometry of the flow model. These edges do not have to be straight, they may be defined as arcs or curves, whichever best describes the geometry.

Once all multi-blocks have been defined, one or a number of interpolation methods can be used to compute the coordinates of the internal grid nodes within each block, based on the number of nodes required in the I, J and K directions. A linear interpolation method known as transfinite interpolation [81], is one of the most widely implemented interpolation methods. This method determines the grid node coordinates within each block by interpolating the block edge nodes into the interior.

Following interpolation, the node coordinates for each block are then output into a grid file, together with the relevant block joining and block face boundary condition type information. This file is then usually input into the flow solver and the solution obtained by applying the appropriate boundary conditions, defined in the command file to the block faces.

The major advantage of multi-block grids is that they are relatively easy to compute and require low storage memory requirements. This is because the connectivity of the

mesh, is implicitly mapped between physical and computational domains. However, the generation of grids about complex geometries, especially in three-dimensions, can require considerable skill.

4.2.1 CFX-MESHBUILD Grid Generator

CFX-MESHBUILD is the basic interactive multi-block grid generation preprocessor supplied with CFX-4.3 [75]. A user-friendly graphical user interface (GUI) allows multi-block grids to be created through the manipulation of the geometrical objects which make up each block. The edge node propagations used to interpolate the interior block nodes are also set through the GUI, along with the face boundary conditions on each block. The interpolated multi-block mesh is then output in the *.geo* format required by the CFX-4.3 flow solver.

There are a number of advantages and disadvantages to using CFX-MESHBUILD. The main advantage of CFX-MESHBUILD is that the GUI allows the user to generate grids relatively quickly. The extensive error checking provided by CFX-MESHBUILD throughout the grid generation process, ensures that complex grids can be constructed free of errors. However, due to the structure in which the multi-block grids are created within CFX-MESHBUILD, it is difficult for changes in geometry to be made without considerable effort on the part of the user. CFX-MESHBUILD also has the disadvantage that it only allows regular, or geometric progression node propagations along block edges. This severely restricts the variety of grids which can be created. Appendix B shows the formulation of the geometric progression node distribution function implemented with CFX-MESHBUILD. As previously mentioned in Chapter 3, the first grid node location away from any wall boundary, must be located at the correct y^+ value required by the turbulence model. Although the geometric progression function can be used to correctly locate the first near wall node, the behaviour of the function is such that it prevents bias clustering of points above this node. It is, therefore, impossible to place the required number of grid nodes within

the boundary layer region, without placing excessive numbers of nodes across the whole domain. This problem severely reduces the capability of the grid generator. The afore-mentioned conclusions were made after CFX-MESHBUILD was used to create the simple grids in the flat plate investigation presented. A full description of the CFX-MESHBUILD grid generator is given in the CFX-4.3 user manual [75].

4.2.2 CFX-MESHIMPORT

CFX-MESHIMPORT is a module within the CFX-4.3 suite which reads any multi-block grid file generated by CFX-MESHBUILD, PATRAN or IDEAS and creates a new multi-block grid file, suitable for use with the CFX-4.3 flow solver. CFX-MESHIMPORT can processes these multi-block grid files and create a new optimised multi-block grid in the CFX-4.3 *.geo* format, consisting of as few blocks as possible. As well as reducing the number of blocks, CFX-MESHIMPORT also re-orientates each block to ensure that the I block direction in the computational domain, points in the same direction as the block edge with the most number of grid nodes. Reducing the number of blocks and re-orientating them, can often enhance the computational efficiency of the flow solver. CFX-MESHIMPORT can be used to partition a grid into blocks with approximately the same number of nodes per block. This is used to balance the processor load when solving the problem on parallel processor machines.

4.2.3 Fleximesh Grid Generator

Following the creation of the simple grids in the flat plate study in Chapter 5, using CFX-MESHBUILD, it was evident that another more versatile grid generation method was needed, if high quality grids were to be produced around rudder sections. To this end the in-house multi-block grid generator "Fleximesh" initially developed by Rycroft [82] was chosen. The Fleximesh grid generator carries out essentially the same function as CFX-MESHBUILD, but without a GUI. A full description of the

Fleximesh grid generator is given by Rycroft [82], along with a detailed topology construction example and the necessary input and output file format information.

The advantage of using an in-house grid generator such as Fleximesh, is that it can be tailored to the specific needs of the problem to which it is applied. The simple input file format which Fleximesh uses to create complex grids is Fleximesh's major advantage over CFX-MESHBUILD. It is possible through a custom written program, to pre-process this file and make quick changes to the topology structure with the minimum of effort. Also, being an in house grid generator means that custom grid propagation functions can implemented, giving the user more control over the distribution of the nodes within the grid. Appendix C shows the formulation of the versatile hyperbolic node distribution function implemented within Fleximesh. This function is much better than the geometric progression function, available within CFX-MESHBUILD, because it allows the biasing of nodes in the near wall region.

Fleximesh can produce various output grid files including CFX-4.3 *.geo* and PATRAN neutral files *.pnf*. These files are then usually pre-processed by CFX-MESHBUILD before being passed to the CFX-4.3 flow solver.

4.3 Multi-Block Rudder Section Grids

A general outline of the multi-block grid generation process has been given, but the process of building multi-block grid topologies has not yet been discussed. The topology definition stage can and often is, the most complex and time consuming part of any CFD analysis. The nature of the multi-block method means that the relative placement, and the shape of the edges making up each block, dictates the way in which the internal block nodes are interpolated. Poor block location and/or edge shapes, can lead to interpolated grids of unsatisfactory quality, which places undue strain on the flow solver. The skill of creating a multi-block grids lies in shaping the multi-block topology so as to produce a grid which is orthogonal and as smoothly

varying as possible.

The two-dimensional topologies created around the rudder sections investigated later in this Thesis were relatively straight forward to create, although rather time consuming. A number of important factors were borne in mind when these topologies were defined. The main considerations were block structure, block outer edge shape and edge node clustering. It was decided that the common C-Grid topology shown in Figure 5, would be used to generate the multi-block grids around the sections studied. Instead of consisting of a single block wrapped around the aerofoil and its wake, a number of blocks were used. It was decided that the curve describing the aerofoil would be broken into six parts of equal length, to allow grid node clustering at the leading and trailing edges. The outer block edges forward of the aerofoil section between the two points of maximum thickness were defined as offset splines to ensure that the normal distance outward from any point on the section was fixed. This was done to ensure that the interpolated nodes, radiating from the section were located the same distance away from the section. All the other outer block vertices were placed directly above or downstream of the node vertices on the aerofoil section. Block structure diagrams, showing how the physical and computational domains are related for the various rudder geometries are detailed in Figures 6 to 9. The most complex block structure developed, was that used for generating grids around flapped rudder sections. Producing a topology which allowed the gap between the flap and the main rudder section and movement of the flap, whilst maintaining a high level of grid quality was challenging. Figure 9 shows the flapped rudder topology developed. Although computations of flapped rudder performance were beyond scope of the work presented, the flapped rudder topologies were generated to highlight the versatility of the grid generation method.

4.4 Conclusion to Chapter

A general overview of the multi-block grid generation method favoured by finite volume flow solvers, like CFX-4.3 was presented. A description of MESHBUILD and Fleximesh, the grid generators used in this research programme was also given, together with a discussion of their respective merits and shortcomings. Because of the flexibility of Fleximesh, it was decided that it would be used to create the rudder section grids investigated in this Thesis.

The generation of high quality multi-block grids, can often be a complex procedure requiring careful multi-block topology definition. A description of the construction of the multi-block topologies used to generate the grids around the rudder sections investigated later in the Thesis, was also given.

Chapter 5

Flat Plate Skin Friction Estimation

5.1 Overview of Chapter

It was decided that a flat plate resistance study would be carried out, to determine the model and grid parameters necessary for accurate viscous flow modelling, in the absence of the grid distortions produced by rudder sections. It was hoped that the results obtained from this study would provide invaluable information as to the critical parameters needed for accurate skin friction evaluation. The effects of grid resolution, Reynolds number, differencing scheme, turbulence model and turbulence model constants were all investigated. Where possible the computations were validated against experimental data, and in the absence of any suitable experimental data, against empirical skin friction lines. A number of the low Reynolds number flat plate computations were validated against the flat plate skin friction data obtained by William Froude [83, 84] in the 1870's. A more detailed overview of skin friction estimation, together with additional results from this investigation can be found in Date and Turnock [85].

5.2 Investigation Description

5.2.1 Investigation Strategy

Steady state two-dimensional laminar and turbulent computations are presented for flat plates of various lengths, over a range of Reynolds numbers. Boundary location and full grid independence studies were conducted, to determine the critical grid requirements needed to accurately predict skin friction. The effects of using different differencing schemes and turbulence models were also investigated. Where possible, the computed skin friction estimates were compared with experimental data, and in the absence of such data, compared to empirical skin friction lines. By carrying out linear regression on the RANS skin friction data, a resistance correlation line was derived, and subsequently compared with those of Schoenherr [86] and the ITTC [87].

5.2.2 Validation Data

The experimental results obtained by Froude [83, 84] were used for validation, along with the empirical skin friction lines of Schoenherr [86] and the ITTC [87]. Froude carried out towing tank tests on flat plates ranging from $L = 1 - 50$ ft $(0.3054 - 15.0$ m) at free stream velocities of between $U_\infty = 50 - 1000$ ft/min $(0.254 - 5.08$ m/s), corresponding to $R_n = 6.7 \times 10^4 - 6.8 \times 10^7$. The towing tank turbulence level was not measured. The empirical skin friction lines of Schoenherr [86] and the ITTC [87] were derived from regression analysis of experimental data over a range of Reynolds numbers.

5.2.3 Computational Model Particulars

Computations were carried out on flat plate models of between $L = 1 - 1000$ ft ($0.3054 - 15.0$ m) at free stream velocities of between $U_\infty = 50 - 1000$ ft/min ($0.254 - 5.08$ m/s), corresponding to $R_n = 6.7 \times 10^4 - 1.4 \times 10^9$. The fluid density was set as $\rho = 1000$ kg/m^3 and dynamic viscosity was set as $\mu = 1.719 \times 10^{-3}$ kg/m s at 2 degrees centigrade. The standard and RNG $k - \varepsilon$ turbulence models were tested, using the standard constants given in Table 1. The inlet turbulence parameters k and ε were set according to the free stream conditions. Various differencing schemes were used for the spatial u and v terms and turbulence quantities k and ε. Pressure correction was carried out using the SIMPLE algorithm. The under-relaxation parameters were set according to Table 3. The mass source residual stopping convergence criteria was set at 1.0×10^{-6} kg/s in all computations. All computations were carried out using the Irixcompute computing facility, as described in Chapter 3.

5.3 Boundary Conditions

There were a number of boundary condition combinations that could be applied to the simple problem of the viscous flow over a flat plate. Figure 10 and Table 5 show the boundary conditions used for the flat plate model. In this skin friction investigation, it was only necessary to model one side of the plate. Halving the problem in this way, reduced the total number of cells and hence the solution time. The plate itself was modelled as a wall with a no-slip condition. The boundary conditions used in this investigation were found to give the most rapid flow solutions. However, the upper inlet boundary condition could have been set either as symmetry plane or as a constant pressure boundary; likewise the downstream boundary could also have been defined as constant pressure boundary. The use of an upper pressure boundary condition was found to be a poor choice, as it needed to be placed at an excessive distance from the lower wall, in order to ensure tangential flow to it.

Since Froude was unaware of the existence of residual turbulence, and thus not taking any measurements of turbulence level, it was assumed that the tank had very little residual turbulence in all of his experiments. The inlet turbulence parameters k and ε were therefore both set to 1.0×10^{-4}, ensuring that k and ε remained positive throughout the solution, as discussed in Chapter 3.

5.3.1 Positioning of Boundaries

A boundary location sensitivity study was carried out to determine the minimum distance at which the inlet, outlet and upper inlet boundaries could be placed in relation to the plate, without affecting the solution. The boundary position sensitivity study involved moving one of the outer boundaries until convergence on the plate skin friction was obtained, whilst the remaining two boundaries were held fixed. This was done in turn for all three outer boundaries. The positioning of the boundaries was based on the plate length L and ranged from $L/8$ to $4L$. All the grids used in this sensitivity study, used a uniform distribution of cells in the x and y-directions of fixed size regardless of boundary position. This ensured that any variations were due to the boundary positioning and not cell size. The longest plate tested by Froude of 50 ft (15.24 m) was used at the maximum test speed of 5.08 m/s, the condition of maximum turbulence. A third order spatial differencing scheme was used on the flow variables and the standard $k - \varepsilon$ turbulence model was employed. The results from the study are shown in Tables 6 to 8. For the inlet and outlet parametric studies, the upper inlet boundary was positioned at a distance $2L$ above the plate. For the upper inlet boundary parametric study, the inlet and outlets were positioned at a distance of L upstream and downstream.

It can be seen that convergence on skin friction has been reached on all of the boundary condition positions. Comparing Table 6 with Table 7, it is evident that the solution to the flow problem is more sensitive to the downstream outlet boundary position, than the upstream inlet position. In fact, the upstream inlet can be placed

as close as half the plate length upstream of the plate without affecting the flow solution, whereas the outlet mass flow boundary must be placed at least one plate length downstream.

It is quite surprising to note, from the data in Table 8, that the upper inlet needs to be placed at least two plate lengths above the plate, before the solution becomes boundary independent. It should be noted from this study, that the number of iterations taken in obtaining a solution, are generally unaffected by the boundary position once convergence has been reached. This is because the additional number of cells resulting from the increased size of the flow domain, have no effect on the flow, having the same transport properties at the outer cells of the previously converged solution. Additional cells merely serve to increase the number of equations being solved and hence, the total time for solution. Based on the results found in this study, it was decided that all inlet and outlet boundaries, would be placed at a distance $2L$ from the plate, to ensure boundary independence.

5.4 Grid Parameters and Independence

In this flat plate investigation, a full independence study was carried out to determine the optimum cell distribution throughout the domain. The study was carried out on the largest plate tested by Froude, the case of maximum turbulent flow; the wall roughness was considered hydraulically smooth. It is known from the previous work done by Reynolds [88], that the transition from laminar to turbulent flow over a flat plate happens near a critical Reynolds number of $R_n = 5 \times 10^5$. From Table 9 it is evident that for all, but the shortest of plates and slowest of speeds, Froude's tests were conducted within the turbulent flow region.

5.4.1 Near-Wall Grid Study

A near-wall independence study was carried out to determine the effect of the near-wall cell spacing on the skin friction prediction. It was necessary in the near-wall independence study to consider both the maximum and minimum velocities at which the model was to be tested, since the y^+ criteria of the wall function is related to velocity and cell spacing. Having to produce a grid, suitable for operation over a range of Reynolds numbers, caused a significant problem with regard to the fixing of the first cell size. This cell size was carefully selected to ensure that the y^+ remained within the 30 to 500 range for all Reynolds numbers, as detailed in Chapter 3. The grid propagation options within CFX-MESHBUILD, allowed either a uniform distribution or geometric progression along the block edges. In this grid independence study, the geometric progression distribution was used in the y-direction, and a simple uniform distribution in the x-direction. The geometric propagation is controlled by the required number of cells and a common factor. The cell distribution parameters in the geometric progression, can be derived using the first and last cell sizes on a block edge, see Appendix B. The uniform distribution in the x-direction consisted of 40 cells in the 2L upstream, and downstream directions and 20 cells along the plate itself. The outer cell in the y-direction had a fixed cell spacing of 10 m, and the near-wall cell size was varied. Equation 48 was used to estimate the cell size needed to give the correct y^+ for the high and low Reynolds numbers, as derived by Schlichting [74].

$$y^+ = 0.172 \left(\frac{y_p}{L}\right) R_n^{0.9} \tag{48}$$

Using $y^+ = 30$ as the criterion for the first cell size, the corresponding y_p was found for both the high and low Reynolds number flow conditions. As can be seen from Table 10, the first cell size at the maximum and minimum Reynolds numbers, vary quite dramatically when y^+ is fixed at 30. In fact, the cell size for the high Reynolds number case is approximately 15 times smaller than that of the low Reynolds number case. For the same grid to be used in solving both the high and low Reynolds number

flow cases, the smallest first cell size had to be no smaller than 0.0035 m, in the y-direction, if y^+ is to be kept above the lower limit of 30. Based on these estimates it was decided that the first cell size spacing would be set at 0.005 m. Two runs were subsequently carried out at the maximum and minimum Reynolds numbers to check that the calculated y^+ values fell within the bounds required. The results from these two runs can be seen in Table 11. For the high Reynolds number case, the y^+ values lie with the range $30 \leqslant y^+ \leqslant 500$, using a cell spacing of 0.005 m. For the low Reynolds number case, the y^+ values fall below these bounds, but above the absolute minimum value of 11.63. Based on the results from this study, it was decided that a first cell size of 0.005 m would be used.

A brief study was carried out to determine the effect of y^+ on the actual calculated skin friction, within the range of $30 \leqslant y^+ \leqslant 500$ for the 50 ft (15.24 m) plate operating at the highest Reynolds number. The results in Table 12, show the results from five different runs, each with a near-wall cell size half that of the previous, and an outer cell size of 5.0 m. It can be seen from these results that there is very little variation in c_f with near-wall cell size. It is obvious from Table 12 that the use of a small near-wall cell size, and hence small y^+, causes excessive computational effort to be used in formulating a solution, with no increase in accuracy.

Although the reduction in the near-wall cell size slightly increases the total number of cells (an extra 1500 cells) within the problem, this alone does not account for the 228 fold increase in CPU time needed to solve the problem. It should be noted that if the cell size is such that the y^+ falls below 5 and is within the purely laminar sub layer, convergence is hard to achieve. This study, therefore, indicates the importance of selecting the correct near-wall cell size, in order to make good use of the wall functions provided.

5.4.2 Boundary layer Flow Support Grid Study

Following the correct selection of the near-wall grid spacing, a convergence study was carried out to determine the optimum outer grid cell size needed to provide the required distribution for flow support in the boundary layer in the y-direction. The near-wall grid spacing was fixed at 0.005 m, and the outer grid cell size was varied between 10 m and 1.25 m, until convergence was achieved. The distributions in the x-direction were the same as those used in the near-wall grid study, and the flow speed was fixed at 5.08 m/s.

From Table 13, it can be seen that full convergence of skin friction coefficient, was reached when the outer cell size was fixed at 1.25 m. It can be seen that the CPU time increases sharply with decreasing outer cell size, as a result of the increased total number of cells. Based on this data, it was decided that the outer cell size of 2.5 m would be used in subsequent calculations, since the small increase in accuracy of the 1.25 m case did not warrant the extra number of cells.

5.4.3 Longitudinal Grid Study

An independence study was carried out for the grid distribution along the length of the plate itself. Again, the study was carried out on the 50 ft (15.24 m) plate at 5.08 m/s. The grid propagation in the y-direction, was set in accordance with the grid independent solution, found in the boundary layer study i.e. $0.005 - 2.5$ m. The propagation used on the upstream and downstream blocks were set as geometric progressions. The outer cell size started at 2.5 m, decreasing in size to 0.1 m at the leading edge of the plate. The distribution used on the plate itself was a symmetric geometric progression, with a matched cell size of 0.1 m at the leading edges and variable middle cell size.

From Table 14, it can be seen that convergence on skin friction coefficient, is achieved

when the middle cell size of the geometric progression reached 0.5 m. It can be seen that further reduction in middle cell size along the plate does not effect c_f. Therefore, it can be said that the solution to this problem is grid independent.

The grids used subsequently in this investigation, were based on the results found in this grid independence study. The x-direction geometric progression distributions on the blocks for the different plate lengths tested, were set with the same parameters as those derived for the 50 ft (15.24 m) plate, tested in the independence study. The y-direction geometric progressions down on to the plate itself were slightly modified to ensure that the first cell size gave the correct y^+ value for the particular plate length. An example of the final grid used to model the 50 ft (15.24 m) is given in Figure 11.

5.5 Validation against Experimental Data

The aim of this investigation was to evaluate the performance of standard and RNG $k-\varepsilon$ turbulence models at predicting skin friction, and to assess the effect of Reynolds number. The investigation involved further modelling Froude's plates of 50 ft (15.24 m), 16 ft (4.88 m), 1 ft (0.30 m) and two ship scale high Reynolds number test cases of 500 ft (152.40 m) and 1000 ft (304.8 m). All of the results obtained were validated against Froude's original test data and the ITTC 1957 and Schoenherr correlation lines.

5.5.1 Differencing Scheme Effects on Accuracy

In this investigation, three of the most common differencing schemes were investigated; upwind, QUICK and hybrid. All the tests were carried out on the 50 ft (15.24 m) plate using the standard $k-\varepsilon$ model. Table 15 shows the differencing schemes tested on the 15.24 m plate. For the high order study, the QUICK differencing scheme

was unable to be implemented on the turbulence equations k and ε, since this gave rise to non-convergent flow solutions, resulting from negative values of k and ε. The hybrid scheme was used instead, ensuring that k and ε remained positive. The results from the study can be seen in Figure 12.

There is only a slight increase in accuracy when the third order differencing scheme is used for solving the flow. It was noted that the use of the QUICK scheme, resulted in an increased solution time compared with that of the upwind solution. Depending on flow velocity, this increase varied between $15 - 45\%$. This is not surprising, as the grid used in this study was refined with extreme accuracy, using the QUICK differencing scheme. The use of the QUICK differencing schemes throughout the boundary positioning and independence studies, was done to ensure a high degree of accuracy in the final comparison studies. If the grid had been refined using the upwind differencing scheme, it is envisaged that there would have been a noticeable increase in accuracy, if a higher order scheme was subsequently used. Following this route would, however, have resulted in the need for a further independence study, to confirm that the maximum level of accuracy had been achieved, and not just an increase in accuracy from the upwind solution.

5.5.2 Comparison of Turbulence Models

A study was carried out to determine which out of the two high Reynolds number turbulence models available within CFX-4.3, gave the most accurate viscous drag predictions. The standard $k - \varepsilon$ and RNG $k - \varepsilon$ turbulence models were verified for the highest and lowest Reynolds number, plate experiments tested by Froude i.e. the 1 ft (0.305 m) and 50 ft (15.24 m) plate cases. The results were assessed using Froude's experimental data as a benchmark. The results from the study can be seen in Figure 12 and Figure 13. It is obvious in Figure 12, that there is little difference in the accuracy of the two turbulence models, when validated against the results from Froude's experimental data, for the 50 ft (15.24 m) case. The standard

$k-\varepsilon$ turbulence model is 2% more accurate in predicting the skin friction than the RNG $k-\varepsilon$ model, providing a skin friction estimate of 99.7% of Froude's actual experimental value. However, the results from the low Reynolds number study on the 1 ft (0.305 m) plate do not show good agreement with Froude's experimental data, as indicated in Figure 13. The skin friction estimates calculated using the two different turbulence models show good agreement with each other as in the high Reynolds number case. However, they both over predict the viscous drag by $15-50\%$, depending on the surface finish of the plates. It is believed that the source of this error is due to the turbulence model's inability to simulate transition from laminar to turbulent flow. Based on the results found in this study, the standard $k-\varepsilon$ model was considered the most appropriate turbulence model for solving this particular viscous flow problem and was consequently used for all the subsequent studies presented.

5.5.3 Laminar-Turbulent Transition

Comparing the experimental data plotted in Figure 13 and considering the Reynolds number range over which the data corresponds ($R_n = 4.0 \times 10^5 - 1.0 \times 10^6$), it is obvious that the flow is within the typical laminar-turbulent transition region of ($R_n = 3.0 \times 10^5 - 1.0 \times 10^7$). The effect of surface roughness on skin friction is also highlighted in Figure 13 on comparison of the experimental data for the varnished and tin foil coated plates tested by Froude. The rougher varnished plate has the effect of tripping the initial laminar boundary layer into becoming turbulent closer to the leading edge, resulting in a greater viscous drag. However, the smooth tin foil covered plate has a greater region of laminar flow extending further aft along its surface, which is triggered into turbulent flow much later and results in greatly reduced skin friction.

The discrepancy between Froude's experimental data and the numerical results are a result of the flow solvers' lack of simulation of this laminar-turbulent transition region. When solving fluid flows using CFX-4.3, the problem has to be specified as

being either laminar or turbulent. Hence, laminar or turbulent flow is simulated over the whole length of the plate from the leading edge, which is physically incorrect. However, the assumption that the flow is fully turbulent over the whole length of the plate is valid for plates travelling at $R_n > 5.0 \times 10^6$. At these high Reynolds numbers, the contribution to skin friction resulting from the laminar boundary layer tends to zero, since transition happens almost instantaneously at the leading edge. Hence, there is good agreement between the experimental and theoretical results, as shown in Figure 12.

At low Reynolds numbers, $R_n < 5.0 \times 10^6$, the situation is reversed, and the laminar boundary layer contribution to viscous drag becomes significant and an assumption that the flow is fully turbulent does not hold. This results in an overestimate of the viscous drag, as shown in Figure 13. With regard to a RANS calculation, there is no simple solution to the problem of transitional flow, since the problem must be specified as either laminar or turbulent.

Other RANS studies such as those carried out by Chung and Min [89], have simulated laminar-turbulent transition using a triggering method in which the critical local Reynolds number or location of transition is specified on the body. However, for most practical full-scale ship flow calculations the problems associated with transition can be ignored, since the flow is predominately turbulent over the whole body.

5.5.4 Comparison Against Skin Friction Lines

A study was conducted to assess the overall performance of the standard $k - \varepsilon$ turbulence model over a range of Reynolds numbers from model to full scale, similar to that conducted by Dolphin [90] using the Baldwin-Lomax turbulence model. The results obtained were compared with the empirical skin friction correlation lines of

Schoenherr; Equation 49 and the ITTC; Equation 50 given below.

$$\frac{1}{\sqrt{c_f}} = 4.13 \log_{10} (R_n c_f) \tag{49}$$

$$c_f = \frac{0.075}{(\log_{10} R_n - 2)^2} \tag{50}$$

In order to make valid comparisons, further calculations were conducted to provide skin friction data at intermediate and high Reynolds numbers. The runs were carried out on flat plates of 16 ft (4.877 m), 500 ft (152.4 m) and 1000 ft (304.8 m). The resistance curves for these plates are shown in Figures 14 to 16.

All of the skin friction data obtained for standard $k - \varepsilon$ turbulence model and laminar studies to third order were subsequently plotted on a Schoenherr Log-Log graph, along with the empirical skin friction lines of Schoenherr, ITTC 1957 and Froude's data, as shown in Figure 17. When the RANS skin friction data is compared with the ITTC model-ship correlation line, the following trends were identified:

- Between $R_n = 5.0 \times 10^4$ and 1.0×10^6, there is good agreement between the RANS predicted skin friction data and the ITTC line, probably due to the modified slope of the ITTC line.
- Between $R_n = 1.0 \times 10^6$ and 1.0×10^9, there seems to be a constant over prediction in skin friction by the RANS method.

The following trends were identified on comparing the RANS method skin friction results with Schoenherr's line.

- There is general agreement between the data and the Schoenherr line across the whole range of Reynolds numbers.
- Between $R_n = 1.0 \times 10^5$ and 2.0×10^7, there is a constant under-estimate, probably due to the inclusion of aspect ratio and edge effects in Schoenherr's original data.

- Between $R_n = 2.0 \times 10^7$ and 1.0×10^9, there is a constant over-prediction.

From this study it can, therefore, be concluded that standard $k - \varepsilon$ turbulence model generally performs well over the range of Reynolds numbers investigated, with only slight differences compared to empirical friction lines of the Schoenherr and the ITTC. However, as highlighted by Kodama [55], only after conducting full scale measured wake surveys can a turbulence model be considered fully valid, as a good turbulence model should be able to capture the Reynolds number dependence of the wake from model to full scale.

5.5.5 Numerically Derived Resistance Correlation Line

Based on all the experimental skin friction data obtained for the standard $k - \varepsilon$ turbulence model, a RANS predicted Schoenherr skin friction formula was derived using Prandtl's approach. A linear least-squares regression fit was then carried out on all of the results, to obtain the the two coefficients in Equation 49. The regression plot of the data can be seen in Figure 18. The modified Schoenherr formula based on the regression analysis of the RANS data is given by Equation 51.

$$\frac{1}{\sqrt{c_f}} = 4.06 \log_{10} (R_n c_f) - 0.729 \tag{51}$$

The form of Equation 51 is similar to that derived by Schoenherr from experimental data, with nearly identical gradient and a slight offset. However, it is not explicitly dependent on experimental data (no influence of shape, aspect ratio or edge effects) and is only implicitly dependent on empirical data on which the turbulence model is based.

5.5.6 Simulating Wall Roughness

A brief investigation was carried out to determine how plate roughness could be simulated in RANS computations. The study was carried out on the 50 ft (15.24 m) plate. When using wall functions, the effect of wall roughness can be simulated by decreasing the log-layer constant E. The skin friction results for smooth wall condition, $E = 9.793$, were compared with two rough wall cases; where $E = 4.897$ and $E = 2.449$. The results are plotted in Figure 19. Decreasing the value of the log-layer results in an increase in predicted skin friction. Using a log-layer constant half that of the smooth wall value ($E = 9.793$) results in an 11% increase in the predicted viscous drag at a speed of 5.08 m/s. Similarly, the use of a value a quarter of the smooth wall value results in a 22% increase in viscous drag.

It is possible to select values of the log-layer constant based on experimental data on sand roughness, values of which can be found in Schlichting [74]. However, finding the sand roughness and its corresponding log-layer constant for a particular surface is difficult. The only accurate way of determining the log-layer constant for a particular surface finish, say a painted ship rudder, would be to conduct a flat plate experiment. The log-layer constant in the RANS calculations could then be adjusted, to make the calculated skin friction consistent with those found by experiment.

5.6 Conclusion to Chapter

This investigation has highlighted the complex procedures that are required in order to obtain accurate viscous skin friction estimates, when using a RANS solver. The procedures carried out in this study can be applied to the modelling of any viscous flow problem, be it a simple pipe flow or the flow round complex ship geometry. The difference is that for a rudder flow problem, the problem definition is further complicated by complex curved surfaces and the existence of viscous pressure interaction.

The following general conclusions are drawn from this skin friction investigation:

- Correct model boundary condition selection and positioning are essential in forming a well-posed problem, capable of efficient solution using a RANS code solver.
- Detailed near-wall and whole fluid domain independence studies are necessary if RANS solutions are to be regarded as being grid independent, and of the highest level of accuracy.
- Correct selection of the first near-wall cell size is important in order to make proper use of the wall function, whereby, avoiding excessive computational effort.
- Effects of Reynolds number on the near-wall grid spacing must be taken into account, when dealing with flow problems operating over a range of velocities.
- Initial specification of the level of accuracy expected from the results is essential, in order to make efficient use of computational resources.

The following conclusions can be drawn from the comparisons made between the RANS results and those of Froude and the empirical skin friction lines:

- The standard $k-\varepsilon$ and RNG $k-\varepsilon$ turbulence models both performed well over a range of Reynolds numbers, with the standard $k-\varepsilon$ model providing a 2% more accurate correlation with Froude's data than the RNG $k-\varepsilon$ turbulence model, at high Reynolds numbers.
- With regard to the skin friction estimation at low Reynolds numbers, the RANS results were in error due to the RANS solvers inability to simulate laminar-turbulent transition.

- As expected there is good correlation between the RANS results and the correlation lines of the ITTC and Schoenherr, over the range of Reynolds numbers investigated, with specific differences within certain bounds of Reynolds number.

- A modified Schoenherr formula was derived from the RANS data, providing constants not dissimilar to those derived by Schoenherr. The important point to note is that this formula does not rely explicitly on Froude's plank data but on the empirical factors included within the $k - \varepsilon$ turbulence model.

- It was shown that surface roughness could be simulated by suitably modifying the log-layer constant within the turbulence model wall function.

Chapter 6

NACA 0012 Section Performance

6.1 Overview of Chapter

The previous Chapter investigated the use of the RANS solver in estimating the viscous drag on a flat plate. The results from this study highlighted how sensitive even the simplest flow models can be to the selection of grid and solver parameters. These results give an insight into the important grid quality solver parameters which need to be considered when seeking accurate frictional drag estimates. However, the flow phenomena about lifting two-dimensional rudders is far more complex than the flow about a flat plate. The existence of high pressure gradients and separation flow features, as well as frictional effects, place specific demands on grid quality and solution strategy. The following Chapter presents a validation study similar to the flat plate, but addressing the specific grid requirements needed to capture the flow features about a two-dimensional NACA 0012 rudder section adequately. The coupling of pressure distribution and boundary layer development will thereby be examined. This study will also address the important topic of convergence criteria and its effect on solution accuracy.

6.2 Investigation Description

6.2.1 Investigation Strategy

The investigation was divided into four parts; a boundary location study, grid independence study, a convergence criteria study together with a validation investigation against experimental data.

The boundary location and grid independence study was deemed necessary, in order to gain an understanding of specific grid requirements, needed to capture the complex flow features about rudder sections adequately. The convergence criteria study, was carried out to determine the effect of mass source residual stopping criteria on solution accuracy. This investigation was regarded as extremely important at this stage of the research, since later transient calculations would require efficient use of computer resources, whilst retaining a high degree of accuracy. The validation study was carried out to assess the performance of the RANS code in computing lifting surface flows.

6.2.2 Validation Data

The NACA 0012 section was chosen as the validation test case, since many systematic experimental investigations had been carried out using it, providing a rich source of validation data. A number of experimental tests have been carried out on the NACA 0012 section, the most comprehensive of which are those conducted by Abbott and Von Doenhoff [91], Thibert et al [92] and Gregory and O'Reilly [93].

Abbott and Von Doenhoff's [91] tests were carried out in a wind tunnel on a wing of chord, $c = 0.6$ m and span, $b = 0.9$ m at Reynolds numbers up to $R_n = 9.0 \times 10^6$ and Mach numbers of less than 0.17. The tunnel turbulence level was low, in the order of a few hundredths of a percent. The low Mach numbers of these tests mean that they can be regarded as incompressible, and suitable for validation against the

computed incompressible results, obtained from the RANS code. The data presented by Abbott and Von Doenhoff [91] consists of plots of c_l versus α and c_d versus c_l, at $R_n = 3.0 \times 10^6$, 6.0×10^6 and 9.0×10^6. Whilst Abbot and Von Doenhoff [91] present a rich set of force measurements, surface pressure measurements are not presented. The results from Abbott and Von Doenhoff's [91] experiments were used to validate the RANS computed rudder force coefficients.

Thibert et al's [92] experiments were carried out in a wind tunnel on a wing of chord, $c = 0.21$ m and span, $b = 0.56$ m at Reynolds numbers up to $R_n = 4.96 \times 10^6$ and Mach numbers between $0.3 - 0.829$. Measurements of turbulence level were not made. The high Mach numbers at which these tests were carried out mean that the results cannot be regarded as incompressible, hence, making them unsuitable for comparison with the incompressible results obtained from the RANS code; They would, however, provide a good source of validation data for any compressible RANS results. The data presented by Thibert et al [92] consists of plots of c_l versus α and c_d versus c_l and surface pressure plots at various Reynolds numbers and Mach numbers.

Gregory and O'Reilly's [93] experiments were carried out in a wind tunnel on a wing of chord, $c = 0.76$ m and span, $s = 2.7$ m at Reynolds numbers up to $R_n = 2.88 \times 10^6$ and Mach numbers of less than 0.16. Measurements of turbulence level were not made. The low Mach numbers of these tests, mean that they can be regarded as incompressible and are, therefore, suitable for validation against the computed incompressible results obtained from the RANS code. Gregory and O'Reilly [93] present plots of c_l versus α and c_d versus c_l, at $R_n = 1.44 \times 10^6$ and 2.88×10^6, along with surface pressure plots at $R_n = 1.44 \times 10^6$. The results from Gregory and O'Reilly's [93] experiments, were used to validate the RANS computed rudder surface pressures computed by the RANS code.

6.2.3 Computational Model Particulars

The NACA 0012 section modelled, had a chord, $c = 0.32$ m and span, $s = 1.0$ m. The chord of $c = 0.32$ m was chosen, because it allowed the grids created, to be used in the subsequent study into the flow about NACA 0012 section with attached Gurney flap. The model was run at $R_n = 2.88 \times 10^6$ and 6.0×10^6 equating to inflow velocities of $U_\infty = 135.37$ m/s and 282.03 m/s respectively, based on an air of density $\rho = 1.204$ kg/m^3 and dynamic viscosity $\mu = 1.811 \times 10^{-5}$ kg/m s at 15 degrees centigrade. The standard and RNG $k-\varepsilon$ turbulence models were both tested, using the standard constants given in Table 1 and Table 2. The inlet turbulence parameters k and ε were set according to the free stream conditions. QUICK differencing was used for the spatial u and v terms and hybrid for the turbulence quantities k and ε. Pressure correction was carried out using the SIMPLE algorithm. The under-relaxation parameters, were set according to Table 3. The mass source residual stopping convergence criteria was set at 1.0×10^{-6} kg/s in all computations. All computations were carried out at steady state, using the Irixresearch computing facility, as described in Chapter 3.

6.3 Boundary Conditions

The multi-block topology structure used to generate the grids around the NACA 0012 section, are shown in Figure 6. The boundary conditions used for the conventional rudder are shown in Figure 20 and Table 16. It must be highlighted, that it was decided that when modelling rudders at angles of incidence, that the inflow angle and not the rudder grid would be altered. This decision resulted in the use of two different boundary conditions, depending on the angle of incidence the section was to be run at. The reasoning behind this decision will be explained.

In many studies of this sort, the rudder is twisted within the grid, whilst holding the inflow direction constant; The author has mixed views on the effect this approach

has on the flow solutions over a range of incidences. The main problem with this approach, is the fact that the cells within the grid become highly skewed as the angle of incidence increases, and it is often hard to control the grid distributions to avoid this. Although these grids can yield acceptable flow results, the creation of highly skewed, and discontinuous cell propagations within the grid, places excessive demand on the flow solver, and often results in solution difficulties and divergence. Even if flow solutions are obtained over a range of incidences using this approach, it is hard to compare the results on the same basis, since the differences in the flow solution will have as much dependence on the grid used, as on the angle of incidence itself. It can be argued that changing the inflow direction, provides a solution to the problem, since it avoids the problem of twisting the rudder within the grid model. Although true, this method also has drawbacks inasmuch as the flow at high angles results in flow diagonally from cell vertex to vertex, within some grid cells of the model. This is far from ideal and can result in numerical diffusion as already mentioned. The problem of numerical diffusion is an inherent problem of both inflow approaches, since no matter what angle the flow is to the grid, at some location within the grid, the flow is likely to be diagonal from cell vertex to vertex. It is believed that this causes less of a problem, than those resulting from twisting the rudder within the grid model. Twisting the rudder within the grid results in regions with have highly skewed cells making the accuarate prediction of cell fluxes difficult, placing excessive demand on the flow solver.

As with the flat plate model in Chapter 5, the rudder section is modelled as a wall with a no-slip condition applied. As shown in Figure 20, the specification of the inflow conditions depend on the angle of incidence of the flow. The constant pressure boundary conditions, were used in this model instead of the mass flow boundary condition, since they are simpler to apply in cases where the mass flow is difficult to calculate, such as on curved boundaries. The inlet turbulence parameters k and ϵ were set according to the free stream conditions, ensuring that k and ε remained positive throughout the solution, as discussed in Chapter 3.

6.3.1 Positioning of Boundaries

As with the flat plate investigation in Chapter 5, a study was carried out to investigate the sensitivity of the flow model to the location of the outer boundaries used to model the unbounded flow field around the rudder. In this investigation, the outer boundary distances from the rudder section were varied between 2 and 15 chord lengths, and the effect on the computed c_l and c_d were noted. The rudder flow incidence angle was set at $\alpha = 8$ degrees, and run at $R_n = 6.0 \times 10^6$ using the standard $k - \varepsilon$ turbulence model. An incidence angle of $\alpha = 8$ degrees was chosen so as to produce a flow regime with a pronounced wake structure, but not so high as to cause problems of convergence with the standard $k - \varepsilon$ turbulence model. The results from this study can be seen in Figure 21. Figure 21 shows that there is asymptotic convergence in both c_l and c_d, as the boundaries are moved further from the rudder. It can be seen that when the boundaries are placed around 15 chord lengths from the rudder, there is little change in the computed c_l and c_d. At this point it is obvious that the solution is no longer affected by the location of the outer boundaries. These results confirm those found by Chau [48], Simonsen [8] and Guilmineau et al [70], who found that the outer boundaries, needed to be placed at between 12 and 15 chord lengths away from the rudder. Many other studies have used boundary locations closer than those found in this study, this is mainly due to constraints on grid size, as a result of limited computational resources. Often, the small errors that result from the application of closer than adequate boundary conditions, can be regarded as acceptable. Based on the results found in this boundary location study, the boundaries were located 15 chord lengths away from the rudder in all subsequent tests.

6.4 Grid Parameters, Independence and Convergence

As in the flat plate study, a full decoupled independence study was conducted, to investigate the effect of changes in near-wall grid node location, number of grid nodes around n_ξ, radiating from n_η and in the wake n_ζ of the NACA 0012 section. The variation in the c_l and c_d, along with the pressure distribution around the rudder section were all studied. Although carrying out such independence studies on every model seems laborious, it is regarded by the author as the only way of ensuring that high quality solutions can be gained from CFD.

An identical approach to the problem of grid independence, has been applied to the NACA 0012 model for the same reasons as was detailed in Chapter 5 for the flat plate model. The only difference between the two flow models, is that the NACA 0012 section experiences pressure forces and separation, at high angles as well as frictional effects; This grid independence study provides important information, as to the specific grid requirements for accurate conventional lifting surface RANS computations. The study was run at a $R_n = 6.0 \times 10^6$ using the standard $k - \varepsilon$ turbulence model.

6.4.1 Near-Wall Grid Study

In an identical way to the study conducted on the flat plate in Chapter 5, the effect of the first cell size on the NACA 0012's drag was investigated. In this study, the rudder section was held at a fixed incidence of $\alpha = 0$ degrees, so that the force acting on it was purely due to drag. This was done to remove any lift induced effects on the solution, thus simplifying the independence analysis.

The outer cells on the outer boundary to the NACA 0012 section were held fixed, whilst the first cell size was varied. The outer cell size was fixed at 0.75 m and the first near-wall cell size was varied between 0.0016 m and 0.0001 m. The results from

the study are shown in Table 17. Here, as was found in the flat plate study in Chapter 5, the c_f tends to vary little between y^+ values of 20 and 400, with the number of iterations and CPU time increasing sharply below the lower y^+ wall function limit of 30.

More importantly, looking at the c_{pv}, it is obvious that use of too large a first cell size, results in an over prediction of the c_{pv}. Good convergence in c_{pv} is shown with decreasing cell size. The reasons for this are two fold. Firstly, the method used to find the wall surface pressure, uses linear interpolation from the cells above the wall; The closer the nearest cell is to the wall, the more accurate the linear interpolation. Secondly, the reduced first cell size means that the total number of cells used in the interpolation are closer to the body, hence, providing better values for interpolation; It is, therefore, not advisable to use the upper y^+ criterion when selecting the first cell size, since this will result in incorrect prediction of the c_{pv}.

These results reiterate the findings of the flat plate study, and highlight the need for the first grid cells near the body, to be small enough not only to resolve the frictional drag correctly, but also ensure the correct computation of the pressure drag too. This finding is significant, since it shows the importance of decoupling a complex flow problem, into simpler sub problems in order to determine the specific grid considerations, necessary to obtain credible flow solutions. Based on these findings it was decided that the near-wall grid cell size would be set at 0.0002 m in all subsequent studies within this section.

6.4.2 Chord-wise Grid Study

A chord-wise grid independence study was carried out to establish the effects of variations in the chord-wise number of cells n_ξ, on the solution, similar to the longitudinal study carried out in the flat plate investigation in Chapter 5. It was necessary to cluster the grid, in order to capture the large velocity gradients in the flow at the

leading and trailing edges. In this study, the NACA 0012 section was placed at an angle of incidence of $\alpha = 8$ degrees, and the effects of different numbers of chord-wise cells on c_l, c_d, and pressure distribution were studied.

The results from this study can be seen in Figure 22 and Figure 23. It is evident from Figure 22 that both c_l and c_l have converged to an almost asymptotic limit. Similarly, looking at Figure 23 there is no identifiable difference between the pressure distribution plots, for all but the coarsest grid tested. In all subsequent tests the chord-wise number of cells were set to $n_\xi = 244$.

6.4.3 Pressure Capture Grid Study

An independence study was carried out, to investigate the effect of increasing the number of cells down onto, n_η, the NACA 0012 section. In this study, the NACA 0012 section was placed at an angle of incidence of $\alpha = 8$ degrees, and the effects of different numbers of cells down onto the section on c_l, c_d and pressure distribution were studied. Here, the inner cell size on the body, was held fixed at 0.0002 m found from the near-wall grid study, and the cell size on the outer body was varied between 3.0 and 0.092 m. The results from this study, can be seen in Figure 24 and Figure 25. It can been seen from Figure 24 that there is good convergence in both c_l and c_d as the number of cells increases. As expected, the pressure distribution in Figure 25, also follows the same trend with convergence in the plotted pressure distribution. This identified convergence in pressure distribution was also found by Zhu and Quin [94] in their research into supercritical aerofoils, using a RANS code. This trend is due to the increased accuracy of the interpolated pressure down onto the body, caused by the increased grid density in the near body region. In all subsequent tests, the number of cells down onto the section were set to $n_\eta = 49$.

6.4.4 Wake Grid Study

An independence study was conducted, to investigate the effects of increasing the number of cells in the wake region, n_ζ, on the NACA 0012 solution. In this study, the NACA 0012 section was placed at an angle of incidence of $\alpha = 8$ degrees, and the effects of increasing the number of cells in the wake region on c_l and c_d were studied. Here, the first cell size at the trailing edge was held fixed, to match the size of the cell on the section, and the outer cell size on the outer boundary was varied between 0.95 m and 0.0887 m. The results from this study can be seen in Figure 26. It is evident that the performance of the section remains generally unaffected by changes in the number of cells in the wake, above 99 cells. In all subsequent tests the wake number of cells were set to $n_\zeta = 99$. The final grid used in all subsequent investigations with the NACA 0012 section can be seen in Figure 27; for clarity alternate grid lines have been plotted.

6.4.5 Convergence Versus Accuracy

As mentioned before, the convergence criteria used in CFX-4.3 for stopping a solution, is the mass source residual. In all the computations up until now, the mass source residual stopping criteria has been set to 1.0×10^{-6} kg/s; It was deemed necessary, to conduct an investigation into the effect this stopping criteria has on solution accuracy.

Using the optimum grid generated through the detailed independence study, a run was carried out at $\alpha = 8$ degrees, with a convergence criteria set at 1.0×10^{-6} kg/s, however, every ten iterations the forces and residuals were output. The data from this study is presented in Figures 28 to 30. Figure 28 shows that after only 600 iterations both the c_l and c_d have converged, indicating that the subsequent 700 iterations have been wasted unnecessarily, in reducing the mass residual down to 1.0×10^{-6} kg/s. In fact, the convergence criteria could have been set at 2.0×10^{-3} kg/s and still given the same results, but for a lower computational overhead.

Out of interest, the c_f and c_{pv} were plotted against the number of iterations in Figure 30. Figure 30 shows that convergence in the frictional drag is reached early on in the computation, at around 100 iterations, with the pressure drag taking a further 450 iterations to converge. This is an important result, since it indicates that the major effort in obtaining a converged solution is in resolving the pressure field within the flow. Using this information, the number of inner iterations on the pressure equation, could have been increased, in order to speed up the convergence rate. Based on these findings, a convergence criteria of 1.0×10^{-4} kg/s was used in all the subsequent runs, unless stated otherwise.

6.5 Validation against Experimental Data

Following the detailed grid independence investigation, the optimum grid was subsequently validated against experimental data. The c_l and c_d were validated against the data presented by Abbot and Von Doenhoff [91] at $R_n = 6.0 \times 10^6$, over a range of incidences past stall. The pressure distribution was compared to the data derived by Gregory and O'Reilly [93] at $R_n = 2.88 \times 10^6$ at an angle incidence of $\alpha = 6$ degrees. The standard and RNG $k - \varepsilon$ turbulence models were both tested. Simulations took between 10 and 100 minutes to converge, depending on the angle of incidence of the section. Solution time increased with increasing angle of incidence, due to the additional complexity of the flow physics, resulting from separation at the higher angles. The convergence times for both the standard, and RNG $k - \varepsilon$ turbulence models were broadly the same across the incidence range.

6.5.1 Lift

The results from the variation of angle of incidence on c_l can be seen in Figure 31. There is good correlation between the computed lift slope and experimental lift

slope obtained by Abbot and Von Doenhoff [91], for both turbulence models up until stall. The maximum lift coefficient $c_{l,max}$, calculated using the RNG $k-\varepsilon$ turbulence model, shows good correlation with experimental data, although the stall angle α_{stall} at which it occurs is slightly over predicted. The standard $k-\varepsilon$ turbulence model severely under predicts the $c_{l,max}$. After stall, there is a drop in the computed c_l but this does not compare well with the experimental data in the case of both turbulence models. These results are broadly similar to those found by Chau [48].

The poor prediction of separation, and hence c_l at high angles is a well known limitation of the standard and RNG $k-\varepsilon$ turbulence models, also identified by Rhie and Chow [71], Chau [48], Rizzeta and Visbal [95] and others. This problem arises due to the use of the wall functions in the near-wall region. Since the first grid points usually lie between a y^+ of 30 and 500, this is usually inadequate when separation is present, as identified by Rizzeta and Visbal [95].

6.5.2 Drag

The results from the variation of angle of incidence on c_d, can be seen in Figure 31. It can be seen that the computed c_d compares well with the experimental results at low angles of incidence, with only a slight over prediction for both the standard and RNG $k-\varepsilon$ turbulence models. At the higher incidences the RNG $k-\varepsilon$ turbulence model does show a slightly better correlation with the experimental drag. Since the lift prediction, which is pressure dominated seems to be accurate, the over prediction in the computed drag values across the incidence range, suggests that the error lies in the computation of frictional drag. From the investigation carried out on the flat plate in Chapter 5, it suspected that this slight over estimate in the frictional drag, is probably due to the laminar-turbulent transition. This problem is addressed by Johansen and Sørensen [96], who carried out an investigation into the influence of transition on lift and drag characteristics of different wing sections, in particular the NACA 0012 section, at $R_n = 3.0 \times 10^6$. They concluded that where possible, transition should be

modelled in CFD calculations, since the laminar-turbulent properties of the boundary layer, have a significant influence on the skin friction and separation experienced by the section, and hence, the computed lift and drag. Johansen and Sørensen [96] found that if transition was not taken into account, a slight under prediction in lift, and a over prediction in drag resulted. It was concluded, that provided the errors in the predicted c_d remained low, quantifiable, and similar for all lifting surface geometries, good qualitative performance comparisons were possible.

6.5.3 Pressure Distribution

The computed pressure distribution, represented by the local pressure coefficient C_p given in Equation 52 for the NACA 0012 is plotted in Figure 32, along with the experimentally determined distribution found by Gregory and O'Reilly [93].

$$C_p = \frac{p - p_\infty}{\frac{1}{2}\rho c U_\infty^2} \tag{52}$$

It is evident, that both the standard and RNG $k - \varepsilon$ turbulence models show good agreement with the experimental data, on pressure and suction surfaces. This was a somewhat expected result, since the lift force, which is predominately pressure dominated, was already shown to be coincident with that determined by experiment. On closer inspection of the pressure distribution, it is noticeable that the curves are not purely smooth and have a number of discontinuities. These small deviations have little effect on the overall performance of the section. It is, however, important to highlight why these small errors have occurred. It is due to the fact that pressure distribution is picking up on the resolution of the grid, which means that the approximated curve which is made up of small linear sections is manifesting itself in the pressure distribution. This problem is unavoidable, using the solution technique implemented by CFX-4.3. The discontinuities in pressure which are noticeable at locations $x/c = 0.33$ and $x/c = 0.66$ result from a problem in the grid generation technique within Fleximesh. These occur at the inter block boundaries because the

gradients of the two splines that meet, are not matched. This results in small errors in the calculation of the section co-ordinates close to the inter block boundaries. This problem was subsequently rectified in a later release of Fleximesh and, therefore, eliminated from later investigations.

6.5.4 Visual Flow Results

Figure 33 and Figure 34 show the streamline plots for the NACA 0012 section at $\alpha = 15$ and 18 degrees (before and after stall) using the standard $k - \varepsilon$ turbulence model. Although no experimental data was available for comparison, it is evident that the predicted separation zone is much smaller than what would be expected, as found by [48]. This is primarily due to the use of a wall function in the standard $k - \varepsilon$ turbulence model.

6.6 Conclusion to Chapter

This Chapter presented the results obtained from steady state calculations, on a NACA 0012 section using a RANS code. Full boundary, independence, convergence and validation studies were conducted for the standard and RNG $k - \varepsilon$ turbulence models.

The following general conclusions are drawn from the NACA 0012 lifting surface investigation:

- The boundary location study, indicated that the outer boundaries should be placed at least 15 chord lengths away from the section, in order to obtain a solution that is unaffected by boundary position.
- The near-wall grid independence study highlighted the need for the first grid cell and density near bodies with high pressure gradients, to be small enough to

resolve the frictional drag, but also ensuring the correct computation of pressure drag.

- The wake grid independence study showed that the solution is largely unaffected by the number of cells placed in the wake region.
- The convergence study indicated the need for careful selection of the mass source convergence criteria, to ensure efficient use of computational resources whilst maintaining a high degree of accuracy in the results.

The following conclusions can be drawn from the comparisons made between the CFD results and those found by experiment:

- There was good correlation between the experimental and computed lift curves for both the standard and RNG $k-\varepsilon$ turbulence models up to stall.
- Both the standard and RNG $k-\varepsilon$ turbulence models fail to predict the location of maximum lift, with the RNG $k-\varepsilon$ turbulence model providing a more reasonable estimate of the point of maximum lift.
- The drag curves for both the standard and RNG $k-\varepsilon$ turbulence models showed a good general agreement with those found by experiment, with only a small offset at low incidences, with the RNG $k-\varepsilon$ providing a better correlation at higher incidences.
- The pressure distribution was shown to have good agreement with that found by experiment.

These conclusions have shown that the RANS code is capable of providing accurate estimates of rudder performance up to stall, and qualitative performance prediction past stall, using the standard and RNG $k-\varepsilon$ turbulence models. A number of limitations of the standard and RNG $k-\varepsilon$ turbulence models have been identified,

such as the lack of a rational way of including laminar turbulent transition, and poor prediction of separation. It is evident that the RANS method can be used to predict conventional rudder performance, with a reasonable degree of accuracy up to the point of stall. For the RANS code to be a truly versatile tool in rudder design, it must be capable of giving performance estimates of non-conventional rudder sections, such as the Schilling, which has a blunt trailing edge.

Chapter 7

Effect of a Gurney Flap on NACA 0012 Section Performance

7.1 Overview of Chapter

A detailed computational investigation into the two-dimensional performance of a NACA 0012 section, fitted with 2 and 4% h/c Gurney flaps, operating at $R_n = 0.85 \times 10^6$ is presented. The aim of the work, was to determine the suitability of the RANS method in modelling the vortex shedding, experienced by lifting sections with blunt, sharp edged features; In particular, whether under-converged steady state calculations could be used for accurate section design performance evaluation, in place of the computationally intensive time-accurate flow simulations. Under-converged steady state, periodic, and time-averaged two-dimensional lift and drag coefficients, vortex shedding frequency and maximum Reynolds stresses are predicted, and compared with the available experimental data. Particular attention is focused on the specific grid and time-accurate time step requirements needed to capture the vortex shedding produced by the Gurney flap.

The flow phenomena over a Gurney flapped NACA 0012 section, is similar to that found over the Schilling high lift sections discussed in Chapter 1. In the absence of detailed validation data for Schilling sections, the Gurney flapped NACA 0012 section provided a comparable, if not more complex validation test case. This investigation was necessary, in order to evaluate the suitability and accuracy of the RANS code for the modelling high lift section performance. From a structural design point of view, i.e. racing car and aircraft applications, the prediction of the frequency and magnitude of any periodic forces acting on Gurney flapped wings, is of considerable importance.

7.2 The Gurney Flap

7.2.1 Description

A Gurney flap is a short thin flap of height h fitted perpendicular to the pressure surface, at the trailing edge of a wing, as illustrated in Figure 35. The most common application of this device, is in racing-car spoilers, where it is used to increase the down-force. This type of device, was first used in this application in the late 1960's by the American racing-car driver and team owner Dan Gurney, who is generally credited with inventing the device that now bears his name. The Gurney height h is usually non-dimensionalised using the chord of the wing c to give a height h/c.

7.2.2 Gurney Flap Effect on Forces

The blunt, sharp edged effect of the Gurney induces an effective camber disproportionate to its size; increasing the C_L for a given incidence, as well as maximum C_L. A number of physical flow phenomena are responsible for this. The vortex shedding, aft of the Gurney, combined with the upstream stagnation region causes an increase

in the circulation and hence lift about the wing. The reduced pressure, aft of the Gurney, also helps to delay separation from the suction surface, increasing maximum C_L. However, the penalty for these increases in C_L is an augment in the zero-lift C_D. Effects similar to these are experienced by high performance ship rudder sections [29]. Of considerable interest is how the lift augment can be maintained, whilst minimising the zero-lift drag. Increments in lift occur with increasing device height, with small Gurneys having a disproportionately large effect.

Jeffery [40] states that generally, fitting a Gurney increases the drag, and reduces the lift-to-drag ratio at low to moderate values of lift. The magnitude of these changes vary with device height, with small Gurneys ($< 1\%$) having relatively small drag penalties. Gurneys also reduce the lift dependent drag, leading to reductions in drag at high values lift. Evidence also suggests that small Gurneys can actually reduce the minimum drag of some sections.

7.2.3 Effect of Gurney Flap on Wake Structure

The first investigation and discussion as to the physical flow around a Gurney, was presented by Liebeck [97], who postulated the flow structure shown in Figure 35. Liebeck [97] hypothesised a short region of separated flow, directly upstream of the Gurney, and two counter-rotating vortices downstream, which he described as having a "tuning effect" on the local flow field. This flow structure, was derived from the twin-bubble structure hypothesised by Küchemann [98], for the trailing-edge region of aerofoils operating at large incidences. Neuhart and Pendergraft [99] also reported that similar vortex structures were observed in water-tunnel experiments. Similar flow structures have been identified by Ashby [100], Ross et al [101] and Jang et al [102] from steady state RANS simulations of aerofoils fitted with Gurneys. These investigations will be discussed in more detail, later in this Chapter.

The RANS studies were all carried out using a steady state solution approach, and

as such failed to provide information regarding any periodicity that may have existed in the wake. It is, therefore, unclear from these studies, whether or not the vortex structure, aft of the Gurney, is in fact stable. Time-accurate calculations have not been carried out using RANS solvers, purely due to computational restraints. To do so, requires large numbers of time steps and extremely fine grids in the wake region, in order to capture vortex shedding.

7.2.3.1 Stable Vortex Structure

Stable vortex structures comparable to those hypothesised by Liebeck [97], can be found downstream of bluff bodies, either at very low Reynolds numbers, $R_n < 50$, or when time-averaged, high Reynolds number flow fields are considered. Carrying out time-averaging on the velocities, in the wake region, results in the alternating velocities far downstream of the body cancelling out, with the only evidence of vortex shedding being two counter-rotating vortices downstream of the Gurney, as hypothesised by Liebeck [97].

7.2.3.2 Unsteady Vortex Structure

For most practical flows about bluff bodies, such as flat plates, cylinders and Gurney flaps, where $R_n > 50$, it is well known that a wake of alternate vortices, known as a Von Kármán vortex street is formed. In these flows, the boundary layers on either side of the bluff body separate at some point, to form two shear layers of opposing vorticity, which roll up to form alternate vortices which then travel downstream.

The mechanism by which these separating shear layers form the vortex street, was first postulated by Gerrard [103]. The first stage of the shedding cycle begins as the shear layer on one side of the body rolls up to form a vortex. As this occurs, it draws the shear layer over from the other side of the body. This shear layer, which contains vorticity of opposing sign, is drawn across the wake centreline, cutting off the supply

of vorticity to the shear layer that is rolling up. At this point, the vortex is shed and moves downstream, whilst the shear layer on the opposite side starts to roll up, so repeating the process.

The vortices shed from the body, travel downstream in the vortex sheet, at typically $70 - 85\%$ of the free-stream velocity [104]. These vortices are shed into the wake, at a frequency f resulting in periodic lift and drag forces to be experienced by the body. The frequency of the shed vortices is often non-dimensionalised, to give what is known as the Strouhal number, given in Equation 53.

$$S_t = \frac{fd}{U_\infty} \tag{53}$$

where, U_∞ is the free-stream velocity and d is some base dimension, which is often the bluff body height, or in the case of the Gurney flap, the flap height h.

7.2.4 Experimental Investigations

A number of experimental investigations have been conducted into the effect Gurneys have on wing performance, since its invention in the 1960's. A detailed overview of these experiments, along with results from his own experiments, are given by Jeffrey [40], circumventing the need for a detailed discussion in this instance.

The earliest reference to the effect of a Gurney on wing performance was made by Liebeck [97], who investigated the effect of a 1.25% device on the lift, drag and wake structure of a symmetrical Neumann aerofoil. Earlier investigations into the performance effect of similar devices, not explicitly known as Gurneys, were evaluated prior to the 1960's and are also discussed in detail by Jeffrey [40].

The recent experimental work by Jeffrey [40] and Jeffrey et al [105, 106], using Laser Doppler Anemometry (LDA), coupled with force and pressure measurements, has furthered the understanding of Gurney flap flows and provided a rich source of validation data for computational fluid dynamics (CFD) simulations.

7.2.5 Computational Simulations

CFD modelling of Gurneys has been limited, mainly due to computational resource constraints, and difficulties associated with the periodic vortex street produced by the Gurney. To date, only two computational approaches have been applied to the problem. The first being a panel method and the second a RANS approach.

Fripp [107] and Jeffrey [40], used panel methods to model sections fitted with Gurney flaps. The Gurney was modelled through the definition of a modified section, with a "virtual" trailing edge, representing the streamlines bounding the recirculation regions upstream and downstream of the Gurney. Fripp [107] reported disappointing results, following comparison with experimental data. Jeffrey [40] managed to obtain reasonable agreement between the computational and experimental results for 2 and 4% Gurneys fitted to a NACA 0012 section. Although this approach has obvious weaknesses, it can be used as a qualitative tool for assessing Gurney flap performance, whilst being simple to develop and computationally inexpensive.

RANS investigations have been carried out by Ashby [100], Ross et al [101], Jang et al [102] and Sims-Williams et al [108]. All these investigations modelled the Gurney directly, yielding time-averaged data through a steady state solution approach.

Ashby [100] carried out both experimental and computational studies of lift-enhancing tabs on a multi-element aerofoil (NACA 63_2-215ModB). The computational study was conducted using a two-dimensional incompressible RANS code, implementing both the Spalart-Allmaras one-equation and Baldwin-Barth one-equation turbulence models. The computed results predicted all of the trends observed in the experimental data reasonably well. The time-averaged flow field indicated by computed streamlines were found to be consistent with the flow field hypothesised by Liebeck [97] and observed by Neuhart and Pendergraft [99].

Ross et al [101] also carried out both experimental, and computational studies of

lift-enhancing tabs on the multi-element aerofoil (NACA 63_2-215 ModB). The computational study was conducted using a two-dimensional incompressible RANS code, implementing the Baldwin-Barth one-equation turbulence model. Whilst the computed lift and drag results did not exactly match those found by experiment, they did manage to indicate the correct trend in the aerodynamic forces, resulting from the addition of the Gurney flap to the geometry.

Jang et al [102] carried out computational studies of Gurney flaps fitted to a NACA 4412 aerofoil. The computational study was conducted using a two-dimensional incompressible RANS code, again implementing the Baldwin-Barth one-equation turbulence model. The trends observed in this study were shown to agree well with the available experimental results. Although not all of the flow physics were captured in the wake downstream of the Gurney flap, enough of the major flow disturbances caused by the application of the Gurney flap were, giving rise to results consistent with those found by experiment.

Sims-Williams et al [108] conducted a single computational study into the effect of fitting a 4.7% Gurney flap to a single element racing car wing. The computational investigation was carried out using a compressible RANS flow solver, implementing the standard $k - \varepsilon$ turbulence model. As such, an elevated Mach number had to be used, although this was considered not to have a great effect on the results. Both viscous and inviscid calculations were carried out for the wing, with and without a Gurney, at one incidence angle. Good agreement was found between the viscous and inviscid computed pressure distributions, and the experimental data, with the lift-enhancing effect of the Gurney being adequately predicted.

Although these RANS studies yielded results broadly similar to those found by experiment, the validity of the steady state solution method used in solving this periodic flow problem has yet to be addressed, along with computations of the time-accurate performance. The aim of this work has been to apply the standard $k - \varepsilon$ turbulence model in both under-converged steady state, and time-accurate calculations and to

compare the results with each other and experimental data. Wake grid resolution and time step sensitivity studies were conducted, in order to establish confidence in the results.

7.3 Investigation Description

7.3.1 Investigation Strategy

In this study both under-converged steady state, and full RANS time-accurate two-dimensional computations, were carried out on a Gurney flapped NACA 0012 section. A boundary location and full grid independence study was not conducted, as the NACA 0012 investigation in Chapter 6 provided the necessary boundary and grid conditions needed to obtain an optimum solution. Subsequently, a wake grid independence study was conducted on the NACA 0012 + 4% Gurney, to investigate the effect of the wake grid on the under-converged steady state solution, in particular its effect on flow structure and performance prediction.

Under-converged steady state computed performance data for a NACA 0012 fitted with a 2 and 4 % Gurney, was then compared with the experimental data obtained by Jeffrey [40], using the optimum grid obtained from the wake study. The under-converged steady state flow about the NACA 0012 + 4% Gurney was also compared with the experimental flow structure obtained by Jeffrey [40].

A time-accurate periodic flow investigation was carried out on the NACA 0012 + 4% Gurney only. This involved a time step study, to examine the effect of time step size on the solution, followed by validation against the experimental data of Jeffrey [40]. The time-averaged periodic data was also compared with the under-converged steady state results, to determine if the under-converged steady state solution approach, captured the same time-averaged flow physics.

Steady state solutions were also obtained for an un-flapped NACA 0012, operating at the same flow conditions as the Gurney flapped NACA 0012 sections. This was done as a comparison, to show how well the solver predicted the effect of fitting a Gurney. These computations were also validated against the data obtained by Jeffrey [40].

7.3.2 Validation Data

The experimental results obtained by Jeffrey [40] were used for validation. These tests were carried out in a wind tunnel, on a wing section of chord $c = 0.32$ m and span $b = 1.6$ m, at a free stream velocity of $U_\infty = 40$ m/s, corresponding to a Reynolds number of between $R_n = 0.77 - 0.89 \times 10^6$ and Mach number of less than 0.11. The variation in the Reynolds number of these tests, was caused by variations in the ambient pressure and temperature. The wind tunnel turbulence level was measured, and found to be of the order of 0.2%. Transition was fixed at 5% x/c from the leading edge. The low Mach numbers of these tests, make them suitable for the validation of the computed incompressible results obtained from the RANS code. Jeffrey [40] presents time-averaged c_l, C_L, c_d and C_D versus α, surface pressures, LDA flow field data and LDA spectral flow field information. Calculations of the uncertainties of the data were made. The accuracy of the inclinometer used to set the incidence angle of the wings was ± 0.1 degrees. An uncertainty of ± 0.0087 in the C_L and ± 0.00078 in the C_D was calculated. The surface pressure measurements were found to have an uncertainty of ± 0.0013 in the C_p.

7.3.3 Computational Model Particulars

Two Gurney flapped, and one un-flapped NACA 0012 sections having a chord, $c = 0.32$ m, span $b = 1.6$ m and flap heights of 2 and 4% were modelled, using the RANS code. These models were run at $R_n = 0.85 \times 10^6$, which equated to an inflow velocity of $U_\infty = 40$ m/s, based on an air of density $\rho = 1.204$ kg/m^3 and dynamic viscosity $\mu =$

1.811×10^{-5} kg/m s at 15 degrees centigrade. The standard $k-\varepsilon$ turbulence model was tested using the standard constants given in Table 1. The inlet turbulence parameters k and ε were set according to the free-stream conditions. QUICK differencing was used for the spatial u and v terms and hybrid for the turbulence quantities k and ε. Quadratic second order time differencing was used in conjunction with fixed time stepping for all time-accurate calculations. Pressure correction was carried out using the SIMPLE algorithm. The under-relaxation parameters were set according to Table 3. The mass source residual stopping convergence criteria was set at 1.0×10^{-4} kg/s in all computations. This convergence level, was determined from a mass source residual versus c_l and c_d convergence study on the NACA 0012 section investigated in Chapter 6. Computations were carried out, using both steady state and transient solution methods. All computations were carried out using the Irixresearch computing facility, as described in Chapter 3.

7.4 Boundary Conditions and Grid

The multi-block topology structure used to generate the grids around the Gurney flapped NACA 0012 section is shown in Figure 7. As with the NACA 0012 topology from Chapter 6, all the outer boundaries were located 15 chord lengths away from the section. The boundary conditions used to model the Gurney flapped NACA 0012 are shown in Figure 36 and Table 18. They were essentially the same as those used in the NACA 0012 study in Chapter 6. The NACA 0012 section was modelled as a no-slip wall, and the Gurney flap was represented by two no-slip wall surfaces back-to-back. It was deemed unnecessary to model the Gurney thickness, as its effect was considered insignificant, and would only serve to further complicate the grid generation process. Facilitating the creation of the two wall surfaces, the topology used in the NACA 0012 investigation in Chapter 6 was divided in two at the Gurney flap height as shown in Figure 36. The grid used for the computations, was based on the final grid derived in the NACA 0012 study in Chapter 6, with small refinements at the trailing-edge

and in the wake regions. Figure 37 shows the finest grid (Grid 4) around the the NACA 0012 section fitted with a 4% Gurney, for clarity only alternate grid lines have been plotted. The first grid node was located $0.000625c$ away from the aerofoil ($y^+ = 39 - 99$).

7.5 Under-converged Steady State Investigation

Before the results of the under-converged steady state investigation are presented, it is deemed necessary to explain what is meant by a "under-converged steady state" solution. Although the flow about a Gurney is unsteady due to the vortex shedding, it is typical to solve these problems as though they were steady, i.e. the time derivatives in RANS equations are set to zero. Steady state computations are much easier and faster than time-accurate computations. Applying this solution approach to unsteady problems can, however, neglect important flow phenomena resulting in incorrect performance prediction. Although theoretically it should be possible to obtain a converged steady state solution, as will become evident, more often than not under-converged steady state solutions are obtained as a result of problems associated with the implementation of steady state method. Although the results obtained from under-converged steady state solutions are not fundamentally correct since global mass conservation has not been satisfied, an investigation was deemed necessary to asses whether useful information could be obtained from these computations. Both under-converged steady state and time-accurate computations have been carried out to determine if this is the case.

7.5.1 Wake Grid Independence Study

It was necessary for a wake grid independence study to be carried out. A refined grid, based on the one obtained in the NACA 0012 independence study in Chapter

6, was used and the wake distribution n_ζ aft of the Gurney refined successively, to produce four grids. The propagation parameters were chosen such that the majority of the grid nodes were located close to the Gurney. The finest (Grid 4) is shown in Figure 37; for clarity alternate grid lines have been plotted. The flow over the four grids was then solved at an angle of incidence of 0 degrees. The computed c_l and c_d are compared in Table 19.

It is evident, that the c_l does not seem to follow any limiting trend with increasing wake grid density. This is somewhat expected, since the lift force is predominantly affected by the flow over the section, and not that occurring in the wake. Although the c_d does not seem to have fully converged to a limiting value, it is evident that the predicted drag is affected by the wake grid density, and would indeed converge further upon refinement. Increased numbers of cells in the wake region, allow more accurate resolution of the pressures aft of the flap, and hence the predicted drag force. These small gains in accuracy in the computed drag, resulting from the increased wake density, does not seem to warrant the large simulation times. It should be noted that the issue of wake grid independence, for the flow in the wake region is problematic. As the grid is successively refined, it becomes increasingly difficult to obtain a converged solution as a result of numerical problems associated with the solution method. A number of steps were taken in an attempt to improve the convergence of the computations. Increasing the number of inner iterations on the pressure equations and further under relaxation were all tried, having little effect on the convergence level. It was decided that further investigation into this lack of convergence would not be conducted as it was far beyond the scope of the research.

The streamlines plotted for the coarse grid (Grid 1) in Figure 41, show the formation of the double vortex structure hypothesised by Liebeck [97] and found by Jeffrey [40]. The streamlines plotted for the fine grid (Grid 4) in Figure 42 indicate the formation of a periodic vortex structure. It is, however, expected that the fine grid solutions would produce similar predicted flow patterns as the coarse grid (Grid 1) solution, if properly converged. The observed wake grid dependent flow structure was implied

by Jang et al [102]. It was found that as the grid in the wake region was refined, the steady state solutions failed to converge, instead oscillating about some mean mass source residual value. This also resulted in oscillations in the predicted c_l and c_d, about some mean or under-converged steady state value as shown in Figure 43.

As a final investigation, the coarse (Grid 2) and fine grid (Grid 4) were run over a range of incidences, $-20 \leqslant \alpha \leqslant 20$ degrees. The results from this study are shown in Figure 45. It can be seen that there is little difference in the c_l and c_d curves of both grids, except around stall, with the coarse grid (Grid 1) predicting a later onset. The effect of wake grid distribution on the section pressure distribution was also plotted for the coarsest (Grid 1) and finest (Grid 4) grids, at an angle of incidence of 10 degrees in Figure 47. As can be seen, there is no noticeable difference in the pressure plots for both grids, supporting the conclusions obtained from the previous c_l comparison.

Although the wake independence study indicated that the wake grid density only has a small effect on the computed c_l and c_d, it was decided that the fine wake grid (Grid 4) would be used in all subsequent under-converged steady state and time-accurate calculations at the expense of increased solution times. This decision was made because the fine grid (Grid 4) was considered to form a closer numerical representation of the physical flow, allowing the unsteadiness to be captured in the later time-accurate calculations. The total number of cells in the fine grid (Grid 4) was 49760.

7.5.2 Validation against Experimental Data

The under-converged steady state section force coefficients of c_l and c_d were validated against those obtained by Jeffrey [40] at $R_n = 0.59 \times 10^6$ for the NACA 0012 + 4% Gurney, over a range of incidences past stall. The under-converged steady state pressure distribution was also compared to the experimental data obtained by Jeffrey

[40] at the same Reynolds number, at angles of incidence of $\alpha = 0$ and 10 degrees. In order to assess the proficiency of the RANS code at predicting the effect of fitting different size Gurney flaps, both an un-flapped NACA 0012 and NACA 0012 + 2% Gurney were also modelled at $R_n = 0.59 \times 10^6$, over a range of incidences past stall. Typically, the under-converged steady state computations took between 2 and 5 hours to converge to an oscillating state, depending on the angle of incidence.

7.5.2.1 Lift

It was decided that the computed c_l data would be compared directly with the measured C_L data obtained by Jeffrey [40]. This decision was taken, because comparing the data with the c_l derived through integration of the pressures around the section was felt to be inadequate, since it fails to take account of any forces acting on the Gurney flap itself. Although this was akin to comparing two-dimensional data ($\Lambda = \infty$), with three-dimensional data ($\Lambda = 5$), it was considered the best option, other than making empirical corrections to the data. Figure 45 compares the computed data with the experimental data. As expected, when carrying out a comparison of this type, there is a decrease in lift slope from the two-dimensional computed data, to the three-dimensional experimental data; When the two-dimensional lift slope from the computed data is corrected to a finite aspect ratio ($\Lambda = 5$), using the finite aspect ratio correction [91], in Equation 54 the lift slopes are in agreement.

$$\frac{dC_L}{d\alpha} = \frac{\frac{dc_l}{d\alpha}}{1 + \frac{2.0}{\Lambda}} \tag{54}$$

Table 20 shows the lift slope corrected data. Agreement of the experimental and corrected computational lift slopes, would suggest that the two-dimensional section c_l curve is correct. The predicted stall angle and maximum c_l are governed by the known limitations of the $k - \varepsilon$ turbulence model as stall is approached.

7.5.2.2 Drag

The computed c_d was compared with the measured C_D found by Jeffrey [40], and not the c_d found though integration of the surface pressures. This decision was made because drag forces calculated through integration of pressures fail to include the skin friction contribution to drag. At low angles of incidence, both the two-dimensional computed data, and the experimental three-dimensional data, should be similar, since the induced drag component is small. Figure 45 compares the computed data with the experimental data. It is noticeable that even at low angles of incidence that the computed data severely under-predicts the drag experienced by the section, even at the point of zero-lift. However, the likely reason for this difference can only be deduced upon comparison of the c_d curve for the NACA 0012 + 2% Gurney, with its experimental equivalent in Figure 48. It can be seen that there is closer agreement between the computed and experimentally derived data for the NACA 0012 + 2% Gurney. A possible explanation for this has been proposed. It is thought that the large upstream low pressure recirculation region, produced in front of the Gurney in the experiments, (even at the zero-lift incidence), promotes the development of vortices close to the trailing-edge. This might explain why the smaller Gurney flap RANS model, has a better correlation with the experimental data than the larger Gurney flap case. Discrepancies in the predicted drag may also occur because the RANS simulation assumes the flow is fully turbulent, neglecting the laminar-turbulent transition occurring near the leading edge, and the drag associated with tripping the flow in the experiments, as already discussed in Chapter 5. With the Reynolds number of the experimental tests being between $R_n = 0.77 - 0.89 \times 10^6$, it is expected that these laminar-turbulent transition effects would be significant.

7.5.2.3 Pressure Distribution

The computed under-converged steady state pressure distribution for the NACA 0012 + 4% Gurney, along with the steady state pressure distribution about an un-flapped

NACA 0012 section at angles of incidence of 0 and 10 degrees, are compared with Jeffreys data [40] in Figure 46 and Figure 47. The Gurney flap's influence on the pressure distribution around the NACA 0012 section is evident when the data for the un-flapped NACA 0012 section is compared to its flapped counterpart. The Gurney unquestionably increases the pressure difference between the suction and pressure surfaces, especially in the vicinity of the trailing edge. Above all, there is good agreement between the computed and experimental data, with small differences only occurring in the leading-edge regions.

7.5.2.4 Effect of Flap Size

The effect of flap size on the c_l and c_d was investigated. Facilitating this, further computations were carried out on an un-flapped NACA 0012 and a NACA 0012 + 2% Gurney. The data obtained is plotted in Figure 48. The computed two-dimensional data, is compared with the experimental three-dimensional results and the lift slopes corrected to a finite aspect ratio ($\Lambda = 5$) in Table 20. It is apparent from Figure 48, that the trends of increasing c_l and c_d with increasing flap height are correctly reproduced in the computations. The computed lift slopes also show good agreement with the experimentally calculated lift slopes.

7.5.2.5 Maximum Reynolds Stresses

As mentioned in Chapter 3, the Reynolds-Averaged approach to turbulence modelling involves the prediction of six known Reynolds stress terms in the RANS equations, through the use of a turbulence model. By comparing the Reynolds stresses in the wake of the Gurney flap predicted by the turbulence model against those found by experiment, an indication of the accuracy of the standard $k-\varepsilon$ turbulence model can be obtained. Turbulence models, like the standard $k-\varepsilon$ model assume that these Reynolds stresses are isotropic, and are related to the production of turbulent kinetic

energy k and the turbulent dissipation rate ε. Therefore, in two-dimensional isotropic flows, the turbulent kinetic energy k is equal to the stream wise normal $\overline{u'^2}$ and cross flow normal $\overline{v'^2}$ stresses. Figure 49 shows a contour plot of non-dimensional isotropic stresses $\overline{u'^2}/U_\infty^2$ and $\overline{v'^2}/U_\infty^2$ in the wake region of the Gurney flap, at the end of the simulation, for the $\alpha = 0$ degree case. A point of maximum stress can clearly be identified, occurring as expected, where one of the shed vortices interacts with the free stream. Tabulated in Table 24, are the locations and values of the maximum non-dimensional Reynolds stress measured by Jeffrey [40] in his LDA experiments. Comparing this data with the data plotted in Figure 49, it is evident that there is a difference of $18 - 35\%$ between the computed and experimental values for the stream wise normal stresses, and a 69% difference for the cross flow normal stresses. It is also evident that the location of the lower point of maximum stream wise Reynolds stress, shown in Figure 49, is in good agreement with that found by experiments. It must, however, be remembered that this plot is a snap shot at the end of the simulation, hence, the point of maximum Reynolds stress will vary from iteration to iteration. It is clear that modelling a highly anisotropic flow problem with an isotropic turbulence model, can result in large differences in the computed and experimental Reynolds stresses.

7.6 Time-Accurate Performance Investigation

A study into the time-accurate performance of the Gurney flapped NACA 0012 section was conducted. In order to keep the number of large time-accurate simulations to a minimum, only the NACA 0012 + 4% Gurney was modelled. The 4% flap height model was chosen, because it is typical of those found on blunt trailing edge rudders, giving a close representation of the expected flow. The aim of this investigation was to obtain information on the flow transients caused by the Gurney flap, and to identify if the RANS code is capable of predicting the principle vortex shedding frequency and periodic performance. Comparison of the time-averaged performance data, with

the data obtained from the under-converged steady state investigation, was used to confirm the validity of the under-converged steady state approach.

7.6.1 Temporal Time Step Study

As already discussed in Chapter 3, the selection of the correct time step value is the single most important parameter which can effect the solution of unsteady flows, such as vortex shedding. To highlight this, a study was conducted to determine the optimum time step needed to capture the vortex shedding behind the Gurney. Computations were carried out on the fine grid (Grid 4) used in the previous under-converged steady state computations at $R_n = 0.59 \times 10^6$ at an angle of incidence of 0 degrees. Solutions were obtained using various time steps, and the time step dependency of the solutions was investigated.

An initial estimate of the smallest time step needed, was made using the residence time approach detailed in Chapter 3. Knowing the smallest cell size in the wake region $\Delta x = 0.001$ m and free-stream velocity $U_\infty = 40$ m/s, an approximation of the required time step was made using Equation 47. This gave an estimate of the smallest time step as being $\Delta t = 0.000025$ s. An estimate of the total simulation time, was made based on the domain size and free-stream velocity. The time taken for the fluid to travel from the inlet to the downstream outlet was calculated as 0.25 s and was subsequently used as the maximum simulation time. Based on these onerous calculations, 10000 time steps were, therefore, required for the whole simulations using the derived time step.

Figure 50 shows the evolution of the transient lift and drag as the simulation progresses. It is evident that the solution is highly oscillatory at the beginning of the computation, and slowly converges to a regular oscillating solution, as the vortex shedding becomes better resolved. It is obvious from Figure 50, that the estimate of the total simulation time was correct, because up until 0.2 s in the simulation, the

solution is still converging. Figure 51 shows the transient lift and drag, near the end of the simulation, over a period of approximately two cycles. Looking at the number of time steps used in evaluating the transient performance over one cycle in Figure 51, it would be correct to assume that an excessive number of time steps have been used. To investigate if this was in fact the case, further solutions were carried out using successively larger time steps of 0.00005, 0.0001, 0.0003 and 0.001 s. The results from this study are also plotted in Figure 51. As can be seen in Figure 51, all but the two largest time steps of 0.0003 and 0.001 s succeeded in predicting the periodic performance of the section, resulting from the vortex shedding aft of the Gurney. It is evident from the plots of lift and drag for the two largest time steps, that the solver has essentially solved the problem as if the flow was at a steady state. On comparison of the transient response curves in Figure 51 and the mean performance data, in Table 21, it is evident that the accuracy of the predicted performance is approximately the same for time steps 0.000025, 0.00005 and 0.0001 s, all except for the drag curve, produced using the smallest time step of 0.000025 s, which has a slight offset.

Although the response curves shown in Figure 51 were all plotted using the data taken from the same time interval near the end of the simulation, the curves all seem to be out of phase. This occurs because of the way in which the vortex shedding is resolved as the solution progresses. Depending on the time step size, the regular vortex shedding might be resolved earlier or later in the simulation. Table 21 shows the amount of CPU time taken in all five time step studies. It is evident that these computations are extremely computationally intensive, with the small time step case taking 230 hours to solve.

7.6.2 Validation against Experimental Data

Following the detailed time step study, the time-averaged c_l and c_d were validated against those obtained by Jeffrey [40] and compared with those found in the under-converged steady state investigation over a range of incidences. The computed principle shedding frequency was validated against the LDA measured value of Jeffrey [40]. The time-averaged pressure distribution, was also validated against Jeffery's [40] data at an angle of incidence of 10 degrees. It was decided, based on the data obtained in the time step study, that a time step of 0.0001 s would be used in all the computations, providing a compromise between accuracy and CPU time. Typically, these time accurate computations took between 100 and 150 hours, to converge to an oscillating state depending on the angle of incidence.

7.6.2.1 Shedding Frequency and Strouhal Number

Table 22 shows the calculated principle shedding frequency and Strouhal number at angles of incidence of 0, -5 and 10 degrees using a time step of 0.0001 s. It can be seen that only the 0 and -5 degrees incidence angle computations managed to capture the periodic vortex shedding. The 10 degree incidence angle case, along with all the other incidence angle computations, failed to capture the periodic vortex shedding. This occurred because the wake grid at these incidence angles, (which would be approximately at the same angle as the aerofoil to the inflow), failed to have enough resolution to capture the unsteadiness. This problem could have been resolved by propagating the fine wake grid in the anticipated wake direction, however, this was not investigated. The -5 degrees incidence case managed to capture the periodic vortex shedding because at this angle the vortex street was displaced closer towards the wake grid centre line, where the grid was of a sufficient resolution to capture the vortex shedding. It can be seen from Table 22 that the computed principle shedding frequency and Strouhal number for the 0 degrees incidence case, compares extremely well with the measured values found by Jeffrey [40] in his LDA experiments.

7.6.2.2 Time-Averaged Lift

As with the under-converged steady state validation of the c_l, the computed time-averaged c_l was also compared directly with the measured C_L data obtained by Jeffrey [40]. Figure 52 compares the time-averaged data with the experimental data and under-converged steady state data. It is apparent that the computed time-averaged c_l data is identical to that obtained in under-converged steady state state investigation, and hence, shows the same correlation with the experimental data. Correction to finite aspect ratio, using the same method as applied to the under-converged steady state data, would therefore, give the same close correlation.

Table 23 shows the minimum, maximum and time-averaged c_l over the incidence range. From this table it is noticeable that the greatest amplitude in the lift force occurs between incidence angles $-10 \leqslant \alpha \leqslant 10$ degrees. This occurs because past these angles of incidence, full separation and stall occurs, with the breakdown of the vortex wake structure into a fully turbulent wake.

7.6.2.3 Time-Averaged Drag

In the same way as the under-converged steady state c_d was validated, the computed time-averaged c_d was compared with the measured wing C_D derived by Jeffrey [40]. Figure 52 compares the computed time-averaged data with the experimental and under-converged steady state data. It is apparent that the computed time-averaged transient drag data is identical to that obtained in under-converged steady state state investigation, and hence, shows the same correlation with the experimental data. Table 23 shows the minimum, maximum, and time-averaged drag coefficients, over the incidence range. From this table, it is noticeable that the greatest amplitude in the drag force, which is actually quite small in comparison to the lift amplitude, occurs between incidence angles $-5 \leqslant \alpha \leqslant 5$ degrees.

7.6.2.4 Time-Averaged Pressure Distribution

The computed periodic pressure distribution at an angle of incidence 0 and 10 degrees, was validated against the experimental data obtained by Jeffrey [40] and compared with the results obtained in the under-converged steady state investigation, in Figure 53 and Figure 54. The pressure distributions at the maximum (1/4 shedding cycle) and minimum (3/4 shedding cycle) and time-averaged positions were compared. It is obvious that there is very little change in the pressure distribution over the shedding cycle, with only small noticeable changes in the pressure distribution occurring in the trailing-edge region. The computed time-averaged pressure distribution was found to be identical to that obtained in the under-converged steady state investigation, and hence, showing the same close correlation with the experimental results.

7.6.2.5 Maximum Reynolds Stresses

Figure 55 shows a contour plot of non-dimensional isotropic shear stresses $\overline{u'^2}/U_\infty^2$ and $\overline{v'^2}/U_\infty^2$ in the wake region of the Gurney flap, at the end of the simulation, for the $\alpha = 0$ degree case. A point of maximum Reynolds stress can clearly be identified, occurring as expected, where one of the shed vortices interacts with the free stream, similar to that previously identified in the under-converged steady state investigation and shown in Figure 49. A slightly higher maximum Reynolds stress than that obtained in the under-converged steady state computations has been found, agreeing better with the experimental data of Jeffrey [40]. The difference between the computed values in Figure 55 and the experimental values tabulated in Table 24 are $9 - 27\%$ for the stream wise normal stresses and 66% for the cross flow normal stresses. Like the under-converged steady state computation, the location of the lower maximum stream wise Reynolds stress is in good agreement with that found by experiments, although this would also change somewhat from time step to time step.

7.7 Conclusion to Chapter

A detailed investigation of the under-converged steady state and periodic performance of a NACA 0012 fitted with 2 and 4% Gurney flaps was conducted using a RANS solver, implementing the standard $k - \varepsilon$ turbulence model.

The following conclusions are drawn from the Gurney flap investigation:

- The under-converged steady state wake resolution sensitivity analysis highlighted that although the wake grid resolution had a profound effect on the flow physics captured within it, the under-converged steady state performance remained largely un-affected. The predicted under-converged steady state performance for both the coarsest and finest grids was found to correlate well with the experimental data. The correct trends in performance, resulting from the addition of different size Gurney flaps was also observed.

- The time-accurate performance investigation highlighted the importance of selecting the correct time step necessary to resolve the periodicity in the wake region. The time-averaged performance was found to be identical to the performance predicted by the under-converged steady state solution approach, showing the same correlation with the experimental data. The principle vortex shedding frequency was also found to correlate favourably.

- The under-converged steady state solution approach used here, and in other investigations, was confirmed as producing the same time-averaged performance predictions as the full time-accurate simulations, however, at 1/30th of the computing cost; For practical applications when transient section performance is of secondary importance, the under-converged steady state solution approach can be used to obtain estimates of time-averaged performance. Care should be taken during grid dependence investigations involving under-converged steady state and time-accurate solution approaches. This is because the local grid size

can have a significant influence on the predicted flow, and this may prevent asymptotic force convergence.

- Comparison of computed and experimental maximum Reynolds stresses, in the wake aft of the Gurney flap highlighted the limitations of using an isotropic turbulence model, like the standard $k - \varepsilon$ model, in predicting flows which are highly anisotropic.

The detailed verification and validation studies presented here, have shown that the typical grid resolution needed for accurate two-dimensional section performance prediction is of the order of 70000 cells. Assuming that a similar level of grid resolution would be required in the third dimension, an estimate of total number of cells needed to model a low aspect ratio wing can be made. It is thought that 21 million cells would probably be needed to resolve the three-dimensional flow features to the same degree of accuracy, as those in the two-dimensional study presented here. Even with this number of cells, there is no guarantee that grid independence would be achieved.

Chapter 8

Conventional and High Lift Rudder Section Performance

8.1 Overview of Chapter

The previous investigations have confirmed the validity of the RANS method for predicting the free stream performance of rudder sections, with both sharp and blunt trailing edge features. This Chapter investigates the performance of different conventional and high lift rudder sections, using the validated RANS method. The rudder sections studied are a conventional NACA 0020 section and a generic three-piece Schilling section. The effects of Reynolds number and flow type (turbulent or laminar) are investigated for the NACA 0020 section. Particular attention is focused on understanding the flow physics produced around the Schilling section. It is hoped that Schilling section study, will provide an insight into how, and why, rudder sections fitted with fish-tail trailing edges produce their high lift characteristics.

8.2 Investigation Description

8.2.1 Investigation Strategy

This investigation was divided into two parts; a brief study of the NACA 0020 performance and a more detailed study of the Schilling rudder performance. The NACA 0020 solutions were obtained using the steady state RANS approach. The Schilling solutions were obtained using the under-converged steady state approach detailed in Chapter 7. One time-accurate simulation was also conducted for the 10 degree trailing edge angle Schilling.

Turbulent flow computations were carried out for both rudder sections, over a range of incidence angles and at three different Reynolds numbers. The Reynolds numbers chosen, corresponded to typical ship service, manoeuvring and model-scale speeds. Laminar flow computations were also conducted on the NACA 0020 at the model-scale Reynolds number, to assess the effect of laminar flow conditions on model-scale rudder performance.

The majority of the Schilling investigation, is focused on assessing the performance of a generic three-piece Schilling section, with a fish-tail trailing edge angle of 10 degrees. A number of computations were also conducted on Schilling sections with 5, 7.5 and 15 degree fish-tail angles to assess their effect on performance.

The single time-accurate Schilling computation was carried out for two reasons. Firstly, to estimate the approximate shedding frequency of the Schilling section operating at the ship service speed, in its undeflected position. Secondly, it was also necessary to determine the smallest time step needed, to correctly capture the periodic vortex shedding. The importance of determining this minimum time step, will become clearer when the periodic propeller influence is introduced in Chapter 9.

It must be stressed, that the results presented in this Chapter must be taken in context, since the accuracy of the results are restricted by the limitations of the

standard $k - \varepsilon$ turbulence model, as already described in Chapter 3.

8.3 Computational Model Particulars

The NACA 0020 and Schilling sections modelled, both had chord of $c = 5.0$ m and span of $b = 8.0$ m, being representative dimensions of a rudder fitted to a typical tanker. The thickness to chord ratio for the Schilling section was $t/c = 20\%$, i.e. the same t/c as the NACA 0020 section. The sections were modelled at $R_n = 8.38 \times 10^6$ and 4.19×10^7, corresponding to inflow free stream speeds of $U_\infty = 2.0$ and 10 m/s. These are typical tanker slow speed manoeuvring and service speeds. Model-scale runs at $R_n = 2.12 \times 10^5$ were also conducted. In order to achieve this low Reynolds number, the flow speed over the full size ship rudder needed to be 0.05 m/s. Derivation of the model-scale Reynolds number is given in Appendix A.

The fluid density properties, were set according to those of salt water; a density of $\rho = 1025$ kg/m^3 and dynamic viscosity $\mu = 1.224 \times 10^{-3}$ kg/m s at 15 degrees centigrade. The turbulent flows past both rudder sections were computed at the three Reynolds numbers, using the standard $k - \varepsilon$ turbulence model, implementing the standard constants given in Table 1. The inlet turbulence parameters k and ε were set to their free stream values. For the $R_n = 2.12 \times 10^5$ model-scale runs, laminar computations were also conducted.

QUICK differencing was used for the spatial u and v terms and hybrid for the turbulence quantities k and ε. Quadratic second order time differencing was used in conjunction with fixed time stepping for all transient calculations. Pressure correction was carried out using the SIMPLE algorithm. The under-relaxation parameters, were set according to Table 3. The mass source residual stopping convergence criteria, was set at 1.0×10^{-4} kg/s in all computations. It must be noted that in the case of the steady state computations on the Schilling sections, this convergence criteria was

never met, for the same reasons as explained in Chapter 7. The steady state computations of the flows over the Schilling sections were only terminated once suitable under-converged steady state solutions were observed. Computations were carried out using the steady state solution approach for both the NACA 0020 and Schilling sections, together with one time-accurate solution for the Schilling section. All computations were carried out using the Irixresearch computing facility, as described in Chapter 3.

8.4 Boundary Conditions and Grids

The multi-block topology structures used to generate the grids around the NACA 0020 and Schilling sections are shown in Figure 6 and Figure 8. The outer boundaries, were located 15 chord lengths away from the section. The boundary conditions for the NACA 0020 were identical to those applied to the NACA 0012 section modelled in Chapter 6 and shown in Figure 56 and Table 25. The boundary conditions used to model the Schilling are shown in Figure 20 and Table 16.

Table 26 and Table 27 tabulate the near-wall cell size and corresponding computed y^+ values for both the NACA 0020 and the 10 degree trailing edge Schilling section at $\alpha = 0$. The low Reynolds number laminar flow NACA 0020 computations were carried out using the same grid as used for the $R_n = 8.38 \times 10^6$ turbulent flow study.

Approximately the same number of cells were distributed chord-wise n_ξ and down onto n_η, both the NACA 0012 and Schilling sections. A higher number of cells were placed in the wake (n_ζ) of the Schilling section, in order to resolve the vortex shedding within this region. Table 28 tabulates the information for both the NACA 0020 and Schilling section grids. Figure 57 shows the grid produced around the 10 degree trailing edge angle Schilling section. For clarity, only alternate grid lines have been plotted. The large number of cells clustered in the trailing edge region should be noted. This fine clustering continued approximately eight trailing edge widths

downstream, before the grid is stretched into the far field.

8.5 NACA 0020 Section Performance

8.5.1 Lift and Drag

Figure 58 and Table 29 present the performance data for the NACA 0020 operating at $R_n = 2.12\times10^5$, 8.38×10^6 and 4.19×10^7. Comparing the model-scale $R_n = 2.12\times10^5$ laminar flow data, with the corresponding turbulent flow data at the same Reynolds number, it is evident the laminar flow condition significantly reduces predicted α_{stall} and $c_{l,max}$. When the laminar flow model-scale $R_n = 2.12 \times 10^5$ data is compared with the full scale $R_n = 4.19 \times 10^7$ turbulent flow data, the laminar flow case is seen to produce a 24% under prediction in α_{stall}, whilst a 36% under prediction in $c_{l,max}$. This result, clearly re-iterates the implications of having a laminar flow regime, over the model ship rudder, as previously discussed in Chapter 2. There is a slight increase in the predicted lift slopes with increasing Reynolds number, with the laminar flow model-scale $R_n = 2.12 \times 10^5$ case, producing the smallest increase. Although the standard turbulence model is poor at predicting α_{stall} and exact value of $c_{l,max}$, the three different Reynolds number turbulent computations, show the expected progressive increase in the α_{stall} and $c_{l,max}$.

The laminar flow model-scale $R_n = 2.12\times10^5$ case produces, as expected, significantly lower c_d values than its turbulent flow counterpart at low incidence angles, $\alpha < 10$ degrees, and higher c_d values at incidence angles, $\alpha > 10$ degrees. It is interesting to see that the c_{d0} for the laminar flow case is of a similar magnitude to the turbulent flow case when $R_n = 8.38 \times 10^6$. Looking at the breakdown of drag components in Table 29, it can be seen that the c_{d0} for the laminar flow case is only brought closer to that of the turbulent flow computation by virtue of a large c_{pv} drag component. This relatively large c_{pv} drag component, is characteristic of non-laminar flow sections like

the NACA 0020.

When the laminar flow c_{d0} from the model-scale $R_n = 2.12 \times 10^5$ is compared with the turbulent flow c_{d0} from the $R_n = 4.19 \times 10^7$ flow case, it is evident that the laminar flow condition at the model-scale would produce a 28% increase in the predicted c_{d0}. This over prediction in c_{d0} would undoubtably have implications in the model-ship scaling procedure, and hence, on the powering calculations. What is probably more alarming, is the fact that even if the flow over the model-scale rudder was tripped into fully turbulent flow, by the upstream hull wake or propeller race, the predicted model c_{d0} would be some 68% greater than that of the ship rudder flow. Caution must be stressed on the accuracy of this result. As was highlighted in Chapter 3, too large a cell size on the rudder surface, can result in large errors in the predicted c_{pv} and hence c_{d0}. As can be seen from Table 26 the near-wall cell size needs to be quite large, in order for the wall function approach to be correctly applied. This condition, therefore, results in the over prediction of c_{pv}, as discussed in Chapter 3. In the event that the c_{pv} was computed correctly and found to be significantly lower, the c_{d0} for the model rudder would still remain considerably higher than that of the full size ship rudder, due to the large c_f contribution to c_{d0}.

Also plotted in Table 29 are $1 + k$ form factors for the NACA 0020 at the different Reynolds numbers. There is clear evidence to suggest that the rudder form factor shows some form of Reynolds number dependence. It interesting to note that Bertram's [5] formulae for predicting rudder drag, incorporate a 1.25 form factor. The calculated form factor values given in Table 29 might be useful to naval architects carrying out simple rudder drag resistance estimates.

8.5.2 Pressure Distribution and Centre of Pressure

Figure 59 and Figure 60 show the pressure distributions, and movement of centre of pressure with varying incidence angle for the $R_n = 4.19 \times 10^7$ case. These pressure

distributions and the movement of pressure are as expected. The centre of pressure is seen to move aft from the 25% chord position towards the 35% location with increasing incidence angle.

8.6 Schilling Section Performance

8.6.1 Under-converged Steady State Lift and Drag

Figure 61 and Table 30 present the under-converged steady state performance data for the 10 degree trailing edge angle Schilling, operating at $R_n = 2.12 \times 10^5$, 8.38×10^6 and 4.19×10^7 in a fully turbulent flow. Note that for commercial confidentiality reasons all c_d values have been normalised, with respect to the c_{d0} of the 10 degree trailing edge Schilling section, operating at $R_n = 4.19 \times 10^7$, to give values of normalised drag c_d^*.

Looking at the c_l curves in Figure 61, it is evident that like the NACA 0020, the Schilling exhibits a progressive increase in α_{stall} and $c_{l,max}$ with increasing Reynolds number. Although the computed location of α_{stall} is considerably less than what would be expected for this type of Schilling section, $c_{l,max}$ is reasonably well predicted. Comparing the predicted lift slopes, it is evident that the $R_n = 8.38 \times 10^6$ and $R_n = 4.19 \times 10^7$ cases have nearly identical lift slopes, only being slightly higher than that of the $R_n = 2.12 \times 10^5$ case. Comparing the $R_n = 4.19 \times 10^7$ c_l curves of both the NACA 0020 and the 10 degree trailing edge Schilling, it can be seen that the Schilling gives a 13% augment in the lift slope, together with 31% increase in the $c_{l,max}$. It must be noted that these estimates are probably conservative in comparison to the NACA 0020 computations, due to the limitations of the standard $k - \varepsilon$ turbulence model. The Schilling flow consists of significant regions of re-circulatory and separated flow (which will be poorly predicted by the turbulence model) even at low incidence angles, hence, the errors in α_{stall} and $c_{l,max}$ are expected to be significantly larger than

those found for the NACA 0020. The fish-tail trailing edge of the Schilling is clearly responsible for the significant increase in the lift slope delayed stall characteristics identified. The flow phenomena which produce these characteristics will be explained later in the Chapter.

It is evident that the predicted c_d^* for the model-scale $R_n = 2.12 \times 10^5$ case is 36% greater than that of the full size ship rudder operating at $R_n = 4.19 \times 10^7$, as opposed to 68% in the case of the NACA 0020 section. This would seem to suggest that model scale Schilling rudder tests would yield values of c_{d0}^* closer to those found at full scale. This is an important result, since it has significant implications with regard to the model-ship scaling process. Clearly, applying the same scaling procedure to a ship model tested with with conventional and Schilling type rudders, will produce biased resistance estimates. This highlights the need for different correlation functions to be derived, and used, when carrying out model-ship scaling on models fitted with different types of rudder.

8.6.2 Trailing Edge Angle Effect

Figure 62 and Table 31 present the under-converged steady state performance data for Schilling sections with trailing edge angles of 5, 7.5 and 10 degrees operating at $R_n = 4.19 \times 10^7$. Note that for commercial confidentiality reasons all c_d values have been normalised with respect to the c_{d0} of the 10 degree trailing edge Schilling section, operating at $R_n = 4.19 \times 10^7$, to give values of normalised drag, c_d^*.

Looking at the c_l curves for the four different Schilling sections, it is apparent that increasing fish-tail angle produces a delay in stall, together with an increase in the $c_{l,max}$. A 10 degree increment in trailing edge angle results in a 14% increase in the $c_{l,max}$. What is more surprising is that trailing edge angle only exhibits a small effect on the predicted lift slope.

As expected, the c_{d0}^* for the Schilling increases considerably within increasing fish-tail

angle. The c^*_{d0} for the 15 degree trailing edge angle Schilling is found to be three times that of the 5 degree trailing edge angle Schilling. However, the downside of reducing fish-tail angle would be a reduction in the Schilling high incidence angle ($\alpha > 70$) performance.

The data presented in Figure 62 and Table 31, therefore, seems to suggest that a Schilling profile with a fish-tail angle of 5 degrees would provide good high lift performance, as well as minimal drag.

8.6.3 Pressure Distribution and Centre of Pressure

Figure 63 and Figure 64 show the under-converged steady state pressure distributions and movement of centre of pressure with varying incidence angle, for the 10 degree trailing edge Schilling at $R_n = 4.19 \times 10^7$. There are a number of features to highlight, with regard to the pressure distributions presented in Figure 63.

The slight dips in the pressure distributions, (more noticeable on suction surface), located at approximately $x/c = 0.06$, highlight a discontinuity in the curvature of the Schilling section. Sharp discontinuities in the pressure distributions, where the forward section, and the fish-tail meet the fiat plate, middle section, can also be observed at the $x/c = 0.66$ and 0.82 locations. At the higher angles of incidence between $\alpha = 20$ and 22 degrees, a large region of constant low pressure exists on the suction side. As will become clear from the visual flow results discussed in the next section, this is caused by a large recirculation region just forward of the fish-tail. The centre of pressure is seen to move aft, from the 25% chord position towards the 40% location with increasing incidence angle.

8.6.4 Visual Flow Results

Figures 65 to 70 show the under-converged steady state streamline plots for 10 degree trailing edge angle Schilling, at $R_n = 4.19 \times 10^7$ at $\alpha = 0$, 21 and 22 degrees at the end of the simulation. Consider the $\alpha = 0$ degree streamline plots, in Figure 65 and Figure 66. The development of periodic vortex shedding aft of the fish-tail, similar to that produced behind the Gurney flapped NACA 0012, investigated in Chapter 7, is apparent. Figure 67 and Figure 68, show the streamline around the Schilling at 21 degrees incidence angle (just before stall). A number of important features need to be highlighted. The large recirculation region, which is responsible for the region of constant low pressure (identified from the pressure distribution plots) upstream of the fish-tail, is clearly visible. Notice how the flow is pulled in as it passes the trailing edge, and is held down as it continues into the vortex street. Two contributing factors result in this effect. The trailing edge accelerates the flow which would probably have separated from a conventional section. Also, in a similar way to the Gurney flap, the reduced pressure aft of the Schilling section, helps to delay separation from the suction surface.

Figure 69 and Figure 70 show the streamlines around the Schilling at 22 degrees incidence angle (just after stall). What is interesting to note from this plot, is how although the flow has separated from the trailing edge, there is a strong tendency for flow to be pulled downward in the region of the vortex street, clearly showing the extent to which the reduced pressure region aft of the Schilling trailing edge effects the flow.

8.6.5 Time-Accurate Performance

As highlighted in Chapter 7, time-accurate computations are highly computationally intensive and provide only limited performance information, which cannot otherwise be obtained from under-converged steady state computations. A single time-accurate

computation was conducted for the 10 degree trailing edge angle Schilling operating at $\alpha = 0$ and $R_n = 4.19 \times 10^7$. A time step of $\Delta t = 0.003$ s was calculated, using the residence time approach detailed in Chapter 3.

Figure 71 and Figure 72 show the periodic c_l and c_d^* response histories for the 10 degree trailing edge Schilling section operating at $\alpha = 0$ and $R_n = 4.19 \times 10^7$. The total flow simulation time was approximately 1 second, taking around 5 days compute time. Although the simulation was run for quite some time, it is evident that it has yet to reach a regular oscillating solution. This, however, was un-important since the aim of the study was to obtain an approximate response frequency, and minimum time step for the Schilling section. Given another 5 days compute time, and based on the findings of the Gurney flap study, the Schilling section computation would probably have converged. It is reassuring to see that the c_d^* response curve presented in Figure 72 seems to be converging towards a periodic state, about some mean c_d^* value, approximately the same as the under-converged steady state computed c_{d0}^* value. It is also interesting to note that the c_l and c_d^* response frequencies are different, unlike the Gurney flap which saw both c_l and c_d^* having approximately the same frequencies. The c_l frequency is $f = 6$ Hz and the c_d^* frequency is $f = 13$ Hz. The reason for the c_d^* response frequency being approximately double that of the c_l response frequency is best explained by Figure 73. This does, however, raise the question as to why the Gurney flap c_l and c_d response frequencies were seeming identical. One possible explanation might have something to do with the flow around the Gurney flapped section being asymmetric, as opposed to symmetric in the case of the Schilling section, but further investigation would be needed in order to confirm this. Figure 74 plots the streamlines aft of the Schilling trailing edge. The formation of trailing edge vortices, and their subsequent convection downstream is clearly evident. Further downstream, when grid stretching begins, the vortex structure undergoes rapid dissipation.

8.7 Conclusion to Chapter

The performance of NACA 0020 and Schilling sections operating under free stream flow conditions have been investigated using a RANS solver, implementing the standard $k-\varepsilon$ turbulence model. The effect of Reynolds number and flow type on the performance of the NACA 0020 section were examined. The aim of this study was to numerically quantify through the use of CFD, the errors which can occur in predicted rudder performance, as a result of Froude model-ship scaling procedures. The Schilling rudder investigation was focused on assessing the performance effect of the Schilling's characteristic fish-tail trailing edge.

The following conclusions are drawn from the NACA 0020 investigation:

- Comparison of the lift curves of the laminar model-scale Reynolds number and turbulent full scale Reynolds number rudder flow cases, showed that the laminar flow over the model-scale rudder resulted in a significant reduction in both α_{stall} and $c_{l,max}$.
- Although the standard $k-\varepsilon$ turbulence model was known to be poor at predicting both α_{stall} and $c_{l,max}$, it did manage to predict a progressive increase in α_{stall} and $c_{l,max}$ with increasing Reynolds number.
- Both the laminar and turbulent model-scale Reynolds number rudder flows showed significantly higher c_{d0} values than that of the turbulent full scale ship Reynolds number rudder flow, highlighting the problem of conducting model-ship scaling in accordance with Froude's law of similitude.

The following conclusions are drawn from the Schilling investigation:

- Although the standard $k-\varepsilon$ turbulence model was known to be poor at predicting both α_{stall} and $c_{l,max}$, it did manage to predict a progressive increase in α_{stall} and $c_{l,max}$ with increasing Reynolds number.

- The fish-tail trailing edge of the Schilling was found to produce large augments in both lift slope and $c_{l,max}$, when compared to the NACA 0020 section.
- The Schilling turbulent model-scale Reynolds number predicted c_{d0} was found to be closer to the full scale ship rudder c_{d0} than in the NACA 0020, highlighting the need for different correlation functions to be derived, and used, when carrying out model-ship scaling on models fitted with different types of rudder.
- Increasing the Schilling section trailing edge angle was found to increase the $c_{l,max}$ and c_{d0} of the section.

Chapter 9

Rudder Section Performance in Periodic Flows

9.1 Overview of Chapter

The research presented up until now has been focused on obtaining accurate performance predictions of two-dimensional rudder sections, operating under steady free stream flow conditions. As was stated in Chapter 1, most ship rudders are subjected to a flow regime which is far from steady. The highly turbulent, periodic and interactive wake produced by a propeller, gives rise to rudder performance characteristics which differ significantly from those experienced in a free stream. The work presented in this Chapter is focused on investigating periodic rudder flows, through the use of a simplified periodic two-dimensional RANS model. By imposing periodic flow conditions, representative of the flow produced in the wake of a propeller, it was hoped that a better understanding of the performance rudders operating in propeller wakes could be achieved. The response prediction of two-dimensional rudder sections subjected to periodic flow conditions, can be regarded as a necessary first step towards understanding the requirements for full periodic three-dimensional rudder

computations.

9.2 Rudder Performance in Periodic Flows

Considering a propeller and rudder in isolation, i.e. neglecting the wake field produced behind a ship hull, the rudder is subjected to a periodically varying flow field. The helical and non-axisymmetric nature of this flow field, means that the velocities within the propeller wake vary as a function of space and time, as given by Equation 55.

$$u, v, w = f(x, y, z, t) \tag{55}$$

A simple way of visualising what is happening to a rudder located in a propeller race, is to consider the two-dimensional flow, i.e. ignoring rotational or cross flow effects, at a span-wise section. The section effectively experiences periodic variations in both flow incidence and speed, as the propeller rotates. Down-stream of a propeller, the variation in axial u and radial v velocities with propeller blade angular position would look similar to data generated by Turnock [21], and reproduced in Figure 75. As can be seen, an almost sinusoidal variation in the axial and radial velocity components occurs, as the propeller rotates. Figure 75 clearly reemphasises, how large the local flow incidence angles produced in the propeller race can be.

Now, consider the same span-wise section, operating within a two-dimensional propeller wake, experiencing a time varying effective flow incidence of α_E, as shown in Figure 76. The resolved axial and normal forces are related to the lift and drag forces by Equation 56 and Equation 57.

$$N(t) = L(t)\cos(\alpha + \alpha_E(t)) + D(t)\sin(\alpha + \alpha_E(t)) \tag{56}$$

$$A(t) = -L(t)\sin(\alpha + \alpha_E(t)) + D(t)\cos(\alpha + \alpha_E(t)) \tag{57}$$

If $\alpha + \alpha_E = 0$, the lift and drag forces act in the normal and axial directions respectively. However, if $\alpha + \alpha_E$ or the lift/drag ratio becomes large enough, a net reduction

in drag can be achieved. It is also theoretically possible for a net propulsive thrust to be produced, in the same way as a sail produces the forward thrust of a yacht, as shown in Figure 76. Consider now, the flow over the whole rudder; the asymmetry of the propeller wake above and below the propeller shaft line, would result in the cancellation of the normal forces. The axial force components above and below the rudder shaft line would be additive. So, over one complete revolution of the propeller, it is theoretically possible for a net thrust force to be produced. This thrust force combined with the stator effect of the rudder, can result in improvements in propulsive efficiency. As stated by Lewis [32], this advantage may be significant enough that a ship may not require any increase in propulsive power, over what would be required if the rudder were not located in the propeller race.

However, the problem is not quite that simple, since the magnitude of lift and drag forces acting on the rudder are periodic, and highly dependent on the circular passage frequency of the propeller. For a propeller with N number of blades and rotating at n revolutions per second, the circular passage frequency ω of the propeller is given by Equation 58.

$$\omega = 2\pi nN \tag{58}$$

For periodic flows, it is more common to characterise the fluid dynamic phenomena, with respect to the non-dimensional or reduced frequency parameter k given in Equation 59.

$$k = \frac{\omega c}{2U_\infty} \tag{59}$$

9.3 Periodic Aerofoil Performance Prediction

The response of a rudder to the periodic flow conditions produced by a propeller, are governed by unsteady aerofoil and boundary layer theory. The main motivation for research in this field has been focused on how the undesirable effects of vibration,

buffeting, gust response, dynamic stall and flutter caused by unsteady flows can be reduced. However, some attention has also been focused on ways of optimising the beneficial effects of flow unsteadiness, such as improvements in propulsive efficiency and stall delay. Assessment of these effects, requires the prediction of both the magnitude and time lag of the unsteady fluid dynamic loads. McCroskey [109] presents an excellent review of the subject of unsteady aerofoil flows.

Although a considerable amount of research has been focused on the periodic response of two-dimensional aerofoils, a great deal of further research is still needed, for both two-dimensional and three-dimensional flows. The research presented here will be focused solely on two-dimensional periodic rudder section flows.

9.3.1 Experimental Methods

Unlike free stream aerofoil performance prediction, unsteady or periodic model testing of aerofoils is extremely difficult. Various methods, as outlined by Commerford and Carta [110] can be used to produce the required fluctuating flow field.

- Oscillating aerofoils
- Flapping upstream aerofoils
- Pulsing jets of air transverse to the flow field
- Moving floor and ceiling test sections
- Moving ramps attached to the floor and ceiling of the test section

Referring to Commerford and Carta [110], all the techniques listed suffer from similar problems. These problems are namely; a large amount of external energy is required to produce the motion, and the upper reduced frequency capabilities are considerably lower than those needed to be modelled. A detailed bibliography of the subject of

unsteady aerofoil testing is given by Gollnick [111]. The difficulties and expense of experimental testing methods has, therefore, prompted research into theoretical methods of predicting unsteady aerofoil performance.

9.3.2 Theoretical Methods

As recently stated by Paterson and Stern [112], historically the rational approach to solving the unsteady aerofoil problem, was through the classical and fundamental work on unsteady boundary layers and unsteady lifting flows. Thus, theoretical unsteady aerofoil flows have often been approached from differing perspectives, depending on the engineering importance of certain aspects of the flow. When, boundary layer effects have been the primary driver, viscous unsteady boundary layer methods have often been implemented; when lift performance has been the driver, unsteady inviscid flow methods have been applied. A detailed discussion of unsteady theoretical flow methods is beyond the scope of this Chapter. However, a brief review of classical lifting surface theory will be given, since it will be used to validate the work presented later in the Chapter. For discussions of the important references in the field of unsteady boundary layers and unsteady lifting surface theory, the Author refers the reader to Paterson and Stern's [112, 113, 114] work on unsteady viscous marine-propulsor flows.

The pioneers of early theoretical unsteady aerofoil performance prediction were Theodorsen [115], Von Kármán [116] and Sears [117]. Using linear potential theory, these researchers investigated various periodic incompressible flows, over flat plate aerofoils of infinite span. By considering only small disturbances to the steady flow, they found that it was possible to linearise the flow about a uniform parallel mean flow, and thus un-couple the time-dependent component of the flow completely from the steady state flow characteristics. The general method used by these researchers was circulation theory. The solution to the unsteady aerofoil problem, basically involved the evaluation of a flow field, which satisfied certain boundary conditions on

the aerofoil surface, the Kutta condition at the aerofoil trailing edge, and Kelvin's theorem of conservation of total circulation.

Unsteady classical aerofoil theory is best explained by considering the changes in circulation around an aerofoil, as it under goes unsteady motion. For every change in circulation about the aerofoil, resulting from the unsteady behaviour of the flow or aerofoil, vorticity of opposing sign must be shed into the wake, and carried away by the mean flow [109]. The vortices shed into the wake represent the time history of the unsteady flow about the aerofoil, and being vortices, they induce a velocity field which is proportional to the vortex circulation, and inversely proportional to the distance away from the vortex centre. In essence, the wake of the aerofoil acts as if it had a memory of the previous aerofoil unsteady flow, and the total velocity field therefore depends on the entire history of the airfoil motion.

Sears' [117] approach involved the derivation of a lift function for a rigid aerofoil subjected to periodic transverse gusts. The form of this function, known as the Sears function, is given in Appendix D. Similar functions have also been derived by other researchers such as Horlock [118], for fluctuations parallel and at an angle to the mean flow direction. The form of these additional functions, is also given in Appendix D. The Sears function will be used to validate the two-dimensional RANS propeller-rudder wake flow model presented later.

Classical linear potential theory does have its limitations; it is limited to small amplitude, low frequency oscillations, due to the use of the steady Kutta condition. Experimental work by Poling and Telionis [119] has shown that the steady Kutta condition on which classical linear potential theories are based, is never satisfied for reduced frequencies above $k = 2$. Linear potential theory also neglects any viscous effects, such as the interaction of the outer unsteady flow, with the mean flow boundary layer development. These non-linear effects, found in real unsteady aerofoil flows, will, therefore, cause a departure from the predicted performance found using classical linear theory. To overcome some of the limitations of classical linear potential theory,

non-linear methods have been developed, which account for the unsteady interaction and distortion of the travelling gust. However, like classical linear theory, non-linear potential theory has also been shown to be invalid, for unsteady flows of high reduced frequency.

It is obvious from this brief discussion of unsteady theoretical methods, that there is scope for a method which can be used in the modelling of high frequency unsteady lifting flows, whilst also accounting for the unsteady boundary layer effects. Unsteady RANS flow methods have offered this capability for a number of years. However, as detailed in Chapter 2, unsteady RANS methods require large computing resources, in order to resolve the different time scales in the flow. As a result, published work in this field is sparse, with Paterson and Stern's [112, 113, 114] work being the most comprehensive to date.

Using a time-accurate RANS approach, implementing the Baldwin-Lomax turbulence model, Paterson and Stern [112, 113, 114] investigated the response of a propeller-blade geometry operating under unsteady flow conditions. The aims of their research were; the validation of time-accurate solutions obtained using the RANS approach and investigation of the response of turbulent propeller-blade boundary layers and wakes to external-flow travelling waves. Validation was carried out using the results obtained from the Massachusetts Institute of Technology (MIT) flapping foil experiment [120, 121] as benchmark.

Paterson and Stern [112, 113, 114] concluded; in comparison with classical and fundamental boundary layer and potential theories, RANS solutions to unsteady lifting surface flows give a consolidated perspective, resolving both viscous and inviscid effects and their interactions. Further more the RANS approach was shown to have permitted the detailed analysis and explanation of the physics of high-frequency flows. Paterson and Stern [112, 113, 114] successfully showed that high-frequency lifting surface flows display a complex response which is significantly different from classical and fundamental boundary layer and potential theories. Viscous-inviscid interaction was

also found to be an important mechanism of lifting surface response.

A number of more specific conclusions were also made by Paterson and Stern [112, 113, 114]. Despite implementing the Baldwin-Lomax turbulence model in a quasi-steady manner, the unsteady velocity profiles over the propeller blade were found to show a close correlation with the experimental data. Quantitative details of the flow such as lift and drag, were found to be highly dependent upon frequency, geometry and waveform. Agreement between the CFD and the experimental unsteady pressure response was found to be poor. The CFD indicated upstream and downstream travelling pressure waves over the foil and in the wake. Detailed analysis showed that distortion of the external flow wave, particularly on the suction side of the propeller blade, was significant and may have been partially responsible for the complex wake structure.

9.4 Investigation Description

9.4.1 Investigation Strategy

The aim of this investigation was to examine in detail what affect periodic changes in inflow angle, i.e. transverse gusts, have on rudder performance, ignoring periodic changes in speed and any rotational flow effects, which would be present in real ship propeller-rudder flows. The investigation was divided into two parts; a validation study conducted using the NACA 0020 section, and a performance response study, conducted using both the NACA 0020 and Schilling sections. To simplify the computational model, and to provide continuity between the two investigations, the rudder sections were modelled in their undeflected positions. As previously mentioned, the typical flow incidence angles experienced by a rudder, in a propeller wake, are between 10 and 15 degrees. Therefore, the flow modelled was representative of the flow experienced by a rudder section aligned with the local propeller wake mean flow

direction.

After confirming the validity of the method, an investigation of the performance effect of subjecting undeflected NACA 0020 and Schilling sections to large amplitude gusts was conducted. Although the sinusoidal amplitude of the effective incidence angle produced behind a ship propeller has been shown to be approximately 2.5 degrees, it was decided that the sections would be subjected to much larger amplitude gusts of approximately 14 degrees, to assess the effect of amplitude on response. The effect of different gust frequencies was investigated. It is worth noting, that the typical upper reduced frequency of the wake produced by a 4 bladed propeller of a VLCC is approximately $k = 3$, based on a propeller R.P.M of 80, rudder chord of $c = 5$ m and mean propeller race speed of $u = 25$ m/s.

Since, the primary aim of this investigation was to determine the performance response characteristics of rudders operating under periodic flow conditions, i.e. lift and drag amplitudes and mean values, only these characteristics were considered, ignoring effects such as phase difference.

It must be stressed, that the results presented in this Chapter must be taken in context, since their accuracy is restricted by limitations of quasi-steady application of the standard $k - \varepsilon$ turbulence model, whose limitations for steady flows have already been described and apply equally to this study.

9.4.2 Validation Data

Paterson and Stern [112, 113, 114] used the results obtained from the MIT flapping foil experiment [120, 121], to validate their computations of unsteady lifting surface flows. This did, however, require a complex computational model in order to emulate the experiments. A full validation study of the unsteady RANS approach used in this Thesis, using the MIT flapping foil data [120, 121] as a benchmark, was deemed beyond the scope of the research. However, a less complex validation procedure was

required in order to confirm the correct implementation of the periodic boundary conditions. To this end, the classical linear theory of Sears [117] was used to confirm the lift response of the NACA 0020 subjected to small amplitude low frequency transverse gusts.

9.4.3 Computational Model Particulars

The NACA 0020 and Schilling sections modelled, both had a chord of $c = 5.0$ m and a span of $b = 8.0$ m. The sections were modelled at $R_n = 4.19 \times 10^7$, corresponding to the flow velocity in water in the x-direction of $u = 10$ m/s. The magnitude of the u velocity component was held fixed throughout the simulation, and the v velocity component was sinusoidally varied according to Equation 60.

$$v = v_0 \Re e^{i\omega(t - \frac{x_v}{U_\infty})} \tag{60}$$

where, v_0 is the amplitude of the transverse gust moving past the aerofoil, t is time, x_v is the vertex node location in the x-direction, on the inlet boundaries.

In the NACA 0020 investigation, small and large amplitude gusts of $v_0 = 0.2$ and 2.5 m/s were investigated for four different reduced frequencies of $k = 0.5$, 1.0, 2.0 and 5.0. Time steps of $\Delta t = T/50$ s were used for all the NACA 0020 computations, where T is the gust period. Table 32 tabulates the transient model data for the NACA 0020 section.

In the Schilling investigation, only large amplitude gusts of $v_0 = 2.5$ m/s were investigated for four different reduced frequencies of $k = 0.5$, 1.0, 2.0 and 5.0. However, unlike the NACA 0020 investigation, a time step of $\Delta t = 0.003$ s was used. The time-accurate investigation presented in Chapter 8 had shown this time step to be sufficiently small, so as to capture the natural periodic vortex shedding produced behind the Schilling. The importance of determining this time step now becomes clear. As was mentioned in Chapter 2, obtaining solutions to flows which exhibit more than one flow time scale can be problematic. It is important that the time step is selected

to allow the smallest significant time scale in the flow to be resolved. In this case, the smallest significant time scale was the natural vortex shedding period. If identical size time steps had been used for the Schilling as determined for the NACA 0020, i.e. $\Delta t = T/50$ s, non-physical interaction between the naturally shed vorticity and that produced as a result of the periodic flow conditions would have occurred.

The fluid density properties, were set according to those of salt water; a density of $\rho = 1025$ kg/m^3 and dynamic viscosity of $\mu = 1.224 \times 10^{-3}$ kg/m s at 15 degrees centigrade. The turbulent flows past both rudder sections, were computed using the standard $k-\varepsilon$ turbulence model, implementing the standard constants given in Table 1. The inlet turbulence parameters k and ε were set to their free stream values.

QUICK differencing was used for the spatial u and v terms and hybrid for the turbulence quantities k and ε. Quadratic second order time differencing was used in conjunction with fixed time stepping for all transient calculations. Pressure correction was carried out using the SIMPLE algorithm. The under-relaxation parameters, were set according to Table 3. The mass source residual stopping convergence criteria, was set at 1.0×10^{-4} kg/s in all computations.

Computations were carried out using the transient solution approach, for both the NACA 0020 and Schilling sections. All computations were carried out using the Irixresearch computing facility, as described in Chapter 3.

9.5 Boundary Conditions and Grid

The multi-block topology structures used to generate the grids around the NACA 0020 and Schilling sections are shown in Figure 6 and Figure 8. Unlike the previous investigations the upper and downstream boundaries were located 2 and 6 chord lengths, respectively, away from sections. This was done in order to reduce the chance of the imposed gust being numerically dissipated, as a result of insufficient

grid resolution. By reducing the outer boundaries closer to the rudder section, whilst keeping the y^+ and the number and distribution of cells identical to that of the previous investigations presented in Chapter 8, a grid with sufficient grid resolution was produced. Although at first this would seem to contradict all that has been talked about with regard to boundary location independence, this is not strictly true for computations of this type. Because an explicit periodic boundary condition is being prescribed, the problem of boundary location independence is less critical than for steady flow computations, so long as the boundary conditions do not over constrain the flow. The boundary conditions for the NACA 0020 were identical to those applied to the NACA 0012 section operating at an incidence of $\alpha = 0$, modelled in Chapter 6 and shown in Figure 20 and Table 16. The boundary conditions for the Schilling were identical to those applied to the Schilling section operating at an incidence of $\alpha = 0$, modelled in Chapter 8 and shown in Figure 56 and Table 25. The periodic gust boundary conditions as per Equation 60 were implemented by means of a user FORTRAN subroutine. This user FORTRAN routine essentially took each inlet patch on the outer domain at each solution time step, looped through every node applying a fixed $u = 10$ m/s and phase lag or lead adjusted v value as per Equation 60.

9.6 NACA 0020 Section Small Amplitude Gust Investigation

9.6.1 Lift and Drag

Figure 77 and Figure 78 show the response histories for the NACA 0020 section subjected to small amplitude transverse gusts of $v_0 = 0.2$ m/s, at $k = 0.5$ and $k = 5$, respectively. As can be seen, both frequency response histories show a first-harmonic response, consistent with the imposed first-harmonic inflow boundary conditions.

Comparing the c_l response histories, it is evident that lower frequencies produce larger c_l amplitudes; with a 10 fold increase in frequency, resulting in a 8% reduction in the c_l amplitude. The c_d response histories, however, show a 100% reduction in c_d amplitude with a 10 fold increase in frequency. It is interesting to note, that the response c_d for the $k = 0.5$ case oscillates about a mean drag coefficient $\overline{c_d}$ equal to the free stream (zeroth-harmonic) c_{d0} value, previously obtained in Chapter 8. However, a zeroth-harmonic response is found for the $k = 5$ case, with the predicted $\overline{c_d}$ being 4.6% higher than the free stream c_{d0} value.

Figure 79 compares the c_l response amplitude for the NACA 0020 section subjected to small amplitude transverse gusts of $v_0 = 0.2$ m/s against the classical linear theory of Sears [117], over a range of reduced frequencies. A general trend of reducing c_l amplitude with increasing frequency can be seen. For low frequencies of around $k = 0.5$, the c_l response amplitude shows reasonable agreement with the classical linear theory, therefore, confirming the correct implementation of the periodic boundary conditions. However, at higher frequencies, departure from classical linear theory is seen to occur. A similar trend to this was found by Paterson and Stern [114]. Whilst not fully understanding the exact reasons for departure from Sears' theory [117], Paterson and Stern [114] postulated a number of likely causes; an outer flow which is increasingly non-irrotational, increasing steady-unsteady interaction and trailing-edge effects which are not resolved by either the inviscid flow approximation or the classical Kutta condition. Also worth noting from the c_l response amplitude plot is the sharp amplitude change which occurs at approximately $k = 1$. This might suggest a change unsteady flow field characteristics or some kind of numerical effect, although further investigation would be needed in order to confirm this either way.

Figure 80 compares the c_d response amplitude and $\overline{c_d}$ for the NACA 0020 section subjected small amplitude transverse gusts of $v_0 = 0.2$ m/s, over a range of reduced frequencies. As can be seen, the c_d response amplitude tends to zero with increasing frequency, with the steepest change in amplitude occurring between $k = 0.5$ and $k = 1$. The $\overline{c_d}$ plot shows convergence to a limiting value which is 4.6% greater than

the free stream c_{d0}. However, at low frequencies of $k < 1$, the $\overline{c_d}$ is found to be slightly less than the free stream c_{d0}.

9.6.2 Pressure Distribution and Centre of Pressure

Figure 81 shows the pressure distributions for the NACA 0020 section subjected small amplitude transverse gusts of $v_0 = 0.2$ m/s at the maximum and minimum transient response values of $c_l = 0$ and $c_l = 0.056$, at $k = 0.5$. For comparison the free stream pressure distributions at $c_l = 0$ and $c_l = 0.056$ have also been plotted, found from the work in Chapter 8. As can been seen, both the pressure distributions for the maximum and minimum response values are nearly identical to their free stream counterparts. Although not shown, the pressure distributions at the minimum and maximum c_l values for the $k = 5.0$ case were identical to the free stream pressure distribution at $c_l = 0$. The best way of explaining this section response behaviour, is to consider the flow at the limiting extremes of frequency, i.e. $k \to 0$ and $k \to \infty$. As $k \to 0$, the section responds as if were in a free stream with a slowly varying effective angle of incidence. This, therefore, results in a pressure distribution not dissimilar to free stream pressure distribution produced at the same c_l. Conversely, as $k \to \infty$, the section response diminishes because the section is experiencing a flow disturbance for a very small period of time. However, between these two limiting frequencies complex flow interactions occur between the travelling gust and the flow about the section.

Figure 82 shows the centre of pressure response history for the NACA 0020 section subjected to small amplitude gusts of $v_0 = 0.2$ m/s, at $k = 0.5$. The centre of pressure is seen to oscillate about the 20% chord position with an amplitude of approximately 10%. Why the centre of pressure tends to infinity at different points throughout the cycle needs to be explained. Based on the assumption that the centre of pressure acts from a point along the centre line of the section, and with knowledge of c_m and c_n, the centre of pressure can be calculated, using Equation 16. However, as $c_m \to 0$ and $c_n \to 0$ as $\alpha_E \to 0$, large errors in the calculated location of centre of pressure occur

as a result of the roundoff error associated with the floating point arithmetic.

9.7 NACA 0020 Section Large Amplitude Gust Investigation

9.7.1 Lift and Drag

Figure 83 and Figure 84 show the response histories for the NACA 0020 section subjected to large amplitude transverse gusts of $v_0 = 2.5$ m/s, at $k = 0.5$ and $k = 5$, respectively. As can be seen, both frequency response histories show a first-harmonic response, consistent with the imposed first-harmonic inflow boundary conditions. Comparing the c_l response histories at $k = 0.5$ and $k = 5$, it is evident that in a similar manner to small amplitude investigation, lower frequencies produce larger c_l amplitudes; with a 10 fold increase in frequency, resulting in a 8% reduction in the c_l amplitude. The c_d response histories also show a 100% reduction in c_d amplitude with a 10 fold increase in frequency, identical to the low amplitude case. It is interesting to note, that the response c_d for the $k = 0.5$ case oscillates about a $\overline{c_d} = -0.037$ showing that an appreciable thrust force is being generated by the rudder. It can be concluded that large amplitude low frequency unsteadiness can result in large reductions in rudder drag. The origin of this force will become obvious when the pressure distribution around the section is considered. The c_d response for the $k = 5$ case shows a zeroth-harmonic response, giving a $\overline{c_d}$ which is 14% greater than the free stream c_{d0} value. Comparing this to the small amplitude result, it can be concluded that large amplitude high frequency unsteadiness can result in an augment in base drag.

Figure 85 compares the c_l response amplitude for the NACA 0020 section subjected to large amplitude transverse gusts of $v_0 = 2.5$ m/s against the classical linear theory of Sears [117], over a range of reduced frequencies. Like the small amplitude case,

a general trend of reducing c_l amplitude with increasing frequency is evident. For low frequencies of around $k = 0.5$ the c_l response amplitude shows reasonable agreement with the classical linear theory. However, at higher frequencies, as with the small amplitude case, departure from classical linear theory is seen to occur. Also present is the same sharp amplitude change initially identified in the small amplitude investigation and located at approximately $k = 1$.

Figure 86 compares the c_d response amplitude and $\overline{c_d}$ for the NACA 0020 section subjected large amplitude transverse gusts of $v_0 = 2.5$ m/s, over a range of reduced frequencies. As can be seen, the c_d response amplitude tends to zero with increasing frequency, with the steepest change in amplitude occurring between $k = 0.5$ and $k = 1$. The $\overline{c_d}$ plot also shows convergence to a limiting value which is 4.6% greater than the free stream c_{d0}. However, at low frequencies of $k < 2$, the $\overline{c_d}$ a thrust force can be generated.

9.7.2 Pressure Distribution and Centre of Pressure

Figure 87 shows the pressure distributions for the NACA 0020 section subjected large amplitude transverse gusts of $v_0 = 2.5$ m/s at the maximum and minimum transient response values of $c_l = 0$ and $c_l = 0.71$, at $k = 0.5$. For comparison the free stream $c_l = 0$ and $c_l = 0.71$ pressure distributions have also been plotted. The pressure distributions for both the minimum and maximum c_l response values show a different behaviour than that found in the low amplitude investigation. Looking first at the the suction surface for the $c_l = 0$, it is apparent that the high amplitude periodic inflow conditions result in a reduction in the suction pressure from the leading edge back as far as the $x/c = 0.4$ location. Aft of $x/c = 0.4$ the suction surface pressure is coincident with the free stream data. The pressure surface on the other hand, undergoes an increase in the leading edge pressure back as far as the $x/c = 0.2$ location, and a reduction in pressure aft of this location. This pressure distribution clearly explains the origin of the mean thrust force identified previously. The pressure

plots for the $c_l = 0.071$ case show a similar response as the $c_l = 0$ case, although less marked.

Figure 88 shows the pressure distributions for the NACA 0020 section subjected large amplitude transverse gusts of $v_0 = 2.5$ m/s, at $c_l = 0$ and $c_l = 0.057$ the maximum and minimum response values, at $k = 5.0$. For comparison the free stream $c_l = 0$ and $c_l = 0.057$ pressure distributions have also been plotted. These pressure plots show as similar behaviour as the low amplitude high frequency pressure distribution plots, with the maximum and minimum response values showing a close correlation with the free stream $c_l = 0.0$ pressure distributions.

Figure 89 shows the centre of pressure response history for the NACA 0020 section subjected to small amplitude gusts of $v_0 = 2.5$ m/s, at $k = 5.0$. The centre of pressure is seen to oscillate about the 20% chord position with an amplitude of approximately 10%, in the same manner as the low amplitude investigation results.

9.7.3 Visual Flow Results

Figure 90 shows the pressure and streamline plot of the flow field around the NACA 0020 section subjected large amplitude transverse gusts of $v_0 = 2.5$ m/s at $k = 0.5$. The flow field data used to generate this plot was taken at the end of the simulation, $t/T = 0.24$. The slow moving transverse gust is clearly visible.

Figure 91 shows the pressure and streamline plot of the flow field around the NACA 0020 section subjected large amplitude transverse gusts of $v_0 = 2.5$ m/s and $k = 5.0$.The flow field data used to generate this plot was taken at the end of the simulation, $t/T = 0.70$. Although the fast moving transverse gust is evident close to the outer inflow boundaries, its propagation into the domain is negligible, giving rise to the apparent free stream flow behaviour.

9.8 Schilling Section Large Amplitude Gust Investigation

9.8.1 Lift and Drag

Figure 92 and Figure 93 show the response histories for the Schilling section subjected to large amplitude transverse gusts of $v_0 = 2.5$ m/s, at $k = 0.5$ and $k = 5$, respectively. Note that all c_d values have been normalised, with respect to the c_{d0} of the 10 degree trailing edge Schilling section studied in Chapter 8, operating at $R_n = 4.19 \times 10^7$, to give values of normalised drag c_d^*. It must also be noted that constraints on computing time, i.e. 5 days, prevented the $k = 5$ case reaching a fully converged periodic solution. As can be seen, the response history for the Schilling at $k = 0.5$ is quite different from that of the NACA 0020 section. Approximately 20 vortices are shed throughout one cycle, identifiable from the wiggles in the c_l and c_d^* response curves. What is interesting, is that the c_l response history for the $k = 5$ case shows a second-harmonic response, whilst the c_d^* shows a first harmonic response. Clearly the natural vortex shedding of the Schilling is interacting with the forced periodic flow field. This not surprising, since the natural c_l frequency of the Schilling was estimated as 6 Hz in Chapter 8, and the forced frequency of the periodic flow is approximately 3 Hz. Comparing the c_l response histories at $k = 0.5$ and $k = 5$, it is evident that in the similarly way to the NACA 0020, lower frequencies produce larger c_l amplitudes. However, unlike the NACA 0020, a 10 fold increase in frequency, produces a 4.8% reduction in the c_l amplitude as opposed to an 8% reduction. The c_d^* response histories also shows a reduction in c_d^* amplitude, with a 10 fold increase in frequency resulting in a 88% reduction in the response amplitude. The c_d^* response for the $k = 0.5$ case oscillates about $\overline{c_d^*} = 1.5$, showing that the Schilling experiences a 50% augment in its mean drag as a result of the periodic flow. The c_d^* response for the $k = 5$ case shows a first-harmonic response, giving a $\overline{c_d^*}$ which is 300% greater than the free stream c_{d0}^* value.

Figure 94 compares the c_l response amplitude for the Schilling section subjected to large amplitude transverse gusts of $v_0 = 2.5$ m/s, against the classical linear theory of Sears [117], over a range of reduced frequencies. A general trend of reducing c_l amplitude with increasing frequency is evident. Unlike the NACA 0020 small and large amplitude gust investigations, the Schilling c_l response amplitude shows closer agreement with the classical theory between $k = 1$ and 5, with the major departure occurring at $k = 0.5$. This is some what surprising, and seems to suggest that Sears' theory [117] would provide better high frequency estimates of periodic performance for sections with a blunt trailing edges, rather than sharp. The Schilling c_l response amplitude also exhibits the same sharp amplitude change in the region of $k = 1$ as found in the NACA 0020 small and large amplitude investigations, although less pronounced.

Figure 95 compares the c_d^* response amplitude and $\overline{c_d^*}$ for the Schilling section subjected to large amplitude transverse gusts of $v_0 = 2.5$ m/s, over a range of reduced frequencies. As can be seen, the c_d^* response amplitude tends to zero with increasing frequency, with the steepest change in amplitude occurring between $k = 0.5$ and $k = 1$. $\overline{c_d^*}$ plot also shows convergence to a limiting value, which is 300% greater than the free stream c_{d0}^*. However, at low frequencies of $k < 1$, the $\overline{c_d^*}$ is found to be 50% greater the free stream c_{d0}^*. These drag results are somewhat misleading, since they corresponds to a Schilling section aligned with the mean flow direction, which is rarely the case for real propeller-rudder flows. In reality the rudder section would experience an effective incidence angle of between approximately 10 and 15 degrees. Because the Schilling section would generate a much larger lift force for a given angle of incidence, when compared to the NACA 0020 section; resolution of this lift force into the ship axis system would result in a larger reduction in drag for the Schilling.

9.8.2 Pressure Distribution and Centre of Pressure

Figure 96 shows the pressure distributions for the NACA 0020 section subjected large amplitude transverse gusts of $v_0 = 2.5$ m/s, at the maximum and minimum transient response values of $c_l = 0$ and $c_l = 1.02$, at $k = 0.5$. For comparison, the free stream $c_l = 0$ and $c_l = 1.02$ pressure distributions have also been plotted. Looking first at the the suction surface for the $c_l = 0$ case, it is apparent that unlike the NACA 0020 case, the high amplitude periodic inflow conditions result in a increase in the suction pressure from the leading edge back as far as the $x/c = 0.3$ location. Aft of $x/c = 0.3$, the suction surface pressure is slightly lower than the free stream data. The pressure surface on the other hand, undergoes a decrease in the leading edge pressure, back as far as the $x/c = 0.2$ location, and slight reduction in pressure aft of this location. The pressure plots for the $c_l = 1.02$ case show a similar response as the $c_l = 0$ case, although less marked.

Figure 97 shows the pressure distributions for the Schilling section subjected large amplitude transverse gusts of $v_0 = 2.5$ m/s, at $c_l = 0$ and $c_l = 0.057$, the maximum and minimum response values, at $k = 5.0$. For comparison, the free stream $c_l = 0$ and $c_l = 0.057$, pressure distributions have also been plotted. Close correlation with the free stream $c_l = 0.0$ pressure distributions is evident, with deviations occurring in the trailing edge suction and pressure surface regions.

Figure 98 shows the centre of pressure response history for the Schilling section subjected to small amplitude gusts of $v_0 = 2.5$ m/s, at $k = 5.0$. The centre of pressure is seen to oscillate about the 20% chord position with an amplitude of approximately 10%.

9.8.3 Visual Flow Results

Figure 99 shows the pressure and streamline plot of the flow field around the Schilling section subjected large amplitude transverse gusts of $v_0 = 2.5$ m/s at $k = 0.5$. The flow field data used to generate this plot was taken at the end of the simulation, $t/T = 0.7$. The slow moving transverse gust is clearly visible. Figure 100 shows a close up of the streamlines in the region of the Schilling trailing edge. The development, convection and interaction of the vortices downstream of the Schilling trailing edge with non-uniform flow can be seen.

Figure 101 shows the pressure and streamline plot of the flow field around the Schilling section subjected large amplitude transverse gusts of $v_0 = 2.5$ m/s at $k = 5.0$. The flow field data used to generate this plot was taken at the end of the simulation, $t/T = 0.58$. Although the fast moving transverse gust is evident close to the outer inflow boundaries, its propagation into the domain is negligible, giving rise to the apparent free stream flow behaviour. Figure 102 shows a close up of the streamlines in the region of the Schilling trailing edge. The development and convection of the vortices downstream of the Schilling trailing edge, in what is essentially a uniform flow can be seen.

9.9 Conclusion to Chapter

Detailed investigations of the effect of small and large amplitude transverse gusts on the performance of NACA 0020 and Schilling sections were conducted using a RANS solver, implementing the standard $k-\varepsilon$ turbulence model. The time-accurate RANS approach has been shown to provide the capability of predicting the performance response of different rudder sections subjected to periodic flow conditions.

The following conclusions are drawn from the NACA 0020 small and large amplitude transverse gust investigations:

- Reasonable agreement was found between the computed response c_l amplitudes and the classical linear theory of Sears [117], for both the large and the small amplitude gusts at low frequencies. Deviation from the classical linear theory was found at higher frequencies. A general trend of reducing c_l amplitude with increasing frequency was also observed.

- Low frequency gusts were shown to produce reductions in base drag, with the large amplitude low frequency gusts giving rise to a net thrust force. However, both the high and the low amplitude high frequency gusts were shown to produce an augment in the base drag above that found through operation in a free stream

The following general conclusions are drawn from the Schilling large amplitude transverse gust investigations:

- Surprisingly, the computed c_l response amplitude for the Schilling section showed closer agreement with the classical linear theory of Sears [117] than the NACA 0020 section, at high frequencies. A general trend of reducing c_l amplitude with increasing frequency was also observed for the Schilling section.

- Low frequency and high frequency gusts were both shown to produce increases in the base drag, above that found through operation in a free stream.

- The natural vortex shedding produced by the Schilling was found to interact strongly with the forced periodic flow, especially when the frequency of the periodic flow was of a similar order of magnitude to the natural vortex shedding frequency.

Chapter 10

Conclusions and Recommendations for Future Work

10.1 Overview

The need for naval architects to predict the rudder performance accurately at the design stage of a vessel, has been the motivation behind the research presented. The difficulties associated with obtaining accurate rudder performance predictions, through traditional experimental procedures have been highlighted, and a demand for research into alternative, potentially more accurate and cost effective theoretical techniques was identified. The research has been focused on exploring, in detail, the capabilities of the RANS technique. This method was chosen in preference to other theoretical methods, because of its ability to predict the viscous performance of arbitrary shaped rudder sections. A review of previous research carried out in the field of hull, propeller and rudder interaction, using the RANS approach, was conducted. From this review, it became apparent that the quality and accuracy of the results obtained were far from satisfactory.

The research was focused on addressing a number of the problems associated with using RANS methods, to predict the performance of rudder sections, thereby, improving the usefulness of the RANS method as a practical rudder design tool. This Chapter, presents the general and more detailed conclusions drawn from the research, together with recommendations for future work.

10.2 General Conclusions

The RANS method has been used successfully to predict the performance of conventional and high lift sections, operating under free stream flow conditions. The high quality grids created around the rudder section investigated, consisted of between 40000 and 85000 grid nodes. The critical parameters which effect the accuracy of these performance predictions have been identified. The RANS method was shown to be capable of providing accurate estimates of rudder section performance, up to stall, and qualitative performance predictions past stall. The inaccurate prediction of separation, and hence, rudder section stall performance, is primarily a function of the turbulence model implemented within the RANS method. Future advances in turbulence modelling techniques should hopefully resolve many of these problems. Turbulence model limitations aside, it has been shown that the standard $k-\varepsilon$ turbulence model performs with the required consistent and quantifiable level of accuracy, needed for rudder section design comparisons, that is equally good or bad for similar rudder sections.

Detailed verification and validation studies have been conducted at every stage of the investigation, to ensure the highest degree of accuracy and credibility in the results. A methodical approach to solving the rudder-propeller flow problem was adopted, whereby, certain aspects of the RANS solution method were validated using progressively more complex flow models; with the final model being representative of a two-dimensional rudder, operating in a propeller race. It has been shown, that

a methodical approach should be adopted when accurate quantitative results are required from a RANS solution. Tackling a complex flow problem in one step makes it difficult, if not impossible to identify the origin of any errors and inaccuracies in the computed results. The results presented, are testimony to the fact that a clear methodical approach to CFD, is rewarded with high quality results. A tendency for researchers to present colourful, and impressive flow visualisation plots, in place of accurate high quality results, has done untold damage, with regard to the perceived credibility of CFD flow solutions. As will have been noticed, only when there has been a specific need, have flow visualisation plots been presented, as an aid to interpreting the raw numerical data, and not in place of it. It is hoped that the work presented, will help to restore confidence in the use of CFD methods, for solving marine flow problems.

Throughout the research, the use of CFD has been approached from a practical naval architecture point of view, in an attempt to dispel some of the "Black Art" stigma which has surrounded it, since its early days. The aim has been to stimulate naval architects, into exploring the potential rewards of using CFD methods. Although commercial RANS codes have become much more user friendly, obtaining high quality results, still requires considerable expertise on behalf of the user. Knowing which parameters to change in order to obtain a converged solution, which is correct in the physical sense, is an art in itself, one which is not readily talked about in CFD texts. As a result, a conscious effort has been made to explain many of the intricacies of using the RANS approach, providing an invaluable source of information for novice and expert users alike.

Detailed grid refinement studies conducted throughout the research, have demonstrated the high levels of grid resolution which are required, in order to obtain fully grid independent solutions to two-dimensional rudder flow problems. Assuming that a similar level of grid resolution would be required in the third dimension, estimates of the total number of cells needed to model a three-dimensional rudder, that is a rudder of finite aspect ratio, with the same degree of accuracy, have been made.

It has been estimated, that 21 million cells would be required to resolve the three-dimensional flow features, to the same degree of accuracy as those resolved in the two-dimensional studies. Computations using grids of this order of magnitude, would require massive computing resources, by current standards. Research has shown, that grid independent solutions, for relatively simple two-dimensional flow problems are often hard to achieve, even when large numbers of successively refined grids are employed. Therefore, claims by researchers, that they have achieved grid independent solutions to complex three-dimensional flow problems, using three grids or fewer, should be regarded with suspicion.

Flows, which exhibit either natural or forced periodic vortex shedding, have been identified as having their own specific problems, with regard to grid independence and grid resolution. Detailed grid refinement studies conducted in the wake region of the Gurney flapped NACA 0012, have shown the modelled flow physics in this region to be highly dependent on grid resolution. In the case of time-accurate computations, the choice of transient time step was found to have a profound effect on the predicted flow physics as well.

Under-converged steady state, and time-accurate computations, of the free stream flow over a NACA 0012 section fitted with a Gurney flap were conducted. As far as the Author is aware, the time-accurate computations for the Gurney flapped NACA 0012 section, were the first of their kind. Both the under-converged steady state and time-accurate computed data was found to agree extremely well with the experimentally derived data. In doing so, the RANS method was validated and shown to be suitable for predicting flows about high lift sections with blunt trailing edge features. An important finding of the Gurney flap investigation, was the fact, that for practical purposes, when transient performance is of secondary importance, the under-converged steady state solution approach can be used to predict time-averaged section performance accurately, for only a fraction of the computing cost of full time-accurate solutions.

The research has presented the first published under-converged steady state and time-accurate RANS computations, for high lift Schilling rudder sections operating under free stream flow conditions. The results obtained, have provided a clearer insight into how, and why Schilling rudder sections fitted with their characteristic fish-tail trailing edge, produce a higher lift force, than conventional sections. Useful design information, relating to the performance effect of different size Schilling fish-tail trailing edges, has also been obtained.

The RANS method, was shown to be capable of predicting Reynolds scale effects, making it a useful compliment to experimental testing procedures. The ability of a RANS code to predict Reynolds scale effects, might, in the future help in the derivation of more representative, model-ship correlation methods.

The RANS method, was successfully used, to predict the performance response, of both conventional and high lift rudder sections, subjected to periodic transverse gusts, similar to the flow produced in the race of a propeller. These investigations, have provided an important insight into the potential capabilities of the RANS method, for predicting the response of rudders located in the race of a propeller. Reasonable correlation was found between the predicted lift response amplitude, of both the conventional and high lift sections, subjected to low frequency gusts, when compared with classical linear theory. At high frequencies, the conventional rudder section response amplitude showed a significant departure from the classical linear theory. However, the Schilling's response at higher frequencies, was found to show closer agreement with the classical linear theory. Interaction between the natural and periodic flow induced shed vorticity from the Schilling section was observed.

10.3 Detailed Conclusions

10.3.1 RANS Method Specific

The research has shown, that for unbounded free stream flow problems, the outer boundaries should be located far enough away from the body, i.e. the rudder section, so as not to have any demonstrable effect on the flow solution. For flows around rudder/aerofoil sections, the outer boundaries should be located at least 15 chord lengths away from the section. If possible, the optimum outer boundary location should be determined by means of a boundary location sensitivity study.

The RNG $k-\varepsilon$ turbulence model was found to provide less accurate skin friction estimates than the standard $k-\varepsilon$ model, for flows with zero pressure gradient. However, for flows with pressure gradients, i.e. flows over rudder/aerofoil sections, the RNG $k-\varepsilon$ turbulence model was found to perform slightly better than the standard $k-\varepsilon$ turbulence model, with regard to prediction of separation and total drag. For highly anisotropic flows, i.e. vortex shedding, the standard $k-\varepsilon$ turbulence model, was found to over predict the cross flow normal stresses.

The near-wall cell size, together with the distribution of cells about it, were found to be the most critical parameters, with regard to the correct prediction of frictional and pressure drag, using the RANS method. The first cell size should be set in accordance with the lower y^+ criterion of 30, and a sufficiently large number of cells (typically 30), should be placed within the boundary layer region, to resolve the flow gradients. When Reynolds number dependence is being studied, using a single grid, the near-wall cell size should be selected carefully, to ensure that it is valid over the range of Reynolds numbers being investigated.

Studies have highlighted, the need for careful selection of mass source residual convergence stopping criteria, in order to ensure efficient use of computational resources, whilst maintaining a high degree of accuracy in the results. Determination of the

correct mass source residual stopping criteria, is problem specific. Ideally, it should be determined after studying the converge history of an important global parameter, such as lift, drag, or a flow property such as velocity or pressure, a location within the flow.

Time-accurate performance investigations carried out, for flows known to exhibit periodic vortex shedding, i.e. bluff bodies, have highlighted the importance of selecting the correct time step, in order to resolve the periodicity produced in the wake. For flows where the time scale of any periodicity or flow unsteadiness is unknown, the CFL criteria, can provide an initial approximation of the lower limit of the time step size needed.

10.3.2 Flat Plate Skin Friction Estimation

The standard $k-\varepsilon$ and RNG $k-\varepsilon$ turbulence models were found to perform well at predicting skin friction, over the range of Reynolds numbers investigated. The standard $k-\varepsilon$ model was found to provide a 2% more accurate correlation with Froude's skin friction data, than the RNG $k-\varepsilon$ turbulence model at high Reynolds numbers.

With regard to the skin friction estimation at low Reynolds numbers, the RANS results were found to be in error due to the RANS solvers inability to simulate laminar-turbulent transition.

Good correlation, was found between the RANS predicted skin friction, and the correlation lines of the ITTC and Schoenherr, over the range of Reynolds numbers investigated.

A modified Schoenherr formula was derived from the RANS generated data, providing constants not dissimilar to those derived by Schoenherr.

It was shown, that surface roughness could be simulated by suitably modifying the

Log-Layer constant within the turbulence model wall function.

10.3.3 NACA 0012 Section Performance

Excellent correlation was found, between the experimental and computed lift curves for both the standard and RNG $k-\varepsilon$ turbulence models up to stall.

Both the standard and RNG $k-\varepsilon$ turbulence models failed to predict the location of maximum lift, with the RNG $k-\varepsilon$ turbulence model providing a more reasonable estimate of the point of maximum lift.

The drag curves for both the standard and RNG $k-\varepsilon$ turbulence models showed good general agreement with those found by experiment, with only a small offset at low incidences. This was error was probably due the laminar-turbulent transition problems. However, the RNG $k-\varepsilon$ model did provide a better correlation at higher incidences. The computed pressure distributions were also found to agree favourably with the experimental data.

10.3.4 Gurney Flapped NACA 0012 Section Performance

The predicted under-converged steady state and time-accurate performance was found to correlate well with the experimental data. The computed pressure distributions were also found to agree favourably with the experimental data.

The principle vortex shedding frequency obtained from the time-accurate computations was found to correlate favourably with the experimentally derived vortex shedding frequency.

The correct trends in performance, resulting from the addition of different size Gurney flaps, was also observed.

Comparison of computed and experimental maximum shear stresses in the wake aft

of the Gurney flap, highlighted the limitations of using an isotropic turbulence model, like the standard $k - \varepsilon$ model, in predicting flows which are highly anisotropic.

10.3.5 Conventional and High Lift Rudder Section Performance

Comparison of the lift curves of the laminar model-scale Reynolds number and turbulent full scale Reynolds number NACA 0020 section flow cases, showed that the laminar flow over the model-scale rudder resulted in a significant reduction in both stall angle and maximum lift coefficient.

Although the standard $k - \varepsilon$ turbulence model was known to be poor at predicting both stall angle and maximum lift coefficient, it did manage to predict a progressive increase in stall angle and maximum lift coefficient, with increasing Reynolds number, for both the NACA 0020 and Schilling sections.

Both the laminar and turbulent model-scale Reynolds number rudder flows showed significantly higher zero-lift drag coefficient values, than that of the turbulent full scale ship Reynolds number rudder flow, highlighting the problem of conducting model-ship scaling, in accordance with Froude's law of similitude.

The fish-tail trailing edge of the Schilling section, was found to produce large augments in both lift slope and maximum lift coefficient, when compared to the NACA 0020 section.

The Schilling turbulent model-scale Reynolds number predicted zero-lift drag coefficient, was found to be closer to the full scale ship rudder value, than the NACA 0020. This highlighted the need for different correlation functions to be derived and used, when carrying out model-ship scaling, on models fitted with different types of rudder.

Increasing the fish-tail trailing edge angle on the Schilling section, was found to increase the maximum lift and zero-lift drag coefficient.

10.3.6 Rudder Section Performance in Periodic Flows

Reasonable agreement was found between the computed response lift coefficient amplitudes and the classical linear theory, for both the large and the small amplitude gusts at low frequencies, in the case of the NACA 0020 section. Deviation from the classical linear theory was found at higher frequencies. A general trend of reducing lift coefficient amplitude with increasing frequency was also observed.

Surprisingly, the computed lift coefficient response amplitude for the Schilling section showed closer agreement with the classical linear theory, than the NACA 0020 section at high frequencies. A general trend of reducing lift coefficient amplitude, with increasing frequency, was observed for the Schilling section. Low frequency gusts were shown to produce reductions in base drag, with the large amplitude low frequency gusts giving rise to a net thrust force. However, both the high and low amplitude, high frequency gusts, were shown to produce an augment in the base drag, above that found through operation in a free stream.

Low frequency, and high frequency gusts, were both shown to produce increases in the base drag, above that found through operation in a free stream.

The natural vortex shedding, produced by the Schilling section was found to interact strongly with the forced periodic flow, especially, when the frequency of the periodic flow was of a similar order of magnitude to the natural vortex shedding frequency.

10.4 Recommendations for Future Work

Based on the findings of the work presented, the following recommendations for further work should be considered.

The research has been solely focused on obtaining accurate two-dimensional rudder

section performance data, using the RANS method. Although this data can provide useful information, with regard to section design, a rational way of predicting the three-dimensional performance of real ship rudders is needed. Using the RANS method with current computing resources, it is not possible to predict with the required level of accuracy demanded by naval architects, the full three-dimensional flow about a finite aspect ratio ship rudder.

A method has, therefore, been proposed which uses the accurate two-dimensional data, generated using the RANS method, to produce estimates of three-dimensional rudder performance. A schematic of the proposed approach, is given Figure 104. The method involves a combination of the lifting line theory (as outlined in Chapter 2), and strip theory [122], applied in a pseudo time-domain approach. In essence, this method is an advancement on Molland and Turnock's [38], blade element-momentum theory/lifting line approach. Steady state RANS computations are used to derive the sectional performance characteristics for the portion of the rudder outside the propeller race; whilst the transient RANS computations, are used to obtain the time-accurate performance characteristics, for the portion of the rudder in the way of the propeller race. Using a combined lifting line and strip theory approach, estimates of viscous three-dimensional rudder performance could be obtained.

Investigation of the performance of more complex turbulence models, is needed, if accurate rudder performance predictions are to be accomplished, for rudders operating close to, or past stall. Investigations using the Wilcox [58] $k-\omega$ and/or Reynolds stress models would be strongly recommended. A rational way of incorporating laminar-turbulent transition into turbulence models is also needed.

Further investigation of the performance of conventional, and high lift sections, subjected to more complex periodic propeller flow conditions is required.

Finally the RANS approach, could be used, to investigate the performance of flap type high lift rudders. The grid generation process, as used in this research, has been shown to be versatile enough, to construct complex multi-block grids around flapped

rudders. Figure 103 shows an example of a grid generated around a generic flapped rudder section. This grid was generated using Fleximesh, and the topology structure described in Chapter 4 and shown in Figure 9. The gap between the main rudder section and the flap, has also been included. An interesting investigation, might be to assess the performance effect of having flow through this gap.

REFERENCES

[1] A.F. Molland and S.R. Turnock, "Wind Tunnel Investigation of the Influence of Propeller Loading on Ship Rudder Performance," Transactions of the Royal Institution of Naval Architects, Vol. 135, pp. 105–120, 1993.

[2] International Maritime Organisation (IMO), Maritime Safety Committee (MSC)/Circ.644, Explanatory Notes to the Interim Standards for Ship Manoeuvrability, May 1994.

[3] Rules and Regulations for the Classification of Ships. Lloyds Register of Shipping, 2000.

[4] Rules for Classification. Det Norske Veritas (DNV), 2001.

[5] V. Bertram, "Practical Ship Hydrodynamics," Butterwoth-Heinemann, 2000. ISBN 0750648511.

[6] Proceedings of the 18th International Towing Tank Conference, Kobe, Japan, October 1987.

[7] Proceedings of the 22nd International Towing Tank Conference, Seoul, Korea and Shanghi, China, September 1999.

[8] C.D. Simonsen, "Rudder, Propeller and Hull Interaction by RANS," PhD thesis, Department of Naval Architecture and Offshore Engineering, Technical University of Denmark, Studentertorvet, Building 101E, DK-2800, Kongens Lyngby, Denmark, May 2000.

[9] M. Abdel-Maksoud and R. Karsten, "Unsteady Numerical Investigation of the Turbulent Flow Around the Container Ship Model (KCS) With and Without Propeller," Gothenburg 2000, A Workshop on Numerical Ship Hydrodynamics, Department of Naval Architecture and Ocean Engineering, Chalmers University of Technology, Götebörg, Sweden, September 2000.

[10] International Maritime Organisation (IMO), Maritime Safety Committee (MSC), Assembly Resolution A.751(18), Interim Standards for Ship Manoeuvring, November 1993.

[11] International Maritime Organisation (IMO), Maritime Safety Committee (MSC)/Circ.389, Interim Guidelines for Estimating Manoeuvring Performance in Ship Design, January 1985.

[12] International Towing Tank Conference (ITTC) Manoeuvring Trial code, 1975.

[13] E.J. Stierman, "The Influence of the Rudder on the Propulsive Performance of Ships - Part I," International Shipbuilding Progress, Vol. 36, No. 407, pp. 303–334, 1989.

[14] E.J. Stierman, "The Influence of the Rudder on the Propulsive Performance of Ships - Part II," International Shipbuilding Progress, Vol. 36, No. 408, pp. 405–435, 1989.

[15] A.M. Wright and S.R. Turnock, "Directly Coupled Fluid Structural Model of a Ship Rudder Behind a Propeller," Marine Structures, Vol. 13, pp. 53–72, 2000.

[16] F.M. White, "Fluid Mechanics," McGraw-Hill International Editions Mechanical Engineering Series, 4th Edition, 1999. ISBN 0070697167.

[17] B. Johnson, D. Clarke, C. Podenzana-Bonvino, and K. Hasegawa, "International Towing Tank Conference ITTC Symbols and Terminology List, Prepared by the 22nd ITTC Symbols and Terminology Group," August 1999.

[18] J.W. English and D.C. Bain, "Some Manoeuvring Devices for use at Zero and Low Ship Speed," Transactions of the Northeast Coast Institute of Engineers and Shipbuilders, Vol. 88, pp. 31–50, 1971.

[19] P.B. Mathis and D.L. Gregory, "Propeller Slipstream Performance of four High Speed Rudders Under Cavitating Condition," Report 4361, U.S. Naval Ship Research and Development Centre, May 1974.

[20] J.C. Kerwin, S.D. Lewis, and B.W. Oppenheim, "Experiments on Rudders with Small Flaps in Free-Stream and behind a propeller," Report 74-16, M.I.T. Department of Ocean Engineering, October 1974.

[21] S.R. Turnock, "Prediction of Ship Rudder-Propeller Interaction using Parallel Computations and Wind Tunnel Measurements," PhD thesis, Department of Ship Science, Faculty of Engineering, University of Southampton, Highfield, Southampton, SO9 5NH, April 1993.

[22] A.F. Molland and S.R. Turnock, "The Prediction of Ship Rudder Performance Characteristics in the Presence of a Propeller," Manoeuvring and Control of Marine Craft, pp. 475–492, July 1992.

[23] J. Smithwick, "Enhanced Design Performance Prediction Methods for Rudders Operating Downstream of a Propeller," PhD thesis, Department of Ship Science, Faculty of Engineering, University of Southampton, Highfield, Southampton, SO9 5NH, April 2000.

[24] B.S.R. Cooke, "An Investigation into the Performance of High Lift Rudder Devices," Undergraduate final year project, Department of Ship Science, Faculty of Engineering, University of Southampton, Highfield, Southampton, SO9 5NH, May 1994.

[25] The Nautical Institute, "Pilotage and Ship Handling," The Nautical Institute, December 1990. ISBN 1870077075.

[26] H. Thieme, "Design of Ship Rudders," David Taylor Research Center Transactions, No. 321, pp. 1–67, November 1965.

[27] J.E. Brix, "Manoeuvring Technical Manual," Seehafen Verlag GmbH, Hamburg, 1993.

[28] K. Schilling, "Das Schillingruder in der Binwenschiffahrt," H.A.N.S.A, No. 18, 1964.

[29] V.P. Bingham and T.P. Mackey, "High-Performance Rudders - with Particular Reference to the Schilling Rudder," Marine Technology, Vol. 24, No. 4, pp. 312–320, October 1987.

[30] "The Rudder that Performs Like a Stern Thruster," Marine Engineers Review, p. 33, October 1988.

[31] P. Mandel, "Some Hydrodynamic Aspects of Appendage Design," The Society of Naval Architects and Marine Engineers, Vol. 61, pp. 465–515, 1953.

[32] E.V. Lewis, "Principles of Naval Architecture," The Society of Naval Architects and Marine Engineers (SNAME), 1988. ISBN 0939773015.

[33] Proceedings of the 21st International Towing Tank Conference, Trondheim, Norway, 1996.

[34] H. Glauert, "The Elements of Aerofoil and Airscrew Theory," Cambridge University Press, 2nd Edition, 1983. ISBN 052127494X.

[35] J. Katz and A. Plotkin, "Low-Speed Aerodynamics," Cambridge University Press, 2nd Edition, 2001. ISBN 0521662192.

[36] A.F. Molland, "The Free-Stream Characteristics of Ship Skeg Rudders," Ph.D Thesis, Faculty of Engineering and Applied Science, University of Southampton, 1982.

[37] A.F. Molland, "A Method For Determining The Free-Stream Characteristics of Ship Skeg-Rudders," International Shipbuilding Progress, Vol. 32, No. 370, pp. 138–150, June 1985.

[38] A.F. Molland and S.R. Turnock, "A Compact Computational Method for Predicting Forces on a Rudder in a Propeller Slipstream," Transactions of the Royal Institution of Naval Architects, Vol. 138, pp. 227–244, 1996.

[39] J.L. Hess, "Panel Methods in Computational Fluid Dynamics," Annual Review of Fluid Mechanics, Vol. 22, pp. 255–274, 1990.

[40] D.R.M. Jeffrey, "An Investigation into the Aerodynamics of Gurney Flaps," PhD thesis, Department of Aeronautics and Astronautics, Faculty of Engineering, University of Southampton, Highfield, Southampton, SO9 5NH, March 1998.

[41] P.R. Couser, "An Investigation into the Performance of High-Speed Catamarans in Calm Water and Waves," PhD thesis, Department of Ship Science, Faculty of Engineering, University of Southampton, Highfield, Southampton, SO9 5NH, 1996.

[42] M. Tamashima, S. Matsui, J. Yang, K. Mori, and R. Yamazaki, "The Method for Predicting the Performance of Propeller-Rudder System with Rudder Angle and its Application to Rudder Design," Transactions of the West-Japan Society of Naval Architects, No. 86, August 1993.

[43] H. Söding, "Limits of Potential Theory in Rudder Flows Predictions," 22nd Symposium on Naval Hydrodynamics, Washington, D.C., U.S.A, 9-14 August, pp. 622–637, 1998.

[44] H. Söding, "Rudder Flows," Proceedings of 31st Wegemt School on CFD for Ship and Offshore Design, Haus Rissen, Hamburg, May 1999.

[45] D.Q. Li and G. Dyne, "Study of Propeller-Rudder Interaction Based on a Linear Method," International Shipbuilding Progress, Vol. 42, No. 431, pp. 235–258, 1995.

[46] Gothenburg 2000, A Workshop on Numerical Ship Hydrodynamics, Department of Naval Architecture and Ocean Engineering, Chalmers University of Technology, Gothenburg, Sweden, September 2000.

[47] 3rd Numerical Towing Tank Symposium (NUTTS), Tjärnö, Sweden, September 2000.

[48] S.W. Chau, "Numerical Investigation of Free-Stream Rudder Characteristics Using a Multi-Block Finite Volume Method," Report 580, Institut Für Schiffbau Der Universität Hamburg, July 1997.

[49] O.A.M. El Moctar and S. Muzaferija, "Numerical Determination of Rudder Forces," Proceedings of Euromech 374 - Recent Computational Developments in Steady and Unsteady Naval Hydrodynamics, Poitiers, France, April 1998.

[50] A. Wright, "Integrated Computational Fluid-Structural Modelling of Rudders," Master's thesis, Department of Ship Science, Faculty of Engineering, University of Southampton, Highfield, Southampton, SO9 5NH, 1996.

[51] J.A. Schetz and S. Favin, "Numerical Solution for the Near Wake of a Body with Propeller," Journal of Hydronautics, Vol. 11, No. 10, pp. 136–141, 1977.

[52] F. Stern, Y. Toda, and H.T. Kim, "Computation of Viscous Flow Around Propeller-Body Configurations: Iowa Axisymmetric Body," Journal of Ship Research, Vol. 35, No. 2, pp. 151–161, June 1991.

[53] F. Stern, H.T. Kim, D.H. Zhang, Y. Toda, J. Kerwin, and S. Jessup, "Computation of Viscous Flow Around Propeller-Body Configurations: Series 60 $C_B = 60$ Ship Model," Journal of Ship Research, Vol. 38, No. 2, pp. 137–157, June 1994.

[54] G.D. Tzabiras, "A Numerical Study of Additive Bulb Effects on the Resistance and Self-Propulsion Characteristics of a Full Ship Form," Ship Technology Research, Vol. 44, pp. 98–108, 1997.

[55] Y. Kodama, "Scope of CFD for Computing Ship Flows," Proceedings of the 3rd Osaka Colloquium on Advanced CFD Applications to Ship Flow and Hull Form Design, Osaka Prefecture University, Osaka, pp. 395–405, May 1998.

[56] H. McDonald and D.L. Whitfield, "Self-Propelled Manoeuvring Underwater Vehicles," 21st Symposium on Naval Hydrodynamics, Trondheim, Norway, June 24-28, pp. 478–489, 1996.

[57] J.D. Anderson, "Computational Fluid Dynamics, The Basics With Applications," McGraw-Hill International Editions Mechanical Engineering Series, 1st Edition, 1995. ISBN 0070016852.

[58] D.C. Wilcox, "Turbulence Modelling for CFD," D.C.W. Industries, 2nd Edition, 1998. ISBN 0963605151.

[59] P. Creismeas, "Application de la LES Implicite à L'étude d'un Écoulement Autour D'un Profil NACA0012," 7th Journees De L'Hydrodynamique, Marseille, France, 8-10 March, 1999.

[60] American Society of Mechanical Engineers (ASME), "Editorial Policy Statement on the Control of Numerical Accuracy," ASME Journal of Fluids Engineering, Vol. 115, No. 3, pp. 339–340, September 1993.

[61] F.G. Blottner, "Accurate Navier-Stokes Results for the Hypersonic Flow Over a Spherical Nosetip," Journal of Spacecraft and Rockets, Vol. 27, No. 2, pp. 113–122, 1990.

[62] F. Stern, H.W. Coleman, R.V. Wilson, and E.G. Paterson, "Verification and Validation of CFD Simulations," Proceedings of the 3rd ASME/JSME Joint Fluids Engineering Conference, San Francisco, California, July 18-23, 1999.

[63] L.F. Richardson, "The Deferred Approach to the Limit," Transactions of the Royal Society, London Series A. 226, pp. 229–361, 1927.

[64] L. Eca and M. Hoekstra, "On the Numerical Verification of Ship Stern Flow Calculations," MARNET-CFD, 1st Annual Worshop, Barcelona, 18-19 November, 1999.

[65] H.K. Versteeg and W. Malalasekera, "An Introduction to Computational Fluid Dynamics," Longman Scientific and Technical, 1st Edition, 1995. ISBN 0582218845.

[66] C.G. Speziale, "Analytical Methods for the Development of Reynolds-stress Closures in Turbulence," Annual Review of Fluid Mechanics, Vol. 23, pp. 107–157, 1991.

[67] O. Reynolds, "On the dynamical theory of incompressible viscous fluids and the determination of the criterion," Phil. Trans. Royal Society., 1895.

[68] J. Boussinesq, "Essai Sur La Théorie Des Eaux Courantes," Mem. Présentés Acad. Sci, Vol. 23, 1877.

[69] M.A. Leschziner, "Computation of Aerodynamic Flows with Turbulence Transport Models Based on Second-Moment Closures," Computers and Fluids, Vol. 24, No. 4, pp. 377–392, 1995.

[70] E. Guilmineau, J. Piquet, and P. Queutey, "Two-Dimensional Turbulent Viscous Flow Simulation Past Airfoils at Fixed Incidence," Computers and Fluids, Vol. 26, No. 2, pp. 135–162, 1997.

[71] C.M. Rhie and W.L. Chow, "Numerical Study of the Turbulent Flow Past an Airfoil with Trailing Edge Separation," AIAA Journal, Vol. 21, No. 11, pp. 1525–1532, 1983.

[72] V. Yakhot, S.A. Orszag, S. Thangam, T.B. Gatski, and C.G. Speziale, "Development of Turbulence Models for Shear Flows by a Double Expansion Technique," Physics of Fluids A, Vol. 4, No. 7, pp. 1510–1520, 1992.

[73] B.E. Launder and D.B. Splading, "The Numerical Computation of Turbulent flows," Computer Methods in Applied Mechanics and Engineering, Vol. 3, pp. 269–289, 1974.

[74] H. Schlichting, "Boundary Layer Theory," Springer-Verlag Berlin and Heidelberg GmbH and Co. KG, 8th Edition, 1999. ISBN 3540662707.

[75] CFX 4.3 Flow Solver Guide. AEA Technology, Harwell Laboratory, Oxfordshire, OX11 ORA, U.K., 1998.

[76] Patankar S.V. and D.B. Spalding, "A Calculation Procedure for Heat, Mass and Momentum Transfer in Three-Dimensional Parabolic Flows," International Journal of Heat and Mass Transfer, Vol. 15, p. 1787, 1972.

[77] Issa R.I., "Solution of Implicitly Discretised Fluid Flow Equations by Operator-Splitting," Journal of Computational Physics, Vol. 62, pp. 40–65, 1986.

[78] N.H. Wakefield, "Helicopter Flight in the Airwake of Non-Aviation Ships," PhD thesis, Department of Ship Science, Faculty of Engineering, University of Southampton, Highfield, Southampton, SO9 5NH, May 2000.

[79] M. Peric and J.H. Ferziger, "Computational Methods for Fluid Dynamics," Springer-Verlag Berlin and Heidelberg GmbH and Co. KG, 2 Edition, 1997. ISBN 3540594345.

[80] Fieldview 7 User's Guide. Intelligent Light, 1290 Wall Street West, 3rd Floor, Lyndhurst, NJ 07071, U.S.A, 2000.

[81] C.A. Hall and W.J. Gordon, "Construction of Curvilinear Coordinate Systems and Applications to Mesh Generation," International Journal of Numerical Methods in Engineering, Vol. 7, pp. 461–477, 1973.

[82] N.C. Rycroft, "Three-Dimensional Multi-block Grid Generation - Fleximesh," Ship Science Report 101, Department of Ship Science, Faculty of Engineering, University of Southampton, Highfield, Southampton, SO9 5NH, November 1997.

[83] W. Froude, "Experiments on Surface-Friction Experienced by a Plane Moving Through Water," Report 42, British Association for the Advancement of Science, 1872.

[84] W. Froude, "Report to the Lords Commissioners of the Admiralty on Experiments for the Determination of the Frictional Resistance of Water on a surface, under various conditions, performed at Chelston Cross, under the Authority of their Lordships," Report 44, British Association for the Advancement of Science, 1874.

[85] J.C. Date and S.R. Turnock, "Compuational Fluid Dynamics Estimation of Skin Friction Experienced by a Plane Moving Through Water," Transactions of the Royal Institution of Naval Architects, pp. 1–16, 2000.

[86] K.E. Schoenherr, "Resistance of Flat Surfaces Moving Through a Fluid," Society of Naval Architects and Marine Engineers, Vol. 40, p. 279, 1932.

[87] Proceedings of the 8th International Towing Tank Conference, Madrid, Spain, 1957.

[88] O. Reynolds, "An Experimental Investigation of the Circumstances which Determine whether the Motion of Water shall be Direct or Sinuous and of the Law of Resistance in Parallel Channels," Phil. Trans. Royal Society. 174, 1883.

[89] K.N. Chung and K.S. Min, "A Study of Viscous Flow Field Around an Axisymmetric Body with Propeller," Proceedings of the 3rd Osaka Colloquium on Advanced CFD Applications to Ship Flow and Hull Form Design, Osaka Prefecture University, Osaka, pp. 3–13, May 1998.

[90] G.W. Dolphin, "Evaluation of CFD for Flat Plate Axisymmetric and Ship Geometries from Model to Full Scale Reynolds Numbers," Master's thesis, Iowa Institute of Hydraulic Research, College of Engineering, University of Iowa, Iowa City, Iowa 52242, U.S.A, May 1997.

[91] I.H. Abbott and A.E. Von Doenhoff, "Theory of Wing Sections," Dover Publications Inc, 1959. ISBN 0486605868.

[92] J.J. Thibert, M. Grandjacques, and L.H. Ohman, "NACA0012 Airfoil," AGARD Advisory Report, 1979.

[93] N. Gregory and O.L. O'Reilly, "Low Speed Aerodynamic Characteristics of NACA0012 Airfoil Section, Including the Effects of Upper Surface Roughness Simulation Hoarfrost," NPL Aero Report 1308, National Physical Laboratory, 1970.

[94] Y. Zhu and N. Qin, "Inclined Suction and Blowing for Shock Control at Transonic Speeds," 22nd International Symposium on Shock Wave, Imperial College, London, U.K., July 1999.

[95] D.P. Rizzetta and M.R. Visbal, "Comparative Numerical Study of Two Turbulence Models for Airfoil Static and Dynamic Stall," AIAA Journal, Vol. 31, No. 4, pp. 784–786, 1993.

[96] J. Johansen and J.N. Sørensen, "Prediction of Laminar/Turbulent Transition in Airfoil Flow," Paper 98-0702 at the AIAA 36th Aerospace Science Meeting and Exhibition, Reno, NV, January 1998.

[97] R.H. Liebeck, "Design of Subsonic Airfoils for High Lift," Journal of Aircraft, Vol. 15, No. 9, pp. 547–561, September 1978.

[98] D.A. Küchemann, "Inviscid shear Flow Near the Trailing Edge of an Aerofoil," Z. Flugwiss, Vol. 15, pp. 292–294, 1967.

[99] D.H. Neuhart and Jr. Pendergraft, O.C., "A Water Tunnel Study of Gurney Flaps," NASA TM 4071, November 1988.

[100] D. Ashby, "Experimental and Computational Investigation of Lift-Enhancing Tabs on Multi-Element Airfoil," NASA-CR-201482, June 1996.

[101] J.C. Ross, B.L. Storms, and P.G. Carrannanto, "Lift-Enhancing Tabs on Multi-Element Airfoils," Journal of Aircraft, Vol. 32, No. 3, pp. 649–655, May-June 1995.

[102] C.S. Jang, J.C. Ross, and R.M. Cummings, "Computational Evaluation of an Airfoil with a Gurney Flap," 10th AIAA Applied Aerodynamics Conference, Palo Alto, C.A., pp. 801–809, June 1992.

[103] J.H. Gerrard, "The Mechanics of the Formation Region of Vortices Behind Bluff Bodies," Journal of Fluid Mechanics, Vol. 25, pp. 401–413, 1966.

[104] P.W. Bearman, "On Vortex Street Wakes," Journal of Fluid Mechanics, Vol. 28, pp. 625–641, 1967.

[105] D.R.M. Jeffrey, X. Zhang, and D.W. Hurst, "Aerodynamics of Gurney flaps on a single-element high-lift wing," Journal of Aircraft, 2000.

[106] D.R.M. Jeffrey, X. Zhang, and D.W. Hurst, "Some Aspects of the Aerodynamics of Gurney Flaps on a Double-Element Wing," Journal of Fluids Engineering, Vol. 123, March 2001.

[107] A.G. Fripp, "Experimental Investigation and Computer Modelling of Flow around Aerofoils with Gurney Flaps," Undergraduate final year project, Department of Aerospace, University of Bristol, March 1991.

[108] D.B. Sims-Williams, A.J. White, and Dominy, "Gurney Flap Aerodynamic Unsteadiness," Sports Engineering, Vol. 2, pp. 221–233, 1999.

[109] W.J. McCroskey, "Unsteady Airfoils," Annual Review of Fluid Mechanics, Vol. 14, pp. 285–311, 1982.

[110] G.L. Commerford and F.O. Carta, "Unsteady Aerodynamic Response of a Two-Dimensional Airfoil at High Reduced Frequency," AIAA Journal, Vol. 12, No. 1, pp. 43–48, January 1974.

[111] A. Gollnick, "The Generation of Periodic Gusts in a Supersonic Wind Tunnel," Report SP276, MIT, Cambridge, Massachusetts, U.S.A, June 1969.

[112] E.G. Paterson and F. Stern, "Computation of Unsteady Viscous Marine-Propulsor Blade Flows - Part 1: Validation and Analysis," Transactions of the American Society of Mechanical Engineers, Journal of Fluids Engineering, Vol. 119, pp. 145–154, March 1997.

[113] E. Paterson and F. Stern, "Computation of Unsteady Viscous Flow with Application to the MIT Flapping-Foil Experiment," Proceedings of the 6th International Conference on Numerical Ship Hydrodynamics, Iowa City, Iowa, August 1993.

[114] E.G. Paterson and F. Stern, "Computation of Unsteady Viscous Marine-Propulsor Blade Flows - Part 2: Parametric Study," Transactions of the American Society of Mechanical Engineers, Journal of Fluids Engineering, Vol. 121, pp. 139–147, March 1999.

[115] T. Theodorsen, "General Theory of Aerodynamic Instability and the Mechanism of Flutter," N.A.C.A Technical Report 496, 1935.

[116] T. Von Kármán and W.R. Sears, "Airfoil Theory for Non-Uniform Motion," Journal of the Aeronautical Sciences, Vol. 5, No. 10, pp. 379–390, 1938.

[117] W.R. Sears, "Some Aspects of Non-Stationary Airfoil Theory and Its Practical Application," Journal of the Aeronautical Sciences, Vol. 8, No. 3, pp. 104–108, 1941.

[118] J.H. Horlock, "Fluctuating Lift Forces on Aerofoil moving Through Transverse and Chord-wise Gusts," Transactions of the American Society of Mechanical Engineers, Journal of Basic Engineering, pp. 494–500, December 1997.

[119] D.R. Poling and D.P. Telionis, "The Response of Airfoils to periodic Disturbances - The Unsteady Kutta Condition," AIAA Journal, Vol. 24, No. 2, pp. 193–199, February 1986.

[120] J.Q. Rice, "Investigation of a Two-Dimensional Hydrofoil in Steady and Unsteady Flows," Master's thesis, Department of Ocean Engineering, Massachusetts Institute of Technology (MIT), Cambridge, Massachusetts 02139, U.S.A, June 1991.

[121] P.M. Delpero, "Investigation of Flows Around a Two-Dimensional Hydrofoil Subject to a High Reduced Frequency Gust Loading," Master's thesis, Department of Ocean Engineering, Massachusetts Institute of Technology (MIT), Cambridge, Massachusetts 02139, U.S.A, February 1992.

[122] A.R.J.M Lloyd, "Seakeeping: Ship Behaviour in Rough Weather," 26, Spithead Avenue, Gosport, Hampshire, U.K., 1998. ISBN 0953263401.

[123] G.O. Roberts, "Lecture Notes in Physics, Volume 1," Springer-Verlag Berlin and Heidelberg GmbH and Co. KG, 1971.

[124] P.R. Eiseman, "A Multi-Surface Method of Coordinate Generation," Journal of Computational Physics, Vol. 33, pp. 118–150, 1979.

[125] N.H. Kemp, "On the Lift Circulation of Airfoils in Some Unsteady-Flow Problems," Journal of the Aeronautical Sciences, Vol. 19, pp. 713–714, 1952.

APPENDICES

Appendix A

Model-Ship Rudder Scaling

Consider the following model-ship scaling problem, neglecting any hull wake or propeller effects. A free running model test is conducted for a vessel with the following particulars.

Length	L_s	=	190 m
Service Speed	V_s	=	10 m/s
Froude No.	Fn_s	=	0.23
Rudder Chord	c_s	=	8 m

Assuming that the free running model is of scale 1:35, then the model length and rudder chord will be, $L_m = 5.43$ m and $c_m = 0.14$ m, respectively. Now since free running model tests are run in compliance with Froude's scaling law, i.e. $Fn_s = Fn_m$, the model free running speed equates to $V_m = 1.69$ m/s. Now, assuming that the kinematic viscosity of the water the model is tested in, is $\nu = 1.19 \times 10^{-6}$, then the Reynolds number of the rudder flow will be equal to $R_n = 2.03 \times 10^5$. It is, therefore, evident from these simple calculations, that the Froude Scaling procedure produces a flow, which is likely to be partially laminar, if not totally laminar, about the rudder. In reality, however, turbulent flow might be triggered in the vicinity of the rudder, as a result of the unsteady hull wake and propeller flow, but there is no guarantee that

this will be the case.

Appendix B

Geometric Progression Distribution Formulae

The function used to set the grid distributions within CFX-MESHBUILD is based on the geometric progression summation formulae expressed by Equation 61.

$$E_L = \sum_{i=1}^{n-1} ar^{i-1} = a + ar + ar^2 + ... + ar^{n-2} \tag{61}$$

where, E_L is the edge length, a is the largest cell size, ar^{n-2} is the smallest cell size, n is the number of nodes along the edge and r is the common ratio.

The sum of geometric progression expressed in Equation 61, can be rewritten in another form given by Equation 62.

$$E_L = \sum_{i=1}^{n-1} ar^{i-1} = a\frac{(1 - r^{n-1})}{(1 - r)} \tag{62}$$

Now, r and n can be determined from knowledge of the E_L and the required ar^{n-2} and a, following the rearrangement of Equation 62, into Equation 63 and substitution of Equation 63, into Equation 62 to give Equation 64.

$$r = \frac{(a - E_L)}{(ar^{n-2} - E_L)} \tag{63}$$

$$n = \frac{log_{10}\left(E_L \frac{r-1}{a} + 1\right)}{log_{10} r} + 1 \tag{64}$$

Figure 105 shows the distributions produced along an edge on length, $E_L = 100$ mm, with the smallest distance between nodes set at, 1.0 mm, and the largest distance between nodes set at 10 mm. It is not possible to increase the number of nodes along the edge, without changing the size of the largest distance between nodes.

Appendix C

Hyperbolic Distribution Formulae

The method used to set the grid distributions within Fleximesh is based on the formulae derived by Roberts [123] and modified by Eiseman [124]. This approach distributes nodes along an edge of unit length, based on a normalised parametric formulation implementing a hyperbolic distribution function, as expressed by Equation 65 and Equation 66. The hyperbolic function, has the advantage that it can produce more than one distribution, with fixed second and second from last node locations.

$$S = \sum_{i=2}^{n} s_i - s_{i-1} = s_2 + (s_3 - s_2) + ... + (s_n - s_{n-1}) = 1 \qquad 0 < s_i \leq 1 \tag{65}$$

$$s_i = p\eta_i + (1-p)\left(1 - \frac{\tanh\left(q(1-\eta_i)\right)}{\tanh q}\right) \qquad 0 \leq \eta_i \leq 1 \tag{66}$$

$$\eta_i = \frac{i-1}{n-1} \tag{67}$$

where, S is the normalised edge length, s_i is the normalised node location, p is the slope parameter, q is the damping factor, n is the number of nodes along an edge and η_i is the normalised uniform node location.

The parametric formulation given above, can then be used to calculate the real node location by multiplying the parametric location s_i by the edge length E_L.

$$E_i = E_L s_i \tag{68}$$

The process of determining the p, q and n parameters needed to produce a distribution with specific second and second from last node locations is complex. The behaviour of the hyperbolic function means there is more than one set of p, q and n which can produce a distribution with the required second and second from last node locations. Specifying the second and second from last node locations along an edge, results in two equations, Equation 69 and Equation 70 and three unknowns i.e. p, q and n.

$$s_2 = p\eta_2 + (1-p)\left(1 - \frac{\tanh\left(q(1-\eta_2)\right)}{\tanh q}\right) \tag{69}$$

$$s_{n-1} = p\eta_{n-1} + (1-p)\left(1 - \frac{\tanh\left(q(1-\eta_{n-1})\right)}{\tanh q}\right) \tag{70}$$

In order to determine the minimum number of n nodes needed to produce the required distribution, the following solution approach is used. First Equation 69 is rearranged to give Equation 71 expressing p in terms of q.

$$p = \frac{s_2 - 1 + \frac{\tanh\left(q(1-\eta_2)\right)}{\tanh q}}{\eta_2 - 1 + \frac{\tanh\left(q(1-\eta_2)\right)}{\tanh q}} \tag{71}$$

Equation 71 is substituted into Equation 70 and the resulting equation, Equation 72, solved for q, using the Newton-Raphson approximation given in Equation 73.

$$f(q) = s_{n-1} - p\eta_{n-1} + (1-p)\left(1 - \frac{\tanh\left(q(1-\eta_{n-1})\right)}{\tanh q}\right) = 0 \tag{72}$$

$$q_{m+1} = q_m - \frac{f(q_m)}{f'(q_m)} \tag{73}$$

As n is also a variable, it must also be globally iterated until the converged value of q produces a positive value of p, when substituted into Equation 71. The minimum

number of nodes n which can produce the required distribution corresponds to the first converged value of q for positive p. By specifically setting the number of nodes to some value above this minimum number, and solving Equation 72 in the same manner as before, other distributions which satisfy the same distribution criteria can be obtained. A maximum number of points capable of producing the required distribution is defined by Equation 74.

$$n < \frac{s_{n-1}}{s_2} + 1 \tag{74}$$

Figure 106 shows the distributions produced along an edge of length, $E_L = 100$ mm, with the smallest distance between nodes set at, 1.0 mm, and the largest distance between nodes set at 10 mm. As can be seen, by increasing the number of nodes from 21 to 30, whilst keeping the smallest and largest distances between nodes fixed, a distribution with more nodes packed towards the end with the smallest node distance can be produced.

Appendix D

Linear Unsteady Aerofoil Theory

D.1 Transverse Flow Fluctuations

Consider a transverse gust, with amplitude v_0, moving past a flat plate aerofoil of chord c, velocity U_∞ and frequency ω. Assume that the origin for x is at the centre of the aerofoil, and that the perpendicular periodic velocity component is written in the form given by Equation 75.

$$v = v_0 \Re e^{i\omega(t-\frac{x}{U_\infty})} \tag{75}$$

Sears [117] found that the unsteady fluctuating lift ΔL_v produced, was equal to the steady lift at the effective gust angle of incidence, multiplied by a complex function $S(k)$, known as the Sears function, as shown in Equation 76

$$\Delta L_v = \pi \rho c U_\infty v_o e^{i\omega t} S(k) \tag{76}$$

A table of Sears function values for reduced frequencies between zero and ∞ are presented by Kemp [125].

D.2 Parallel Flow Fluctuations

Now consider a velocity fluctuation, with amplitude u_0, moving parallel with a flat plate aerofoil of chord c, velocity U_∞ and frequency ω. Assume that the origin for x is at the centre of the aerofoil, and that the parallel periodic velocity component is written in the form given by Equation 77.

$$u = u_0 \Re e^{i\omega(t-\frac{x}{U_\infty})} \tag{77}$$

Horlock [118] found that the unsteady fluctuating lift ΔL_u produced, was equal to the steady lift slope, multiplied by the angle of incidence of the aerofoil and the velocity fluctuation u_0 multiplied by a complex function $T(k)$, known as the Theodorsen [115] function, as shown in Equation 78.

$$\Delta L_u = \pi \rho c U_\infty u_o e^{i\omega t} T(k) \tag{78}$$

A table of Theodorsen function values for reduced frequencies between zero and ∞ are presented by Horlock [118].

D.3 Transverse and Parallel Flow Fluctuations

Next, consider the general case of a gust, at an angle to the stream-wise direction. The solution is found by the direct addition of the linearised equations, described in the two proceeding sections, Equation 76 and Equation 78. The new equation for the fluctuating lift force is given by Equation 79.

$$\Delta L = \pi \rho c U_\infty u_o e^{i\omega t}(S(k) + \alpha T(k)) \tag{79}$$

TABLES

c_μ	σ_k	σ_ε	$c_{\varepsilon 1}$	$c_{\varepsilon 2}$
0.09	1.00	1.30	1.44	1.92

Table 1: Standard $k-\varepsilon$ turbulence model constants

c_μ	α_k	α_ε	$c_{\varepsilon 1}$	$c_{\varepsilon 2}$	η_0	β
0.085	1.39	1.39	1.42	1.68	4.38	0.015

Table 2: RNG $k-\varepsilon$ turbulence model constants

Variable	SIMPLE	PISO
u	0.6	0.7
v	0.6	0.7
p	0.4	1.0
k	0.6	0.8
ε	0.6	0.8
$\overline{u_i' u_j'}$	0.5	0.5

Table 3: Under-relaxation factors

Service	Processor	No. Processors	Memory	Maximum job time
Irixcompute	195 Mhz MIPS R10000	8	1 Gbyte	5 Days
Irixresearch	300 Mhz MIPS R12000	8	8 Gbyte	5 Days
Irixresearch	400 Mhz MIPS R12000	8	8 Gbyte	5 Days

Table 4: Computing resources

Edge	Boundary condition
$\overline{AB}$	Symmetry
$\overline{BC}$	Wall
$\overline{CD}$	Symmetry
$\overline{DH}$	Mass Flow
$\overline{AE}$	Inlet
$\overline{EF}$	Inlet
$\overline{FG}$	Inlet
$\overline{GH}$	Inlet

Table 5: Flat plate boundary conditions

Outlet position	c_f $\times 10^{-3}$	N_{it}	CPU time (s)	No. of cells
$L/8$	2.211	191	515	6800
$L/4$	2.210	171	503	7200
$L/2$	2.210	172	583	8000
L	2.209	165	706	9600
$2L$	2.209	187	1141	12800
$4L$	2.209	227	2217	19200

Table 6: 15.24 m flat plate outlet boundary position study

Inlet position	c_f $\times 10^{-3}$	N_{it}	CPU time (s)	No. of cells
$L/8$	2.213	176	450	6800
$L/4$	2.211	170	463	7200
$L/2$	2.209	176	581	8000
L	2.209	165	656	9600
$2L$	2.209	172	980	12800
$4L$	2.209	166	1666	19200

Table 7: 15.24 m flat plate inlet boundary position study

Upper inlet position	c_f $\times 10^{-3}$	N_{it}	CPU time (s)	No. of cells
$L/4$	2.217	96	31	1200
$L/2$	2.212	99	69	2400
L	2.210	111	183	4800
$2L$	2.209	165	706	9200
$4L$	2.209	364	4322	19200

Table 8: 15.24 m flat plate upper inlet boundary position study

Plate length (ft), (m)	Max U_∞ (m/s)	Min U_∞ (m/s)	Max R_n $\times 10^6$	Min R_n $\times 10^5$
50, 15.24	5.08	0.25	68.0	330
1, 0.305	5.08	0.25	1.4	0.67

Table 9: Reynolds numbers for Froude's flat plates

U_∞ (m/s)	R_n $\times 10^6$	Δy_p (m)	y^+
5.08	68.0	0.00024	30
0.254	3.3	0.00350	30

Table 10: 15.24 m flat plate estimated minimum near-wall cell sizes at high and low Reynolds numbers

U_∞ (m/s)	R_n $\times 10^6$	Δy_p (m)	y^+
5.08	68.0	0.005	$246 - 335$
0.254	3.3	0.005	$16 - 22$

Table 11: 15.24 m flat plate near-wall cell size and RANS calculated y^+

Δy_p (m)	y^+	c_f $\times 10^{-3}$	N_{it}	CPU time (s)	No. of cells
0.0050	$246 - 335$	2.370	649	856	4000
0.0025	$126 - 171$	2.360	1234	1850	4300
0.00125	$58 - 79$	2.350	2981	4850	4700
0.000625	$30 - 40$	2.360	5728	10200	5100
0.0003135	$15 - 20$	2.390	10452	196000	5500

Table 12: 15.24 m flat plate effect of near-wall cell size on computed skin friction

Last cell size (m)	c_f $\times 10^{-3}$	N_{it}	CPU time (s)	No. of cells
10.0	2.390	293	168	2000
5.0	2.369	649	856	4000
2.5	2.365	1100	2910	7400
1.25	2.364	1541	10600	13300

Table 13: 15.24 m flat plate outer cell independance study

Middle cell size (m)	c_f $\times 10^{-3}$	N_{it}	CPU time (s)	No. of cells
4.0	2.380	1345	225	5464
2.0	2.374	1208	355	7548
1.0	2.373	1185	413	8732
0.5	2.372	1109	481	10434
0.25	2.372	1008	574	12728
0.125	2.372	906	669	15964

Table 14: 15.25 m flat plate longitudinal cell independance study

Flow field variable	First order	Third order
u	upwind	QUICK
v	upwind	QUICK
ρ	upwind	QUICK
k	upwind	hybrid
ε	upwind	hybrid

Table 15: Differencing schemes tested

Edge	Boundary condition $\alpha = 0$ deg	Boundary condition $\alpha > 0$ deg
$\overline{AB}$	Inlet	Inlet
$\overline{BC}$	Inlet	Inlet
$\overline{CD}$	Inlet	Inlet
$\overline{DE}$	Inlet	Inlet
$\overline{FG}$	Wall	Wall
$\overline{GH}$	Wall	Wall
$\overline{HI}$	Wall	Wall
$\overline{AJ}$	Pressure	Pressure
$\overline{JP}$	Pressure	Pressure
$\overline{FK}$	Wall	Wall
$\overline{KL}$	Wall	Wall
$\overline{LI}$	Wall	Wall
$\overline{EM}$	Inlet	Wall
$\overline{MN}$	Inlet	Pressure
$\overline{NO}$	Inlet	Pressure
$\overline{OP}$	Inlet	Pressure

Table 16: NACA 0012 & 0020 boundary conditions

Δy_p (m)	y^+	c_f $\times 10^{-3}$	c_{pv} $\times 10^{-3}$	c_d $\times 10^{-3}$	N_{it}	CPU time (min)	No. of cells
0.016	$270 - 765$	7.145	3.478	10.623	1697	26	14400
0.008	$118 - 398$	7.090	2.960	10.051	1693	29	15552
0.004	$65 - 200$	7.076	2.711	9.788	1686	31	16704
0.002	$39 - 99$	7.070	2.508	9.578	1672	34	18432
0.001	$20 - 49$	7.080	2.485	9.565	2704	55	19584

Table 17: Effect of near-wall cell size on computed NACA 0012 drag, $\alpha = 0$ deg

Edge	Boundary condition $\alpha = 0$ deg	Boundary condition $\alpha > 0$ deg
$\overline{AB}$	Inlet	Inlet
$\overline{BC}$	Inlet	Inlet
$\overline{CD}$	Inlet	Inlet
$\overline{DE}$	Inlet	Inlet
$\overline{FG}$	Wall	Wall
$\overline{GH}$	Wall	Wall
$\overline{HI}$	Wall	Wall
$\overline{KJ}$	Pressure	Pressure
$\overline{JL}$	Pressure	Pressure
$\overline{IO}$	Wall	Wall
$\overline{NI}$	Wall	Wall
$\overline{MN}$	Wall	Wall
$\overline{FM}$	Wall	Wall
$\overline{EP}$	Inlet	Inlet
$\overline{PQ}$	Inlet	Pressure
$\overline{QR}$	Inlet	Pressure
$\overline{RS}$	Inlet	Pressure
$\overline{LS}$	Pressure	Pressure
$\overline{AK}$	Pressure	Pressure

Table 18: Gurney flapped NACA 0012 boundary conditions

Grid No.	n_ζ	c_l $\times 10^{-1}$	c_d $\times 10^{-1}$	CPU time (min)	No. of cells
1	37	6.517	0.304	140	39840
2	59	6.533	0.315	177	43360
3	79	6.538	0.320	193	46560
4	99	6.501	0.338	200	49760

Table 19: 4% Gurney under-converged steady state wake grid study

Gurney	$\frac{dc_l}{d\alpha}$ (1/rad) CFX ($\Lambda = \infty$)	$\frac{dC_L}{d\alpha}$ (1/rad) Corrected ($\Lambda = 5$)	$\frac{dC_L}{d\alpha}$ (1/rad) Jeffrey [40]($\Lambda = 5$)
None	5.632	4.022	4.091
2 %	6.440	4.600	4.647
4 %	6.469	4.621	4.738

Table 20: Lift slope correction

Δt (s)	f_p (Hz)	c_l $\times 10^{-1}$	c_d $\times 10^{-1}$	CPU time (hrs)
0.000025	526	6.812	0.369	230
0.00005	526	6.844	0.363	115
0.0001	526	6.801	0.356	104
0.0003	416	6.525	0.309	57
0.001	–	6.497	0.305	13

Table 21: 4% Gurney temporal time step study

α (deg)	f (Hz) CFX	f (Hz) Jeffrey [40]	S_t CFX	S_t Jeffrey [40]
0	526	485 – 490	0.168	0.155 – 0.157
−5	526	–	0.168	–
+10	–	440 – 445	–	0.141 – 0.142

Table 22: 4% Gurney shedding frequency and Strouhal No. comparison

	$c_l \times 10^{-1}$			$c_d \times 10^{-1}$		
α (deg)	Min	Max	Average	Min	Max	Average
−20	−8.056	−8.057	−8.057	1.863	1.863	1.863
−15	−9.582	−9.582	−9.582	0.867	0.867	0.867
−10	−5.479	−5.481	−5.480	0.421	0.422	0.422
−5	0.454	0.719	0.587	0.323	0.328	0.326
0	6.618	6.984	6.801	0.336	0.376	0.356
+5	10.181	10.181	10.181	0.491	0.491	0.491
+10	15.097	15.097	15.097	0.975	0.974	0.975
+15	13.788	13.789	13.789	1.960	1.960	1.960
+20	13.096	13.096	13.096	3.938	3.938	3.938

Table 23: 4% Gurney time-accurate performance

x/h	y/h	$\overline{u'^2}/U_\infty^2$	$\overline{v'^2}/U_\infty^2$
1.0	−0.31	0.1290	–
0.75	−1.06	0.1618	–
1.19	−0.69	–	0.3453

Table 24: 4% Gurney positions of maximum shear stress

Edge	Boundary condition $\alpha = 0$ deg	Boundary condition $\alpha > 0$ deg
$\overline{AB}$	Inlet	Inlet
$\overline{BC}$	Inlet	Inlet
$\overline{CD}$	Inlet	Inlet
$\overline{DE}$	Inlet	Inlet
$\overline{EF}$	Inlet	Inlet
$\overline{FG}$	Inlet	Inlet
$\overline{HI}$	Wall	Wall
$\overline{IJ}$	Wall	Wall
$\overline{JK}$	Wall	Wall
$\overline{KL}$	Wall	Wall
$\overline{LM}$	Wall	Wall
$\overline{AN}$	Pressure	Pressure
$\overline{NO}$	Pressure	Pressure
$\overline{OZ}$	Pressure	Pressure
$\overline{PQ}$	Wall	Wall
$\overline{QR}$	Wall	Wall
$\overline{RS}$	Wall	Wall
$\overline{ST}$	Wall	Wall
$\overline{TH}$	Wall	Wall
$\overline{GU}$	Inlet	Inlet
$\overline{UV}$	Inlet	Pressure
$\overline{VW}$	Inlet	Pressure
$\overline{WX}$	Inlet	Pressure
$\overline{XY}$	Inlet	Pressure
$\overline{YZ}$	Inlet	Pressure

Table 25: Schilling section boundary conditions

R_n	Δy_p (m)	y^+
2.12×10^5	0.04	$24 - 64$
8.38×10^6	0.003	$38 - 142$
4.19×10^7	0.0006	$21 - 120$

Table 26: NACA 0020 near-wall cell size and RANS calculated y^+, $\alpha = 0$ deg

R_n	Δy_p (m)	y^+
2.12×10^5	0.04	$22 - 70$
8.38×10^6	0.003	$39 - 153$
4.19×10^7	0.0006	$19 - 380$

Table 27: Schilling near-wall cell size and RANS calculated y^+, $\alpha = 0$ deg

Section	n_ξ	n_η	n_ζ	n_ψ	No. of cells
NACA 0020	390	59	149	–	40592
Schilling (5 deg T.E.)	414	59	299	32	69276
Schilling (7.5 deg T.E.)	414	59	299	44	72864
Schilling (10 deg T.E.)	414	59	299	58	77050
Schilling (15 deg T.E.)	414	59	299	84	84824

Table 28: NACA 0020 and Schilling grid information

Flow	R_n	$\frac{dc_l}{d\alpha}$ (1/rad)	$c_{l,max}$	α_{stall} (deg)	c_{d0} $\times 10^{-3}$	c_f $\times 10^{-3}$	c_{pv} $\times 10^{-3}$	$1+k$
Laminar	2.12×10^5	5.504	0.957	16	10.075	5.971	4.104	1.687
Turbulent $(k-\varepsilon)$	2.12×10^5	5.546	1.251	18	21.041	14.816	6.225	1.420
Turbulent $(k-\varepsilon)$	8.38×10^6	5.878	1.399	19	10.073	7.310	2.763	1.378
Turbulent $(k-\varepsilon)$	4.19×10^7	6.043	1.495	21	7.858	5.759	2.099	1.364

Table 29: NACA 0020 performance information

Flow	R_n	$\frac{dc_l}{d\alpha}$ (1/rad)	$c_{l,max}$	α_{stall} (deg)	c^*_{d0}
Turbulent $(k-\varepsilon)$	2.12×10^5	7.100	1.649	17	1.361
Turbulent $(k-\varepsilon)$	8.38×10^6	6.895	1.824	18	1.00
Turbulent $(k-\varepsilon)$	4.19×10^7	6.828	1.957	21	1.00

Table 30: Schilling (10 deg T.E.) under-converged steady state performance information at different Reynolds numbers

Fish-tail T.E. angle (deg)	$\frac{dc_l}{d\alpha}$ (1/rad)	$c_{l,max}$	α_{stall} (deg)	c^*_{d0}
5	6.865	1.821	21	0.549
7.5	6.875	1.901	21	0.768
10.0	6.828	1.957	21	1.0
15.0	6.672	2.083	21	1.565

Table 31: Schilling performance information for different fish-tail T.E. angles, $R_n = 4.19 \times 10^7$

k	ω (rad/s)	T (s)	Δt (s)
0.5	2	π	$\pi/50$
1.0	4	$\pi/2$	$\pi/100$
2.0	8	$\pi/4$	$\pi/200$
5.0	20	$\pi/10$	$\pi/500$

Table 32: NACA 0020 transient model data

FIGURES

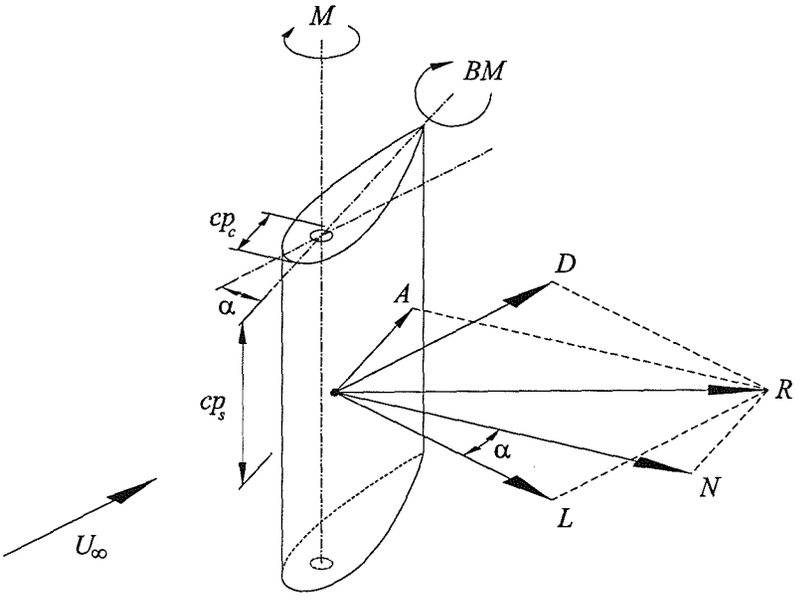

Figure 1: Rudder forces and moments

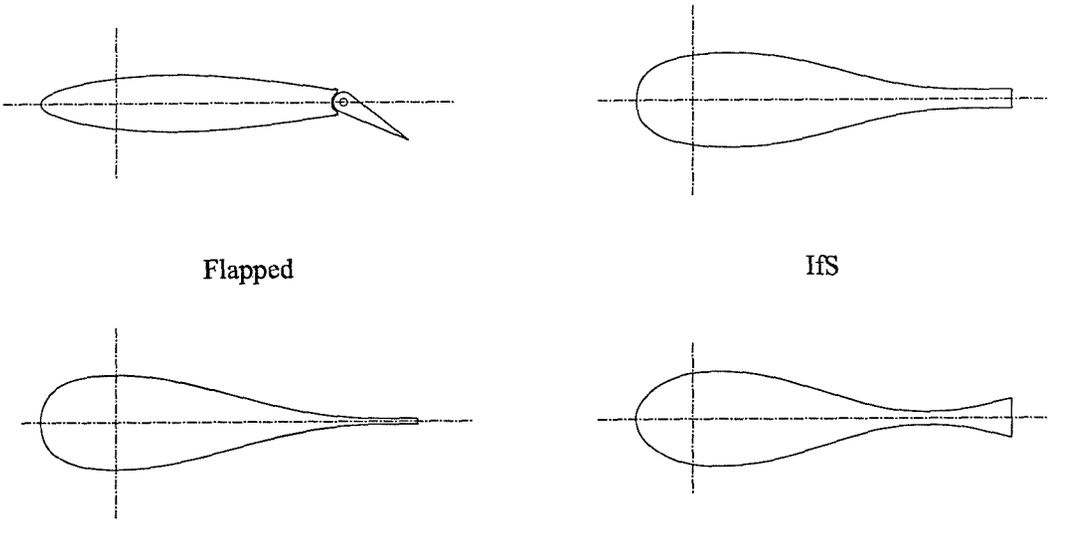

Figure 2: High lift rudder devices

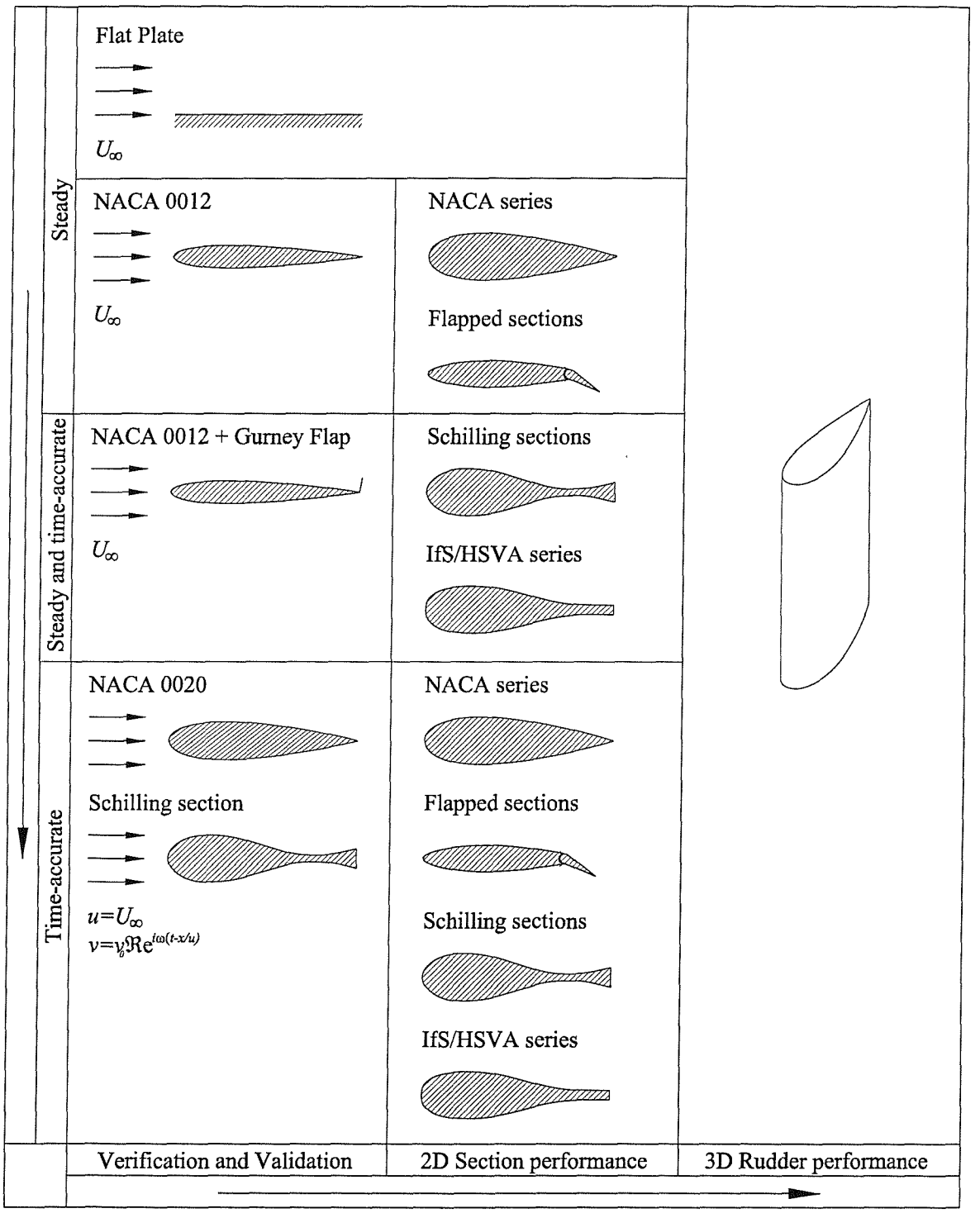

Figure 3: Rudder performance prediction

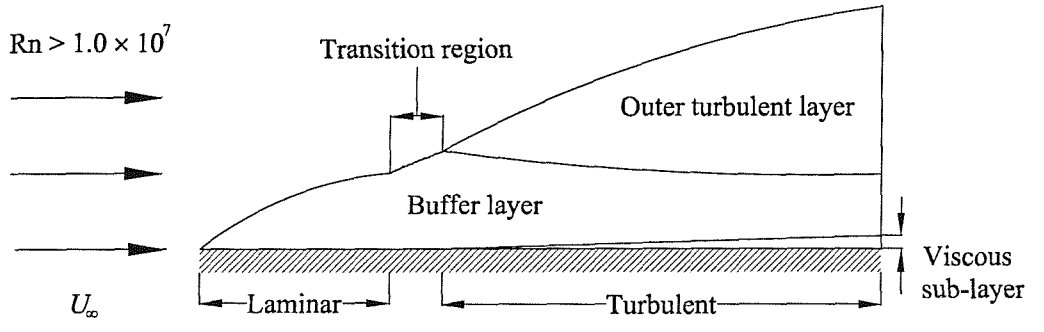

Figure 4: Flat plate boundary layer

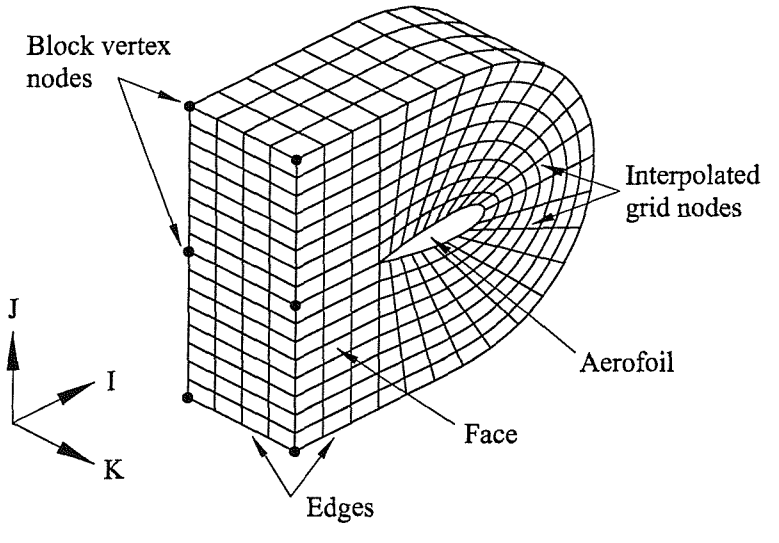

Figure 5: Aerofoil single block C-Grid

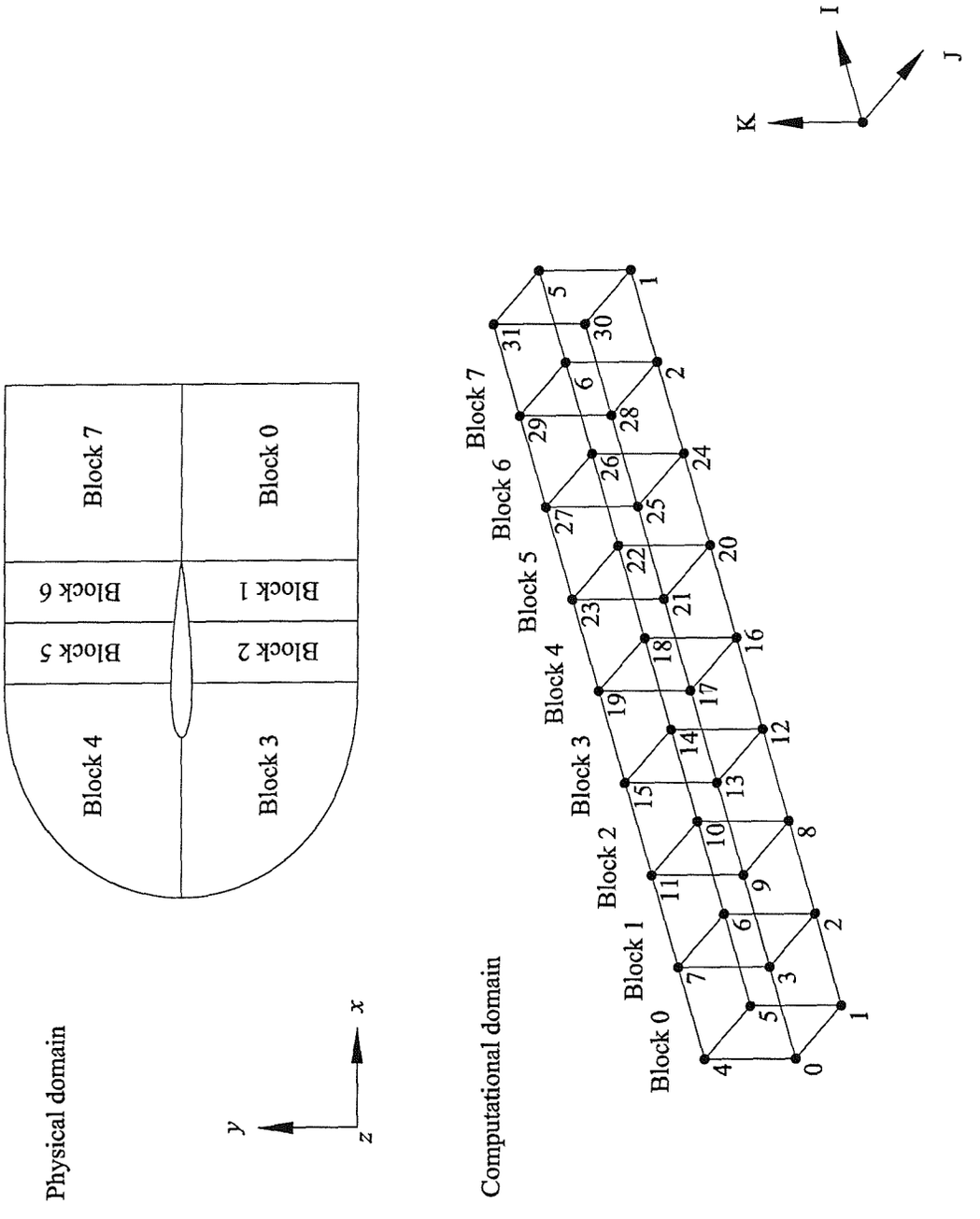

Figure 6: NACA 0012 & 0020 block structure

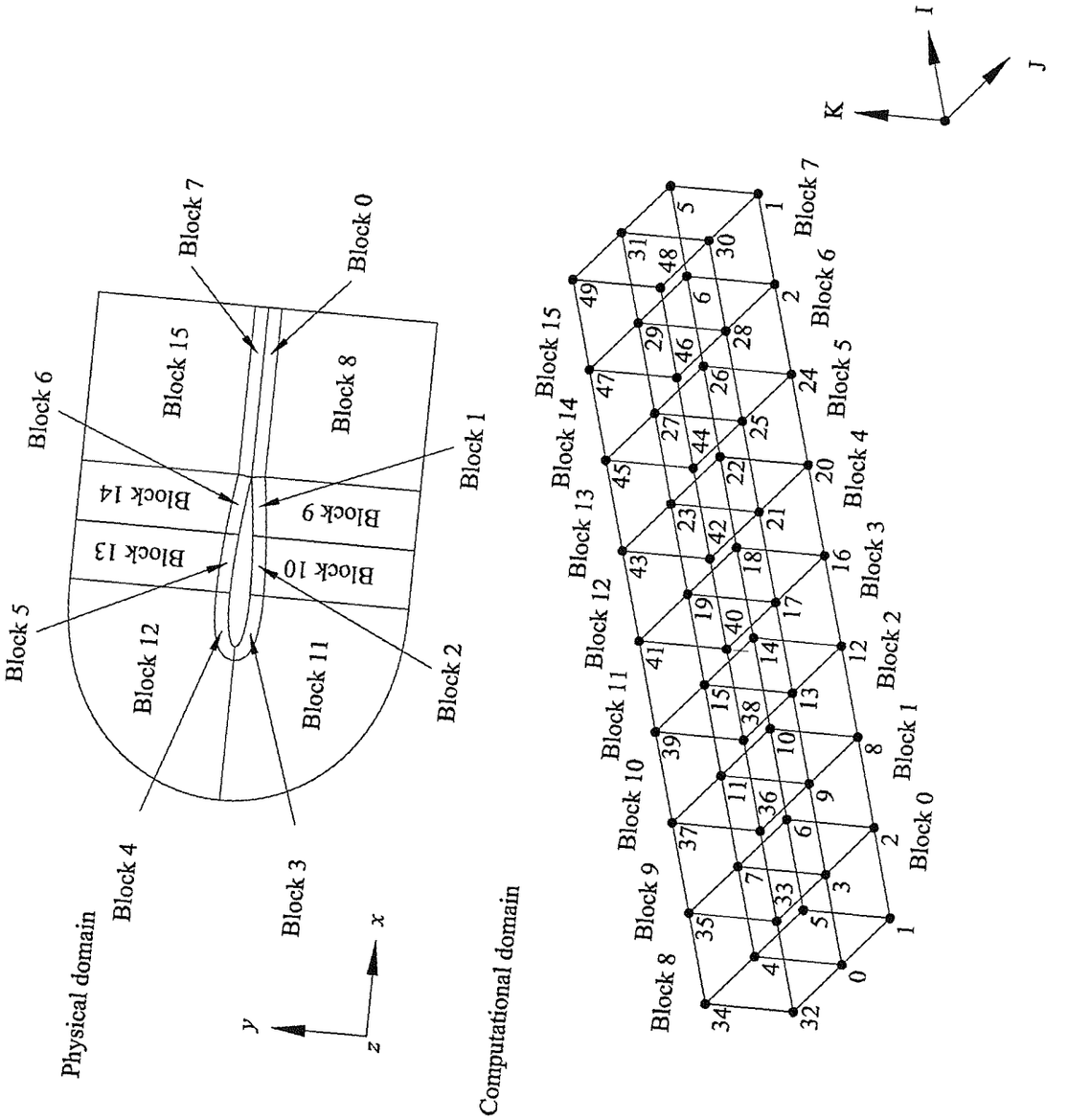

Figure 7: Gurney flapped NACA 0012 block structure

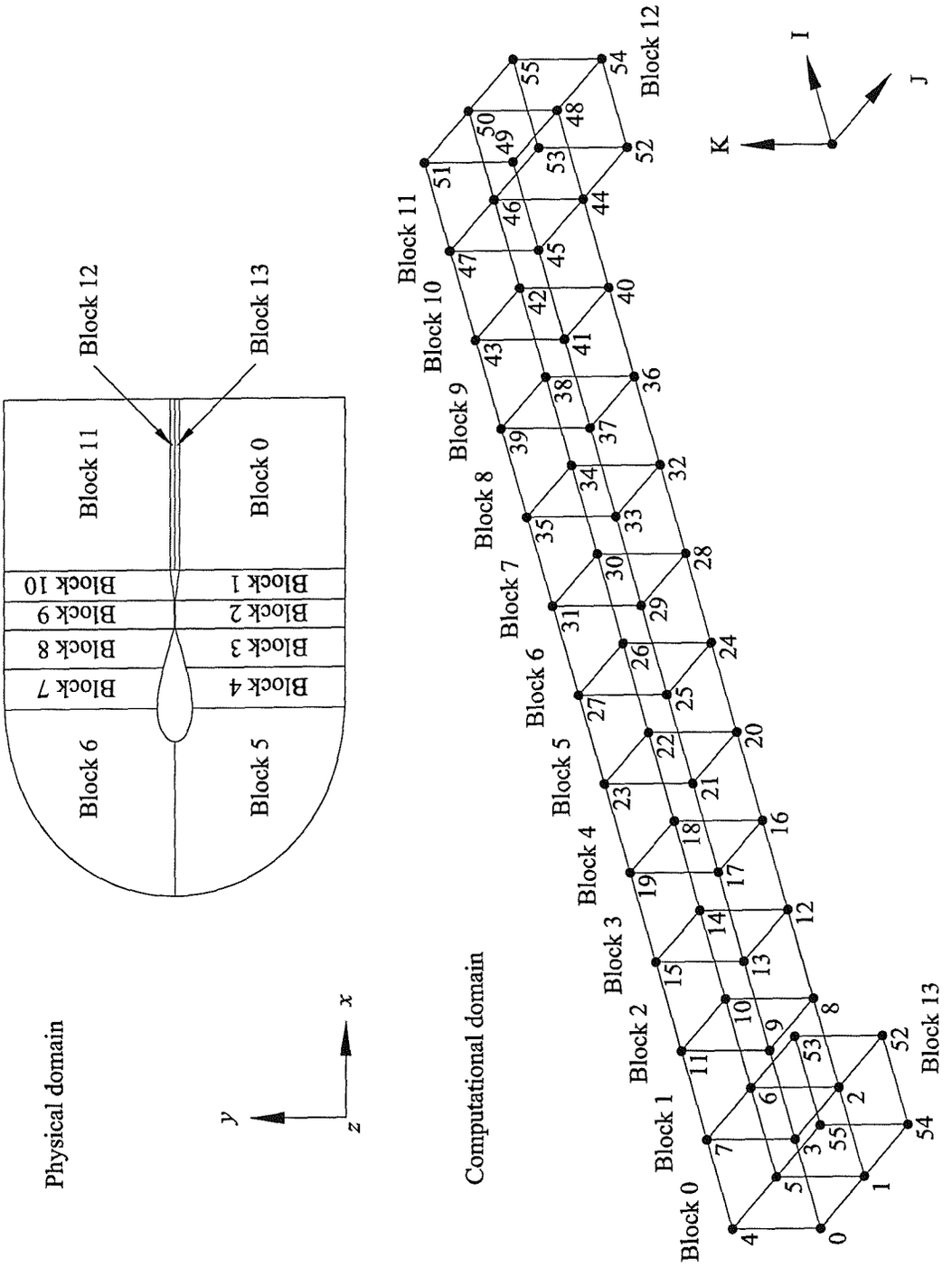

Figure 8: Schilling block structure

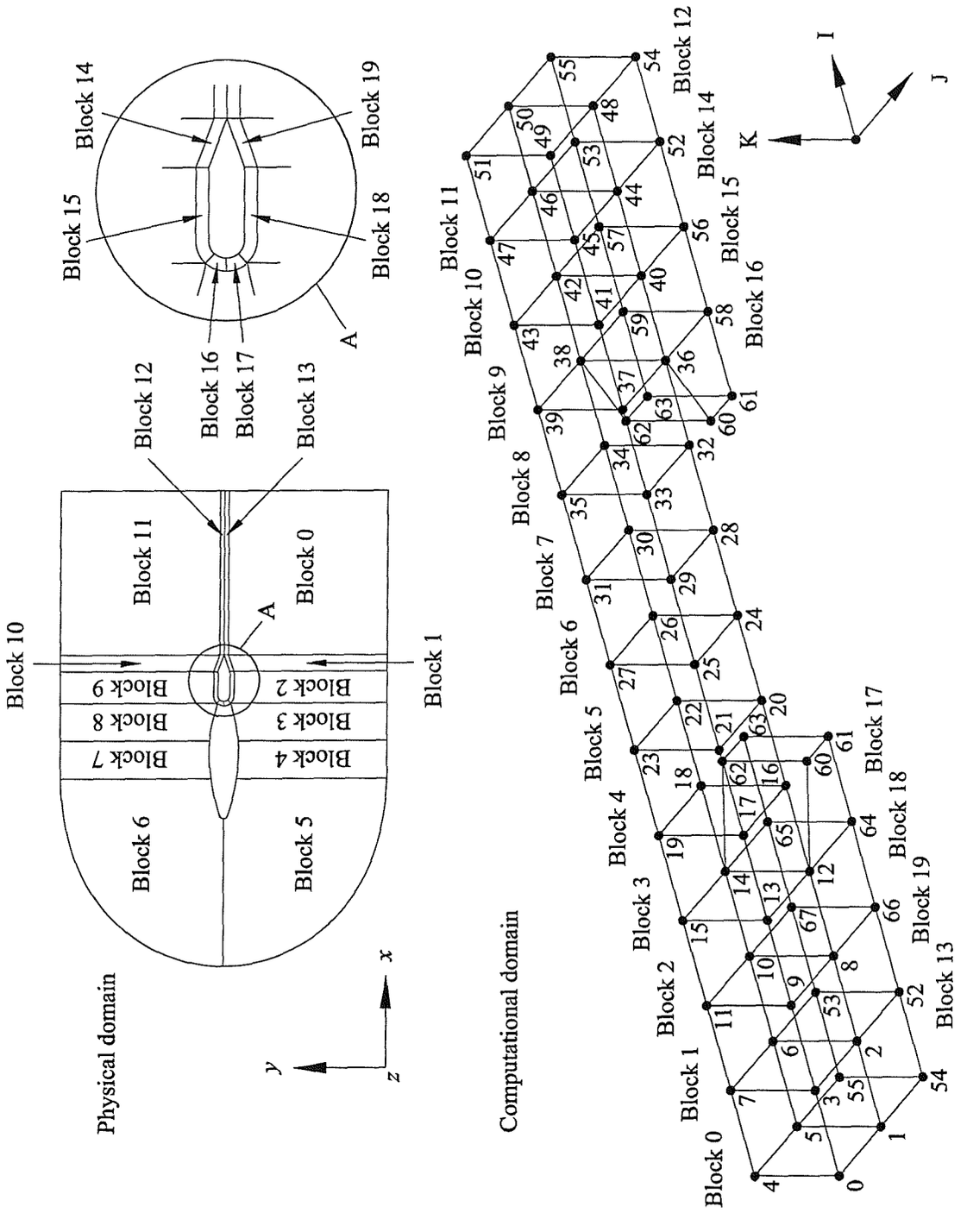

Figure 9: Flapped block structure

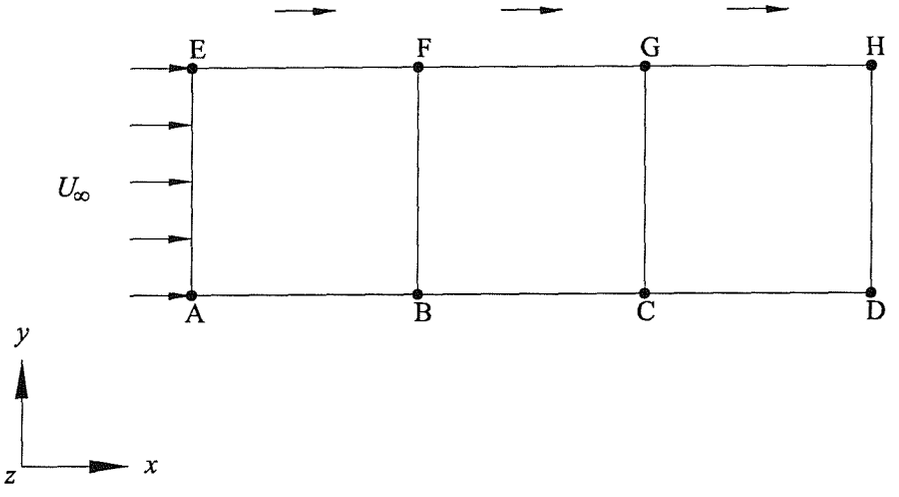

Figure 10: Flat plate boundary conditions

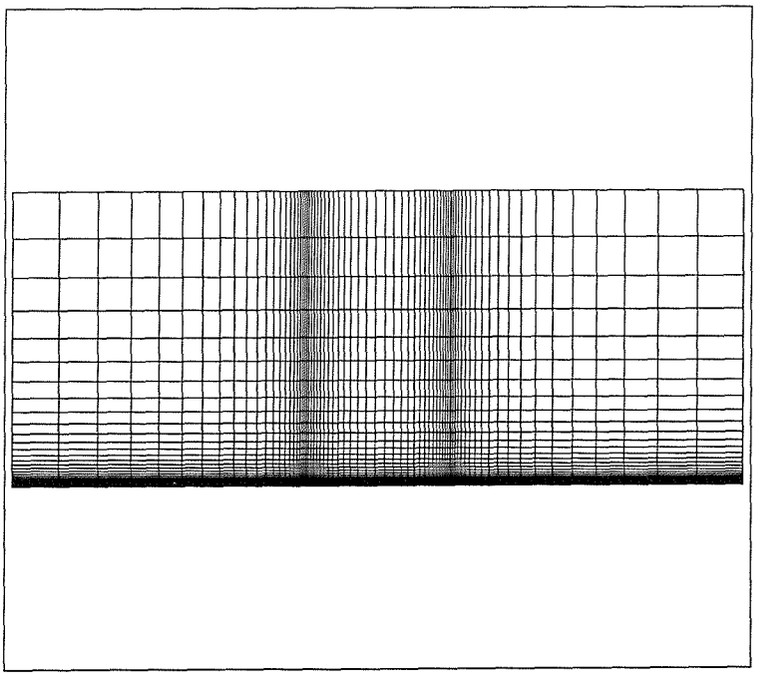

Figure 11: Flat plate grid

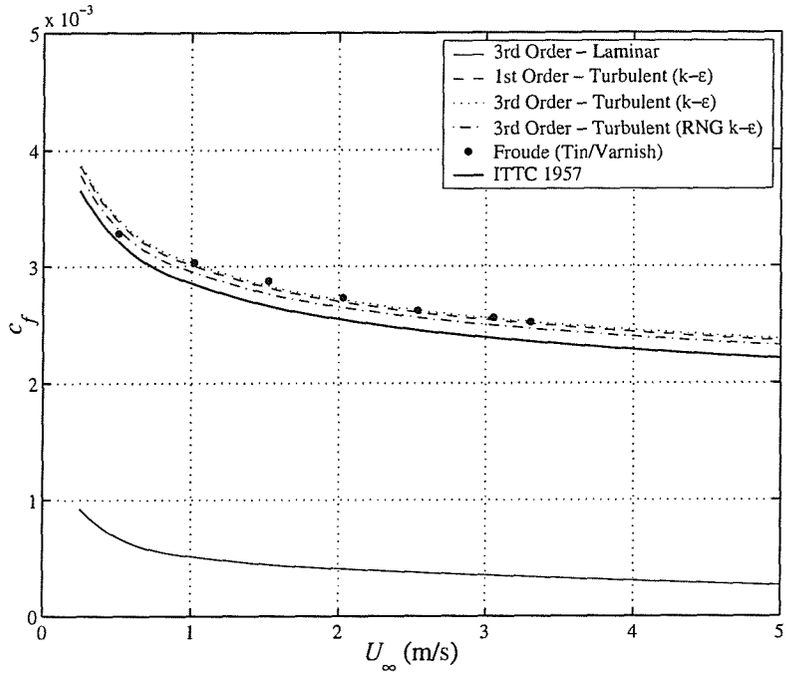

Figure 12: Skin friction line for 15.24 m flat plate

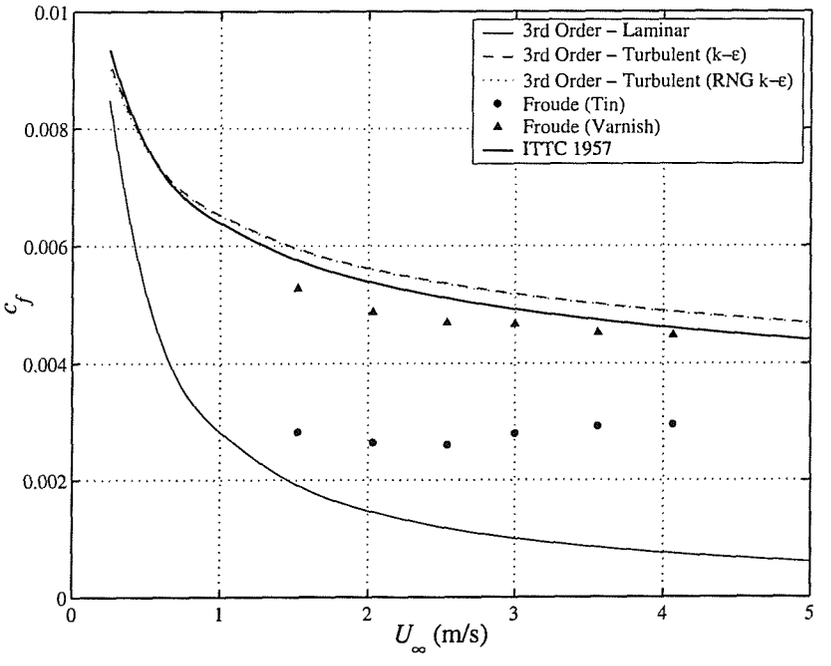

Figure 13: Skin friction line for 0.305 m flat plate

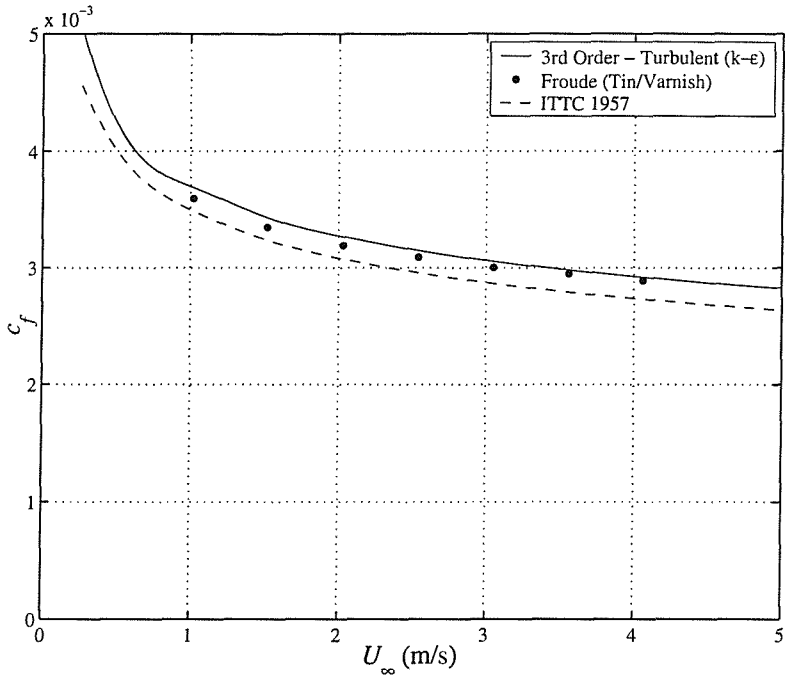

Figure 14: Skin friction line for 4.877 m flat plate

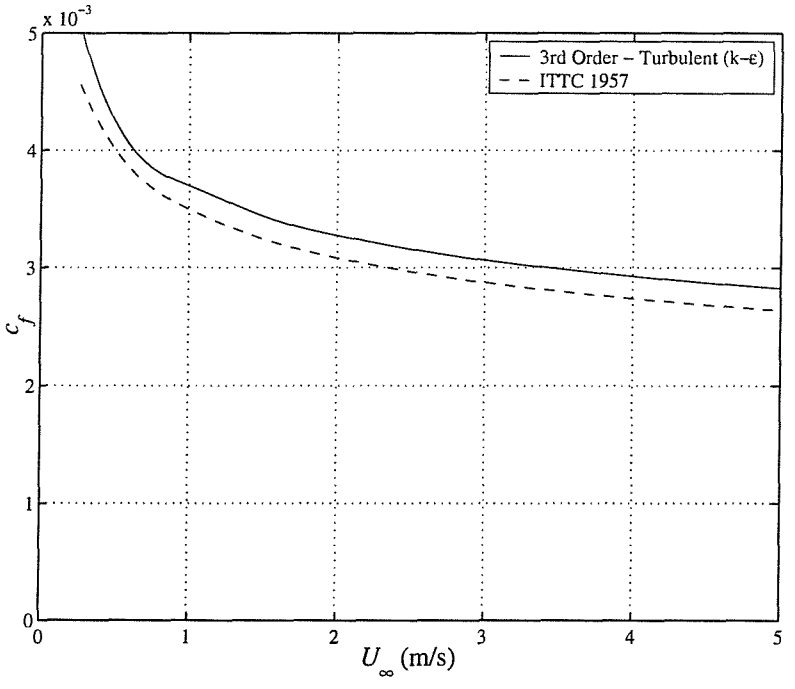

Figure 15: Skin friction line for 152.4 m flat plate

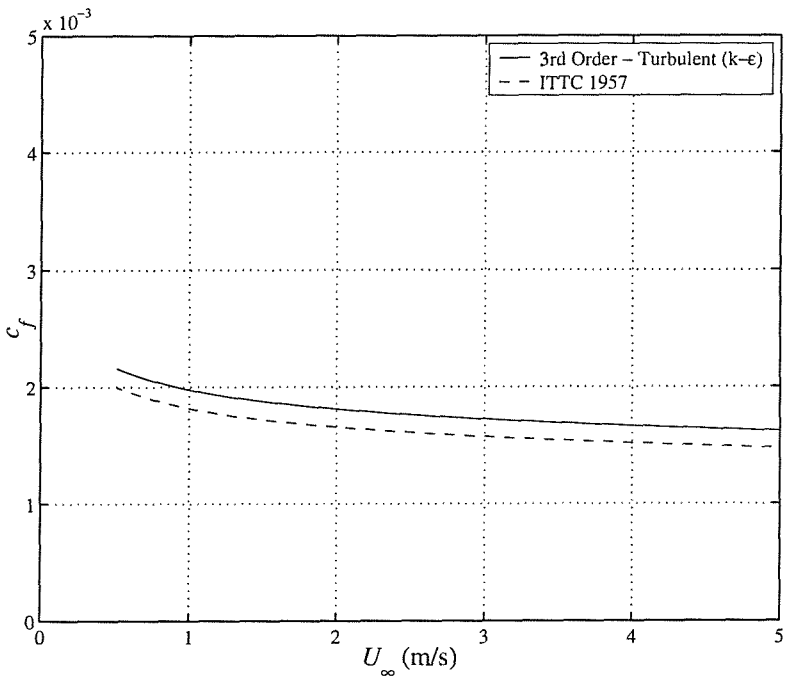

Figure 16: Skin friction line for 304.8 m flat plate

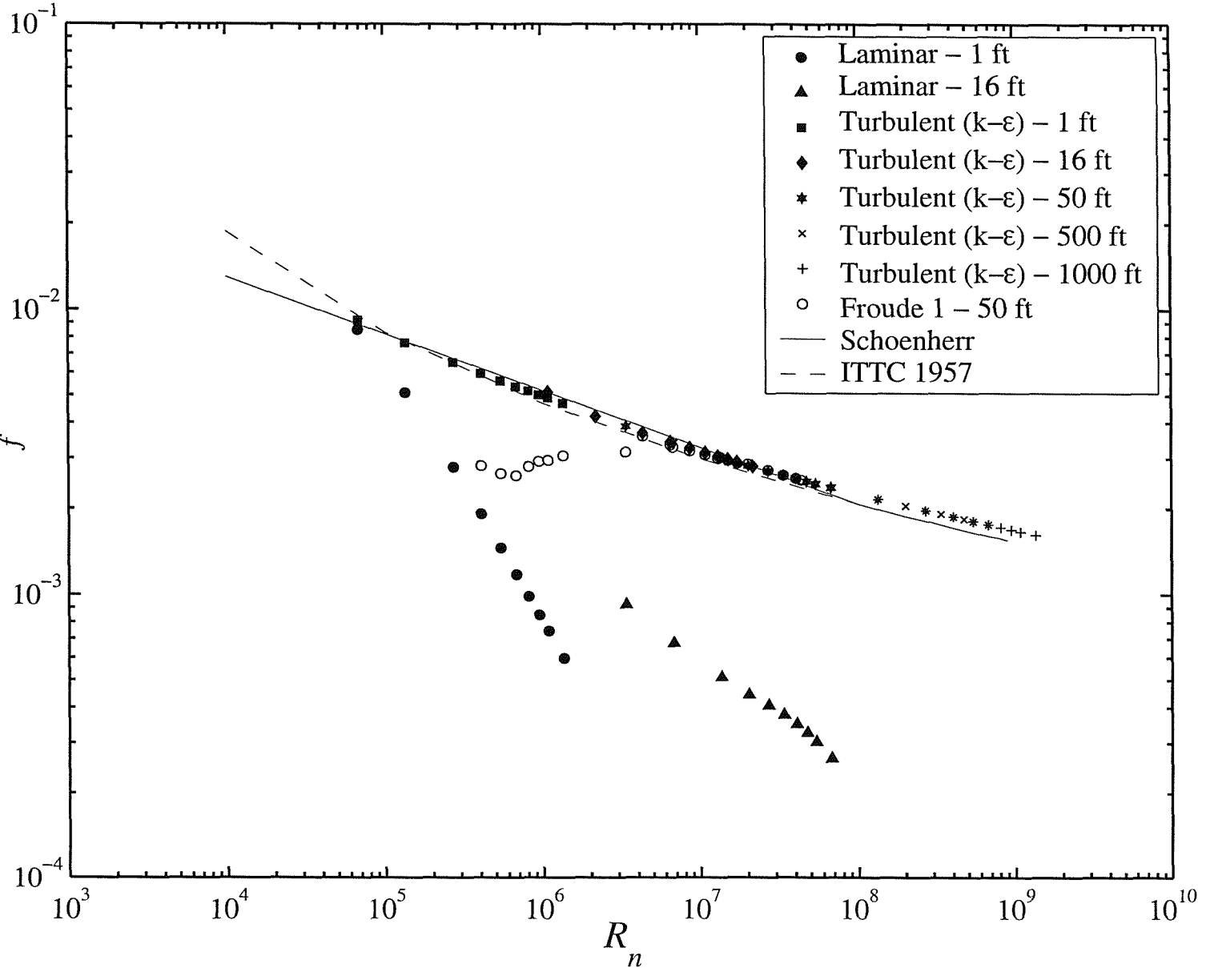

Figure 17: Schoenherr's log-log plot for skin friction

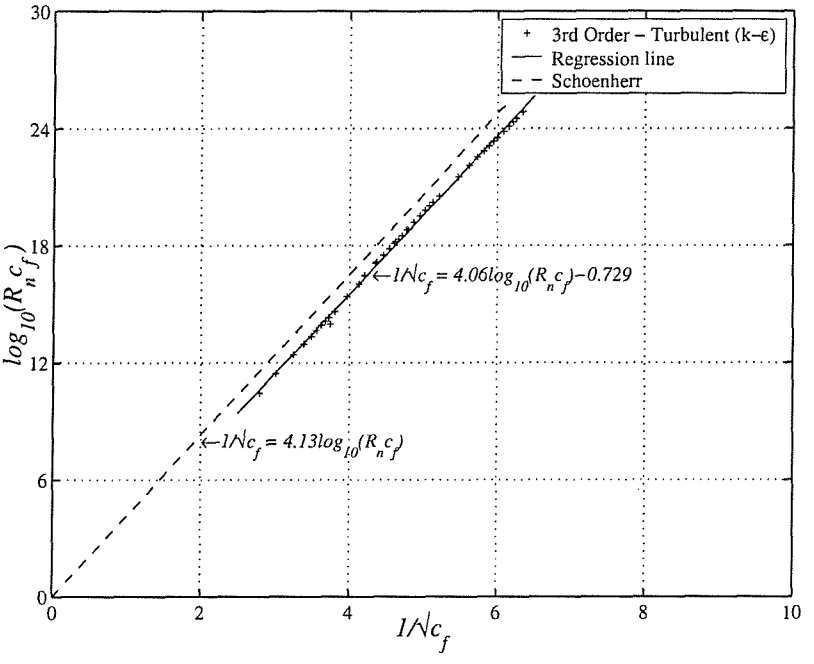

Figure 18: Prandtl logarithmic skin friction plot

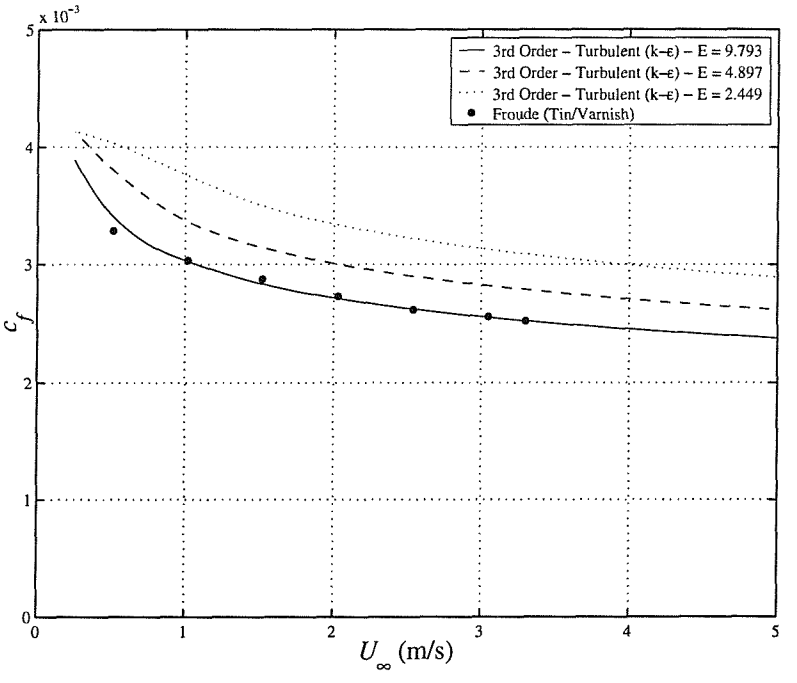

Figure 19: Variation of skin friction with log-layer constant for 15.25 m flat plate

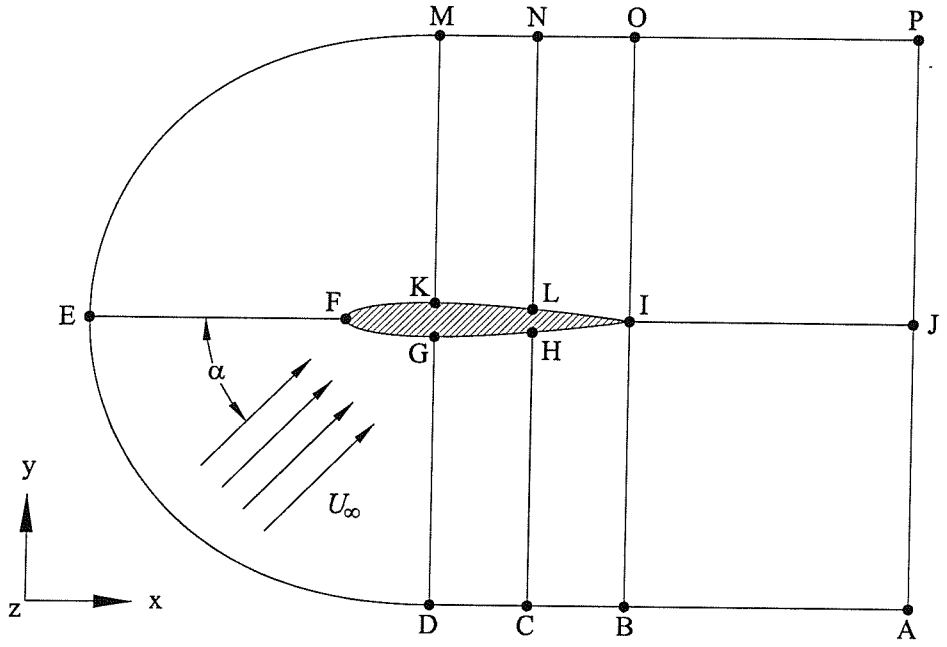

Figure 20: NACA 0012 & 0020 boundary conditions

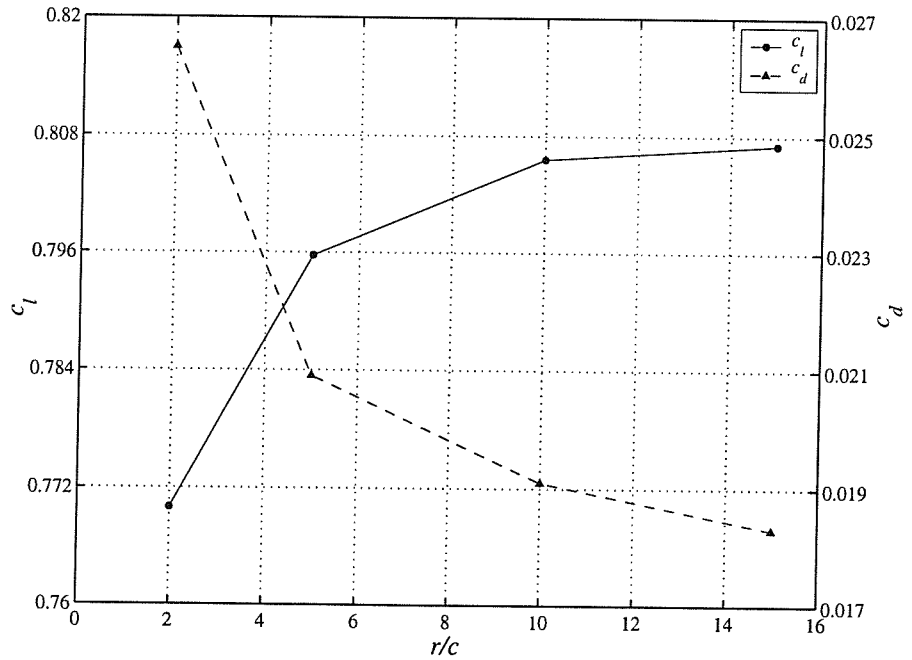

Figure 21: NACA 0012 boundary location study, $\alpha = 8$ deg, $R_n = 6.0 \times 10^6$

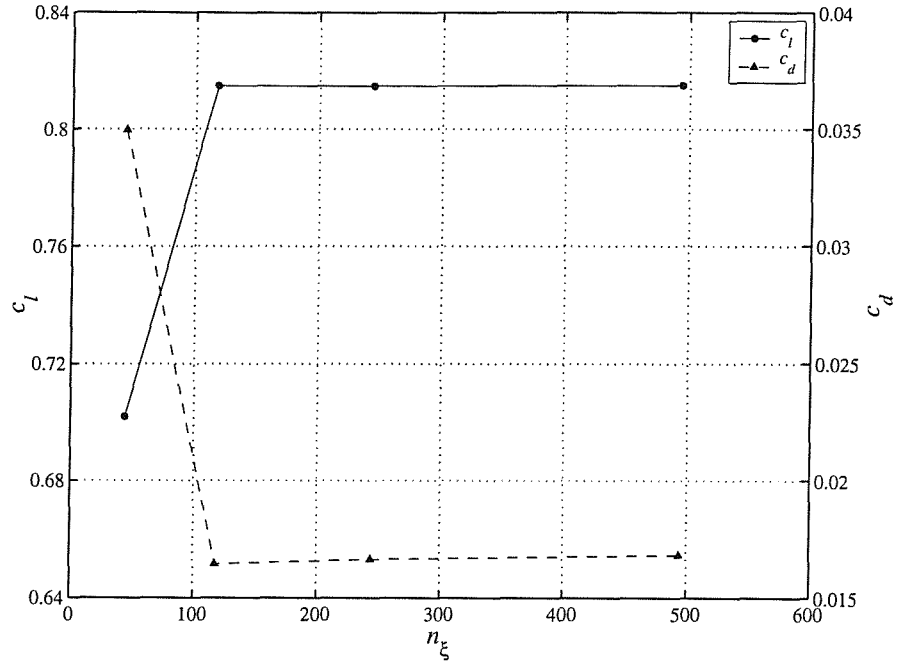

Figure 22: NACA 0012 chord-wise grid study, $\alpha = 8$ deg, $R_n = 6.0 \times 10^6$

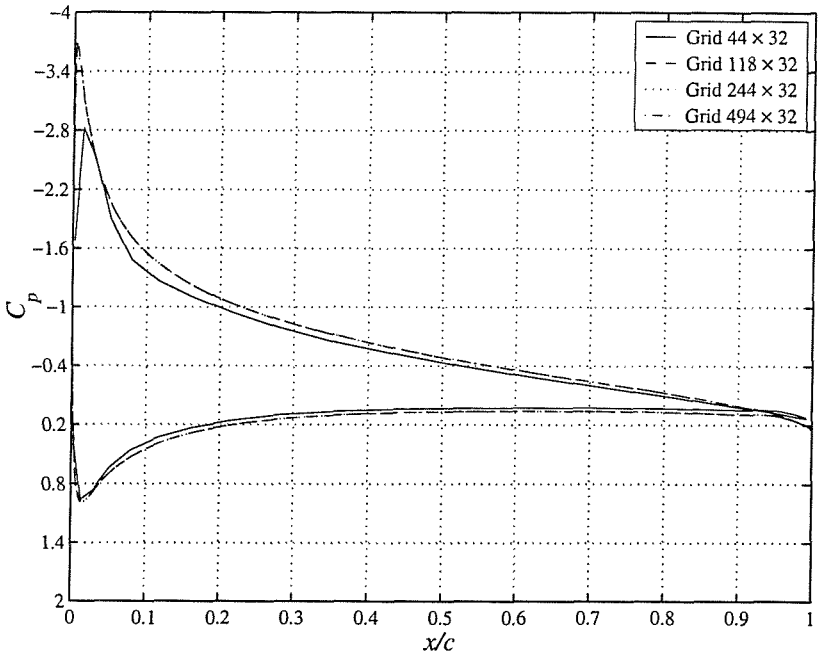

Figure 23: NACA 0012 chord-wise grid study C_p distribution, $\alpha = 8$ deg, $R_n = 6.0 \times 10^6$

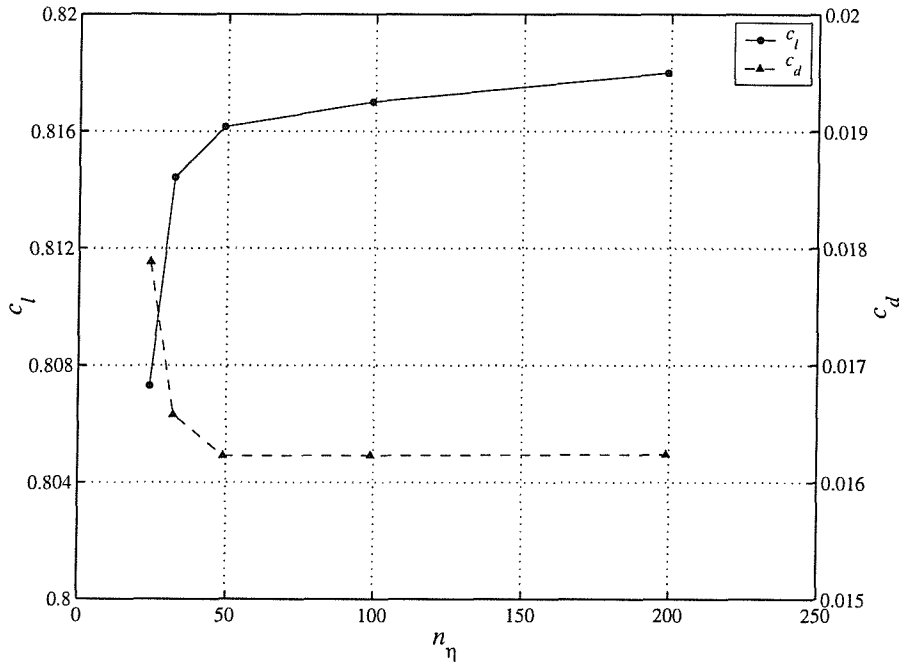

Figure 24: NACA 0012 pressure capture grid study, $\alpha =$ 8 deg, $R_n = 6.0 \times 10^6$

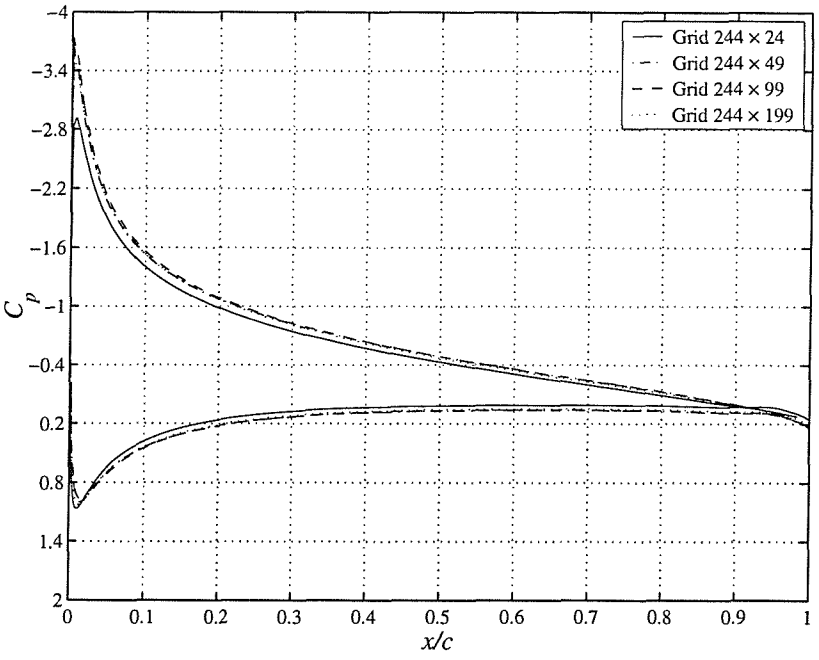

Figure 25: NACA 0012 pressure capture grid study C_p distribution, $\alpha = 8$ deg, $R_n = 6.0 \times 10^6$

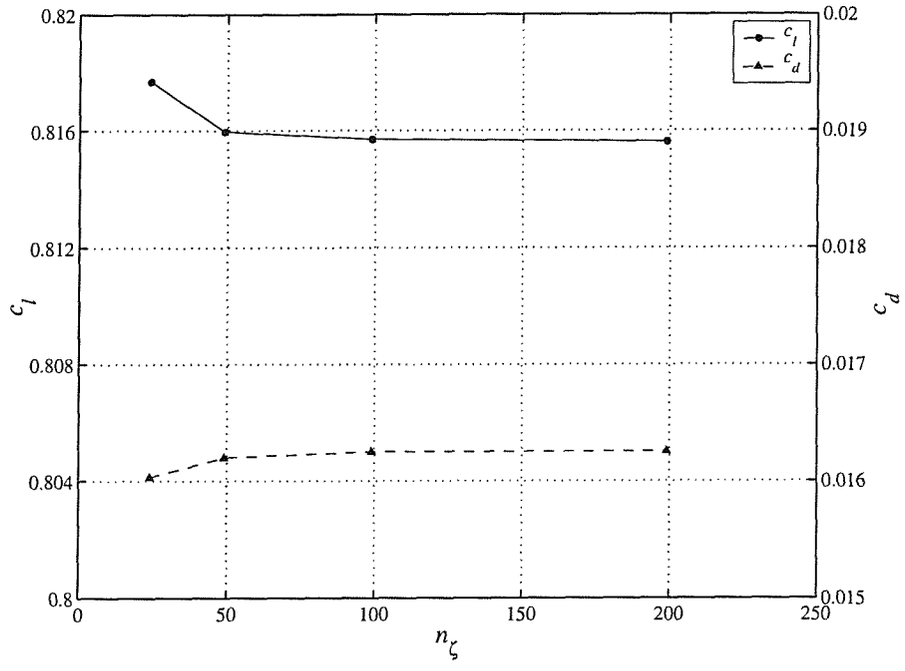

Figure 26: NACA 0012 wake grid study, $\alpha = 8$ deg, $R_n = 6.0 \times 10^6$

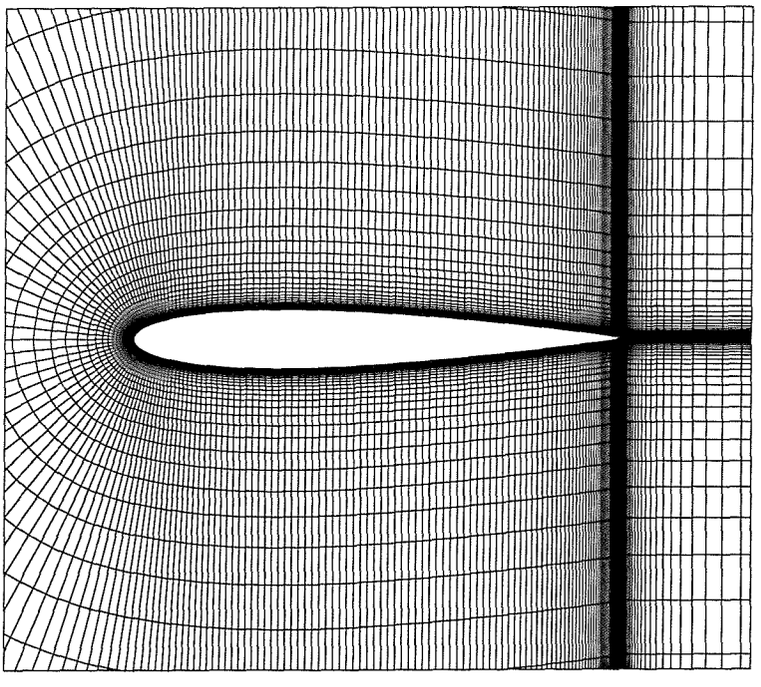

Figure 27: NACA 0012 final Grid

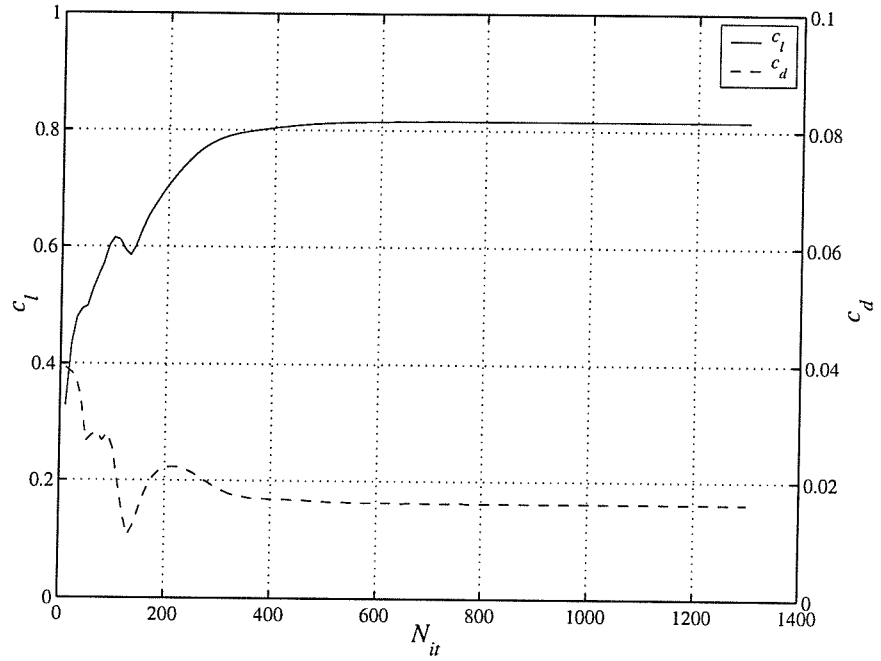

Figure 28: NACA 0012 c_l and c_d convergence history, $\alpha = 8$ deg, $R_n = 6.0 \times 10^6$

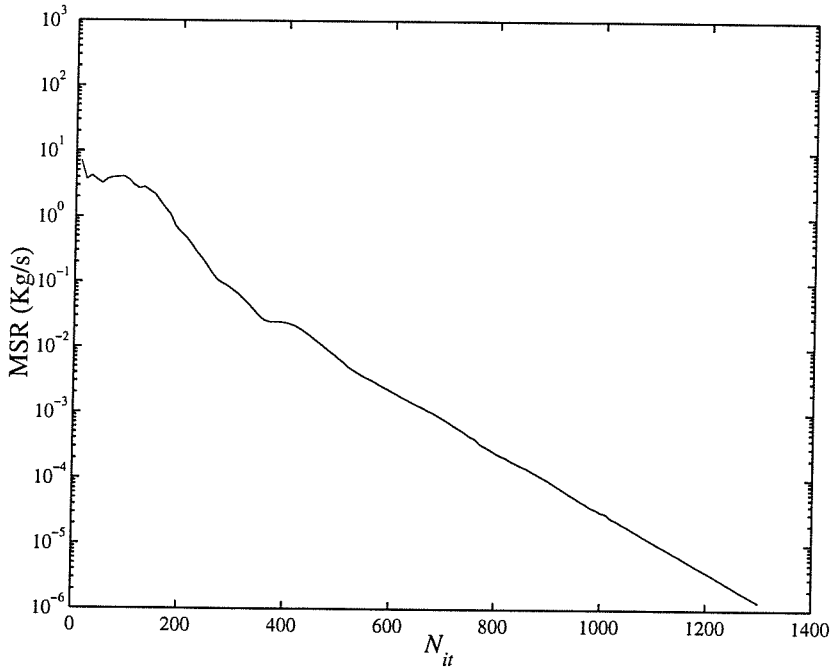

Figure 29: NACA 0012 MSR convergence history, $\alpha = 8$ deg, $R_n = 6.0 \times 10^6$

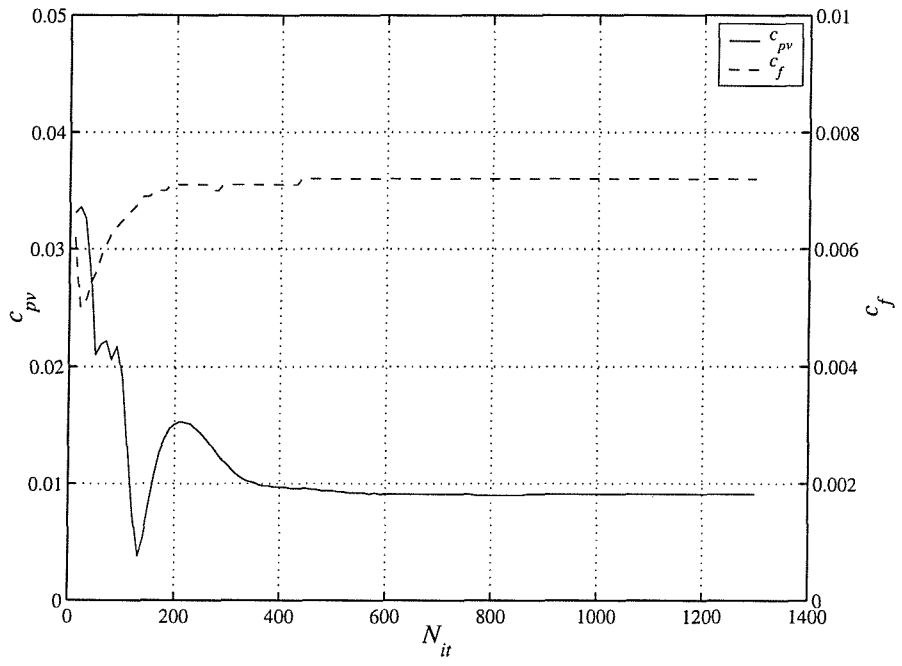

Figure 30: NACA 0012 c_f and c_{pv} convergence history, $\alpha = 8$ deg, $R_n = 6.0 \times 10^6$

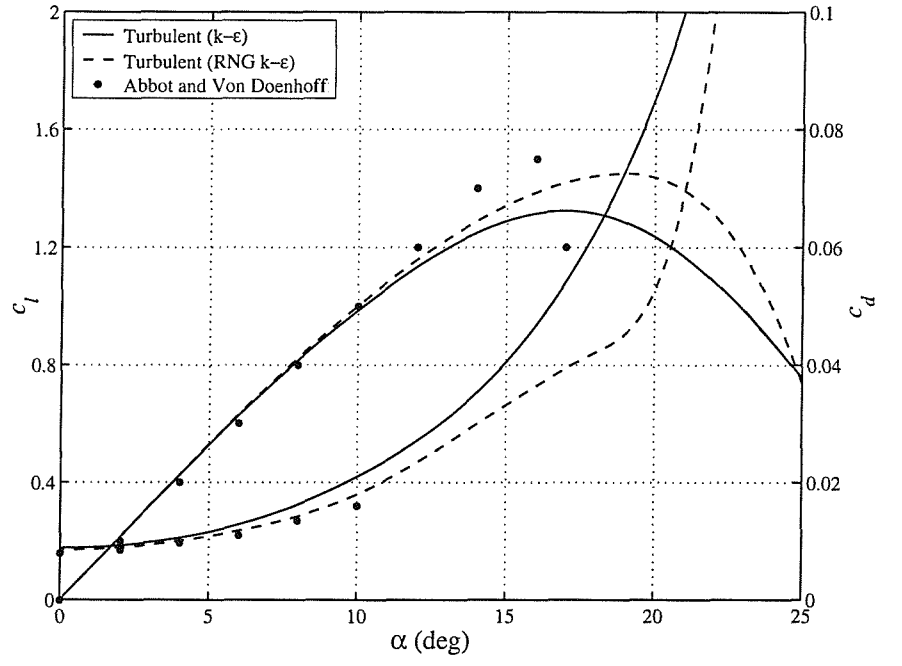

Figure 31: NACA 0012 performance, $R_n = 6.0 \times 10^6$

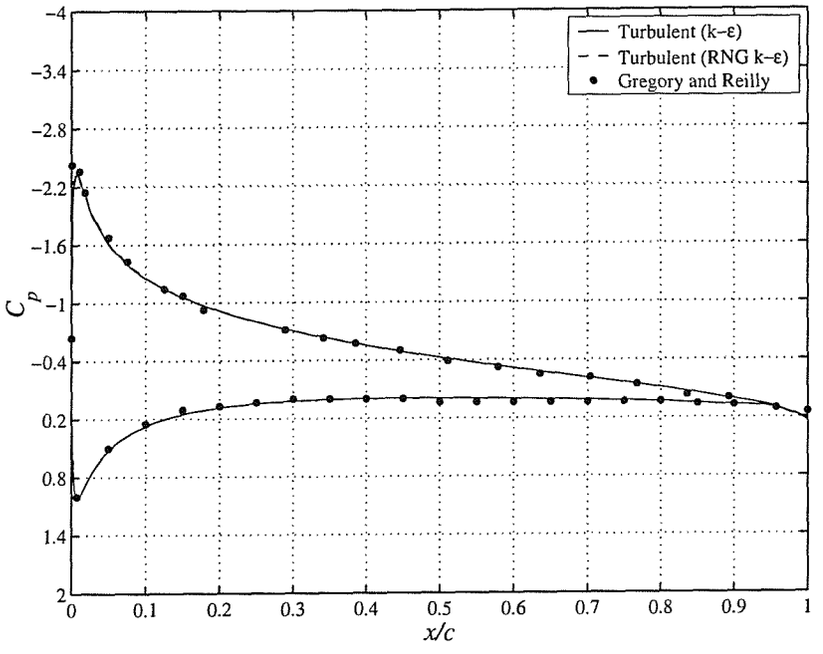

Figure 32: NACA 0012 Cp distribution, $\alpha = 6$ deg, $R_n = 2.88 \times 10^6$

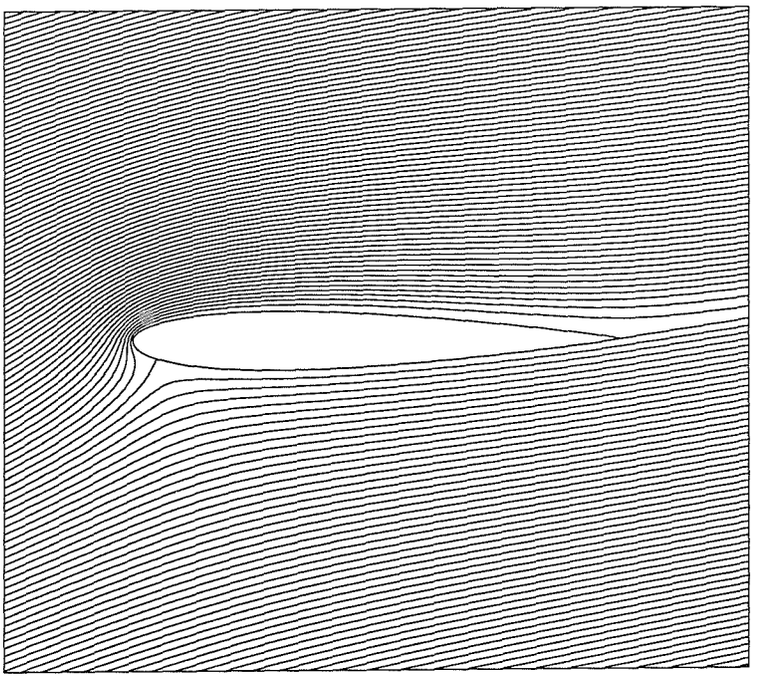

Figure 33: NACA 0012 streamlines, $\alpha = 15$ deg, $R_n = 6.0 \times 10^6$

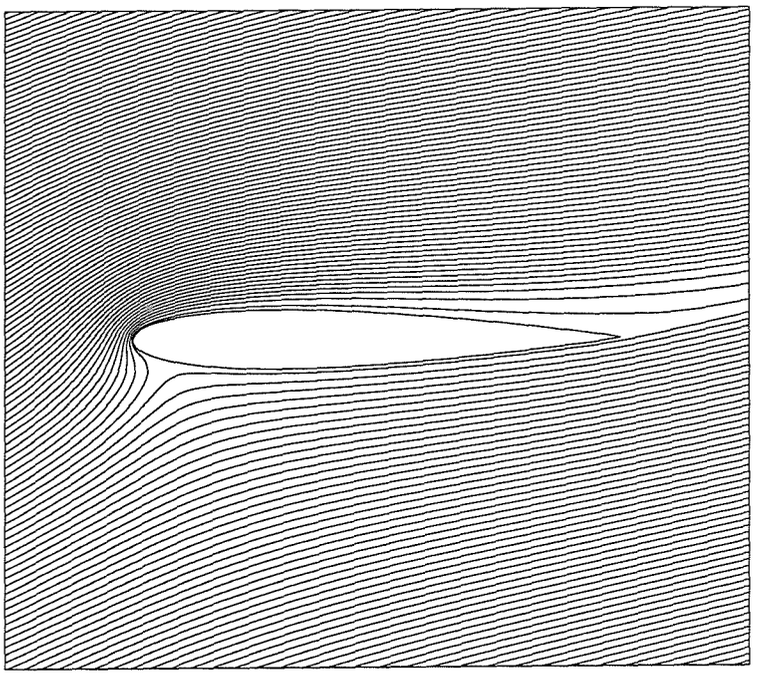

Figure 34: NACA 0012 streamlines, $\alpha = 18$ deg, $R_n = 6.0 \times 10^6$

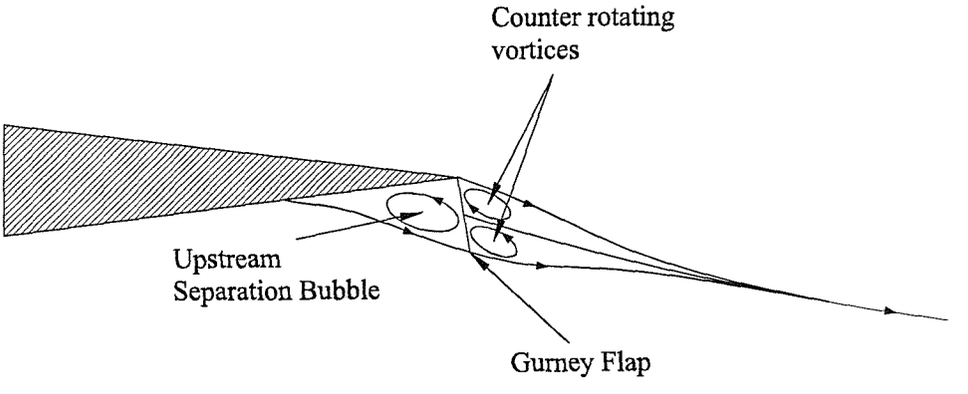

Figure 35: Typical Gurney showing Liebeck's [97] hypothesised flow downstream

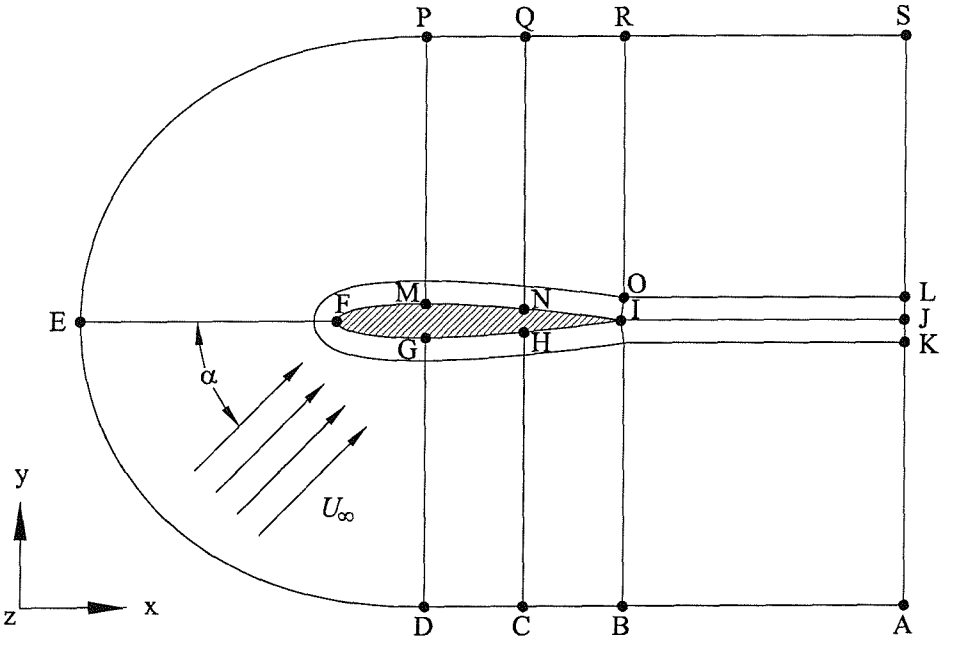

Figure 36: Gurney flapped NACA 0012 boundary conditions

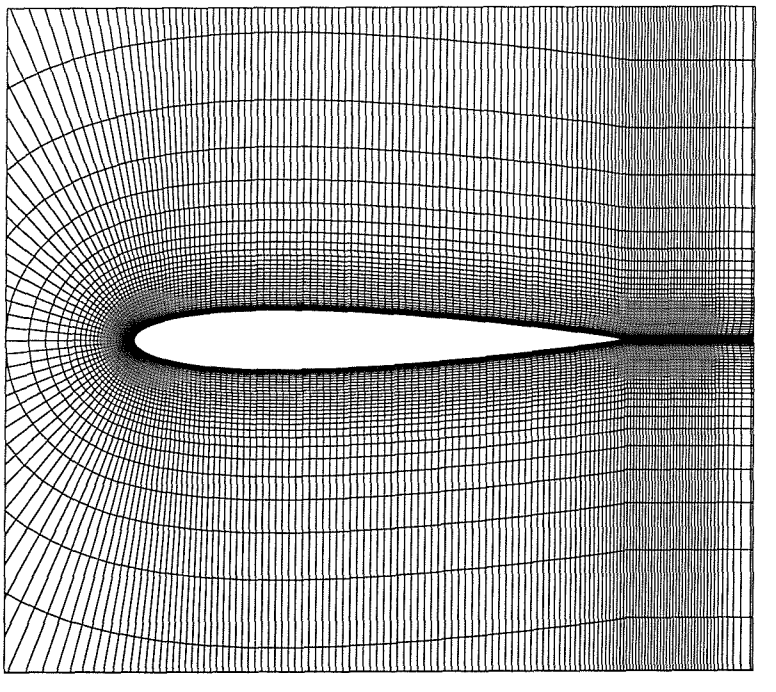

Figure 37: 4% Gurney fine grid

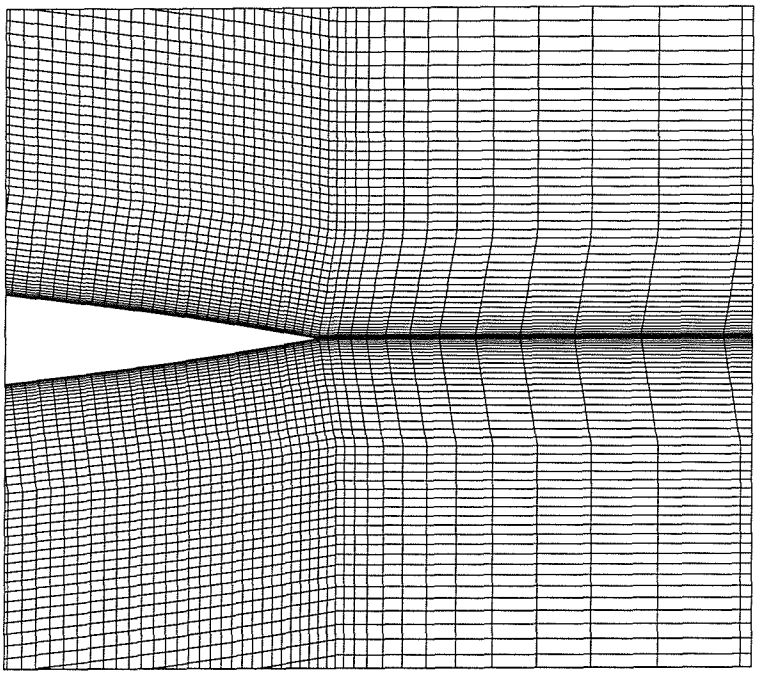

Figure 38: 4% Gurney coarse grid wake region

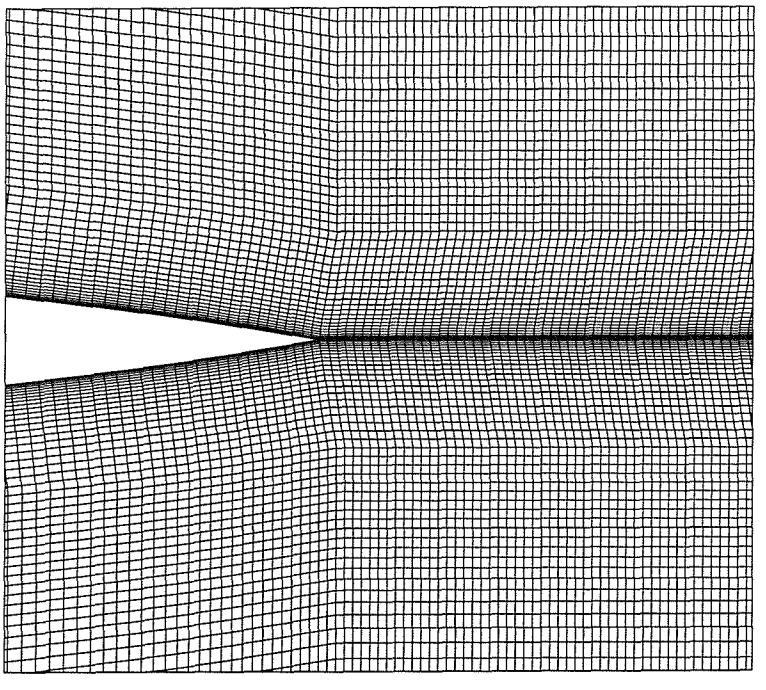

Figure 39: 4% Gurney fine grid wake region

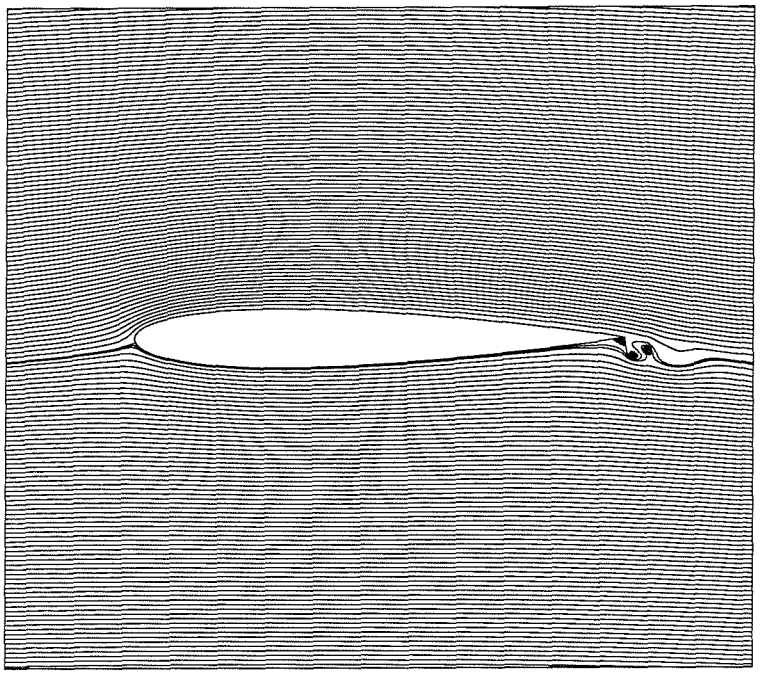

Figure 40: 4% Gurney under-converged steady state fine grid streamlines, $\alpha = 0$ deg, $R_n = 0.85 \times 10^6$

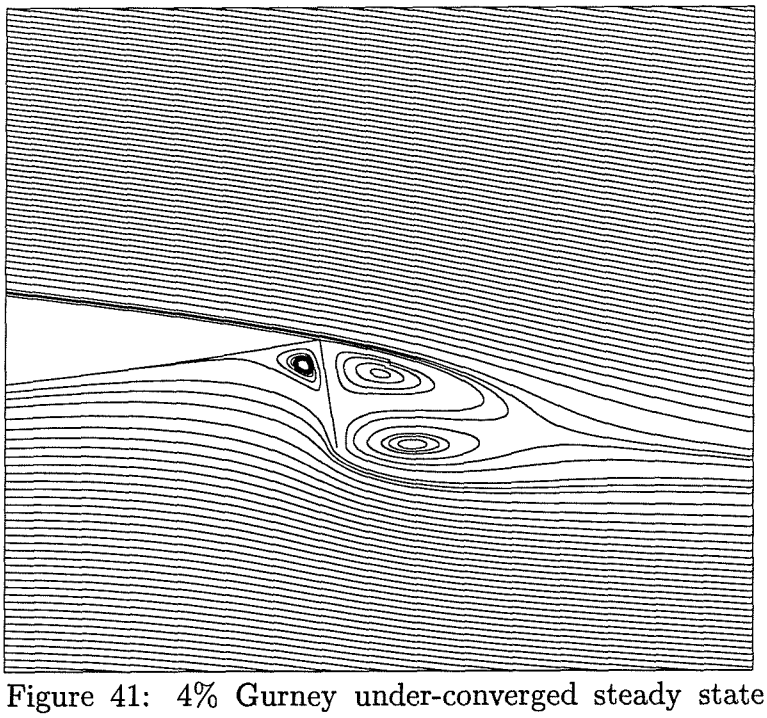

Figure 41: 4% Gurney under-converged steady state coarse grid wake region streamlines, $\alpha = 0$ deg, $R_n = 0.85 \times 10^6$

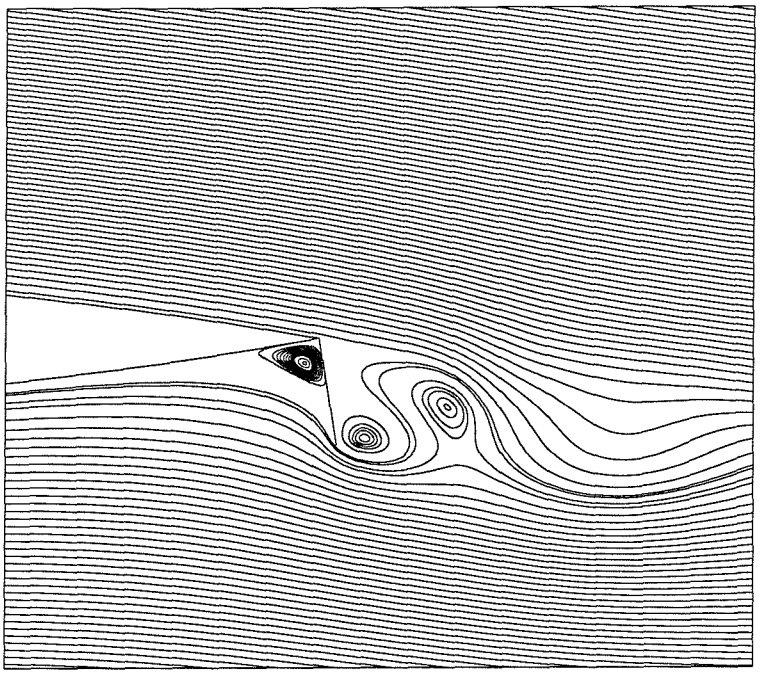

Figure 42: 4% Gurney under-converged steady state fine grid wake region streamlines, $\alpha = 0$ deg, $R_n = 0.85 \times 10^6$

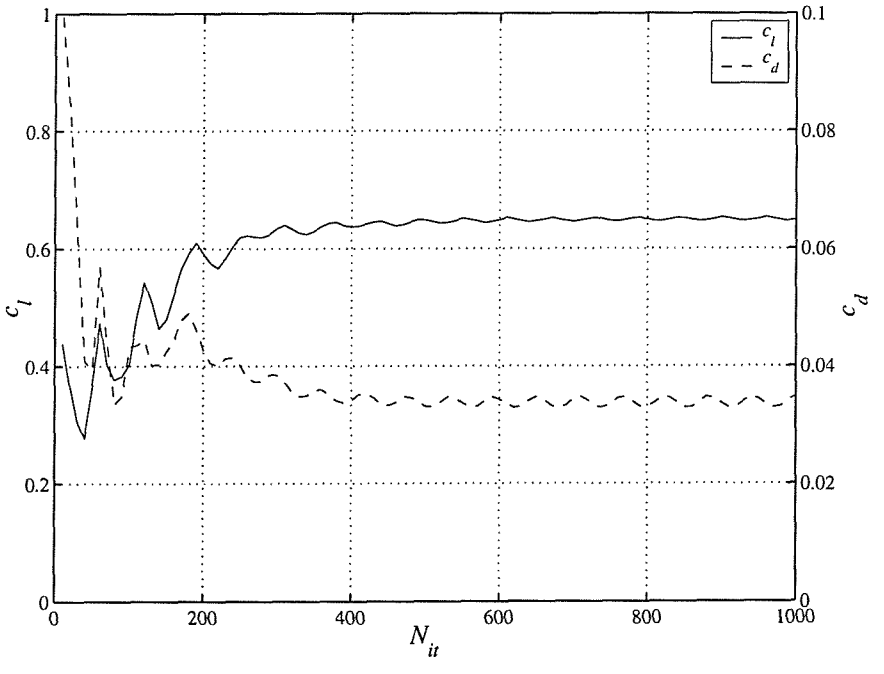

Figure 43: 4% Gurney under-converged steady state c_l and c_d convergence history, $\alpha = 0$ deg, $R_n = 0.85 \times 10^6$

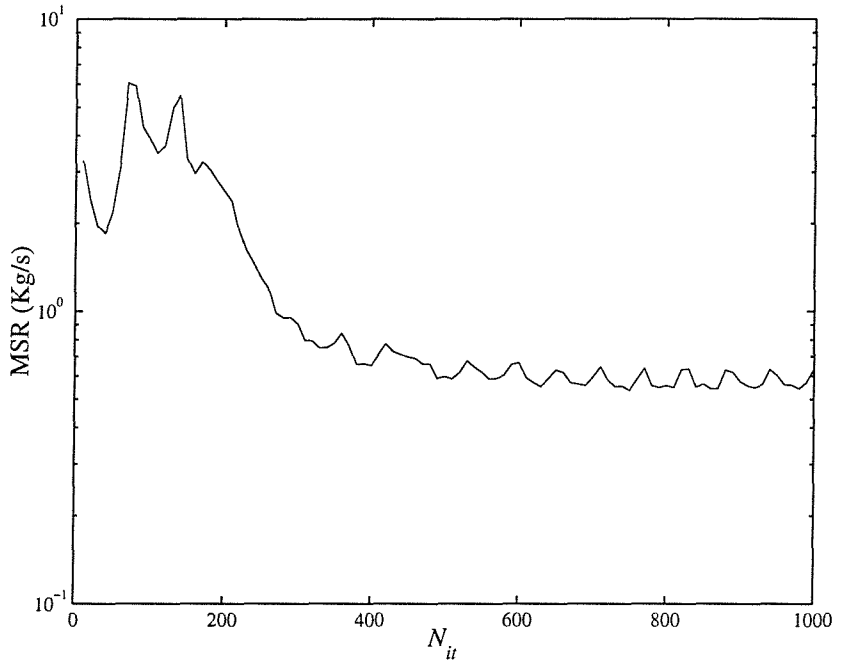

Figure 44: 4% Gurney under-converged steady state MSR convergence history, $\alpha = 0$ deg, $R_n = 0.85 \times 10^6$

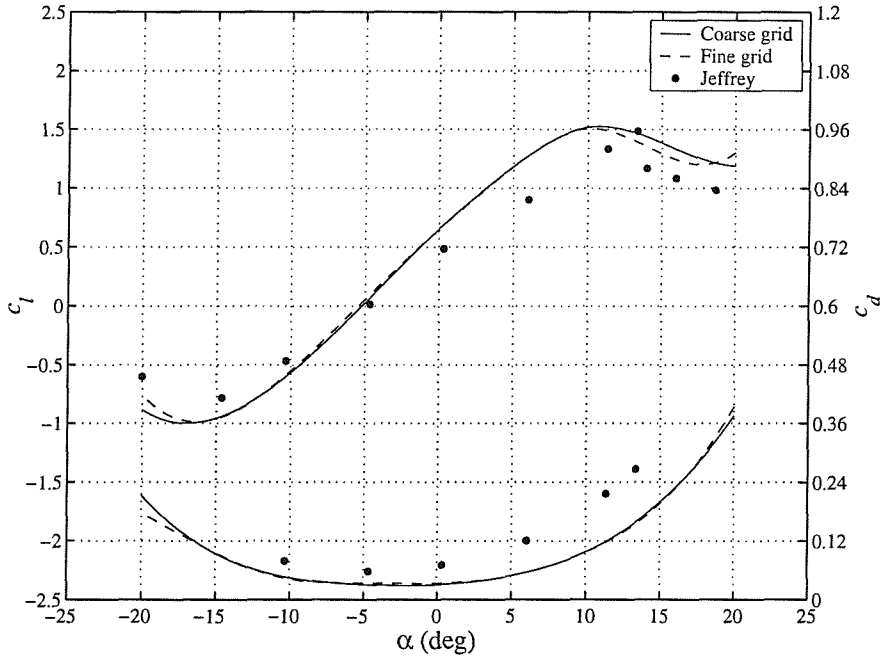

Figure 45: 4% Gurney under-converged steady state performance, $R_n = 0.85 \times 10^6$

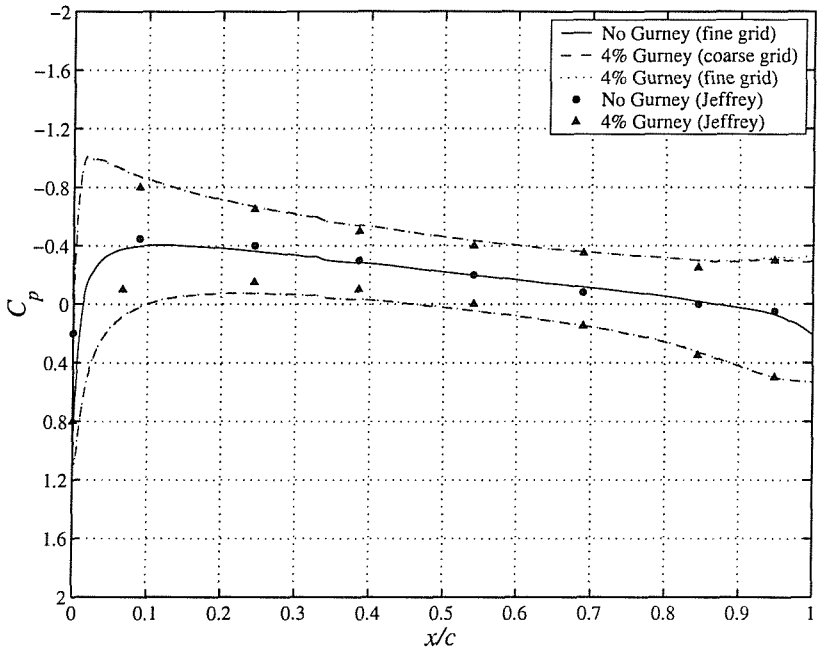

Figure 46: 4% Gurney under-converged steady state Cp distribution, $\alpha = 0$ deg, $R_n = 0.85 \times 10^6$

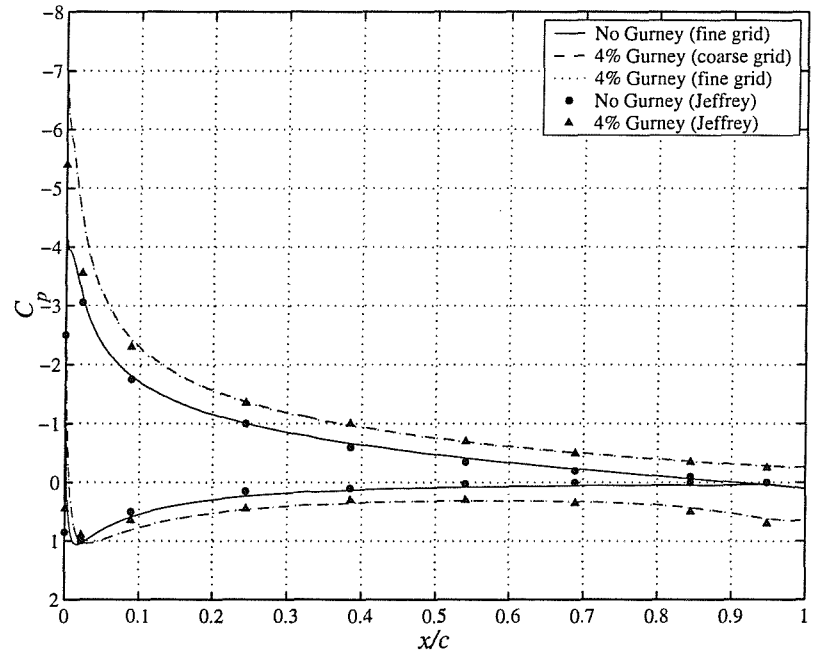

Figure 47: 4% Gurney under-converged steady state Cp distribution, $\alpha = 10$ deg, $R_n = 0.85 \times 10^6$

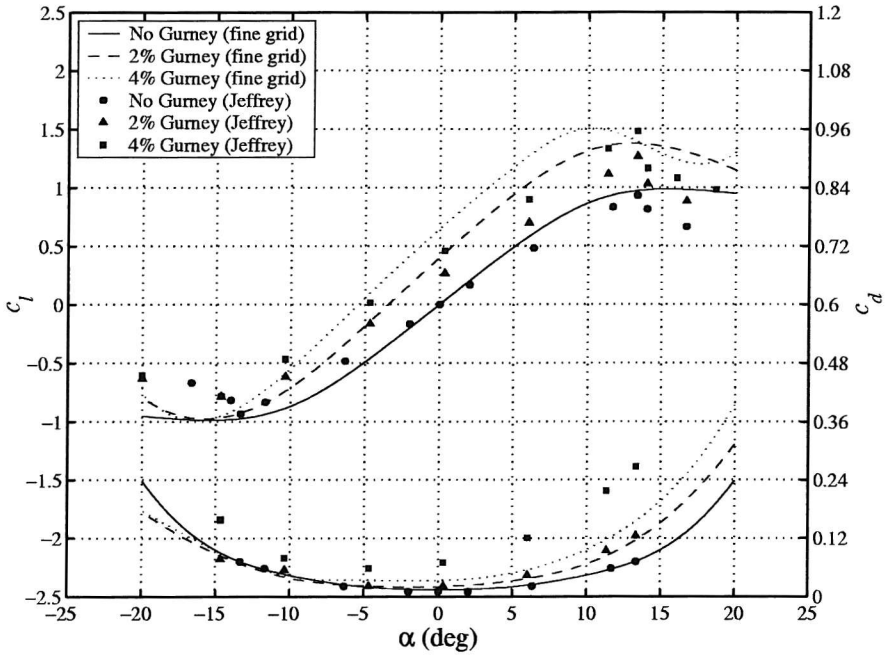

Figure 48: 2 and 4% Gurney under-converged steady state performance, $R_n = 0.85 \times 10^6$

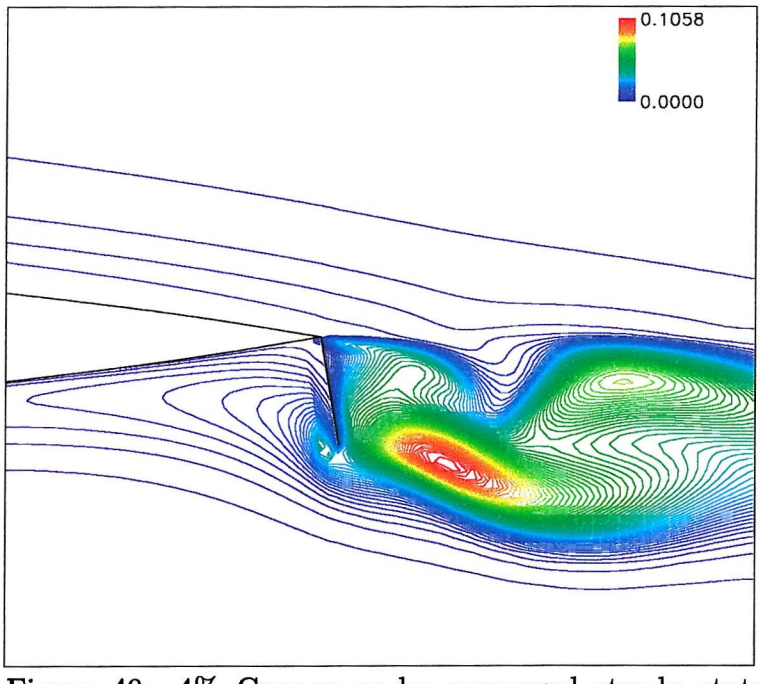

Figure 49: 4% Gurney under-converged steady state Reynolds stresses, $\overline{u'^2}/U_\infty^2 = \overline{v'^2}/U_\infty^2$, $\alpha = 0$ deg, $R_n = 0.85 \times 10^6$

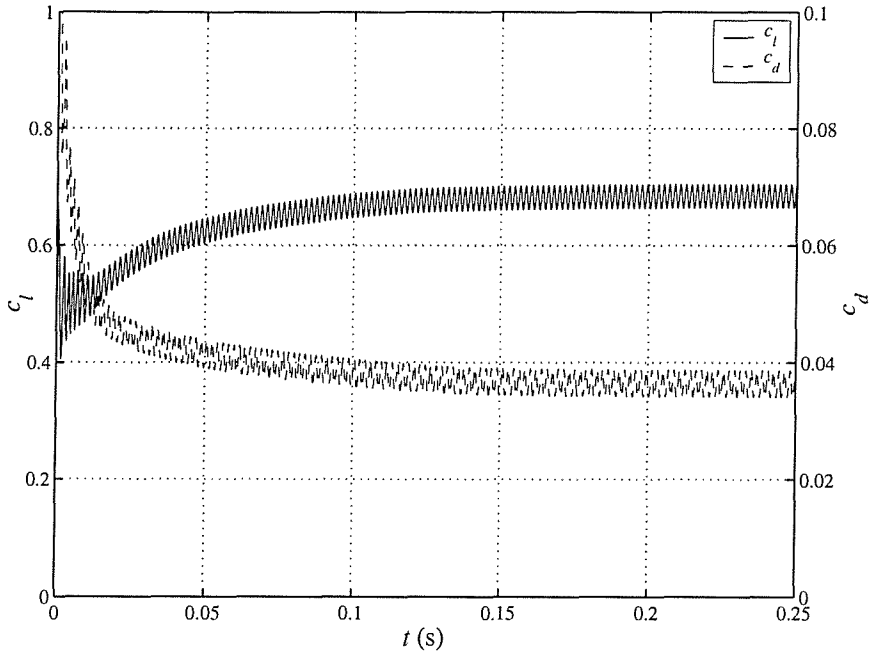

Figure 50: 4% Gurney time-accurate force evolution, $\alpha = 0$ deg, $\Delta t = 0.000025$ s, $R_n = 0.85 \times 10^6$

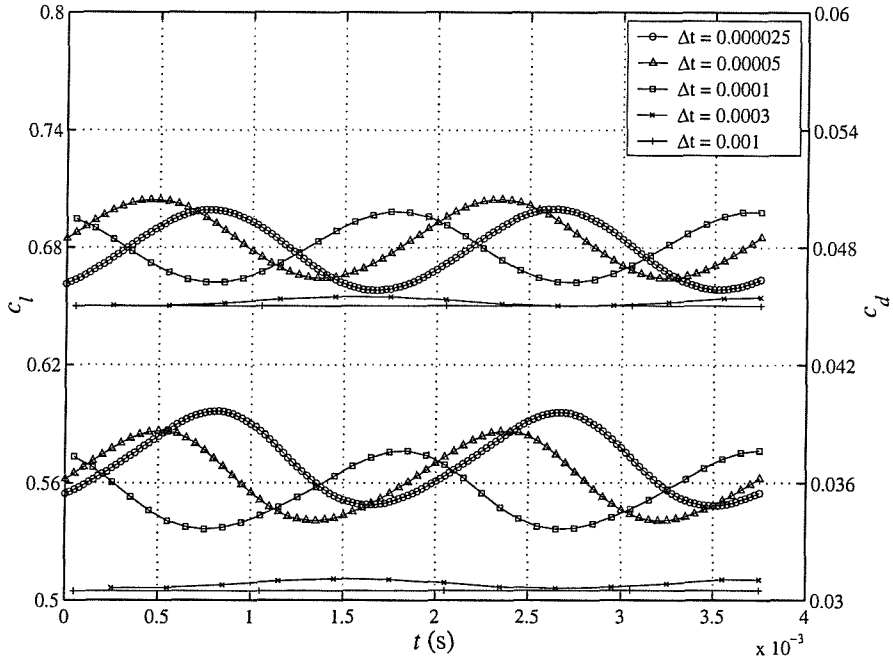

Figure 51: 4% Gurney time-accurate performance response over two cycles, $\alpha = 0$ deg, $R_n = 0.85 \times 10^6$

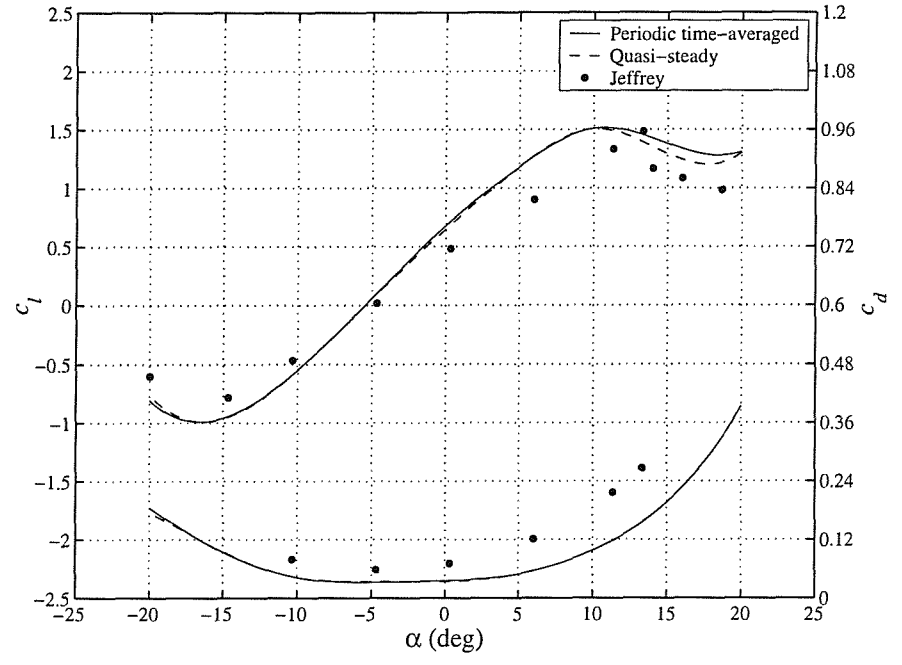

Figure 52: 4% Gurney time-averaged performance, $R_n = 0.85 \times 10^6$

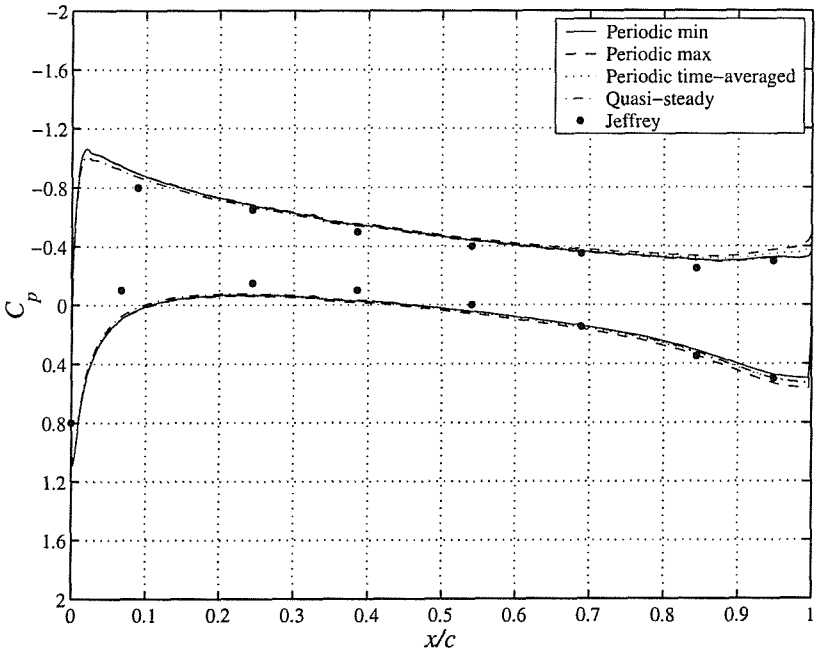

Figure 53: 4% Gurney time-accurate Cp distributions, $\alpha = 0$ deg, $R_n = 0.85 \times 10^6$

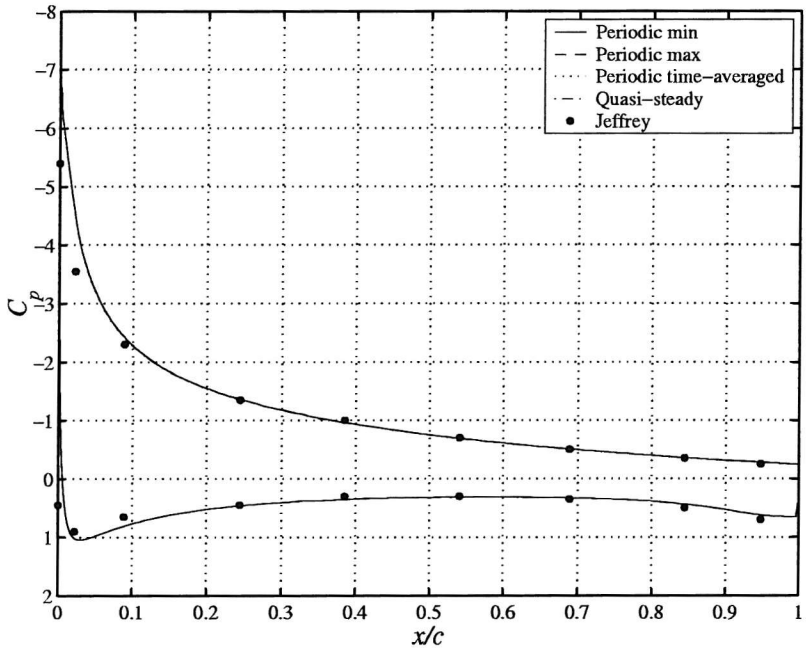

Figure 54: 4% Gurney time-accurate Cp distributions, $\alpha = 10$ deg, $R_n = 0.85 \times 10^6$

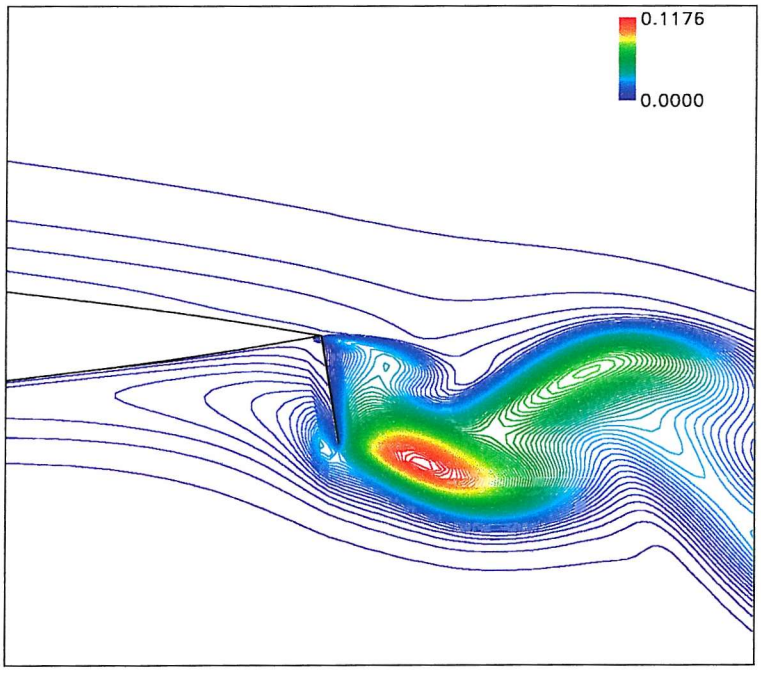

Figure 55: 4% Gurney time-accurate Reynolds stresses $\overline{u'^2}/U_\infty^2 = \overline{v'^2}/U_\infty^2$, $\alpha = 0$ deg, $R_n = 0.85 \times 10^6$

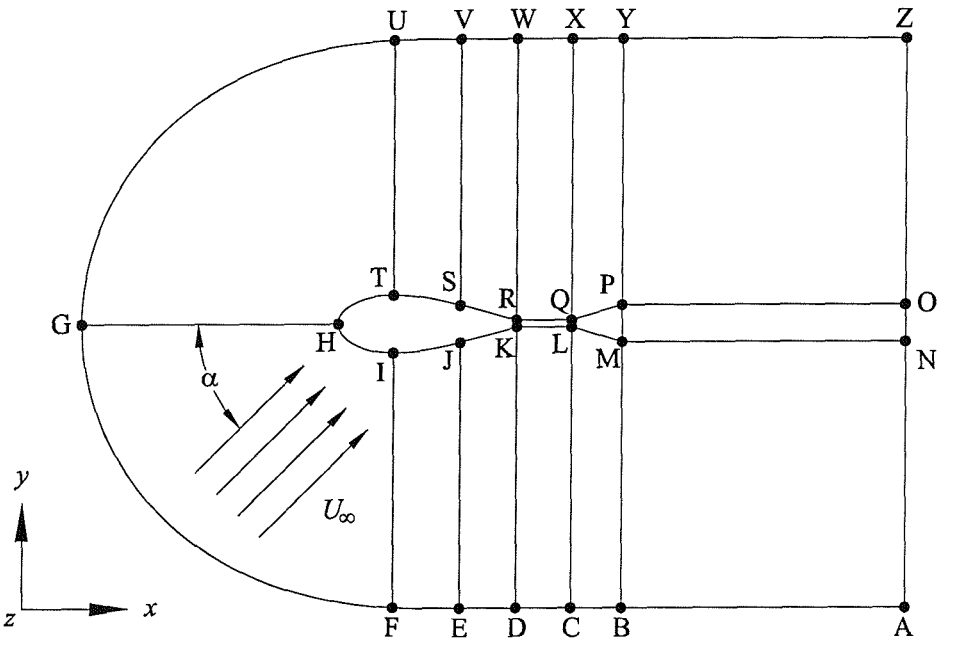

Figure 56: Schilling boundary conditions

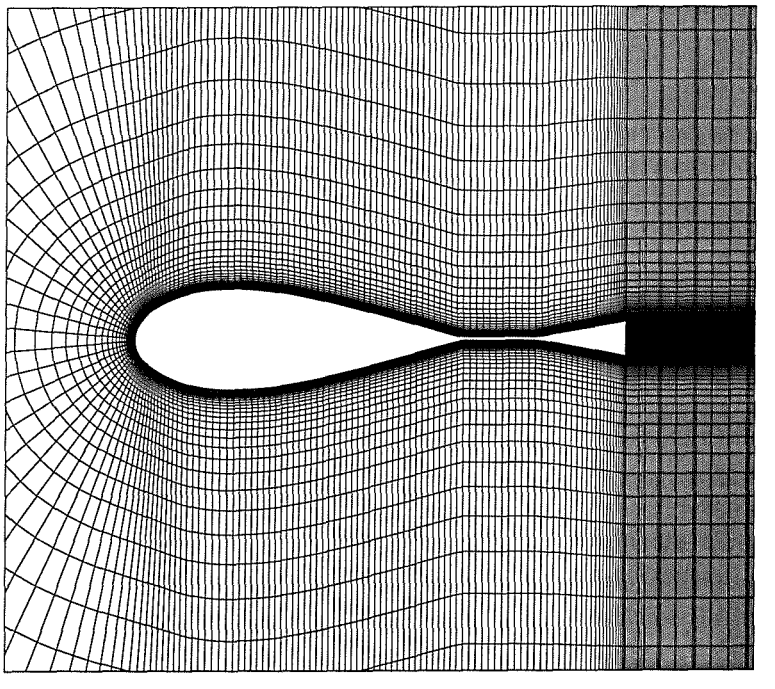

Figure 57: Schilling Grid

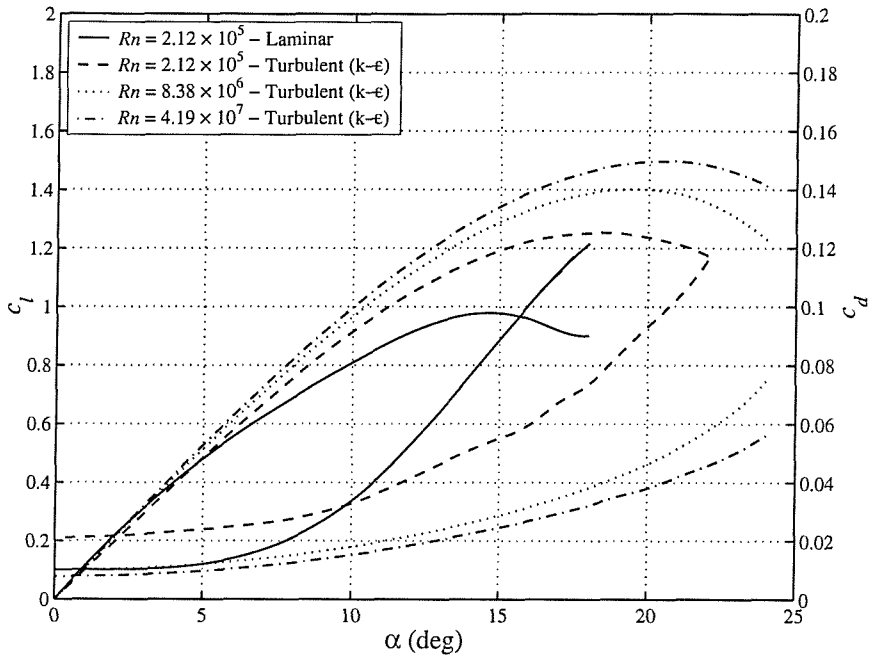

Figure 58: NACA 0020 performance at different Reynolds numbers

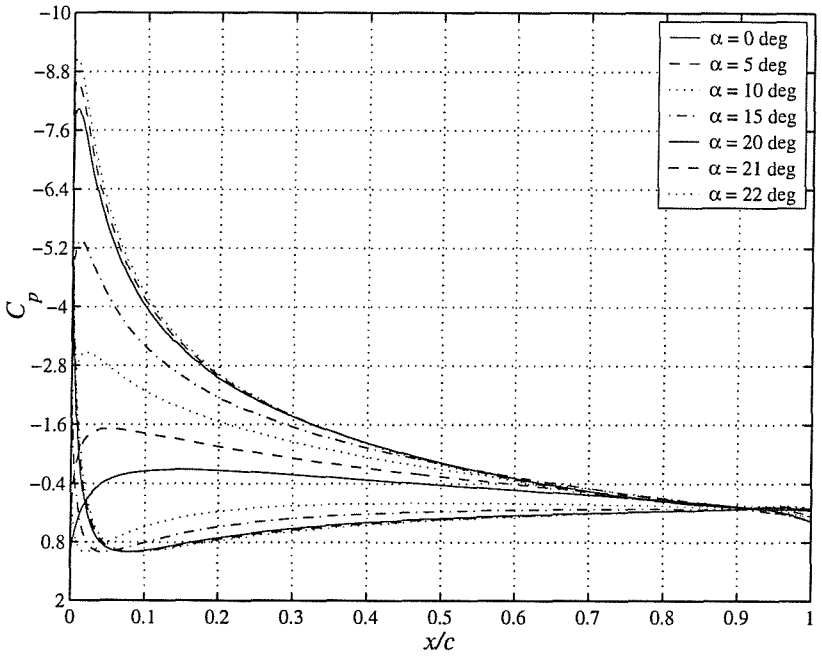

Figure 59: NACA 0020 C_p distribution, $R_n = 4.19 \times 10^7$

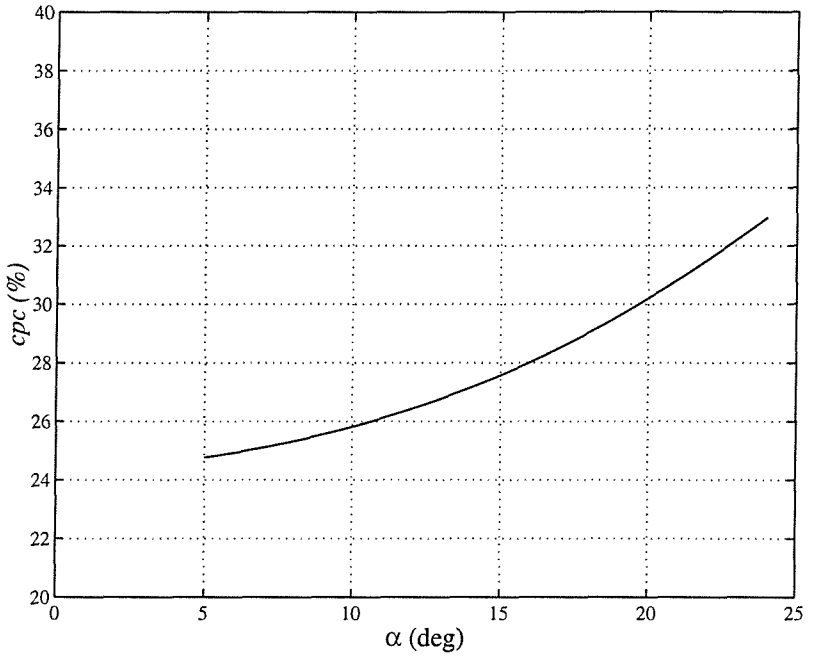

Figure 60: NACA 0020 centre of pressure variation, $R_n = 4.19 \times 10^7$

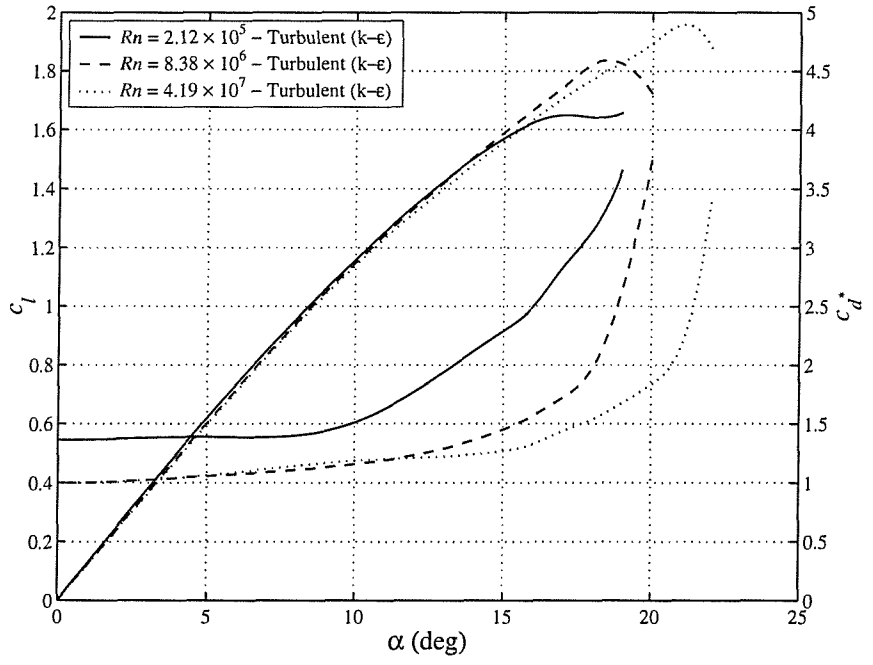

Figure 61: 10 deg T.E. Schilling under-converged steady state performance at different Reynolds numbers

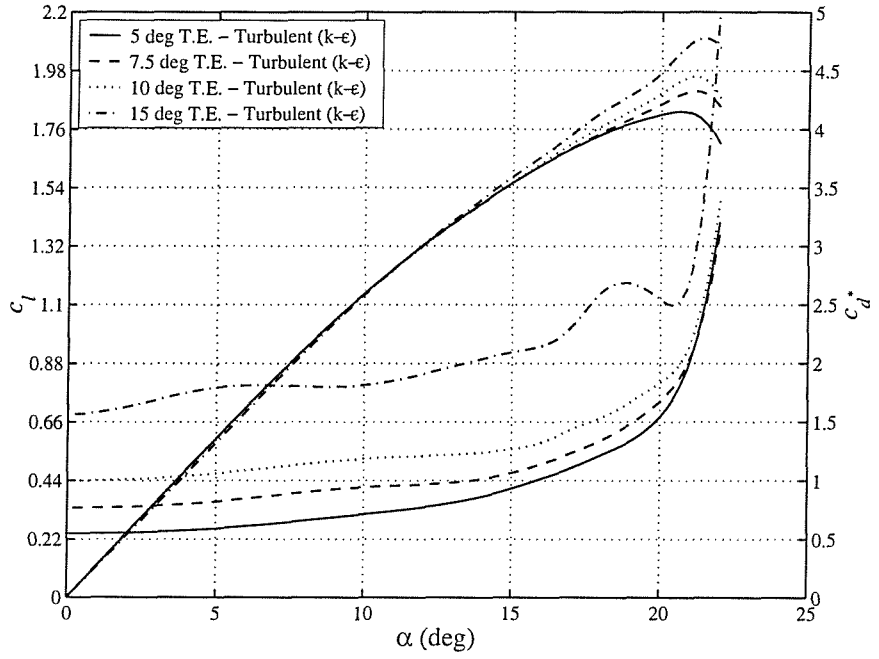

Figure 62: Schilling T.E. effect on under-converged steady state performance, $R_n = 4.19 \times 10^7$

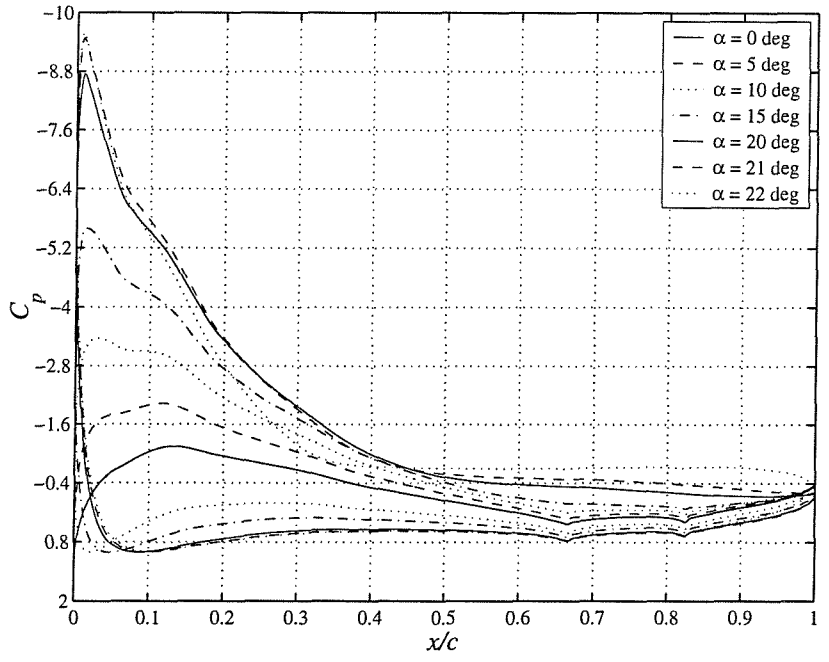

Figure 63: 10 deg T.E. Schilling under-converged steady state C_p distribution, $R_n = 4.19 \times 10^7$

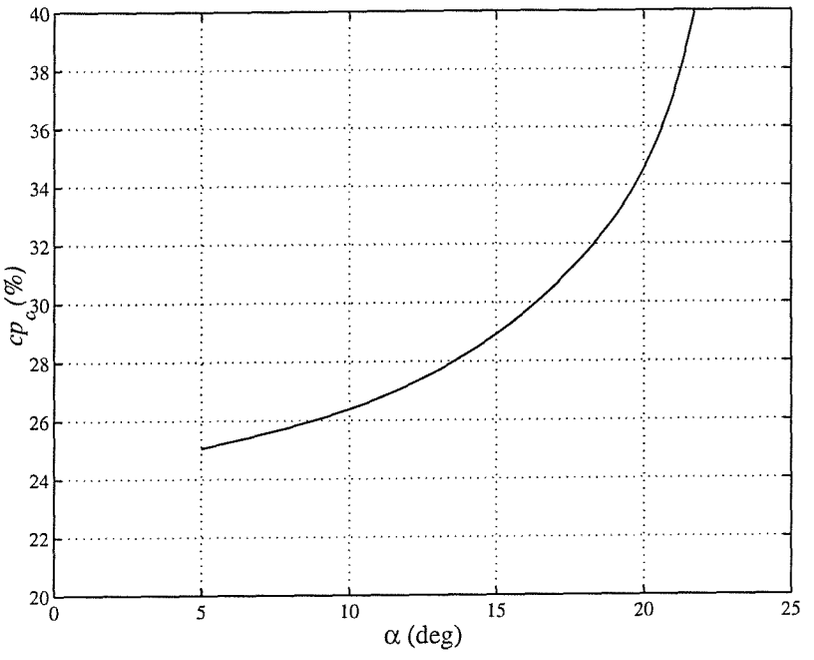

Figure 64: 10 deg T.E. Schilling under-converged steady state centre of pressure variation, $R_n = 4.19 \times 10^7$

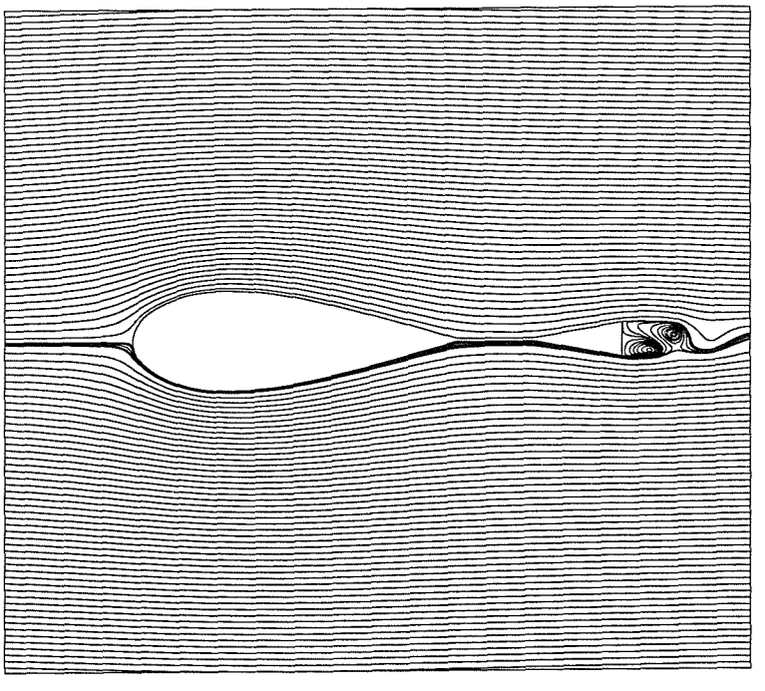

Figure 65: 10 deg T.E. Schilling under-converged steady state streamlines, $\alpha = 0$ deg, $R_n = 4.19 \times 10^7$

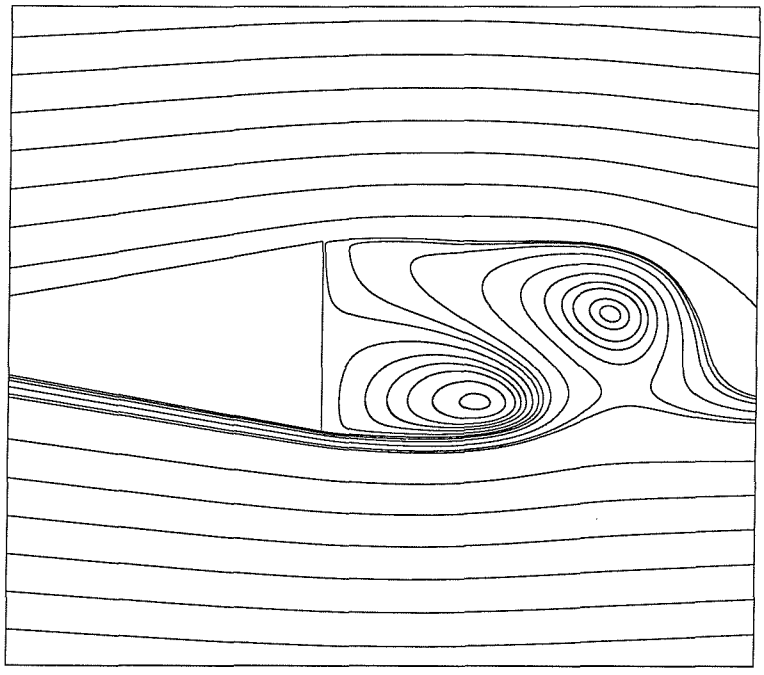

Figure 66: 10 deg T.E. Schilling under-converged steady state close up streamlines, $\alpha = 0$ deg, $R_n = 4.19 \times 10^7$

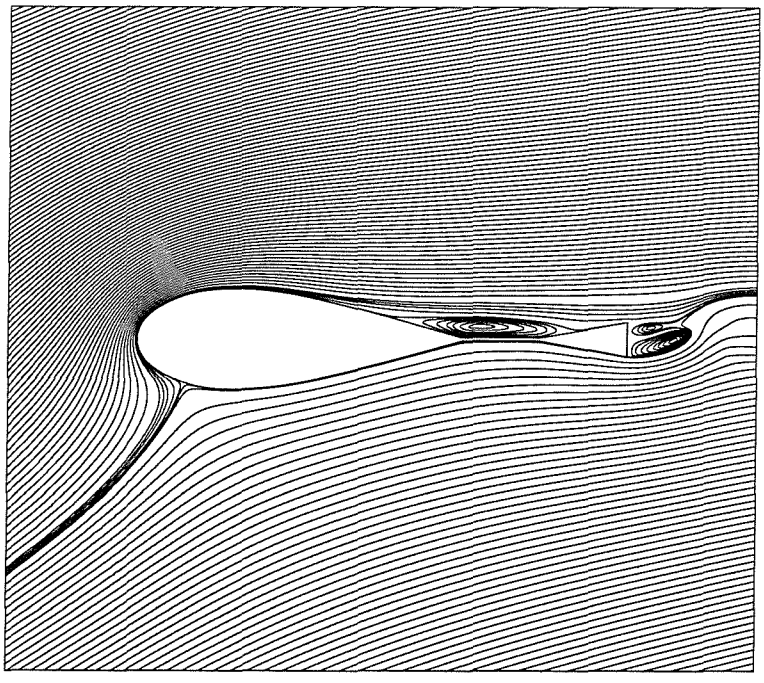

Figure 67: 10 deg T.E. Schilling under-converged steady state streamlines, $\alpha = 21$ deg, $R_n = 4.19 \times 10^7$

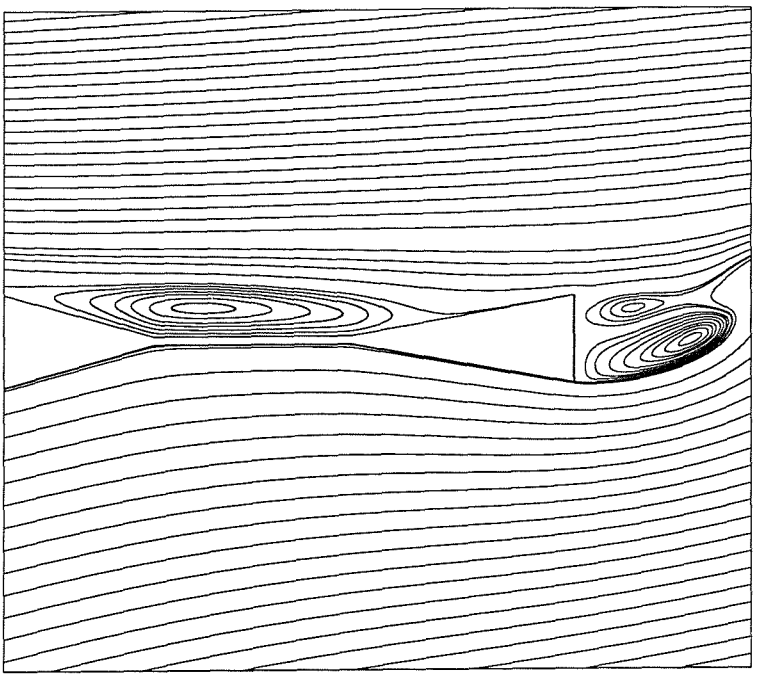

Figure 68: 10 deg T.E. Schilling under-converged steady state close up streamlines, $\alpha = 21$ deg, $R_n = 4.19 \times 10^7$

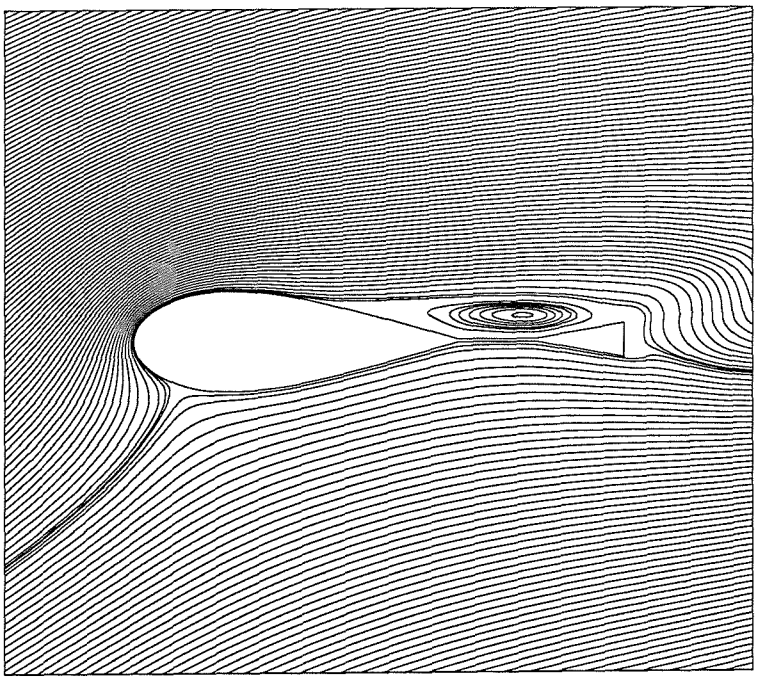

Figure 69: 10 deg T.E. Schilling under-converged steady state streamlines, $\alpha = 22$ deg, $R_n = 4.19 \times 10^7$

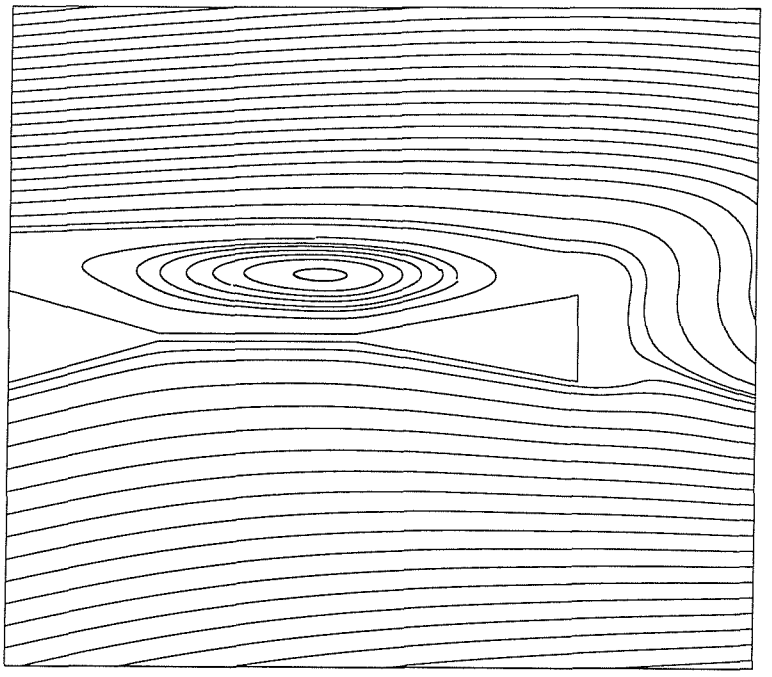

Figure 70: 10 deg T.E. Schilling under-converged steady state close up streamlines, $\alpha = 22$ deg, $R_n = 4.19 \times 10^7$

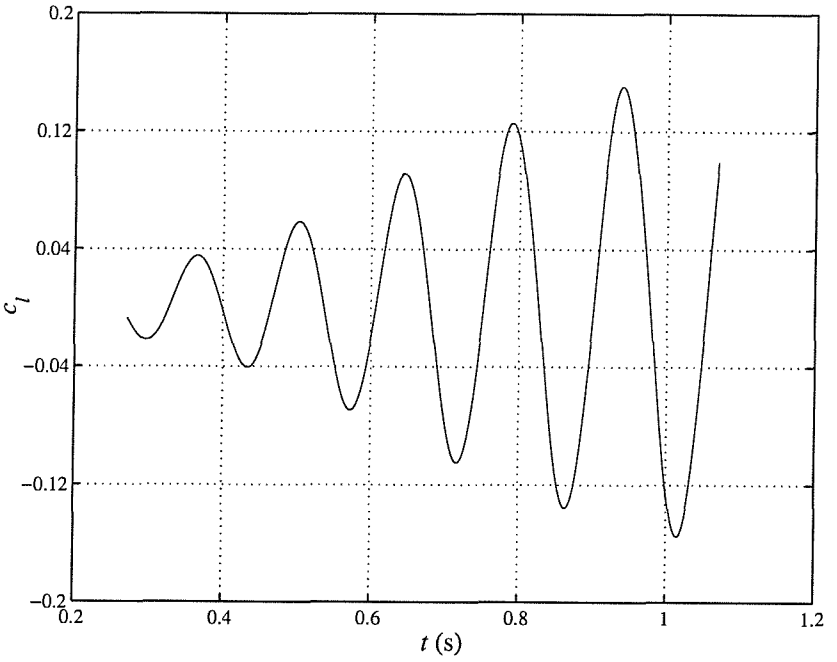

Figure 71: 10 deg T.E. Schilling time-accurate c_l, $\alpha = 0$ deg, $\Delta t = 0.003$ s, $R_n = 4.19 \times 10^7$

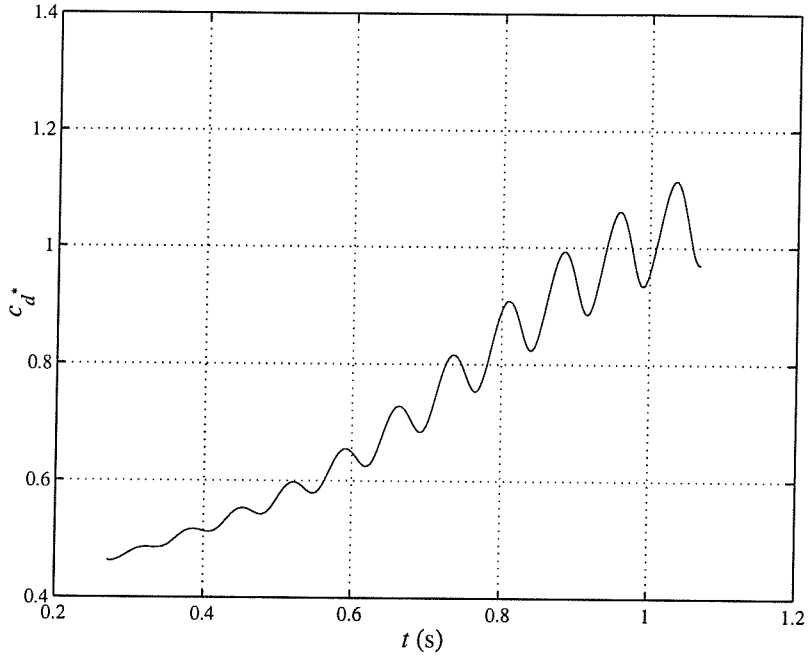

Figure 72: 10 deg T.E. Schilling time-accurate c_d, $\alpha = 0$ deg, $\Delta t = 0.003$ s, $R_n = 4.19 \times 10^7$

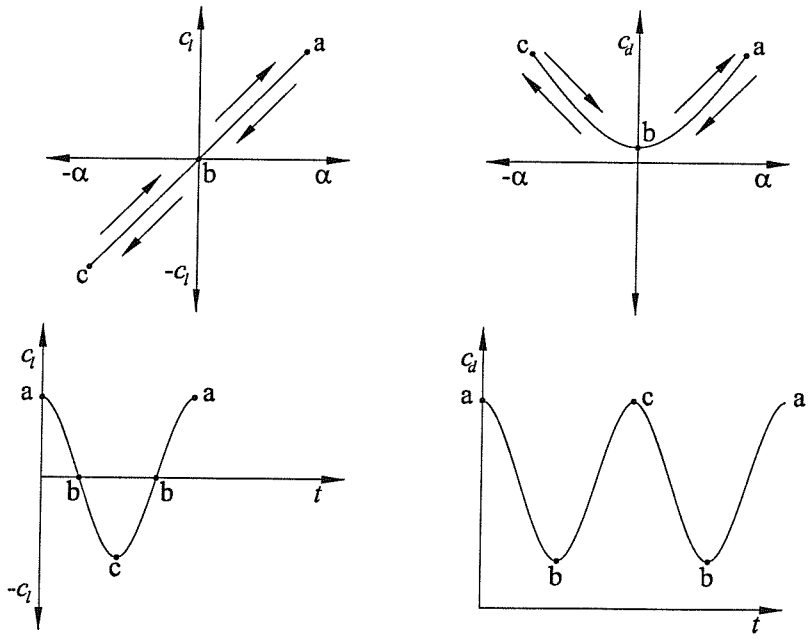

Figure 73: Response curve diagram

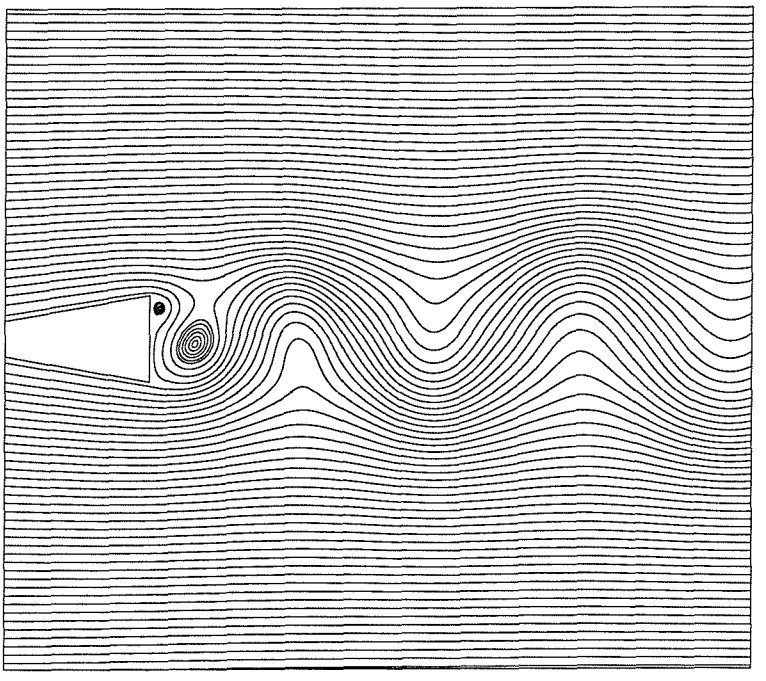

Figure 74: 10 deg T.E. Schilling time-accurate close up streamlines, $\alpha = 0$ deg, $\Delta t = 0.003$ s, $R_n = 4.19 \times 10^7$

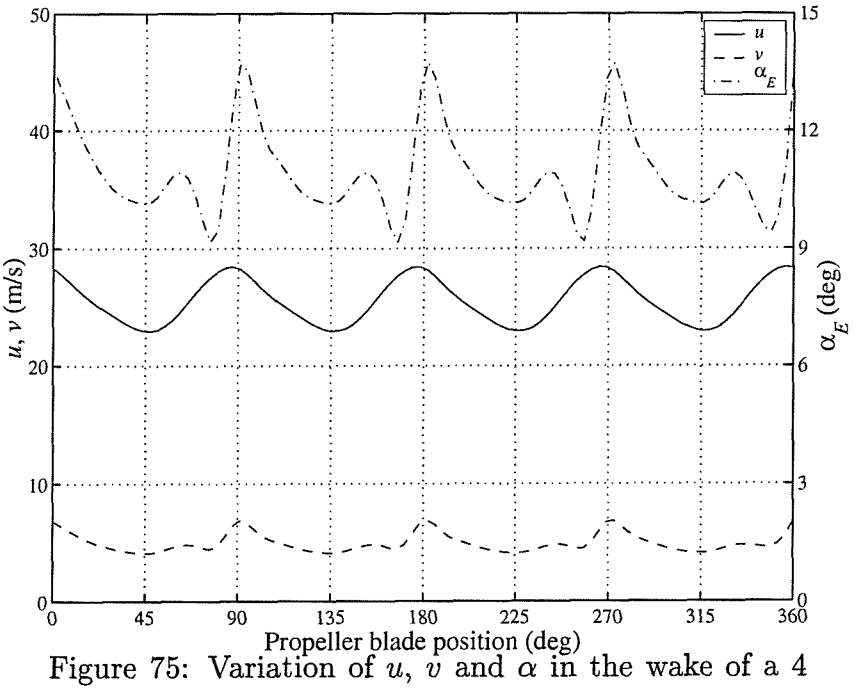

Figure 75: Variation of u, v and α in the wake of a 4 bladed propeller, $X/D = 0.39$, $r/D = 0.35$, $J = 0.35$ Turnock [21]

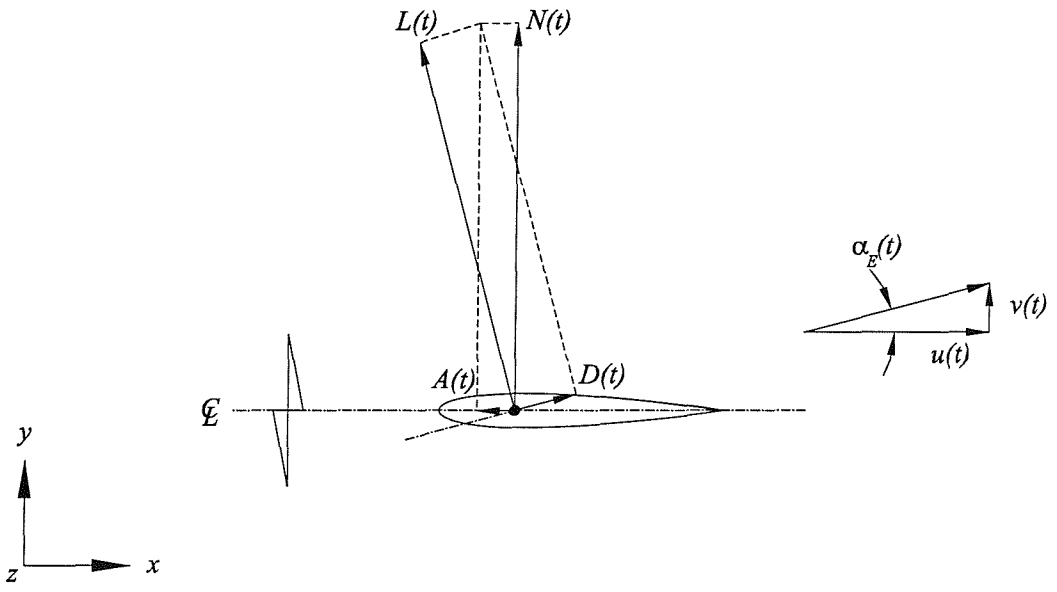

Figure 76: Resolution of lift and drag forces in the normal and axial directions

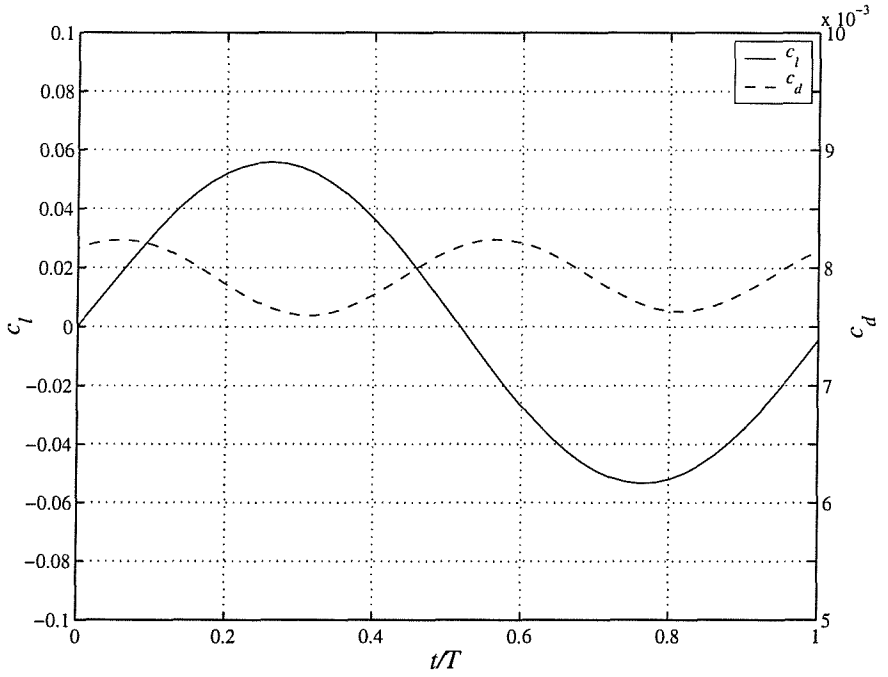

Figure 77: NACA 0020 c_l and c_d response history, $u = 10$ m/s, $v_0 = 0.2$ m/s, $k = 0.5$

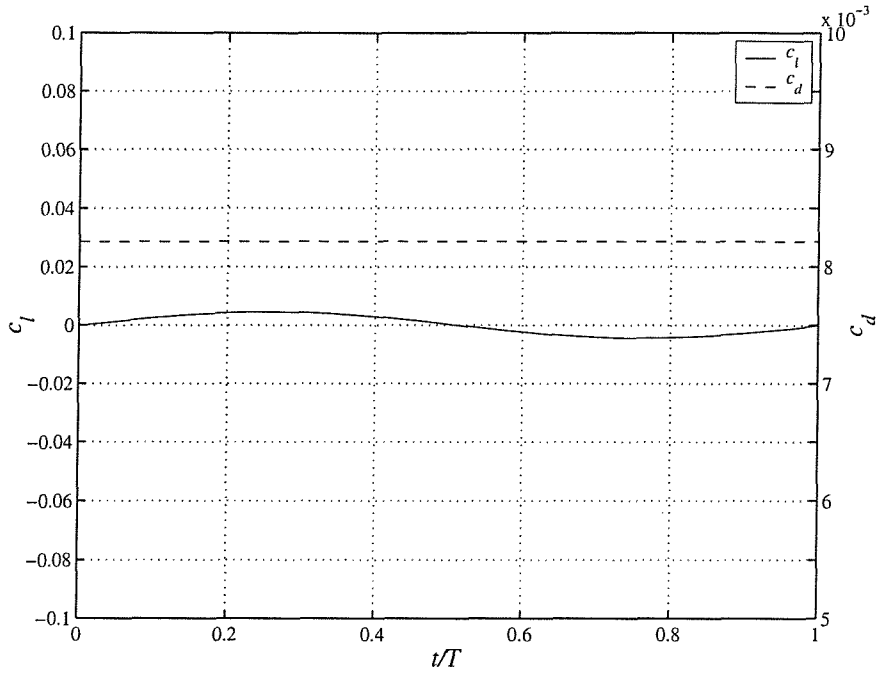

Figure 78: NACA 0020 c_l and c_d response history, $u =$ 10 m/s, $v_0 = 0.2$ m/s, $k = 5$

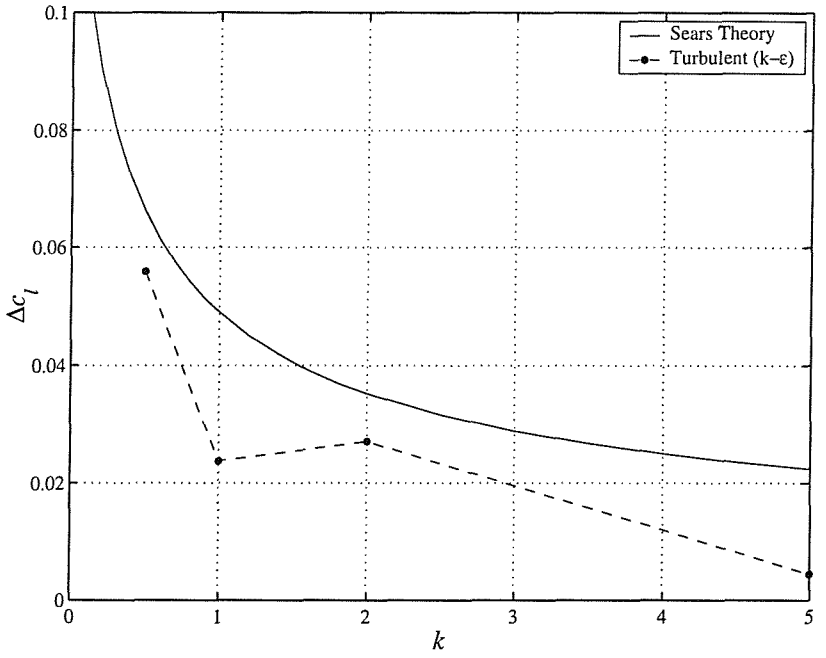

Figure 79: NACA 0020 c_l response amplitude, $u = 10$ m/s, $v_0 = 0.2$ m/s

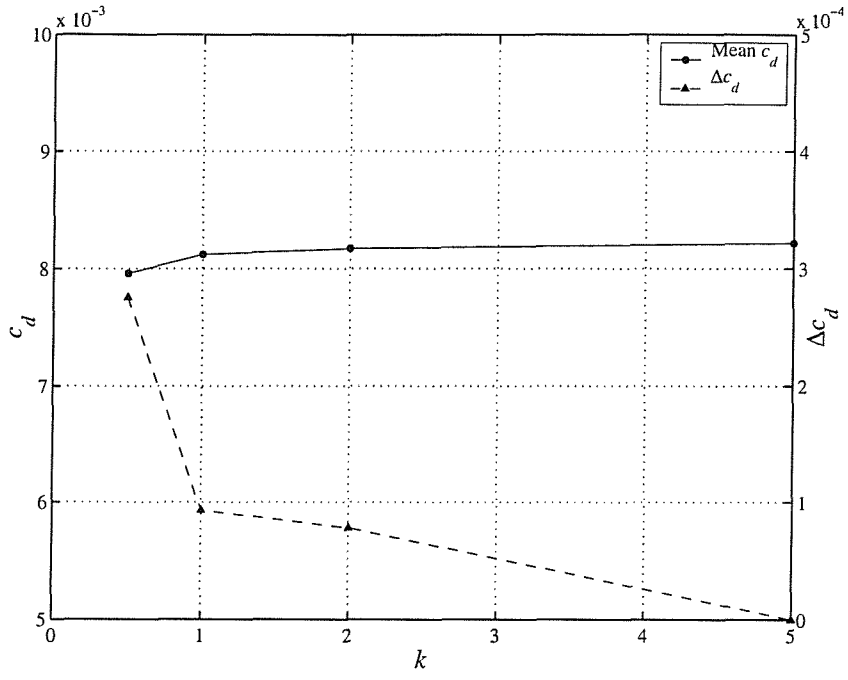

Figure 80: NACA 0020 c_d response amplitude and mean c_d, $u = 10$ m/s, $v_0 = 0.2$ m/s

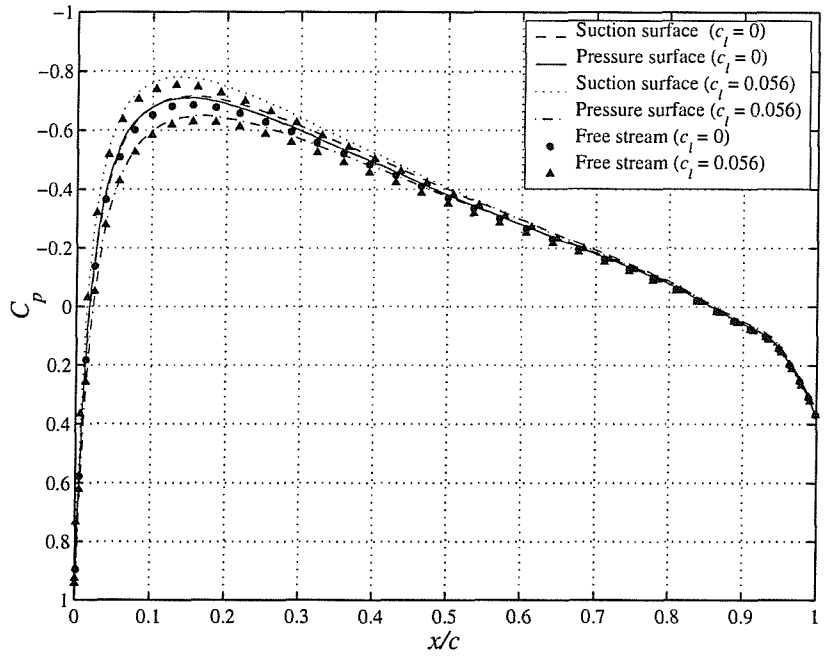

Figure 81: NACA 0020 C_p distribution, $u = 10$ m/s, $v_0 = 0.2$ m/s, $k = 0.5$

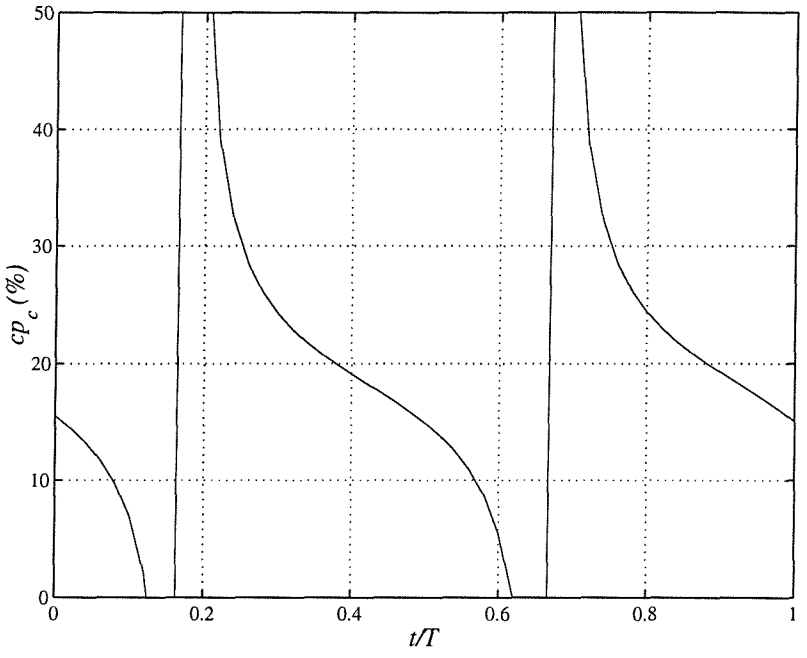

Figure 82: NACA 0020 centre of pressure variation, $u =$ 10 m/s, $v_0 = 0.2$ m/s, $k = 0.5$

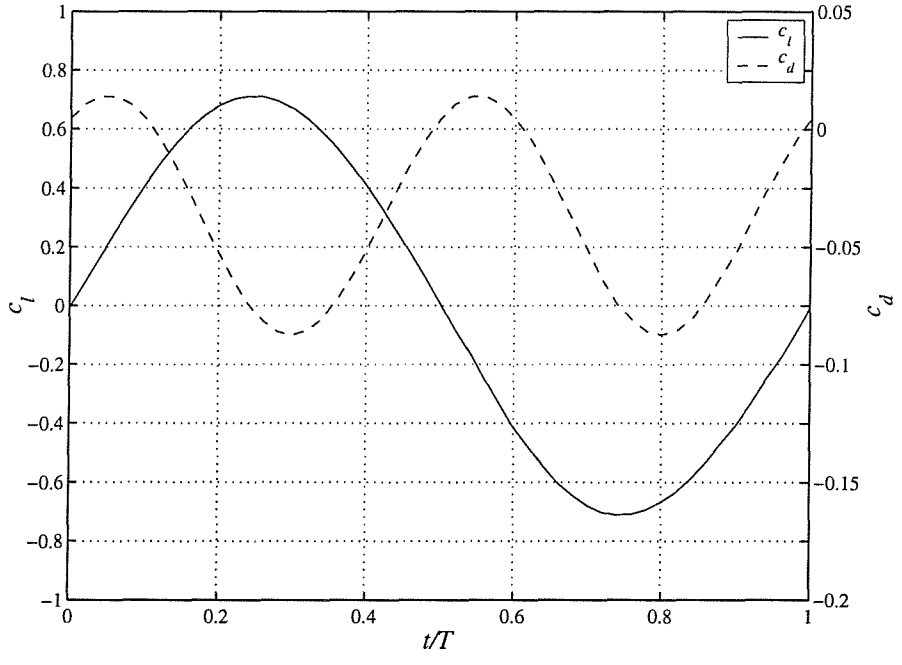

Figure 83: NACA 0020 c_l and c_d response history, $u =$ 10 m/s, $v_0 = 2.5$ m/s, $k = 0.5$

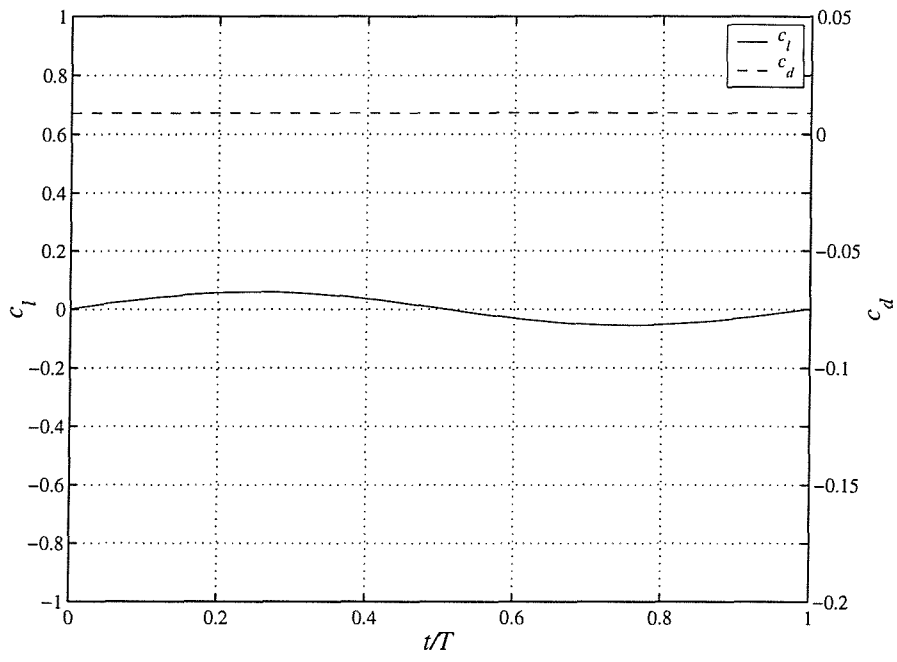

Figure 84: NACA 0020 c_l and c_d response history, $u =$ 10 m/s, $v_0 = 2.5$ m/s, $k = 5$

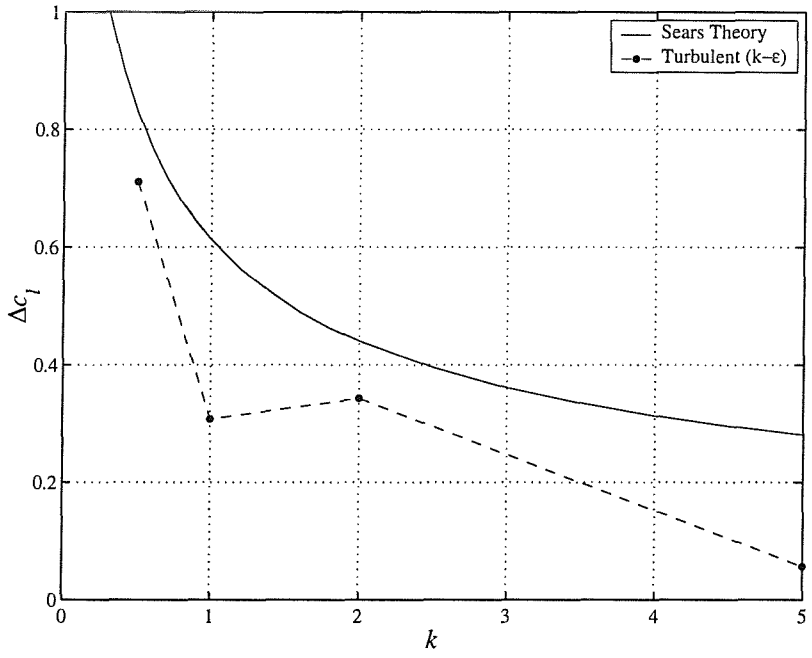

Figure 85: NACA 0020 c_l response amplitude, $u = 10$ m/s, $v_0 = 2.5$ m/s

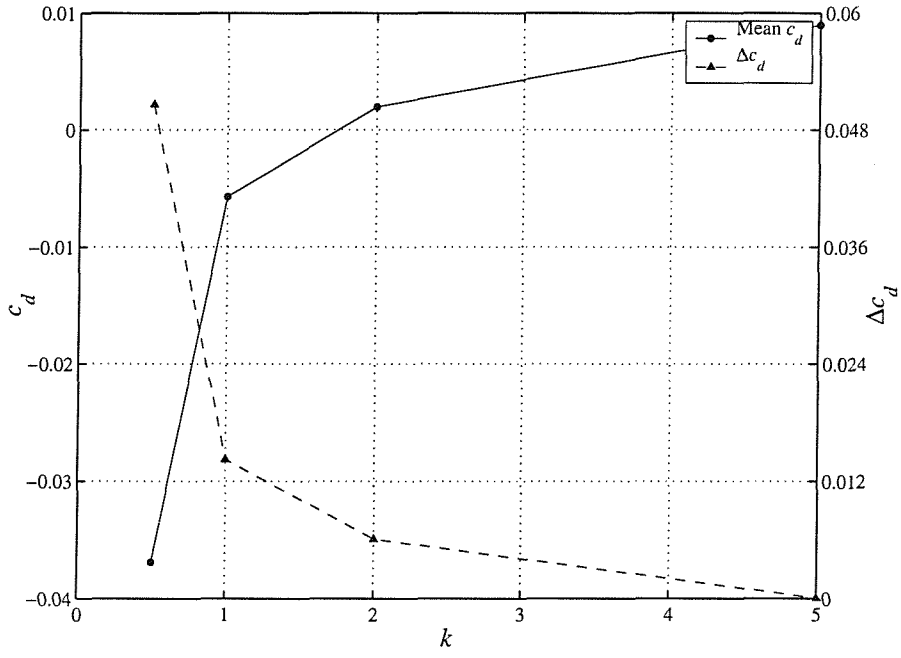

Figure 86: NACA 0020 c_d response amplitude and mean c_d, $u = 10$ m/s, $v_0 = 2.5$ m/s

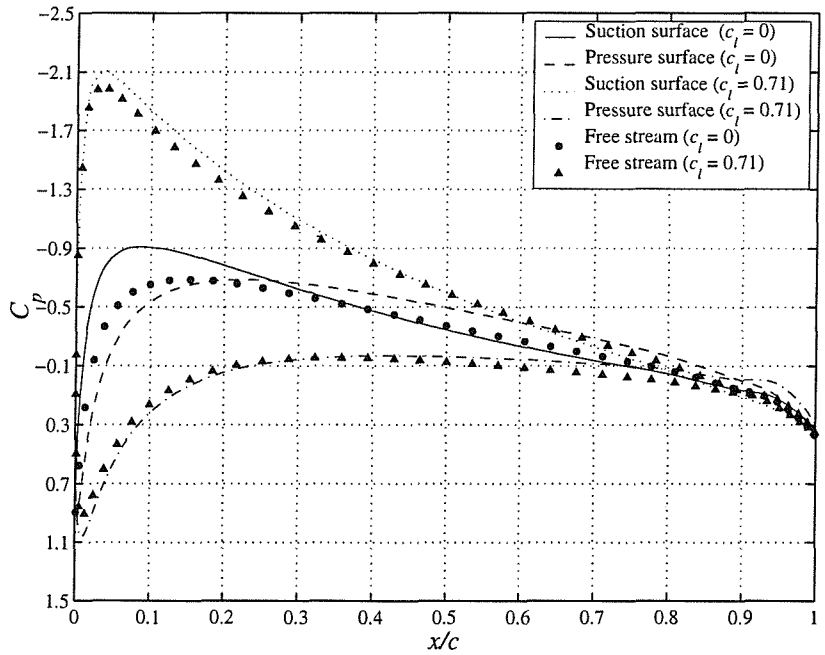

Figure 87: NACA 0020 C_p distribution, $u = 10$ m/s, $v_0 = 2.5$ m/s, $k = 0.5$

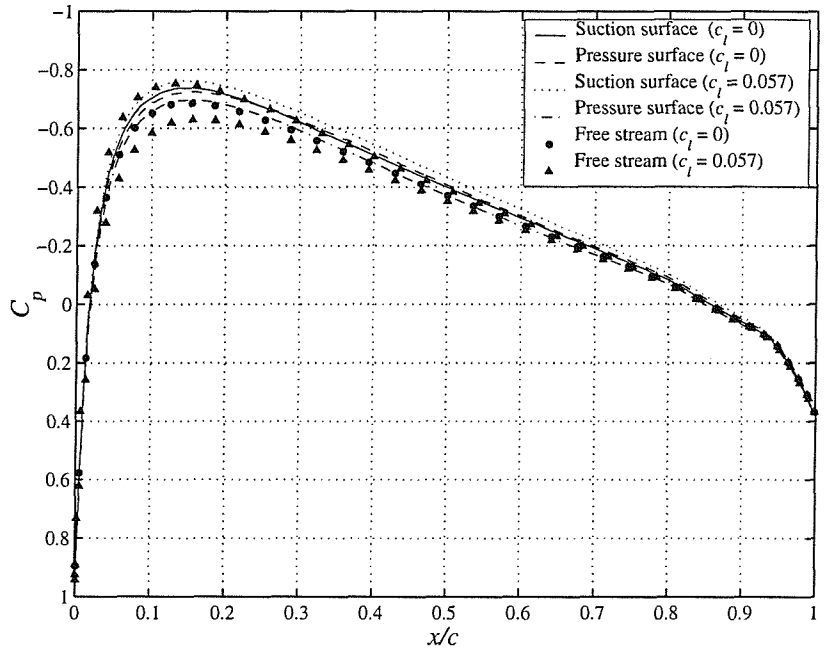

Figure 88: NACA 0020 C_p distribution, $u = 10$ m/s, $v_0 = 2.5$ m/s, $k = 5$

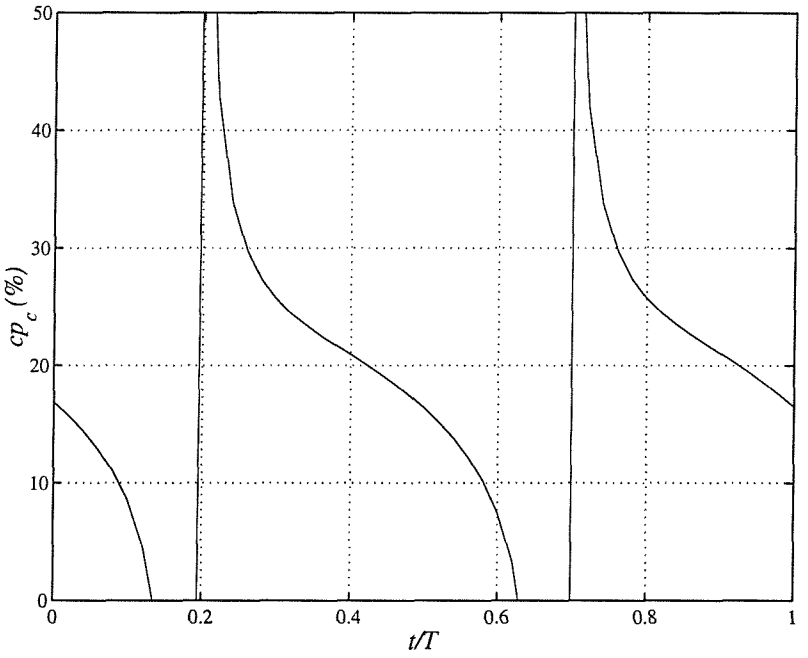

Figure 89: NACA 0020 centre of pressure variation, $u = 10$ m/s, $v_0 = 2.5$ m/s, $k = 0.5$

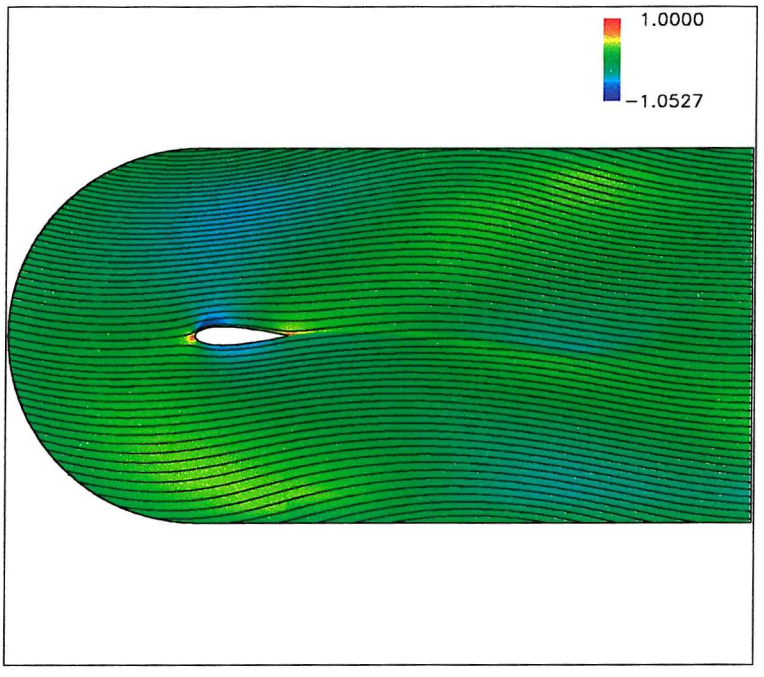

Figure 90: NACA 0020 streamlines and C_p plot, $u = 10$ m/s, $v_0 = 2.5$ m/s, $k = 0.5$, $t/T = 0.24$

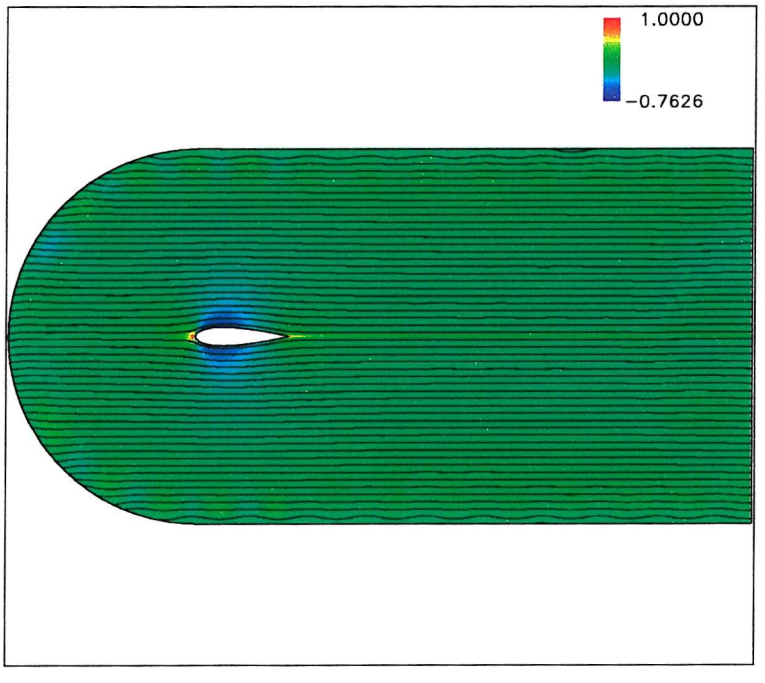

Figure 91: NACA 0020 streamlines and C_p plot, $u = 10$ m/s, $v_0 = 2.5$ m/s, $k = 5$, $t/T = 0.70$

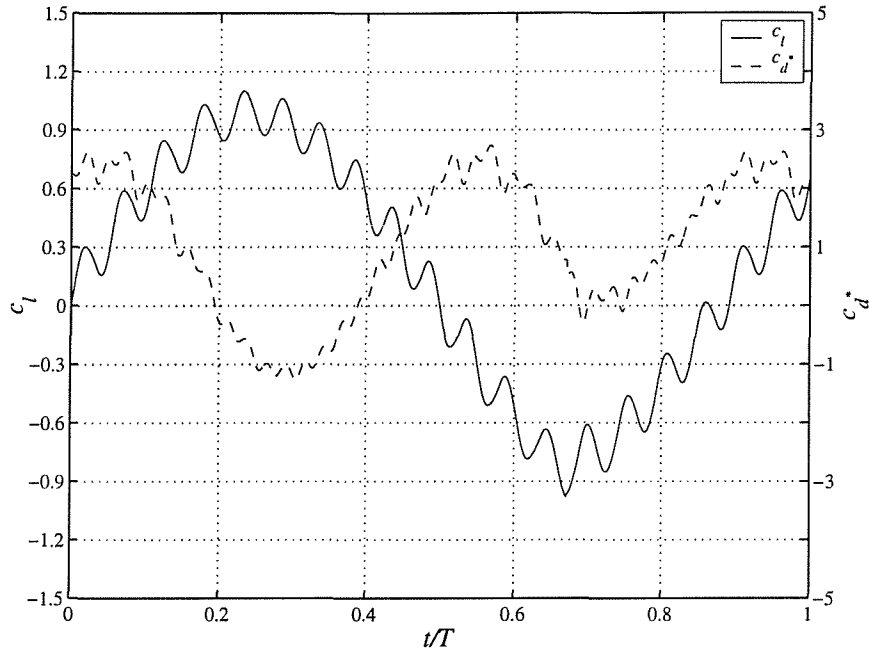

Figure 92: 10 deg T.E. Schilling c_l and c_d response history, $u = 10$ m/s, $v_0 = 2.5$ m/s, $k = 0.5$

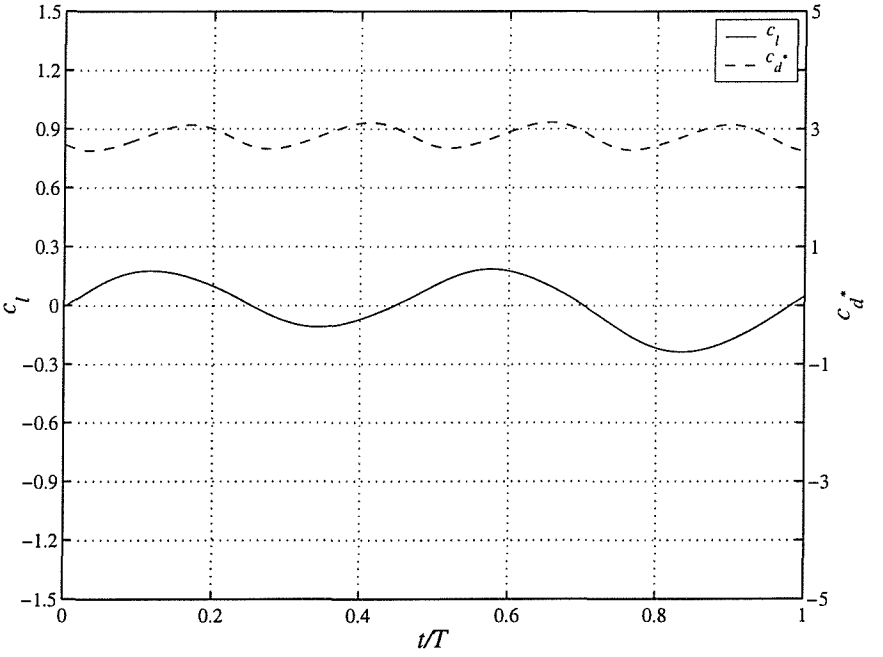

Figure 93: 10 deg T.E. Schilling c_l and c_d response history, $u = 10$ m/s, $v_0 = 2.5$ m/s, $k = 5$

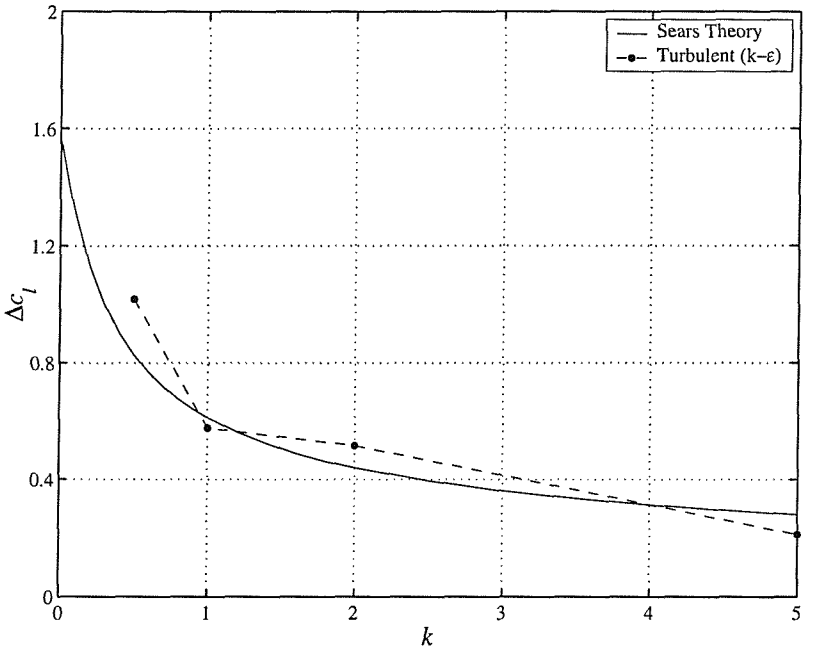

Figure 94: 10 deg T.E. Schilling c_l response amplitude, $u = 10$ m/s, $v_0 = 2.5$ m/s

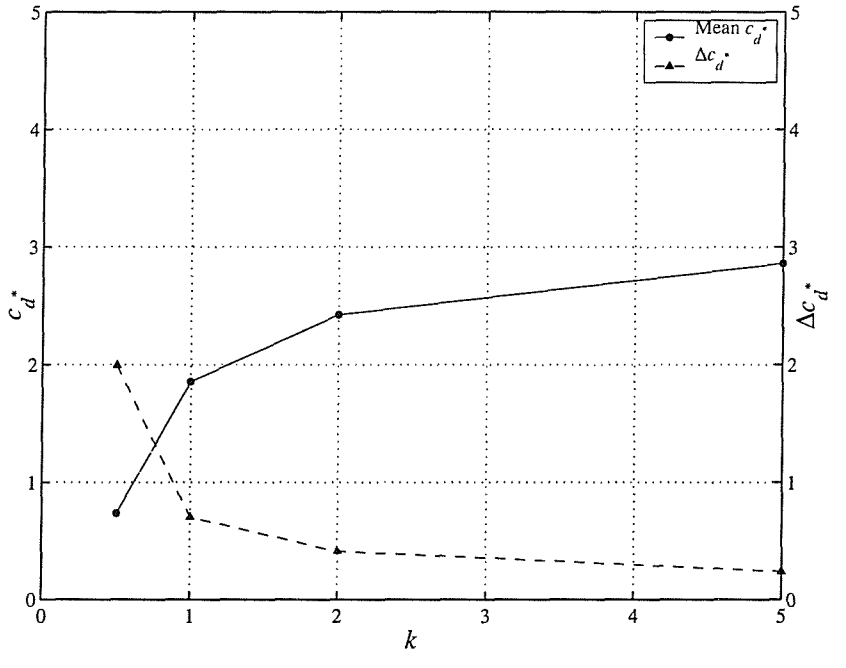

Figure 95: 10 deg T.E. Schilling c_d response amplitude and mean c_d, $u = 10$ m/s, $v_0 = 2.5$ m/s

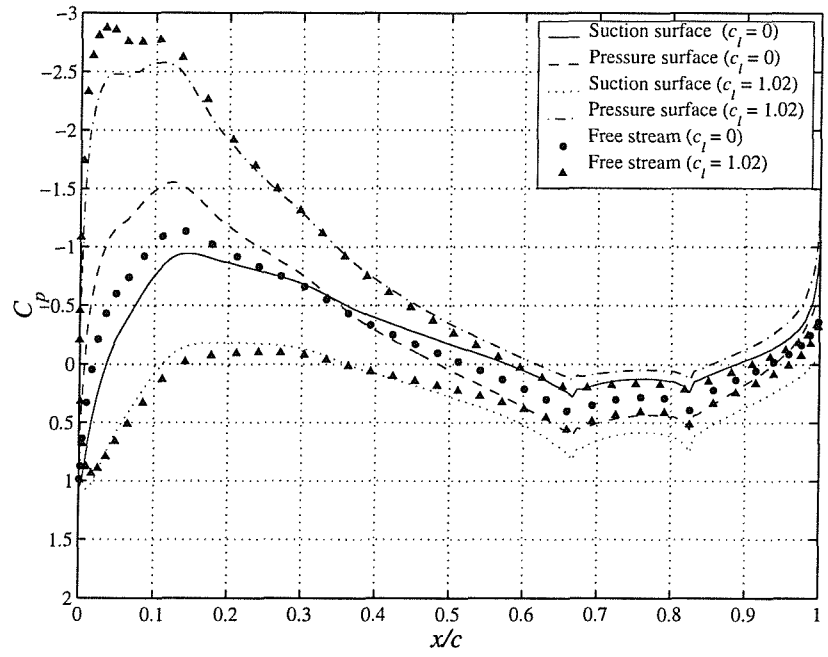

Figure 96: 10 deg T.E. Schilling C_p distribution, $u = 10$ m/s, $v_0 = 2.5$ m/s, $k = 0.5$

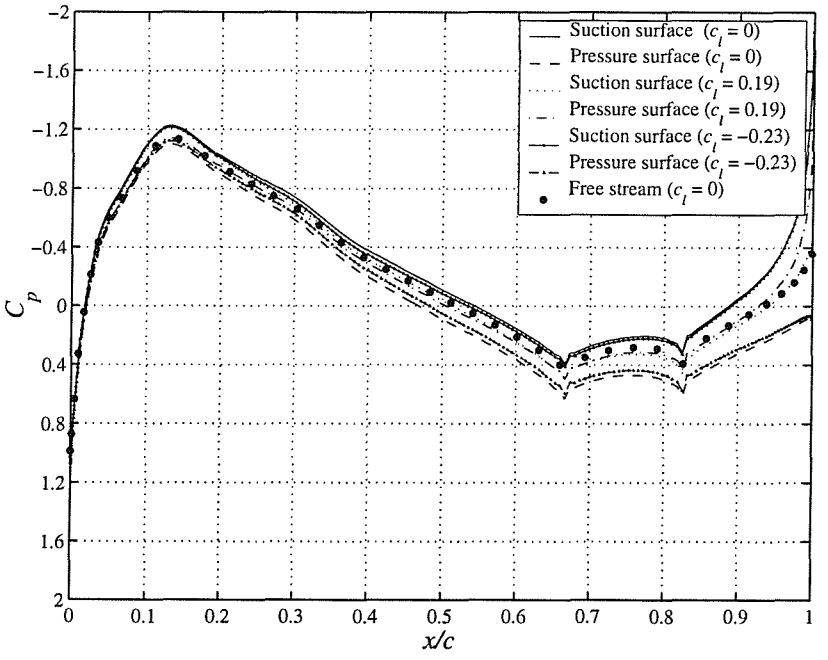

Figure 97: 10 deg T.E. Schilling C_p distribution, $u = 10$ m/s, $v_0 = 2.5$ m/s, $k = 5$

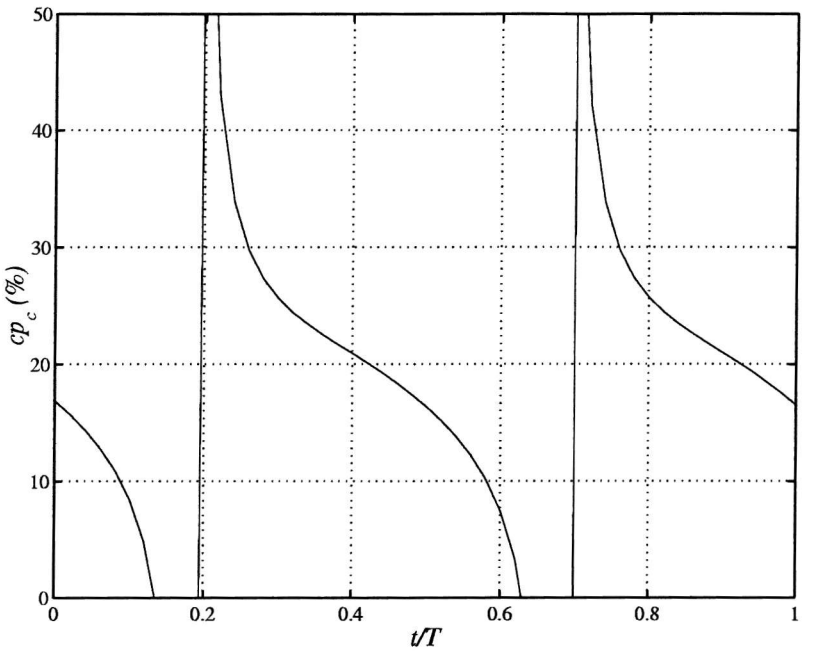

Figure 98: 10 deg T.E. Schilling centre of pressure variation, $u = 10$ m/s, $v_0 = 2.5$ m/s, $k = 0.5$

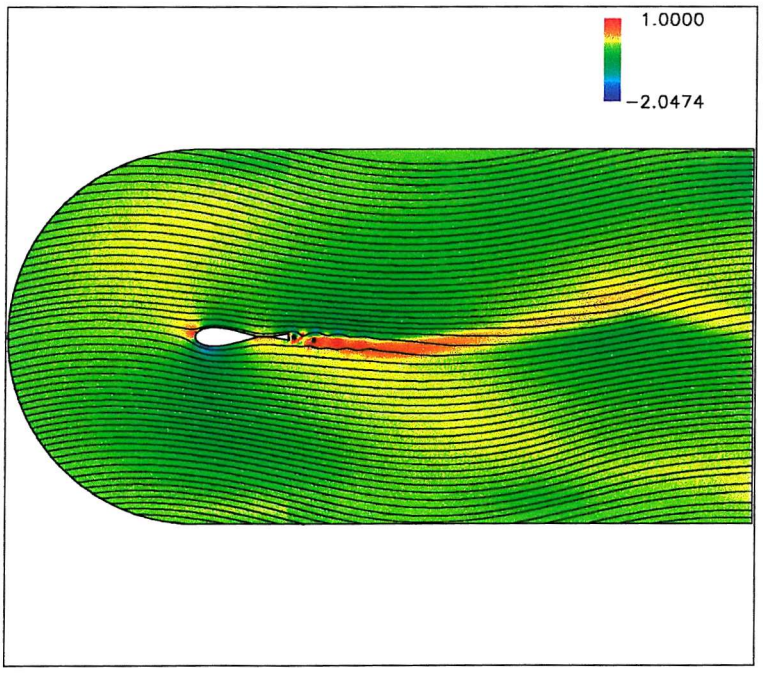

Figure 99: 10 deg T.E. Schilling streamlines and C_p plot, $u = 10$ m/s, $v_0 = 2.5$ m/s, $k = 0.5$, $t/T = 0.70$

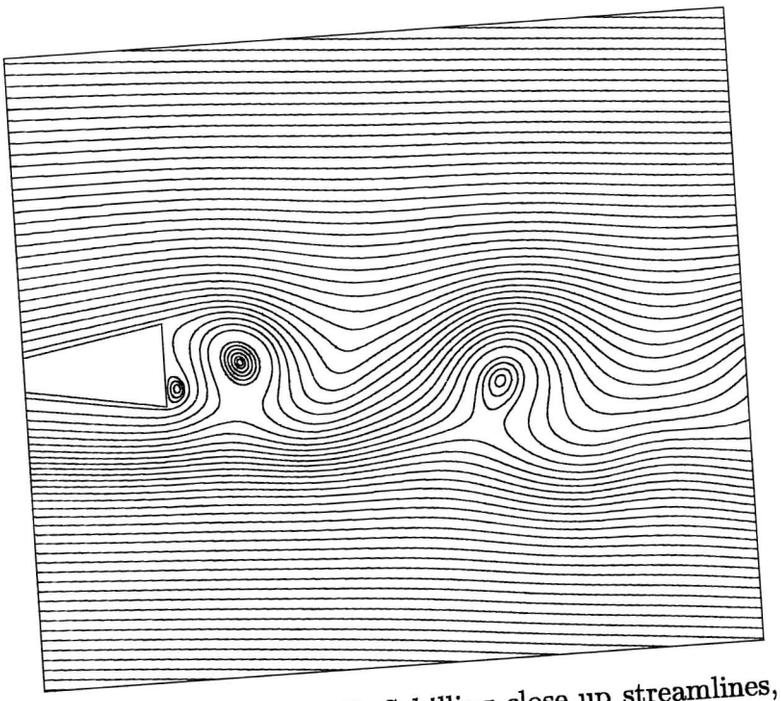

Figure 100: 10 deg T.E. Schilling close up streamlines, $u = 10$ m/s, $v_0 = 2.5$ m/s, $k = 0.5$, $t/T = 0.70$

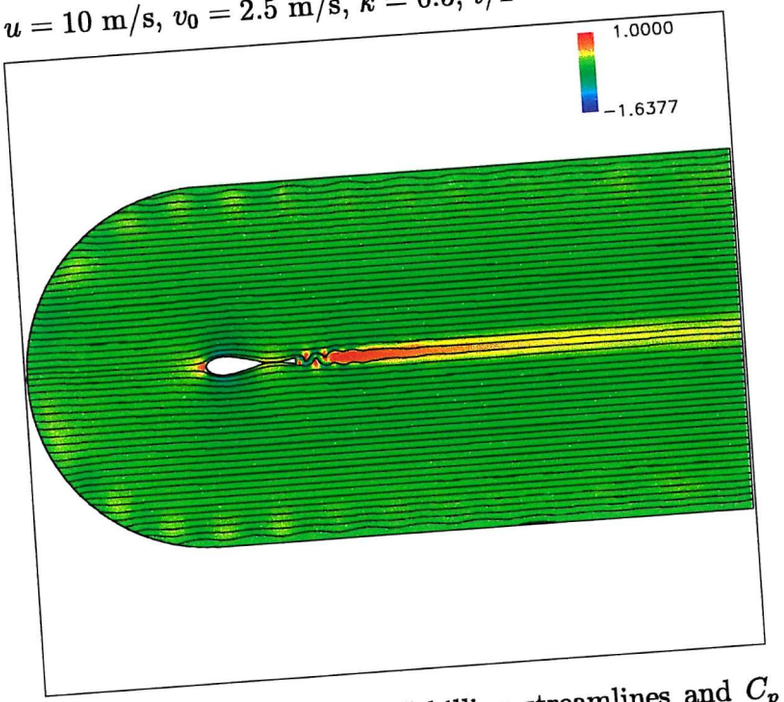

Figure 101: 10 deg T.E. Schilling streamlines and C_p plot, $u = 10$ m/s, $v_0 = 2.5$ m/s, $k = 5.0$, $t/T = 0.58$

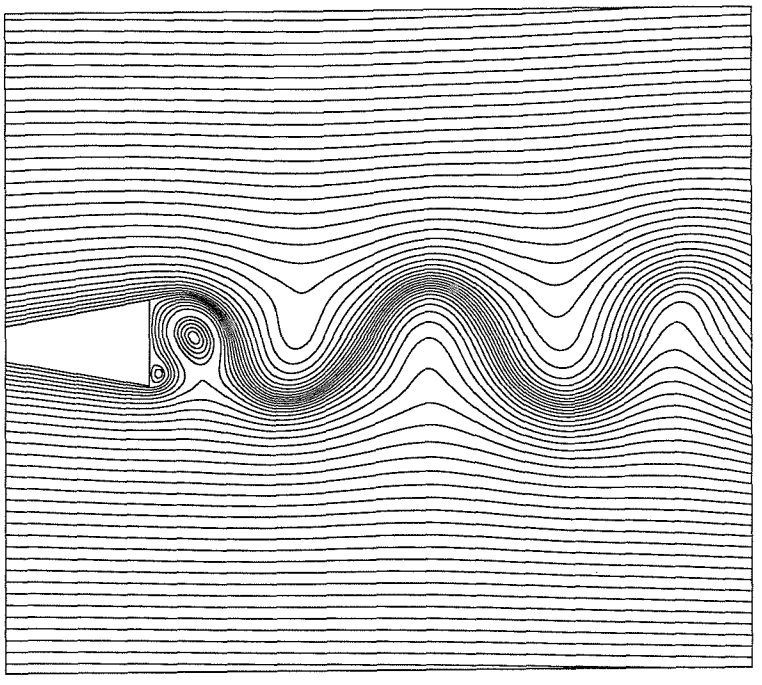

Figure 102: 10 deg T.E. Schilling close up streamlines, $u = 10$ m/s, $v_0 = 2.5$ m/s, $k = 5.0$, $t/T = 0.58$

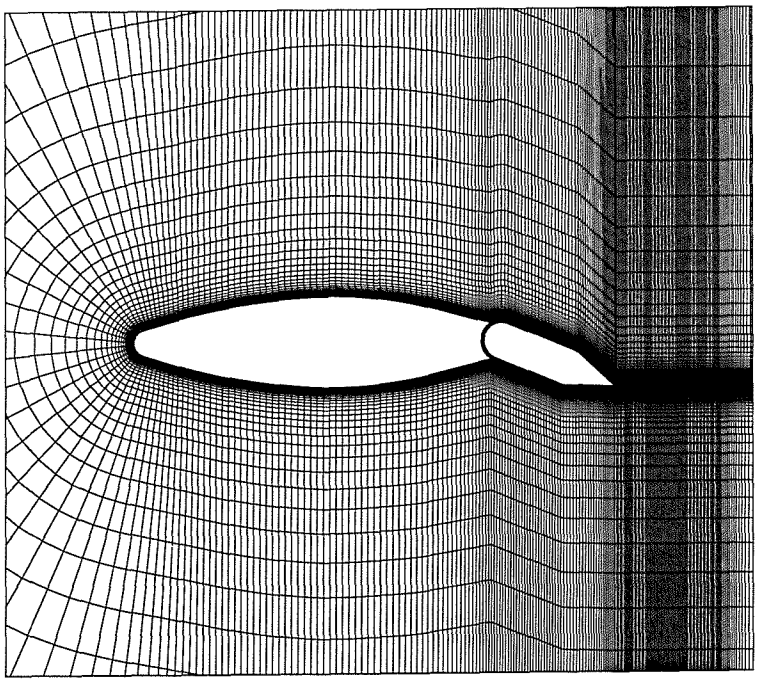

Figure 103: Example of a flapped rudder grid

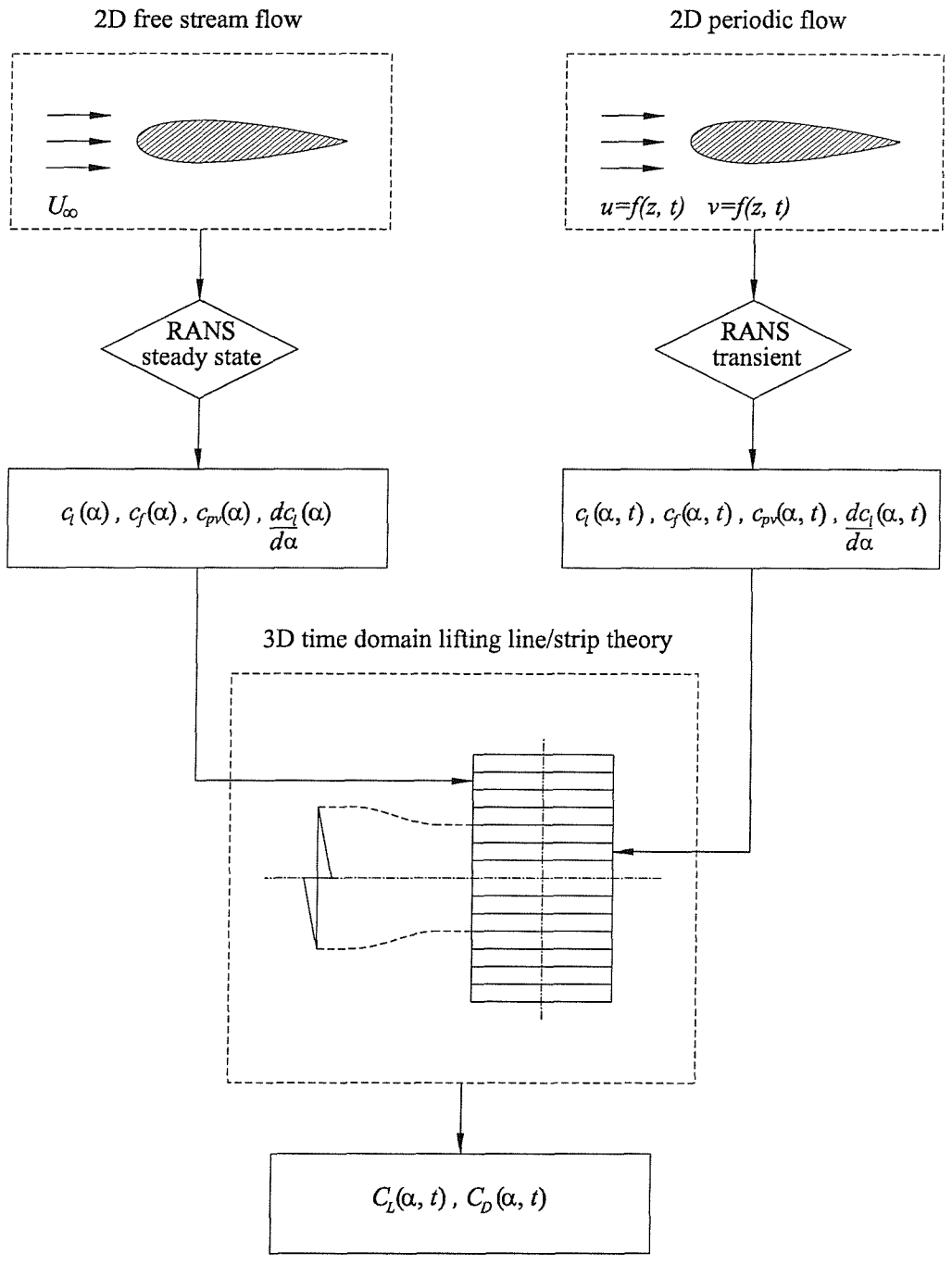

Figure 104: Proposed three-dimensional rudder performance prediction method

n = 25, r = 0.0909

Figure 105: Geometric progression distribution along an edge

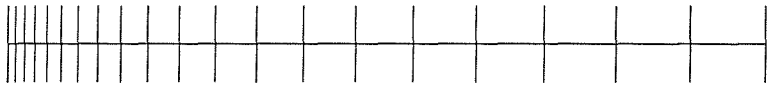

n = 21, p = 0.0364, q = 1.9656

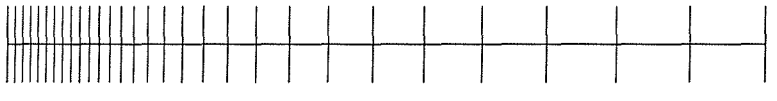

n = 30, p = 0.2821, q = 3.6611

Figure 106: Hyperbolic distributions along an edge